Leibniz Institute for
Astrophysics Potsdam

An inside out view of the coronae and winds of cool stars

Judy Chebly

"doctor rerum naturalium"

(Dr. rer. nat.)
in the scientific discipline of

Astrophysics

submitted to the
Faculty of Mathematics and Natural Sciences
of the University of Potsdam

Disputation: Potsdam, 2024

Supervisors:
Principal supervisor: Prof. Dr. Katja Poppenhäger
Second supervisor: Dr. Julián D. Alvarado-Gómez
Mentor: Dr. Iris Traulsen

Reviewers:
Prof. Dr. Katja Poppenhäger
Prof. Dr. Dr. Stephan Geier
Dr. habil. Konstantin Herbst

CONTENTS

LIST OF FIGURES

LIST OF TABLES

Zusammenfassung

Die Sonne, der am besten untersuchte kühle Stern, hat eine Korona mit Millionen Grad. Die Energie der Korona strahlt nach außen und ermöglicht es Teilchen, genügend Wärmeenergie zu gewinnen, um der Schwerkraft der Sonne zu entweichen. Diese freigesetzten Teilchen werden "Sonnenwind" genannt. Kühle Sterne sind in der Lage, beträchtliche Mengen an hochenergetischer Röntgenstrahlung aus ihren Koronen zu erzeugen, die gelegentlich sogar die der Sonne übertreffen. Dies deutet darauf hin, dass diese Sterne über genügend Energie verfügen, um Winde durch ähnliche Mechanismen wie die des Sonnenwinds zu erzeugen. Wenn sich ein kühler Stern entwickelt, verliert er aufgrund der magnetisierten Sternwinde, die seine Rotationsentwicklung beeinflussen, an Masse und Drehimpuls. Diese Veränderung hat Folgen, die von Veränderungen in seiner Aktivität bis hin zu Einflüssen auf die Atmosphäre eines Planeten in seiner Umlaufbahn reichen.

Während sich unser Verständnis des Sonnenwinds erheblich verbessert hat, was vor allem auf Missionen wie dem Solar Orbiter zurückzuführen ist, ist unser Verständnis ähnlicher Phänomene bei anderen kühlen Sternen noch nicht sehr weit fortgeschritten. Die direkte Messung der Massenverlustrate, der einzigen beobachtbaren Größe, hat sich als schwierig erwiesen, was zu einer begrenzten Anzahl von Beobachtungseinschränkungen und Obergrenzen führt. Außerdem können Windmessungen nur anhand ihrer Wechselwirkungen mit der Umgebung abgeleitet werden. Angesichts des Mangels an Beobachtungsdaten bieten numerische Simulationen ein wertvolles Mittel, um die Struktur und die Eigenschaften der stellaren Winde in kühlen Sternen zu verstehen.

Ein wichtiger Aspekt dieser Dissertation ist die Quantifizierung der Windeigenschaften von kühlen Sternen. Ich verwendeein modernes 3D-magnetohydrodynamisches (MHD) Modell, das Space Weather Modeling Framework. Im ersten Teil der Arbeit (Kapitel 6) habe ich eine numerische Vergleichsstudie mit idealistischen Modellen durchgeführt, um den Einfluss des Magnetfelds und seiner Komplexität auf die Windparameter zu untersuchen. Die Ergebnisse weisen auf einen neuen Ansatz zur Definition der habitablen Zone (HZ) hin und betonen die Bedeutung der Alfvén Oberfläche (AO) - der Grenze zwischen der Korona des Sterns und seinem Sternwind.

Beim Übergang von idealistischen zu realistischen Ansätzen wird im zweiten Teil der Arbeit (Kapitel 7) ein Netz von realistischen MHD-Modellen vorgestellt. Diese Forschung stellt die erste systematische Quantifizierung der stellaren Winde in F-, G-, K- und M-Sternen durch die Analyse der großräumigen Magnetfeldverteilung in 21 gut beobachteten Sternen. Sie bietet neue Einblicke in die Art und Weise, wie die Eigenschaften des Sterns die Dynamik und Struktur der Sternwinde und ihre Bedingungen in der HZ beeinflussen. Die Ergebnisse stellen die vorherrschenden Annahmen über die Geschwindigkeit von Sternwinden in Frage und stellen ein Vorhersagemodell vor, das zur Bestimmung der Größe von AO verwendet werden kann. Dies ist entscheidend für die Ermittlung möglicher magnetischer Wechselwirkungen zwischen Stern und Planet.

Die Erforschung verschiedener kühler Sterne ermöglicht es uns, Muster und Unterschiede zu entdecken und sowohl die Einzigartigkeit und Gemeinsamkeiten unserer Sonne im Vergleich zu anderen. Diese Erkundung ergab faszinierende Muster der vorhandenen Element in der Korona von aktiven M-Zwergen. Während kühle Sterne mit geringer Aktivität, wie F, G und K, typischerweise den FIP-Effekt aufweisen - charakterisiert durch eine Anreicherung von Elementen mit niedrigem ersten Ionisierungspotenzial in der Korona im Vergleich zur Photosphäre - zeigen hochaktive Sterne (M-Zwerge) einen inversen FIP-Effekt (iFIP).Trotz der umfangreichen Untersuchungen der Elementhäufigkeiten in der Korona bleibt es unklar, ob mäßig aktive M-Zwerge die gleichen Muster aufweisen wie aktivere M-Zwerge.

Im zweiten Teil meiner Dissertation (Kapitel 8) untersuche ich einen kritischen koronalen Temperaturbereich, um die Beständigkeit des iFIP-Musters in M-Zwergen mit geringer Aktivität zu bestimmen. Dies geschah durch die Analyse von Beobachtungen des XMM-Newton-Teleskops. In dieser Studie beobachten wir zum ersten Mal ein Häufigkeitsmuster, das mit einem Null-FIP- oder iFIP-Effekt in einem mäßig aktiven M-Zwerg vereinbar ist. Dies stellt das Bild in Frage, dass alle untersuchten M-Zwerge einen iFIP-Effekt aufweisen, und deutet auf einen möglichen Übergang zu einem FIP-Muster bei noch niedrigeren Aktivitätsniveaus von M-Zwergen hin. Die Ergebnisse legen nahe, dass die Beobachtung von Sternen mit geringer koronaler Aktivität von entscheidender Bedeutung ist, um unser Verständnis der (i)FIP-Muster und ihrer Ursachen zu verfeinern.

Die Dissertation gliedert sich in drei verschiedene Teile. In Teil I gebe ich eine Einführung in die Korona und die Windeigenschaften der Sonne und der kühlen Sterne F, G, K und M. Dieser Teil befasst sich mit Elementhäufigkeiten und die Antriebsmechanismen hinter dem FIP-Effekt und den stellaren Wind. In Teil II verlagert sich der Schwerpunkt vom Stern selbst auf seine Umgebung, wo ich verschiedene Arten von magnetischen Wechselwirkungen zwischen Sternen und Planeten untersuchen werde. In Teil III werden verschiedene Aspekte der stellaren Koronen und Winde detailliert untersucht. An diesen Teil schließt sich ein Ausblick auf zukünftige Forschungsrichtungen. Diese Arbeit soll den Weg zu einem tieferen Verständnis der Winde und Koronen von kühlen Hauptreihensternen ebnen.

Abstract

The Sun, the most extensively studied cool star, has a million degrees corona. The energy from the corona radiates outwards, allowing particles to gain enough thermal energy to escape the Sun's gravity. These released particles are called "solar winds". Cool stars can produce significant amounts of high-energy X-rays from their coronae, occasionally exceeding even that of the Sun. This suggests that these stars have enough energy to generate winds by mechanisms similar to the solar winds. As a cool star evolves, it loses mass and angular momentum due to the magnetized stellar winds that influence its rotational evolution. This change has consequences ranging from changes in its activity to influences on an orbiting planet's atmosphere.

While our understanding of the solar wind has significantly improved, mainly due to missions like the Solar Orbiter, our comprehension of similar phenomena in other cool stars remains limited. Directly measuring mass-loss rates, the sole observable, has proven challenging, leading to a limited number of observational constraints and upper limits. Additionally, wind measurements can only be inferred from their interactions with the surroundings. Given the scarcity of observational data, numerical simulations offer a valuable means of comprehending the structure and properties of stellar winds in cool stars.

An important aspect of this Thesis is quantifying the wind properties of cool stars. I use a state-of-the-art 3D magnetohydrodynamics (MHD) model, the Space Weather Modeling Framework. In the first part of the study (chapter 6), I conducted a numerical comparative study with idealistic models to investigate the influence of the magnetic field and its complexity on the wind parameters. The results suggest a new approach to define the habitable zone (HZ) and emphasize the importance of the Alfvén surface (AS)- the boundary between the star's corona and its stellar wind.

Transitioning from idealistic to realistic approaches, the second part of the study (chapter 7) introduces a grid of realistic MHD models. This research presents the first systematic quantification of stellar winds in F, G, K, and M stars by analyzing the large-scale magnetic field distribution in 21 well-observed stars. It provides new insights into how star properties influence the dynamics and structure of stellar winds and their conditions at the HZ. The results challenge prevailing assumptions about the speed of stellar winds and present a predictive model that can be used to determine the size of AS. The AS is crucial for the assessment of possible star-planet magnetic interactions.

Exploring different cool stars allows us to uncover patterns and differences, highlighting the uniqueness and similarities of our Sun compared to others. This exploration revealed intriguing element abundance patterns in the corona of active M dwarfs. While low-activity cool stars, such as F, G, and K, typically exhibit the FIP effect—characterized by an enrichment of elements with low first ionization potential in the corona compared to the photosphere—highly active stars (M dwarfs) show an inverse FIP effect (iFIP). Despite the extensive studies of elemental abundances in the corona, it remains unclear whether moderately active M dwarfs exhibit the same patterns as more active M dwarfs.

In the second aspect of this Thesis (chapter 8), I investigate a critical coronal temperature range to determine the persistence of the iFIP pattern in low-activity M dwarfs. This was done by analyzing observations from *XMM-Newton* telescope. In this study, we observe for the first time an abundance pattern compatible with a null FIP or iFIP effect in a moderately active M dwarf. These results challenge the current picture that all M dwarfs studied exhibit an iFIP effect and hint at a possible transition to an FIP pattern at even lower activity levels of M dwarfs. The results suggest that observing stars with low coronal activity is crucial to refining our understanding of (i)FIP patterns and their causes.

The dissertation is structured into three distinct parts. In part I, I will provide an introduction to the coronae and wind properties of the Sun and cool stars F, G, K, and M. This section will delve into the discussion of element abundances and the driving mechanisms behind the FIP effect and stellar winds. In part II, the focus will shift from the star to its vicinity, where I will explore various magnetic interactions between stars and planets. Part III will encompass a detailed exploration of various aspects of the stellar coronae and winds. An outlook on future research directions will follow this part. This work aims to pave the way for a more profound understanding of the winds and coronae of cool main sequence stars.

Per Aspera Ad Astra

Through hardships to the stars

Let us embark on this journey of exploration, where each star is a new world waiting to be unraveled.

Part I

Introduction Into the Physics of Cool Stars Coronae and Winds

Preface

Our Sun, classified as a G2V spectral type, belongs to the most abundant group of stars in the Milky Way known as "cool stars". Despite their name, these stars are not cool in the conventional sense. The term "cool" is used in a relative context when compared to the range of stellar temperatures. These stars typically have surface temperatures ranging from about 2773 K to about 6773 K. They are categorized into four main groups (F, G, K, and M) and 9 sub-groups. These temperatures are considered low compared to hotter stars (such as O, B, and A stars), which can have surface temperatures ranging from about 10273 K to tens or even hundreds of thousands of degrees Kelvin. A cool star, also known as a cool dwarf, is a late-type star located in the lower part of the main sequence (as shown in Fig. 3.1). These stars have masses $\leq 1.5\,R_{\odot}$. Further details can be found in Böhm-Vitense (1989).

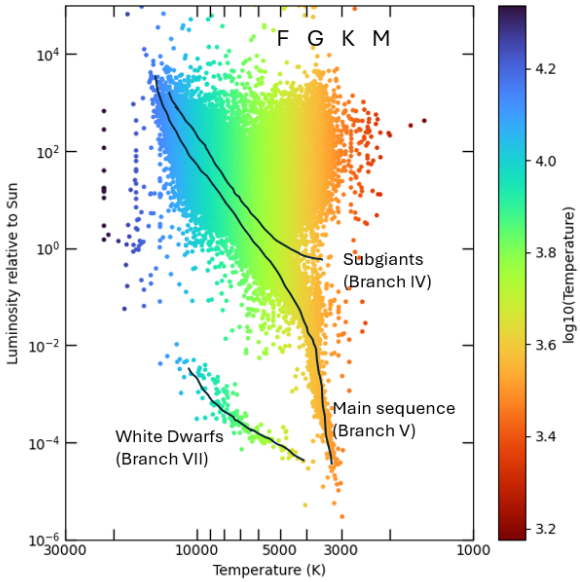

Figure 3.1: Hertzsprung-Russell (HR) diagram in which the Roman numbers V, VII, VI denote selected branches of stellar evolution. Data are from the Gaia DR3 Catalog of Nearby Stars. Picture credit: J. Chebly.

The main sequence is the evolutionary stage in which a star is in hydrostatic equilibrium[1] and has a hydrogen-burning core. The inner core of a cool star, is shown in Fig. 3.2. For late-F, G, K stars ($0.5\,M_{\odot} < M_{\star} < 1.5\,M_{\odot}$) and early M dwarfs ($M_{\star} \geq 0.5\,M_{\odot}$), consists of an inner radiative core and an outer convective zone, while mid to late M dwarfs ($M_{\star} < 0.5\ M_{\odot}$) are fully convective. Partially convective stars have a radiative core surrounded by a convective shell. On the other hand, fully convective stars do not have a radiative core. More about the physics of the radiative and convective zone in Sec. 4.1.

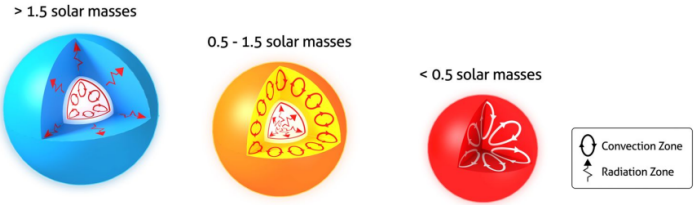

Figure 3.2: The differences in internal structure between stars of different masses. Ultracool dwarfs have fully convective interior. Picture credit: AAS NOVA.

In this thesis, I investigate the stellar winds and coronal properties (i.e., FIP effect) of cool main-sequence stars from late-F to M dwarfs. The introduction is divided into two parts. In Part I, I explore the structure of the sun, the magnetic field, the solar cycle, and the mechanism that influences wind acceleration and element fractionation in the solar atmosphere. This background will serve as a foundation before studying other low-mass cool main sequence stars. Finally, Part II places this knowledge in the context of exoplanets and habitability.

[1] Known as gravitational equilibrium, describes a balance between gravity and pressure. The outward pressure of hot gas is balanced by the inward force of gravity.

The Sun

From Core to Wind

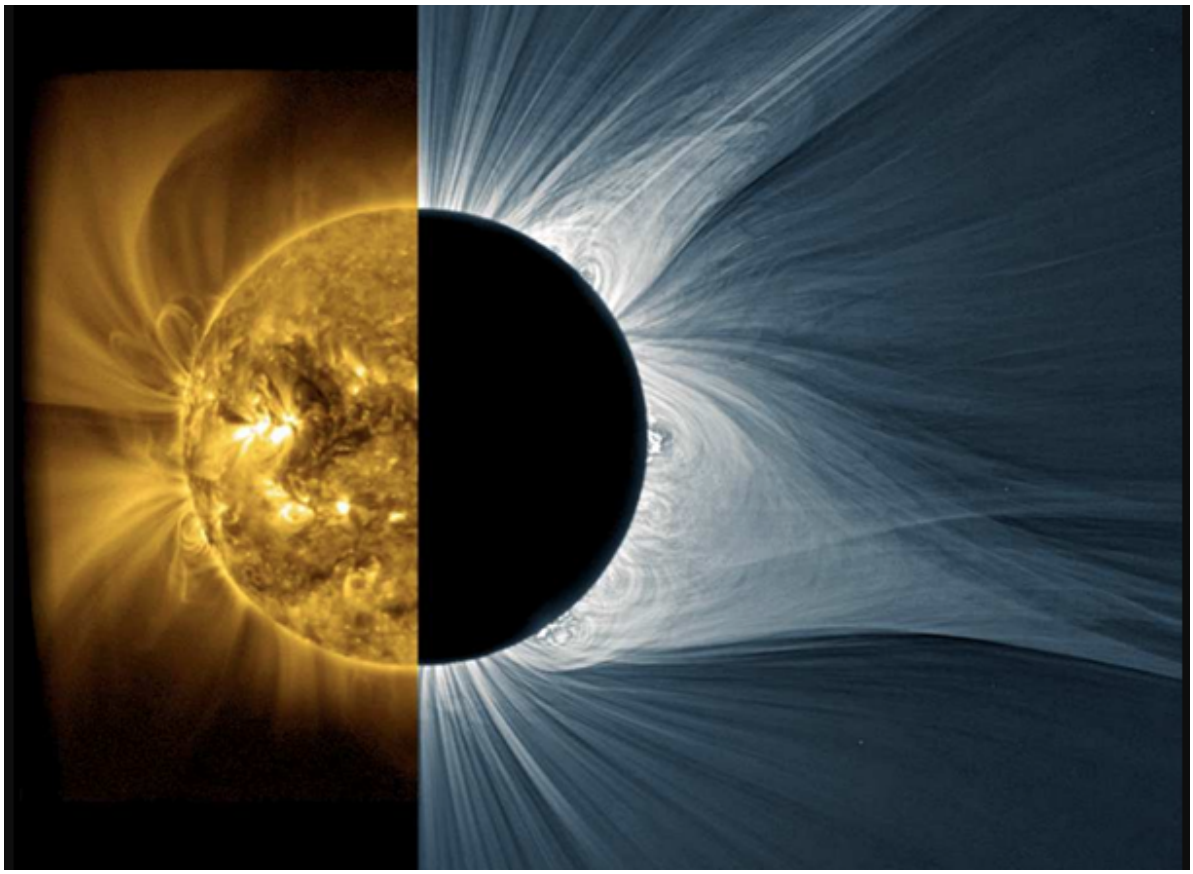

Figure 4.1: Complementary views of the solar corona. *Left*, image with extreme ultraviolet emission from the SWAP (Sun Watcher using Active-pixel-system detector and image processing) telescope on the PROBA2 spacecraft (Seaton et al., 2013). The image was taken in the 17.1 nm wavelength band on July 25, 2014. The Sun's wispy atmosphere glows with ultraviolet light, captured by the PROBA2 satellite of the European Space Agency's PROBA2 satellite. Loops and arcs of the plasma follow the magnetic field lines coming from the Sun. *Right*, a visible band from the total solar eclipse on August 21, 2017. Light scattered by particles in the corona is visible on the right during the 2017 total solar eclipse that passed over the United States. Figure adapted from original images obtained and processed by M. Druckmüller, P. Aniol and S. Habbal (Druckmüller, Rušin, & Minarovjech, 2006).

Coronal plasma is constantly blown away from the Sun, dragging the solar magnetic field. This steady stream of charged particles is the solar wind, constantly bombarding the Earth's magnetic field and causing space weather such as geomagnetic storms and auroras.

4.1 The Sun: Structure and Dynamics

"A star's a star, some matter in a ball."
J. R. R. Tolkien

The Sun is a partially convective star with a mass of 1.989×10^{33} g and a core consisting of gaseous, ionized plasma. The inner core of the Sun reaches extreme temperatures of 15 million degrees Kelvin. In this hot environment, some protons have enough energy to overcome the Coulomb barrier[1] of the nuclear charge. These protons penetrate hydrogen (H), carbon (C), and nitrogen (N) nuclei and trigger nuclear reactions that catalyze the conversion of hydrogen into Helium (Bethe, 1939; Clayton, 1983; Prialnik, 2009). The energy released during this process is radiated and reabsorbed as it diffuses outwards through the *radiative* zone. This diffusion process generates enough heat and pressure to counteract the gravitational force that would otherwise cause the star to collapse.

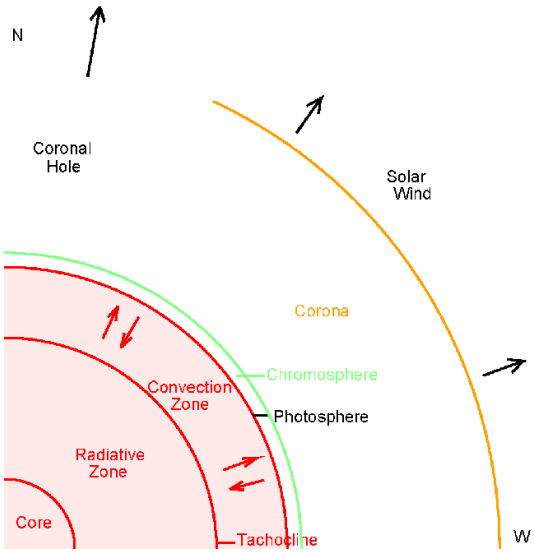

Figure 4.2: A cross-section of the Sun shows its major radial structure from the core to the escaping solar wind (If we look at the Sun with North at the top and South at the bottom, West is to the right and East to the left). The solar limb is the edge of the visible disk. Picture credit: Reames (2021)

The outer convective zone of the Sun exhibits differential rotation, in which the Sun rotates faster at the equator than at the poles (Thompson et al., 2003). At the equator, the Sun rotates approximately every 25 d, but this increases to 34 to 35 d at the poles. The rotation rates obtained by tracking magnetic patterns correspond to helioseismic flows located at 25 to 28 Mm, suggesting that the Sun's rotation also changes with depth (Lang, 2013; Mahajan et al., 2024). This contrasts the radiative interior, which maintains a uniform rotation rate.

This transition from uniform rotation to differential rotation is facilitated within a thin, critical region, the *tachocline* (Spiegel & Zahn 1992; Hughes 2007, see Fig. 4.2). Its location is not fixed, but varies from about $\sim 0.693\, R_\odot$ close the equator, and at $\sim 0.717\, R_\odot$ at higher latitudes (Charbonneau et al., 1999; Basu & Antia, 2003).

The differential rotation within the convective zone rapidly changes the rotation rate, resulting in significant shear within the tachocline. The shear winds up the magnetic field lines of the Sun and transforms the weaker poloidal magnetic field (in the south-north direction, α effect[2]) into a much stronger toroidal magnetic field (in the east-west direction, Ω effect[3]). This transformation is a crucial part of the solar dynamo mechanism that leads to the formation of small- and large-scale magnetic fields. Some models suggest that the tachocline may act as a reservoir for magnetic fields in stars to stabilize and prolong their global cycles, rather than the primary site of magnetic field formation (Bice & Toomre, 2020). Check figure 4.3, for a representation of the α and Ω effect.

[1] Energy barrier due to electrostatic interaction that two nuclei need to overcome so they can get close enough to undergo a nuclear reaction.

[2] Due to the Coriolis force. By definition, this force acts on objects that move in a reference frame that rotates relative to an inertial frame. In the case of the α effect, this means that the force causes the moving plasma to follow curved paths instead of straight lines.

[3] Due to the differential rotation.

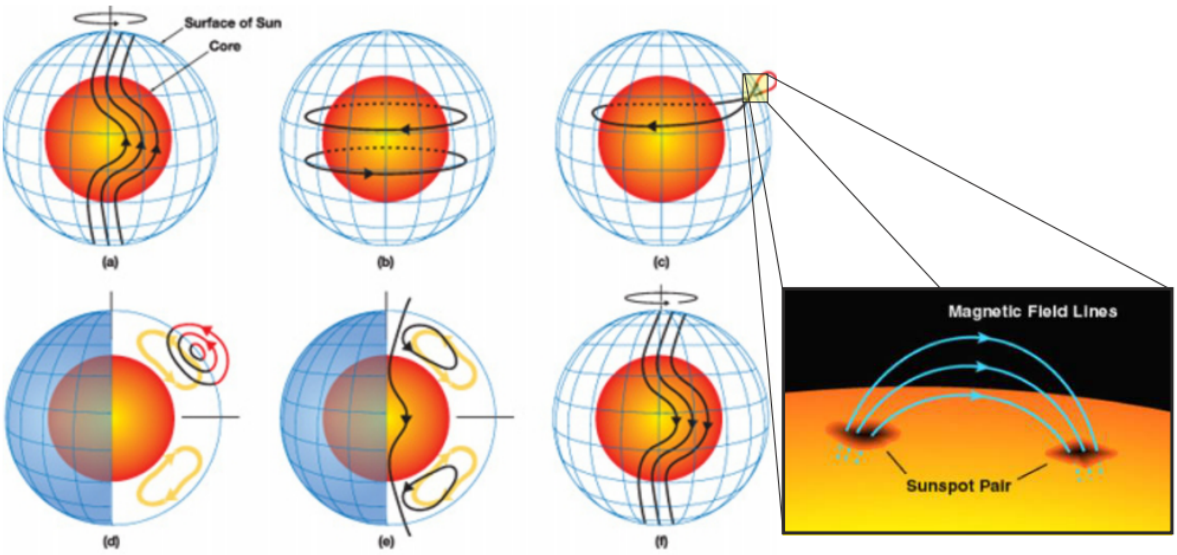

Figure 4.3: Illustration of the Ω effect (top row) and α effect (bottom row). In *Panel a*, we see that poloidal magnetic field lines in the solar convection zone are deformed by differential rotation. After several rotations, the field lines wind around the Sun, forming toroidal structures known as flux tubes in the tachocline (*panel b*). Magnetic buoyancy instabilities cause the flux tubes to rise towards the surface (*panel c*). When these field loops pierce the photosphere (the solar surface), a sunspot pair appears. These sunspots eventually decay and rearrange the magnetic field back into the poloidal direction (*panel d*). The surface field is carried by meridional circulation towards the poles (*panel e*). This contributes to the increase of the global toroidal component of the field (*panel f*). Picture credit: NASA.

The Sun and stars of spectral type; late F, G, K, and early M dwarfs have convective envelopes that extend deeper into the interior of the star. Stars cooler than M4 ($M_\star < 0.4\,M_\odot$) have no tachocline. If the tachocline is crucial for generating magnetic fields on the stellar surface, fully convective stars should not be able to generate a magnetic field. Instead, they are generally thought to generate magnetic fields solely through helical turbulence (Durney, De Young, & Roxburgh, 1993; Boldyrev, Cattaneo, & Rosner, 2005; Browning, 2008). More information on cool main sequence stars with and without tachocline, in; Durney, De Young, & Roxburgh (1993); Reiners (2012); Wright & Drake (2016).

During the transition from the radiation zone to the *convection* zone, the temperature drops so much that some atoms can recombine with their electrons. This process leads to the formation of convection cells, similar to bubbles in a boiling soup pot. These cells are filled with hot gas, which rises and releases heat to the outer layers of the Sun. These cells create granulation in the photosphere due to turbulence (see section 4.2). As the gas cools, it becomes denser and sinks back into the lower layers of the convection zone, a process known as "convection".

An electrically conductive fluid, such as the plasma in the Sun, can amplify a magnetic field through a process known as *dynamo*. In this process, the kinetic energy of the fluid's motion is converted into magnetic energy. The movement of the fluid relative to a magnetic field induces electric currents in the fluid, which in turn generate a magnetic field. This newly generated field can then amplify or distort the original field. The magnetic field goes through a cycle of amplification, distortion, and attenuation, but it is constantly regenerated by the dynamo process. For this reason, we observe a cycle of solar activity and periodic reversals in the polarity of the Sun's magnetic field (11-year cycle). The regeneration of the magnetic field takes place under certain conditions: the presence of conductive fluid (such as the plasma in the Sun), turbulent motions (such as those caused by convection), and the global rotation of the star. For a review of astrophysical dynamo theory, see Brandenburg & Subramanian (2005).

4.2 Photosphere

"The sun, with all those planets revolving around it and dependent on it, can still ripen a bunch of grapes as if it had nothing else in the universe to do."
Galileo Galilei

The photosphere, Greek for "the sphere of light", is the lower atmosphere of the Sun, located above the convective zone. Temperatures in the solar photosphere range from ∼6500 K at its base to ∼4000 K at its upper boundary. This temperature gradient is due to the decreasing density of the plasma with altitude, which results in less energy being transferred from the Sun's core to its surface. Temperatures in the photosphere favor the emission in visible light, as the emitted light shifts from low-energy infrared wavelengths (λ) to higher energy. Direct observations of the photospheric magnetic field have been made with both *ground-based* and *space-based* instruments.

At first glance, the photosphere looks like a seemingly featureless disk of light (Fig. 4.4, *left*). On closer inspection, however, it reveals intricate features, particularly granulation, which appears as a pattern of bright cells and dark lanes on its surface (Fig. 4.4, *right*). The granules are the result of processes that take place in the Sun's convection zone, as mentioned earlier. Each granule, or cell, is a mass of hot gas that rises due to convection inside the Sun, radiates energy, and sinks back within a few minutes to be replaced by other granules in a constantly changing pattern.

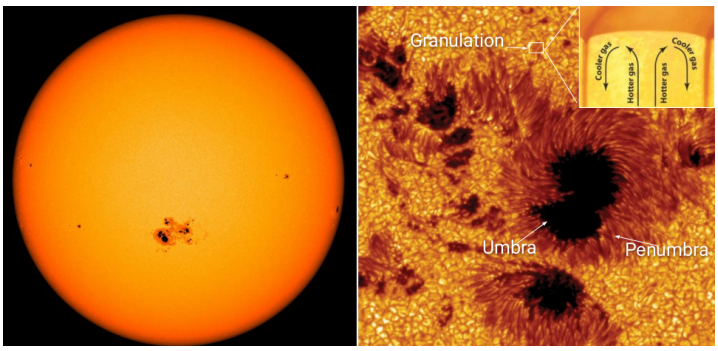

Figure 4.4: *Left*, solar photosphere with sunspots in visible light. Picture credit: NASA/SDO. *Right*, granulation; pattern of bright cells and dark lanes. Adapted from: York University

This pattern is occasionally disrupted by regions of strong magnetic activity known as sunspots (see Fig. 4.4, *left*). These sunspots appear as dark regions on the solar disk. Each sunspot consists of a dark inner core, the umbra, which is surrounded by less dark, irregular shapes, and the penumbra (see Fig. 4.4, *right*). Sunspots are regions on the surface of the Sun that are cooler and darker than the surrounding areas. They occur because the Sun's magnetic field inhibits heat convection to the surface. These areas along the magnetic flux in the upper photosphere and chromosphere heat up and are often visible as faculae (in the photosphere) and plage (in the chromosphere), often referred to as active regions. These sunspots often occur in pairs, with one acting like the north pole of a magnet and the other like the south pole. The two poles (sunspots) are connected by loops of the magnetic field which arch through the Sun's corona (Beckers, 1976). Check; Solanki, Inhester, & Schüssler 2006 for a comprehensive overview of the Sun's magnetic activity.

Elements with low **f**irst **i**onization **p**otential (FIP) ≤ 10 eV (e.g., Si, Mg, Fe)- slightly lower than that of hydrogen (13.6 eV)- remain ionized in the photosphere due to its temperature range. These elements do not require much energy to remove an electron from their outer layer, transforming them into an ion. Conversely, elements with a higher FIP (> 10 eV, e.g., O, Ne, N) can capture and hold electrons, making them neutral atoms. This means that the high FIP element will not follow the magnetic field lines. These low FIP element are observed to be enhanced in the corona, as we will see in Sec. 4.4. This enhancement in element abundance is known as the FIP effect. We will see in chapter 5, that for F, G, and K stars, the element abundances follow the same pattern, however, for active M dwarfs, we have the inverse FIP effect (iFIP effect). Whether moderately active M dwarf exhibits this pattern is still unsure, highlighting the need for further research. I will present a comprehensive study of this in the stellar regime in chapter 8 of this Thesis.

4.3 Chromosphere and Transition Region

"When the sun has set, no candle can replace it."
George R.R. Martin

Chromosphere comes from the Greek meaning "sphere of color". It is the layer directly after the photosphere. In the chromosphere, the temperature begins to rise again. The temperature in the chromosphere is $\sim 4000\,\mathrm{K}$ at the bottom (the so-called temperature minimum) and 8000 K at the top. The chromosphere can store and release energy through a process known as magnetic reconnection. This is believed to occur in all the layers of the solar atmosphere. This process rearranges the magnetic field lines and releases a significant amount of stored magnetic energy in the form of heat and light (Ni et al., 2015, 2018; Díaz Baso, de la Cruz Rodríguez, & Leenaarts, 2021). In addition to magnetic reconnection, shock waves also heat the chromosphere. These waves are generated by the convective motion of the plasma in the lower photosphere and propagate upwards into the chromosphere, heating the plasma and further contributing to the temperature rise (Nindos et al., 2022).

The temperature gradient in the chromosphere causes it to be much more structured in 3D than the photosphere, which makes images of the Sun in chromospheric lines more interesting (see Fig. 4.5). Both layers exhibit convective cell patterns, with the chromosphere showing larger-scale convection known as super-granulation (Giovanelli, 1974; Rieutord & Rincon, 2010). However, while the photosphere is marked by granules and sunspots, the chromosphere is characterized by spicules (dark hair) and prominences (Fig. 4.5, *right*). The loops (prominences) are extensions of the chromosphere further up along magnetic field lines rooted in the photosphere (Loukitcheva, Solanki, & White, 2009).

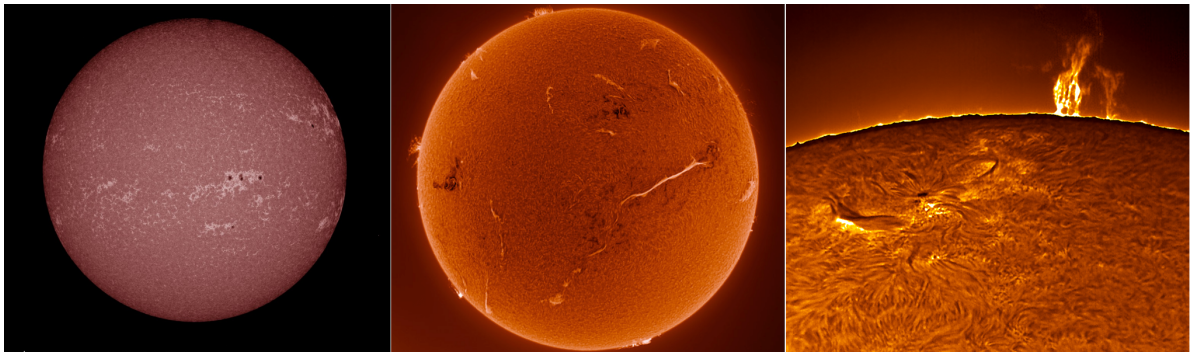

Figure 4.5: *Left*, ultraviolet light continuum showing the surface of the sun (SDO AIA 1700 Å). As well as a layer of the Sun's atmosphere, the chromosphere lies directly above the photosphere, where the temperature begins to rise. It is typically a pink color. Picture credit: C. Alex. Young. *Middle*, chromosphere observed in visible light with Hα. Picture credit: mehmet-erguen. *Right*, a prominence of hydrogen gas and spicules that appear as dark "hair". Picture credit: Voyageur Press.

The chromosphere is best observed in the ultraviolet (UV) and far-UV (FUV) part of the spectrum. This is due to the high opacity and temperatures in the chromosphere. The UV spectrum starts below about 3300 Å, where the Earth's atmosphere becomes opaque (blocks light). The FUV spectrum lies between about 1700 Å and the hydrogen-Lyman continuum[4]. Since the Earth's atmosphere blocks UV and FUV light, observations of the chromosphere in these parts of the spectrum must be gathered outside the Earth's atmosphere.

Only the most opaque visible atomic spectral lines are suitable for observing the chromosphere in images with visible light. The chromosphere and its magnetic features are essentially transparent to visible light. The chromosphere has a characteristic red color caused by electromagnetic emissions in the Hα spectral line (Jess et al., 2015). Hα is one of its strongest lines with $\lambda = 6563$ Å[5]. The chromosphere is also visible in the light emitted by ionized calcium, Ca II (the calcium K-line), in the violet part of the solar spectrum at $\lambda = 3934$ Å. These wavelengths fall within the visible light, which typically ranges from 3800 to 7000 Å.

[4]The energy threshold for the ionization of hydrogen.
[5]This line is emitted by a hydrogen atom when its electron makes a transition from energy level $n = 3$ to $n = 2$.

The chromosphere is followed by a thin layer in which the temperature rises by two orders of magnitude. This layer is called the *transition region*. It *cannot be seen in visible light*. Its emission occurs almost entirely in UV, FUV, and extreme ultraviolet (EUV) parts of the spectrum. The transition region is a very narrow (~ 100 km) layer between the chromosphere and the corona where the temperature rises abruptly from 10000 K (typical of the chromosphere) to nearly a million degrees. Figure 4.6 summarizes how the temperature changes in the solar atmosphere.

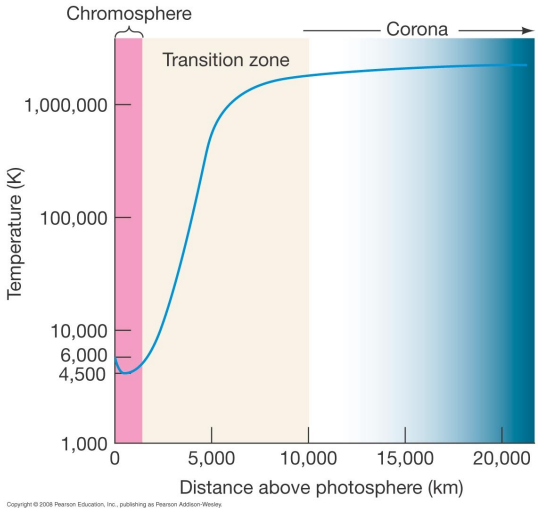

Figure 4.6: Temperature is shown to increase upward the further we are from the photosphere. Note the rapid temperature increase over a very short distance in the transition region between the chromosphere and the corona. The temperature, indicated by the blue line, reaches a minimum of 4500 K in the chromosphere. Then, it rises sharply in the transition zone, finally leveling off at around 3 MK in the corona. Picture credit: Pearson education 2014.

4.4 Solar Corona

"The sun is but a morning star."
Henry David Thoreau

The corona, derived from the Latin word for "crown" or "halo", represents the outermost layer of the Sun. Its temperature ranges from ~500000 K to a few million Kelvin. The idea that the Sun's outer atmosphere is so hot was initially far from obvious and even seemed implausible. The study of the Sun's corona began in the late 1930s and early 1940s. At that time, the work of Edlén & Swings and Grotrian led to the identification of the "red" line at 6375 Å which is observed during eclipses (Fig. 4.7, *panel a*). This is a forbidden line of Fe X, indicated by a temperature of 1 MK. Interestingly, the visible spectrum of the corona also contains a green emission line at 5303 Å. Its identification with Fe XIV in the 1930s provided early evidence of the high temperature of the corona. Current theories suggest that the corona is heated either by numerous small sites of magnetic reconnection, known as nanoflares (see Parker 1988), or by the absorption (or attenuation) of Alfvén waves (Alfvén, 1957). However, a definitive solution to the problem of coronal heating remains elusive.

The white light of the corona, is the photospheric light scattered by electrons-also known as Thompson scatter[6]. The impressive filamentary structure betrays the beautiful complexity and dynamic of the magnetic field (Fig. 4.7, *panel b*). The fully ionized plasma is tied to the magnetic field via the Lorentz force[7].

There is a general dipole component, which manifests itself near the poles as a series of *open field* lines (dark areas in Fig. 4.7, *panel c*). The X-ray emission in the coronal holes is relatively weak due

[6] Photons scatter off free electrons.
[7] Force exerted on a charged particle q moving with a velocity through an electric field and magnetic field.

to lower temperatures near the bottom of the corona; they look dark in contrast to the hotter, denser coronal closed-loop regions. In these regions, the plasma is not magnetically trapped. These regions are the origin of the fast solar wind (see Sec 4.5). For more information on the coronal holes, I refer the reader to the review paper by Cranmer (2009).

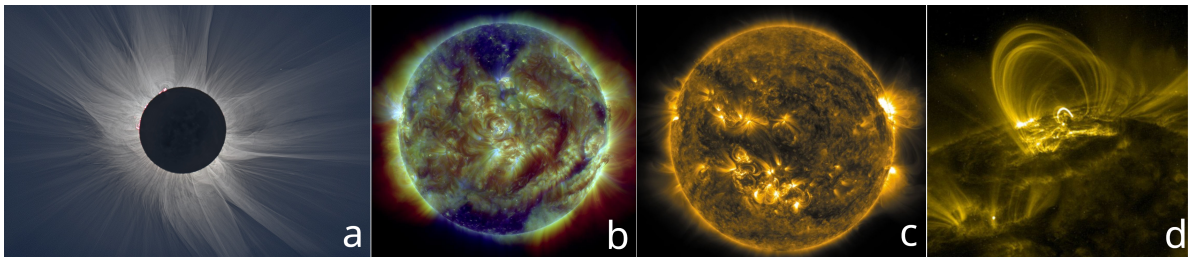

Figure 4.7: *Panel a*, total eclipse image taken Mar. 20, 2015 at Svalbard, Norway. Picture credit: S. Habbal, M. Druckmüller, and P. Aniol. *Panel b*, RGB composite image of the solar corona seen in three different passbands: 21.1 nm (formed at temperatures around 2 MK) is shown in red, followed by 19.3 nm (roughly 1.3 MK) in green and 17.1 nm (formed around 800000 K) in blue, with NASA's SDO/AIA instrument. The brightest areas correspond to active regions which also show the presence of coronal loops that connects magnetic islands of opposite polarities. Picture credit: Heliophysics Events Knowledge base, Lockheed Martin Solar and Astrophysics Lab, Palo Alto. *Panel c*, shows the Sun in extreme ultraviolet wavelengths (171 Å) colorized in gold. This wavelength of light highlights the extremely hot material in flares. Picture credit: Atmospheric Imaging Assembly instrument on board NASA's SDO. *Panel d*, shows coronal loops. Picture credit: NASA/SDO.

We observe *closed* loops near the equator. If the latter lie over regions of opposite magnetic polarity, a helmet streamer is created (Fig. 4.7, *panel a*). X-ray emissions originate mainly from closed magnetic field loops rooted in the photosphere. These loops, have the highest density when anchored in active regions, resulting in higher emissivity compared to open fields (Fig. 4.7, *panel d*). The brightness of the coronal loops is directly proportional to the strength of the field in the active region, and the intensity $\propto n_e^2$ (electron density) in the emitting region (for more information check the review paper by Reale 2014). These loops are dynamic and constantly changing due to turbulent motions in the photosphere and magnetic field rearrangements. Occasionally, these dynamics lead to massive "flares" caused by a sudden magnetic field dissipation. These flares emit extremely hot, high-energy radiation (X-rays and γ-rays) and accelerate particles that heat the chromosphere and photosphere and generate visible and UV radiation. It is important to note that the flares are trapped energetic particles. Disruptions of coronal loops or prominences can lead to "coronal mass ejections" (CMEs). For a more in depth review of flares and CMEs dynamics and formation, check review articles such as, i.e., Webb & Howard (2012); Benz (2017); Shen et al. (2022).

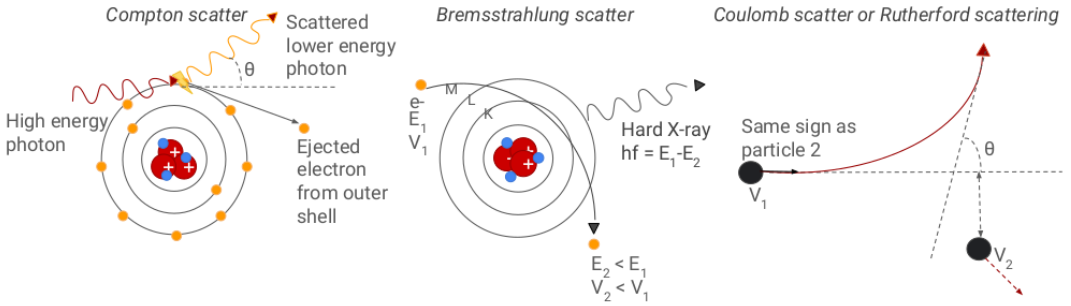

Figure 4.8: Illustration of the different scattering phenomena in the corona of the Sun. Picture credit: J. Chebly.

The corona is far more transparent and much hotter than the chromosphere, so the EUV (< 912 Å where the hydrogen Lyman continuum starts). Intrinsic coronal emission occurs at X-ray wavelengths that can only be observed from space. Both *soft* and *hard* X-rays are used to observe the solar corona,

providing different types of information due to their different energy levels. *Soft* X-rays ($< 10\,\mathrm{keV}$) are low in energy and are typically used to observe hot and dense regions of the solar corona. They can reveal features such as active regions, coronal holes, solar flares, and coronal loops. Within dense regions, *soft* X-rays are produced by electron and ion heating as they stop and lose their energy to the plasma by Coulomb scattering[8] (Fig. 4.8, *left*). A good review paper on the energetic particles on the Sun can be found in Reames (2021).

Hard X-rays ($> 20\,\mathrm{keV}$) are generated by a process known as Bremsstrahlung, in which high-energy electrons are scattered by ions (Miller et al., 1997; Fletcher et al., 2011). This interaction slows down the electrons and emits a broad spectrum of X-ray energies (Fig. 4.8, *middle*). This radiation either escapes from the atmosphere and propagates through space or deposits its energy in the atmosphere through Compton scattering (Fig. 4.8, *right*).

Observations dating back to the 1960s reveal significant differences in the chemical composition of coronal plasma compared to the solar photosphere (see Sec. 4.2). Low-FIP elements, easily ionized in the chromosphere, are preferentially enhanced by factors of 3-4 (Pottasch, 1963; Meyer, 1985; Feldman, 1992). In contrast, high-FIP elements, which remain neutral in the chromosphere, retain their photospheric abundances. The "FIP effect" arises from ion-neutral fractionation as particles expand from the chromosphere into the corona. While low-FIP elements readily ionize at photospheric and chromospheric temperatures, high-FIP elements often remain neutral. Ultimately, all elements become highly ionized in the $\sim$1 MK corona, with helium (He) having the longest ionization time due to its highest FIP of 24 eV. The most probable mechanism to efficiently fraction elements is the ponderomotive force exerted by Alfvén waves as they travel from the photosphere to the corona. More details on the mechanism driving element fractioning is in section 4.7.

4.5 Solar Wind

"As the solar wind whispers across the void,
it brings with it the stories of the Sun's fiery heart."
Carl Sagan

Our understanding of the solar wind has evolved considerably over time. Today, we understand it as a continuous outflow of plasma from the Sun, consisting mainly of protons and electrons. This idea is based mainly on Alfvén's 1957 theory, which suggested the presence of magnetic fields associated with corpuscular solar radiation (Alfvén, 1957). Alfvén's findings triggered a paradigm shift that challenged previous ideas about the nature of the solar wind. Prior to Alfvén, observations by Biermann in 1951 had suggested the existence of a solar wind when he noticed that comet tails always point away from the Sun (Biermann, 1951). Six years later, Chapman & Zirin (1957) described the solar corona as a continuously outward streaming fast solar corpuscular radiation. However, it was Parker's revolutionary idea in 1958 that solidified the concept of the solar wind as an expansion of the solar corona.

Parker's model shows that the corona is in a state of constant expansion and as a result the magnetic field lines are pulled out by the expanding plasma (Parker, 1958). This phenomenon is commonly referred to as the "solar wind" and occasionally as the "Parker wind". The magnetic fields are rooted in the photosphere, which is characterized by high electrical conductivity[9]. Consequently, the magnetic fields behave as they would in a conductive fluid:

$$\frac{\partial B}{\partial t} = \nabla \times (v \times B) + \eta \nabla^2 B, \tag{4.1}$$

where v is the plasma velocity, η is the magnetic diffusion, ∇ denotes the gradient operator, and the magnetic Reynolds number is defined as $R_m \sim 1/\eta$.

In the scenario where the magnetic R_m approaches infinity, which indicates a perfectly conducting fluid, magnetic diffusion becomes negligible. As a result, the induction equation becomes completely

[8] Consider two particles 1 and 2, with the same charge sign. Let 2 be initially at rest and 1 approach it with velocity v_1. Coulomb repulsion causes 1 to deflect by an angle θ_1 and pushes 2 away in the process.

[9] This is due to its plasma state. This plasma consists of free electrons and ions that can move freely. The high temperature and ionization level of the photosphere enable these particles to conduct electricity efficiently.

dependent on the plasma flow. Without the solar rotation, the solar magnetic field would assume a radial configuration. However, the presence of solar rotation causes the magnetic field lines to wind up into a spiral pattern (Archimedean pattern), sometimes referred to as a "Parker" spiral (see Fig. 4.9).

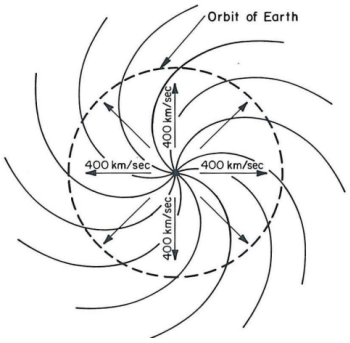

Figure 4.9: 2D illustration of Parker spiral arms, as suggested by Parker (1958). Picture credit: Parker (1963).

Parker's solar wind model is predicated on the assumption that the gas in the solar wind is isothermal. This means that despite the expansion and the associated decrease in density, the temperature of the solar wind remains roughly constant due to the balance between heating and cooling processes. Consequently, the plasma density in the solar corona decreases inversely with the square distance from the Sun as the solar radiation propagates outward (equation 4.2). This is the typical behavior between density and distance in an isothermal plasma.

$$\rho = \frac{k}{r^2} \tag{4.2}$$

where ρ is the density of the solar wind, r is the distance from the Sun, and k is a constant that depends on the specific conditions of the solar wind.

This model is supported by observations, which suggest that near the Sun, the heating mechanisms are efficient enough to maintain the solar wind in an approximately isothermal state (Suess et al., 1977; Roussev et al., 2003). Furthermore, Parker understood that the structure of the magnetic field, together with the decreasing gravitational field, would cause a hot thermal wind to accelerate from subsonic to supersonic within a few solar radii. The critical distance (r_c) at which the wind goes from subsonic to supersonic is defined as $r_c = \frac{GM}{2u_c^2}$ (where u_c is the speed of sound, M is the mass of the Sun and G is the gravitational constant). For a detailed derivation of the Parker equation and the critical radius, see (Parker, 1958).

The continuous expansion of the solar corona, leading to the "solar wind", has been directly observed by many satellites and space probes (e.g., Gringauz 1963; Bonetti et al. 1963; Snyder & Neugebauer 1964). The first direct evidence of the solar wind came from the Soviet Luna missions (Gringauz et al., 1962) and the U.S. Mariner 2 mission in the early 1960s (Neugebauer & Snyder, 1962). These missions measured the properties of the solar wind and validated Parker's theoretical predictions. The data showed that the solar wind velocity at the Earth's distance from the Sun was about 300-800 km/s, aligning well with Parker's calculations (see Fig. 4.10).

Parker's model laid the foundation for understanding the solar wind as a continuous outflow from the Sun and was successful in predicting wind speed. However, it was not able to explain the heating mechanism of the corona and the acceleration mechanisms of the wind. The model attributed the solar wind primarily to the thermal expansion of the corona and initially overlooked the effects of the Sun's magnetic field. It was only when Hannes Alfvén discovered the existence of magnetohydrodynamic waves, the so-called "Alfvén waves" in the Sun, that our understanding of the heating of the corona and wind acceleration improved (Alfvén, 1957). These are transverse waves that propagate along magnetic field lines in a conducting fluid. These waves can transfer energy from the Sun's magnetic field to the solar wind plasma and provide an additional mechanism for heating the corona and accelerating the solar wind (more about the Alfvén waves in section 4.7).

Despite its limitations in reproducing some aspects of wind properties, the Parker model continues to be a valuable tool in solar wind modeling. For instance, in the study by Shivamoggi, Rollins, & Pohl (2021), they expanded upon the original Parker model. They adapted Parker's hydrodynamic,

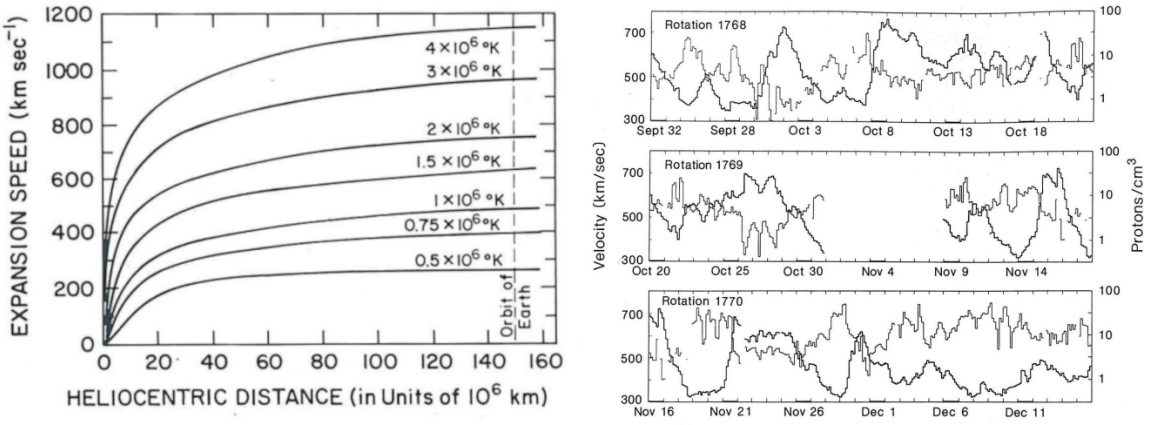

Figure 4.10: *Left*, the wind velocity of an isothermal Parker wind, for different temperature values. The vertical dashed line indicates the mean radius of the Earth's orbit. Picture credit: Parker (1958). *Right*, the velocity and density of the solar wind at R = 1 AU from the Sun, as measured by the Mariner spacecraft in 1962. Picture credit: Hundhausen, A. J. (1995).

isothermal solar wind model to account for a more realistic polytropic gas flow, which can result from variable, extended heating of the solar corona. The Parker model also finds applications in stellar physics. For example, the study by Scherer et al. (2015) they used the Parker spiral model to estimate the magnetic field required for the diffusion coefficients in their astrosphere model.

Later in 1977, a study by Alfvén (1977) proposed the "ballerina skirt" model. It is a 3D visualization of the heliosphere and the stream-structured solar wind (Fig. 4.11). It represents the separatrix[10] between positive and negative solar magnetic field lines, known as the heliospheric current sheet, which is dragged out into interplanetary space by the radially outflowing solar wind plasma. This separatrix, which resembles the skirt of a spinning ballerina, forms a spiral pattern due to the rotation of the Sun (Fig. 4.11, *green area*). This separatrix forms generally in the middle *near-equator*.

The Sun's magnetic field lines, which are rooted in the photosphere, rotate with the Sun at an angular velocity of ($\Omega_\odot = 3\times10^{-6}$ sec^{-1}). These magnetic field lines move at different speeds, resulting in a spiral pattern (Archimedean pattern, Eq. 4.3). The spirals depict the trajectories of plasma parcels emitted from the same point on the Sun but at different times (more details in Hundhausen 1972).

$$r(\phi) - r_0 = \frac{u_r}{\Omega_\odot}(\phi - \phi_0). \tag{4.3}$$

where $r(\phi)$ is the radial distance at angle ϕ, r_0 is the initial radial distance, u_r is the constant radial wind speed, $\Omega_\odot$ is the Sun's angular velocity, ϕ is the angular position, ϕ_0 is the initial angular position.

Just as a spinning ballerina slows down when she stretches out her arms to release the angular momentum, the Sun behaves similarly. The Sun gradually slows down by transferring its angular momentum to the solar wind. The speed at which the Sun loses its angular momentum is given by:

$$\dot{J} = -L\dot{M}_\odot = -\Omega_\odot r_A^2 \dot{M}_\odot \tag{4.4}$$

where L is a constant indicating the specific angular momentum carried away by the solar wind, r_A is the Alfvén radius. This radius separates a star's corona from the stellar wind (further information in Sec. 4.7). The mass loss rate is represented by $\dot{M}_\odot$[11]. The negative sign indicates that the angular momentum decreases with time due to mass loss.

[10] In plasma physics and magnetohydrodynamics, a separatrix typically denotes a boundary between regions with different magnetic field topology or different plasma behavior

[11] Mass lost to the Sun by the magnetized winds per unit time. The mass loss rate depends on the proton flux which is $\sim 3\times10^8$ protons cm^{-2} sec^{-1} at 1 AU (Ryden, 2020)

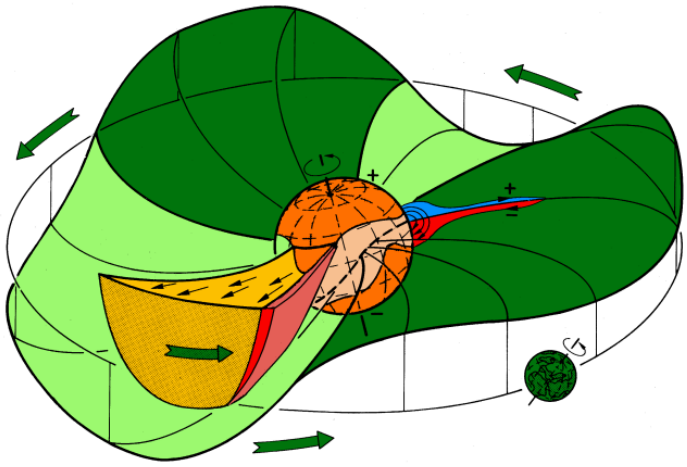

Figure 4.11: Sketch of the "ballerina model" of the 3D heliosphere, according to Alfvén (1977). The Sun's poles are occupied by large coronal holes of opposite magnetic field polarity, typical for odd cycles. Solar wind with opposite magnetic field polarity will be observed on both sides of the heliospheric current sheet (HCS). A co-rotating interaction region where a fast solar wind stream interacts with a low-speed one is cross-sketched. Note how the rotating Sun dances across the Earth with its warped HCS. Picture credit: Schwenn (1990).

For typical models of the magnetized solar wind, the Alfvén radius is $r_A = 1.7 \times 10^{12}\,\mathrm{cm} = 24\,R_\odot$ (Parker, 1958). With the sun's $\Omega_\odot = 3 \times 10^{-6}\,\mathrm{sec}^{-1}$ and $\dot{M}_\odot = 2 \times 10^{-14}\,M_\odot\,\mathrm{yr}^{-1}$, this implies $\dot{J} = -1 \times 10^{31}\,\mathrm{g\,cm^2\,sec^{-2}}$. Since the sun's total angular momentum is $J = 1.6 \times 10^{48}\,\mathrm{g\,cm^2\,sec^{-1}}$, the time scale over which the sun will be spun down is

$$t_J = \frac{-J}{\dot{J}} \approx 2 \times 10^{17}\,\mathrm{sec} \approx 5 \times 10^9\,\mathrm{yr} \tag{4.5}$$

This time scale is comparable to the age of the Sun, in contrast to the mass loss time scale ($t_\mathrm{M} = \frac{M_\odot}{\dot{M}} \approx 5 \times 10^{13}$ yr). Although the solar wind does not significantly affect the total mass of the Sun, it does affect J of the Sun and thus also the dynamo behind the generation of the magnetic field. The changes in the angular momentum does not only alter the Sun interior but also affect the atmosphere of surrounding planets.

The equatorial region, where the Sun loses angular momentum more efficiently, is dominated by closed loops covering active regions. The *slow* solar wind, which is characterized by strong chemical fractionation effects in its composition and a more balanced (or lower cross-helicity) turbulence, is thought to originate in closed coronal loops where fractionation takes place (e.g. Antiochos et al. 2011, 2012). This *slow* wind is then released into the solar wind through interchange reconnection with the surrounding open field. Alternatively, it can also originate directly from regions with open fields, similar to the fast solar wind (Cranmer, van Ballegooijen, & Edgar, 2007). The emission of the slow solar wind is confined to a belt of about 30° width in the middle of the warped current band (Fig. 4.11, *blue* and *red* regions). The *slow* winds speed near Earth are about 300-400 km/s (McComas et al., 1998, 2000).

Fast solar wind has its origin in coronal holes, with speeds near Earth of about 700-800 km/s (McComas et al., 1998, 2000). The poles are characterized by large coronal holes, areas with open magnetic field lines, with the northern hole having a positive polarity and the southern hole a negative polarity. These holes extend into the equatorial regions and give the Sun an inclined magnetic dipole (Fig. 4.11, *orange* and *red* tongue-shaped region). There are no closed magnetic field lines in these coronal holes, so there are no counter-propagating waves. This environment favors a largely unbalanced Alfvénic turbulence (Bruno & Carbone, 2013; Ko, Roberts, & Lepri, 2018).

The *slow* solar wind is cooler and exhibits more significant short-term variability than the *fast* solar wind. They differ in their heavy ion abundances (von Steiger, Zurbuchen, & McComas, 2010). Nevertheless, both components have similar mass fluxes (proton flux), indicating that the solar mass outflow is nearly isotropic.

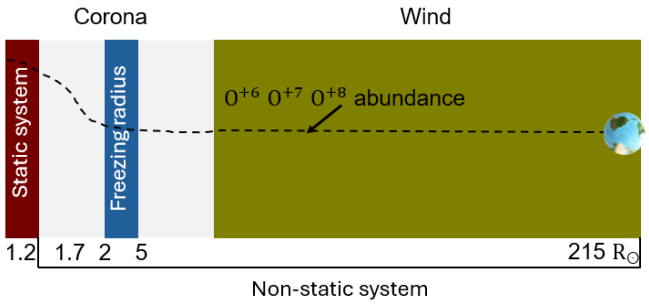

Figure 4.12: Illustration of the position of freezing radius (r_f) in solar radii ($R_\odot$) in relation to the corona and the earth. The corona is considered as a static system for radius $< 1.2\,R_\odot$. Beyond this distance, the static approximation breaks down. Also, beyond $\sim 1.7\,R_\odot$ the ionization state can hardly change with the expansion (Hundhausen, Gilbert, & Bame, 1968). Picture credit: J. Chebly.

The solar wind, primarily composed of ionized hydrogen and fully ionized helium, also contains a variable mixture of H^{+2} (0% to 15%) and oxygen ions, as detected by high-resolution measurements on the Vela 3 satellites. The two most abundant oxygen ions at the coronal temperature $\sim 10^6$ K are O^{+6} and O^{+7} (see Tucker & Gould 1966; Laming 2015). As the oxygen ions transition from the corona to the solar wind, the electron density drops sharply[12], causing the ionization state of the solar wind to be "frozen" in the high-density corona within a few solar radii from the solar photosphere to 1 AU (Hundhausen, Gilbert, & Bame, 1968; Hundhausen, 1968). This state is determined by the local electron temperature. We can infer the electron temperature at a specific coronal radius (r_f) by analyzing ion fractions measured far from the Sun. The exact position of the freezing radius depends on the atomic properties of the ions and the details of the coronal expansion, but it is estimated to range between $2\,R_\odot$ and $5\,R_\odot$ (see Fig. 4.12 for guidance).

As the wind moves in the Sun's vicinity, it is slowed down and compressed at the termination shock, located about 100 AU from the Sun. The Sun moves with respect to the local interstellar medium (ISM), creating a comet-like heliosphere. In the immediate vicinity of the Sun, the ISM is dominated by H, which makes up 90% of all interstellar matter in molecular, neutral or ionized form. In the inner heliosphere, the plasma density and the magnetic field strength decrease with the distance R from the Sun approximately with R^{-2} and with $B \sim R^{-1.5}$ by 1 AU (Burlaga, Ness, & McDonald, 1995; Burlaga, 2001). The interstellar plasma is compressed and diverted at the heliospheric bow shock. However, *neutral atoms* such as H, He, O, and Ne can traverse inside the heliosphere and interact with the solar wind plasma via charge exchange. These interactions create non-thermal ions that are "picked up" by the solar wind and energetic neutral atoms that propagate ballistically through the heliosphere.

Table 4.1: Table summarizing important values of the solar wind and heliosphere structure. References: Parker (1965); Laming (2015); Opher et al. (2015).

Medium	ρ (cm^{-3})	T (K)
Solar Wind	10^{-3}	$\geq 10^5$
Inner Astrosheath	$\geq 10^{-3}$	$\geq 10^6$
Outer Astrosheath	0.1	$\geq 10^4$
Interstellar Medium (ISM)	$\approx 10^{-2}$	$\approx 10^2$

1st charge exchange: Plasma wind–Inner heliosheath through termination shock

Inside the heliosphere, when the wind travels through the termination shock toward the inner-heliosheath (inner heliosphere), H^+ from the wind encounters the neutral hydrogen of the ISM. See the illustration in Fig. 4.13 for guidance and the table 4.1 for more information about the wind and the heliosphere. Once $H^+(n = 1)$ encounters neutral particles in the case of ISM (H^0) there is an *inelastic*

[12]This means that the ions of the solar wind rarely encounter an electron.

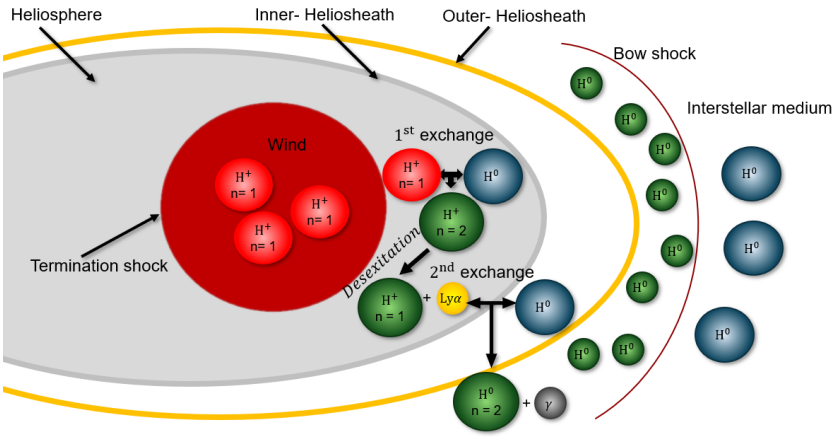

Figure 4.13: Simplified illustration showing how the charge exchange between the hydrogen ion in the wind interacts with the neutral hydrogen in the ISM to produce the Lyα photons. It also shows how the hydrogen wall was formed. Picture credit: J. Chebly.

collision[13] that takes place, $H^+(n = 1)$ will be excited and becomes $H^+(n = 2)$ where $n = 2$ representative of excited state (Eq. 4.6). $H^+(n = 2)$ quickly decay to the ground state with the emission of Lyα (1216 Å, 10.2 eV) radiation (Eq. 4.7). The radiation is in the Lyα regime as the emitted atoms are generated from the corona (we saw that we are in the Lyα continuum section 4.4).

$$H^+(n = 1) + H^0(n = 1) \rightarrow H^+(n = 2) + \gamma \tag{4.6}$$

$$H^+(n = 2) \rightarrow H^+(n = 1) + Ly\alpha \tag{4.7}$$

2nd charge exchange: Inner Heliosheath–Outer Heliosheath through Heliopause

Beyond the termination shock, the solar wind plasma continues to flow away from the Sun until it is diverted around the heliopause–the boundary separating the solar wind and ISM. Thanks to charge exchange reactions between the protons and neutrals (Eq. 4.6), these high temperatures and high densities are transmitted to the interstellar neutrals, creating what has been called a "hydrogen wall" (Baranov & Malama, 1993, 1995; Zank et al., 1996). The existence of the hydrogen wall is due to the Lyα photon absorption (Eq. 4.8). Lyα photon (wind) absorption happens whenever its energy matches the energy required to transition the neutral H atom (ISM) from the $n = 1$ to $n = 2$.

$$\text{Ly}\alpha + H^0(n = 1) \rightarrow H^0(n = 2) + h\nu \tag{4.8}$$

where $h\nu$ represents the energy of the absorbed photon.

The hydrogen wall is important because it is a structure in the outer heliosphere that can actually be detected and studied observationally, not only around the Sun but also around other stars[14] (Linsky & Wood, 1996; Wood, Alexander, & Linsky, 1996; Gayley et al., 1997; Wood et al., 2002). We will see in Sec. 5 that measurements of the stellar winds through the detection of the Lyα absorption signature laid the foundation for our understanding of wind-activity relation. Note that, the *only* measurable parameter of the winds is the mass-loss rate ($\dot{M}_\star$).

For the wind to exist, a non-gravitational force must oppose the inward gravitational force and propel the outermost layers of the star's atmosphere outward from the star. Depending on the type of wind, this wind acceleration can be due to a gradient in gas pressure, a gradient in radiation pressure or a gradient in magnetic pressure. We will see in section 4.7 that the most probable mechanism behind wind acceleration of cool main sequence stars is a gas gradient pressure.

[13] The system is not in energy equilibrium.
[14] The heated heliospheric HI creates a detectable absorption signature in the HI Lyα lines observed by the Hubble Space Telescope (HST) from nearby stars.

4.6 Element Abundances and the FIP effect

"Two possibilities exist: either we are alone in the universe or we are not. Both are equally terrifying."
Arthur C. Clarke

At this point, you are already familiar with the FIP effect and what we have observed as element abundance differences between the corona and the photosphere. But how does this actually work? Early on, explanations of the FIP effect involved diffusion flows or some sort of turbulent mixing in the chromosphere to prevent any gravitational settling[15] (see, e.g., Marsch, von Steiger, & Bochsler 1995; Schwadron, Fisk, & Zurbuchen 1999). Schwadron, Fisk, & Zurbuchen (1999) favored the hypothesis of turbulent wave heating in the chromosphere as a way to both prevent a mass-dependant fractionation and to obtain a low-FIP bias. Later on, Laming (2004) proposed ponderomotive acceleration as the origin of the FIP effect. Both processes rely on Alfvén waves propagating parallel and anti-parallel to the magnetic field to trigger a turbulent cascade through non-linear interactions and heating (more on this mechanism and Alfvén waves in Sec. 4.7).

By analyzing the A/Fe ratio (where A is the abundance of different high FIP elements) in the corona relative to the photosphere, researchers can ascertain the FIP bias "F_{bias}"–a parameter that indicates the strength of the FIP effect (Wood, 2004; Wood et al., 2021). This bias factor is crucial for understanding the enrichment of low FIP elements in the corona and the dynamics within the solar atmosphere. In the case of a low FIP effect, the fractioning of the elements might not have been efficient. What can cause this? Do we have a case where there is no FIP effect? We will return to this in Sec. 4.7 and Sec 5.8.

The photospheric abundances are usually determined relative to hydrogen, which serves as the basis for absolute abundance measurements. When measuring coronal abundance, however, the approach is different. This is because it is difficult to detect H in the corona, as it does not emit observable lines in the same spectral bandwidths in which the emissions of the other elements are prominent. In the field of X-ray and EUV observations, Fe with its robust emission line is used as a representative for low FIP elements taking the place of H (Feldman & Widing, 1993). The spectral lines of Fe also provide valuable diagnostic information about the temperature and density of the solar plasma.

4.7 Alfvén Wave

"Nothing happens until something moves."
Albert Einstein

In 1942, Hannes Alfvén conducted a groundbreaking study on the properties of plasma, which he characterized as a highly conductive, magnetized, and incompressible fluid (Alfvén, 1942). His research led to the discovery of a unique wave mode within the plasma, now known as Alfvén's shear or torsional wave. These waves, which are low-frequency electromagnetic waves typically below 300 Hz, can propagate through conductive fluids such as plasmas. Even minor movements in an electrically conductive fluid within a magnetic field can trigger the propagation of MHD waves. When there are discontinuities in density or magnetic field strength, various wave eigenmodes[16] can emerge.

Alfvén waves (AWs) stand out for their suitability for energy transport. This is due to their inherent property of minimal reflection and highly incompressible nature, which leads to minimal energy dissipation[17]. The reflection of AWs at steep density gradients leads to a local wave reflection which ensures a continuous source for both types of waves. The equation for the propagation, dissipation and

[15] Tendency of heavier elements to sink towards the solar surface while lighter elements rise to higher altitudes.

[16] Eigenmodes, which include Alfvén waves, magnetoacoustic waves, and kink modes, are wave patterns that occur in magnetized fluids such as plasmas. They are shaped by magnetic and fluid interactions and exhibit different spatial and temporal properties influenced by factors such as the strength of the magnetic field, the plasma density, the temperature, and the system boundaries (He, Xu, & Yu, 2016; Qiu, Chen, & Zonca, 2023).

[17] Dissipation of MHD waves can occur due to various mechanisms, including resistive dissipation. Where the wave energy is converted into heat due to the resistance of the plasma, and turbulent dissipation.

reflection of the Alfvén turbulence can be found in van der Holst et al. (2014).

$$\frac{\partial w_\pm}{\partial t} + \nabla\left[(\vec{u} + \vec{V}_\mathrm{A})w_\pm\right] + \frac{w_\pm}{2}(\Sigma\vec{u}) = -\Gamma_\pm w_\pm \pm \mathscr{R}\sqrt{w_- w_+} \tag{4.9}$$

where $\vec{V}_\mathrm{A} = \vec{B}/\mu_0\rho$ is the Alfvén velocity, ρ represent the mass density, μ the permeability, and $\vec{B}$ the magnetic field. $w_\pm$ are the energy densities for the turbulent waves propagating along the magnetic field (w_+) or in the opposite direction (w_-). The plasma speed is represented by $\vec{u}$. The dissipation rate ($\Gamma_\pm$) and the reflection coefficient ($\mathscr{R}$) are given by:

$$\Gamma_\pm = \frac{2}{L_\perp}\sqrt{\frac{w_\pm}{\rho}} \tag{4.10}$$

and

$$\begin{aligned}\mathscr{R} = \min\Big\{\sqrt{(\mathbf{b}.[\nabla\times\vec{u}])^2 + [(\vec{V}_\mathrm{A}.\nabla)\log V_\mathrm{A}]^2}, \max(\Gamma_\pm)\Big\} \\ \times\left[\max\left(1 - \frac{I_\mathrm{max}}{\sqrt{\frac{w_+}{w}}}, 0\right) - \max\left(1 - \frac{I_\mathrm{max}}{\sqrt{\frac{w_-}{w_+}^2}}, 0\right)\right]\end{aligned} \tag{4.11}$$

where $\mathbf{b}$ a unit vector in the direction of the magnetic field, $L_\perp$ is the transverse correlation length of AWs in the plane perpendicular to the magnetic field line and $I_\mathrm{max} = 2$ is the maximum degree of turbulence "imbalance." If $\sqrt{w_+/w-} < I_\mathrm{max}$, then AW reflection is neglected and $\mathscr{R} = 0$.

Another property of AWs, shown by Jacques (1977), is that they exert an isotropic pressure. Moreover, AWs typically generate a Ponderomotive force, a nonlinear force that occurs when charged particles, like ions, encounter an inhomogeneous oscillating electromagnetic field. In contrast to the symmetrical oscillation around a fixed point observed in a homogeneous field, the Ponderomotive force drives particles toward areas of lower field strength. The underlying mechanism for this movement is the differential force that the particle experiences throughout the oscillation cycle. This force is more pronounced in regions of higher field intensity (Alfvén, 1957).

$$F_\mathrm{pond} = -\nabla(\frac{q^2}{2mw^2}|E|^2) \tag{4.12}$$

where q is the charge of the particle, m is the mass of the particle, ω is the angular frequency of the wave, E is the electric field of the wave, ∇ denotes the gradient operator.

The Sun, with its high electrical conductivity, low viscosity[18], and an extended magnetic field provide an ideal environment for MHD waves, especially AWs, to occur. Hot plasma circulates in the convection zone (Sec. 4.1), releasing energy that eventually reaches the surface and contributes significantly to the cooling of the photosphere[19]. As the hot plasma releases its energy, it cools down and becomes less dense. This cooler, less dense plasma does not exert as much pressure as the hotter, denser plasma below it. This pressure difference between the plasma layers creates a *pressure* gradient. Since any motion that changes the shape of a magnetic field lines causes a magneto-hydrodynamic oscillation of the line, we must assume that the turbulence of the photosphere, which we observe as granulation, causes magneto-hydrodynamic waves (more on the granulation in Sec. 4.2).

At the surface of the Sun, the Poynting flux ($\vec{S}_\mathrm{A}$) is defined as the place where $\vec{E}$ and $\vec{B}$ are interacting to produce electromagnetic radiation (Eq. 4.13).

$$S_\mathrm{A} = \mathbf{E}(R_\odot) \times \mathbf{B}(R_\odot) = \mathrm{Const} \approx 1.1 \times 10^6\,(\frac{\mathrm{W}}{\mathrm{m^2T}}) \tag{4.13}$$

As the magnetic field strengthens, the distance over which correlated variations or structures are observed in a direction perpendicular to the magnetic field also increases. This implies that stronger

[18] In the outer layers of the Sun, such as the convective zone and the photosphere, plasma motions play a crucial role in transporting energy from the interior to the surface and drive phenomena such as convection and magnetic field generation. Low viscosity allows for efficient convection motion, where heated plasma rises and cooler plasma sinks, facilitating energy transfer in these layers.

[19] This is because the plasma at the surface is cooler and less dense, resulting in fewer collisions that trap the energetic photons inside the Sun.

magnetic fields are associated with larger-scale spatial variations or structures that extend further away from the central axis of the magnetic field. Moreover, it is assumed that the transverse correlation length scales ($L_\perp$) with the strength of the magnetic field (Eq. 4.14, following the approach of Hollweg 1986).

$$L_\perp = B^{-1/2}, 100\,(\mathrm{km.T^{1/2}}) \leq \mathrm{L_\perp}\sqrt{\mathrm{B}} \leq 300\,(\mathrm{km.T^{1/2}}) \tag{4.14}$$

Magneto-hydrodynamic waves are transmitted upwards from the photosphere along the magnetic field lines. As these waves ascend through the solar atmosphere, their speed changes, mainly due to alterations in mass density. This change is equivalent to a shift in the refractive index. If this shift is fast, partial reflection of the waves can occur, meaning that only a fraction of the energy reaches the chromosphere or corona (Laming, 2015). Conversely, the speed increases as the density decreases. These waves then propagate upward through the chromosphere and corona and contribute to the dynamic processes in the solar atmosphere, such as wind acceleration and element fractioning (Laming, 2015).

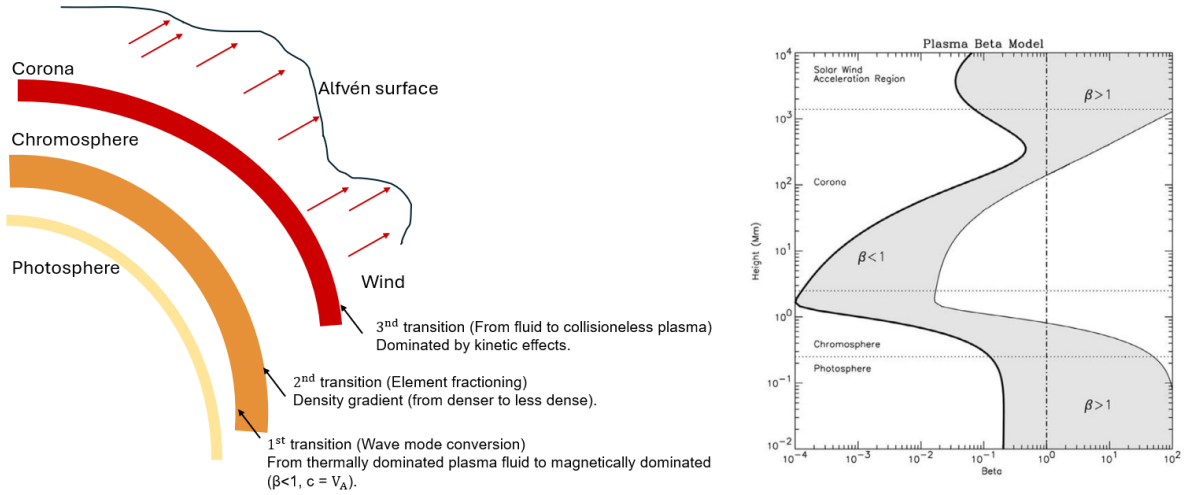

Figure 4.14: *Left*, a cross-section of the Sun shows its atmosphere layers with the different transitions for wind acceleration, element fractioning and AS formation. Picture credit: J. Chebly. *Right*, variation of β_{plasma} as a function of distance in the solar atmosphere. Picture credit: Verscharen (2012).

In Fig. 4.14 I illustrate the different transitions that the AW goes through to achieve the acceleration of the solar wind and the fractioning of the elements. This illustration serves as a guide for the following description. We must keep in mind that we consider the plasma as a single *fluid* from the photosphere to the lower corona.

1st Transition Layer: Wave Mode Conversion (*lower chromosphere*)

Two pressures come into play in the photosphere: the gas pressure (nkT, which results from the movement of the particles) and the magnetic pressure ($B^2/8\pi$). The gas pressure[20] dominates the magnetic pressure[21]. The ratio between gas and magnetic pressure, called plasma (β_{plasma}), is given by Eq. 4.7. This means that in the photosphere $\beta_{\mathrm{plasma}} > 1$.

$$\beta_{\mathrm{plasma}} = \frac{P_{\mathrm{g}}}{P_{\mathrm{m}}} = \frac{nkT}{B^2/8\pi} \tag{4.15}$$

where n is the particle number density, k is Boltzmann's constant, T is the plasma temperature.

Although the gas pressure dominates the magnetic pressure in the photosphere (except in sunspots), this is reversed in the upper layers of the solar atmosphere ($B^2/8\pi > nkT$). In the low chromosphere, where the pressure changes from being thermally dominated to being magnetically dominated (see Sec. 4.5). In this region the *sound speed and Alfvén speed are equal* and several processes

[20] Tends to exert a force that pushes outwards.
[21] Creates a tension that pulls inwards.

involving wave mode conversion and other wave–wave interactions can occur. This is where a significant fraction of the MHD waves that eventually accelerate the solar wind are generated (Laming, 2015).

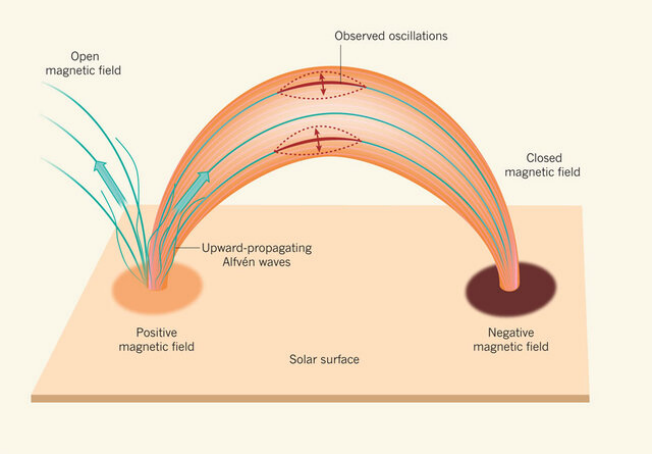

Figure 4.15: Illustration of AWs transport in a closed loop. The solid lines represent magnetic field lines, with the blue lines extending into space representing coronal holes on the left and closed structures in the corona on the right, as seen in the quiet Sun and active regions. Wavy blue lines show upward transverse displacements (AWs), with solid blue arrows indicating the direction of energy transport. Dashed lines with red arrows represent oscillatory displacements observed by McIntosh et al. (2011) in loops in active regions. These are interpreted as AWs postulated for heat transport in the solar corona and observed by the Hinode spacecraft. Picture credit: McIntosh et al. (2011).

2nd Transition Layer: Element Fractioning (*upper chromosphere*)

At the upper boundary of the chromosphere, there is a sudden drop in electron density (n_e) of about 10^{11} cm^{-3} to 10^9 cm^{-3}, while the temperature (T_e) in the solar corona rises rapidly to over 1 MK (e.g. Aschwanden 2005). This occurs further up in the chromosphere, where the mostly neutral gas becomes ionized plasma that forms the solar corona and solar wind. This transition creates strong *density gradients*, which in turn cause the waves to be reflected and refracted. When AWs interact with this density gradient, they generate a ponderomotive force (Eq. 4.7) on charged particles. The latter will effectively push ions from regions of high to low wave amplitude. Since the waves are fundamentally magnetic in character, only ions are susceptible to the force, and ion–neutral separation is the result, giving rise to element fractionation in the upper atmosphere known as the FIP effect.

Alfvén waves travel along magnetic fields, similar to the way sound waves travel along a plucked guitar string (see Fig. 4.15). These waves can resonate in closed magnetic loops and increase their amplitude when their frequency matches the natural frequency of the loop. When AWs travel, they efficiently transport energy and create turbulence, which leads to additional heating and mixing of the solar plasma (Réville et al., 2021). The fractionation occurs at the base of the loop's footprint. (see Fig. 4.15 for guidance). In contrast to closed magnetic fields, open magnetic field lines do not exhibit resonance behavior, resulting in an ongoing process of element fractioning in the chromosphere. Within regions characterized by open magnetic field lines, AWs, which are essentially oscillations of the plasma coupled to the magnetic field, propagate unhindered.

3rd Transition Layer: Alfvén Surface Formation (*top of the corona*)

At the top of the corona, the transition of the solar plasma from a fluid to a collisionless plasma takes place (dominated by kinetic effects).[22] This transition occurs because β_{plasma} increases with height in the corona. When $\beta_{\text{plasma}} > 1$, the plasma is no longer trapped in magnetic loops or flux tubes but can expand into space and pull the magnetic fields outward into the solar wind (see section 4.5). This

[22] Refer to the behavior of individual particles within the plasma, whose motion is determined by electromagnetic fields and particle-particle interactions rather than collisions

tends to define the "peak" of the corona and typically occurs near $2\,R_\odot$, where $n_e \sim 10^6\,\mathrm{cm}^{-3}$. This is where the ion-proton collision rate becomes slower than the expansion rate of the solar wind, $v_w(r)/r$, where $v_w(r)$ is the velocity of the solar wind and r is the heliocentric radius. Ions of different elements make this transition at different radii, resulting in a much less "clean" transition than the first two. However, this transition is significant for the wave-driven acceleration of the solar wind. The different heliocentric radii form the so-called *Alfvén surface* (AS). In this region, the density varies the most and largely controls this transition (Laming, 2015).

Figure 4.16: Visualization of the Alfvén surface (Wobbly shape) and the Parker Solar probe entering the surface. Picture credit: NASA.

The surface acts as a divider between the end of the solar atmosphere and the beginning of the solar wind. The shape and size of AS depends on several factors as we will see in chapters 6 and 7. The solar AS is between 0.046 and 0.093 AU (Cranmer et al., 2023). Distances of less than 0.04 AU are in the AS where the wind is still accelerating. The Parker Solar Probe entered the AS of the Sun in 2018 (see Fig. 4.16). This will help us better understand wind acceleration and properties and coronal heating. In the case of the Sun, all planets are outside the AS, but this is not always true for exoplanets orbiting Sun-like stars and other cool main-sequence stars. Whether a planet is inside or outside the AS, whether it is magnetized or not, plays a crucial role in its atmosphere's survival. A planet orbiting inside the AS will experience a different interaction with its host star. I will talk more about this in part II.

The role of AWs in the heating and acceleration of the solar wind has been a topic of interest since the dawn of in-situ space exploration. This interest was sparked by seminal works such as those by Belcher, Davis, & Smith (1969); Belcher (1971), and by Alazraki & Couturier (1971). A comprehensive and consistent theoretical framework describing AW turbulence and its impact on average plasma motion has been established over time. Notably, significant contributions were made by Dewar (1970) and by Jacques (1977, 1978). More recent efforts to simulate solar wind acceleration utilize the approach developed by Usmanov et al. (2000).

The latest generation of coronal models uses AWs to heat and accelerate the solar wind (see Usmanov et al. 2000; van der Holst et al. 2014). This approach promises to explain the origin of both the fast and the slow solar wind. Alfvén wave turbulence has the potential to drive the solar wind in a manner consistent with observations at 1 AU (Coleman, 1968). Several groups have developed 1D AW-driven models (Suzuki & Inutsuka, 2006; Cranmer, van Ballegooijen, & Edgar, 2007), 2D (Usmanov et al., 2000; Matsumoto & Suzuki, 2012), and 3D (Sokolov et al., 2013; van der Holst et al., 2014; Usmanov et al., 2018). Of all the solar models that incorporate AWs as the driving mechanism for corona heating and wind acceleration, the 3D MHD Alfvén Wave Solar Model, known as AWSoM, stands out as one of the most sophisticated physics-based models that have been able to recreate the Sun's corona (Fig. 4.17).

The Alfvén wave solar model is used as part of the Space Weather Modeling Framework (SWMF; Sokolov et al. 2013; van der Holst et al. 2014; Gombosi et al. 2018). The SWMF is a set of physics-based models (from the solar corona to the outer edge of the heliosphere, Tóth et al. 2012. This model uses the numerical schemes of the Block Adaptive Tree Solar Roe-Type Upwind Scheme (BATS-R-US; Powell et al. 1999) MHD solver. A detailed description of the model can be found in Gombosi et al. (2021). The multi-domain solution starts with a calculation using the Solar corona (SC) module, which incorporates AWSoM. The continuity, induction, and momentum equations

used in the AW turbulence driven solar atmosphere model are as follows:

$$\frac{\partial \rho u}{\partial t} + \nabla(\rho \vec{u}) = 0 \tag{4.16}$$

$$\frac{\partial \vec{B}}{\partial t} + \nabla(u\vec{B} - \vec{B}u) = 0 \tag{4.17}$$

$$\frac{\partial \rho \vec{u}}{\rho t} + \nabla(\rho \vec{u}\vec{u} - \vec{B}\vec{B}/\mu_0) + \nabla(p_i + p_e + \frac{B^2}{2\mu_0} + P_A) = \frac{-GM_\odot \rho \vec{r}}{r^3} \tag{4.18}$$

where the mass density is represented by ρ, $\vec{u}$ is the bulk velocity (u = $|\vec{u}|$ is assumed to be the same for the ions and electrons), $\vec{B}$ is the magnetic field, G is the gravitational constant, $M_\odot$ denotes the solar mass, **r** is the position vector relative to the center of the Sun, μ_0 is the magnetic permeability of vacuum. The Alfvén wave pressure, P_A, provides additional solar wind acceleration. The isotropic ion pressure P_i and electron pressure P_e are determined by the energy equations:

$$\begin{aligned} &\frac{\partial}{\partial t}\left(\frac{P_\mathrm{i}}{\gamma-1} + \frac{\rho u^2}{2} + \frac{\vec{B}^2}{2\mu_0}\right) + \nabla \cdot \left[\left(\frac{\rho u^2}{2} + \frac{\gamma P_\mathrm{i}}{\gamma-1} + \frac{B^2}{\mu_0}\right) u - \frac{\vec{B}(\vec{u}\cdot\vec{B})}{\mu_0}\right] \\ &= -(\vec{u}\cdot\nabla)(P_\mathrm{e} + P_\mathrm{A}) + \frac{N_\mathrm{i} k_\mathrm{B}}{\tau_\mathrm{ei}}(T_\mathrm{e} - T_\mathrm{i}) + Q_\mathrm{i} - \rho\frac{GM}{r^3}\vec{r}\cdot\vec{u} \end{aligned} \tag{4.19}$$

and

$$\frac{\partial}{\partial t}\left(\frac{P_\mathrm{e}}{\gamma-1}\right) + \nabla \cdot \left(\frac{P_\mathrm{e}}{\gamma-1}\vec{u}\right) + P_\mathrm{e}\nabla\cdot\vec{u} - \nabla\cdot\vec{q_\mathrm{e}} + \frac{N_\mathrm{i} k_\mathrm{B}}{\tau_\mathrm{ei}}(T_\mathrm{i} - T_\mathrm{e}) - Q_\mathrm{rad} + Q_\mathrm{e} \tag{4.20}$$

where, $T_\mathrm{e,i}$ are the electron and ion temperatures, $N_\mathrm{e,i}$ are the electron and ion number densities, and k_B is the Boltzmann constant. We use the simple equation of state $P_\mathrm{e,i} = N_\mathrm{e,i} k_\mathrm{B} T_\mathrm{e,i}$ and the polytropic index is $\gamma = 5/3$. The electron and ion heating functions are denoted by Q_e and Q_i, respectively. The electron heating flux is represented by $\vec{q_e}$.

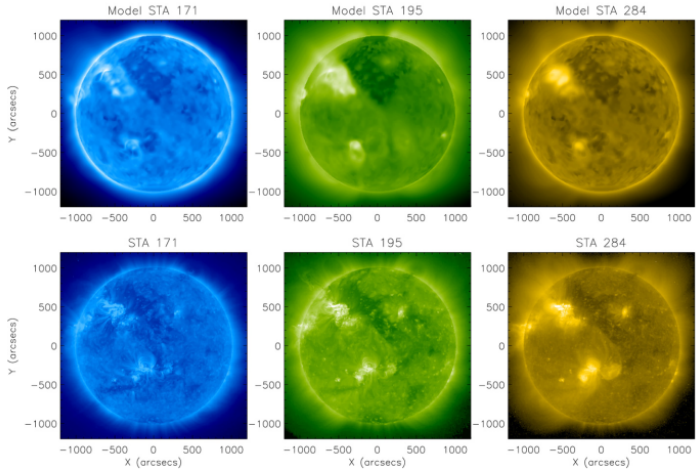

Figure 4.17: Comparison of synthesized EUV images of the model with observational STA/EUVI images. The columns are from left to right for 171 Å, 195 Å, and 284 Å. *Top panels*, synthesized EUV images of the model. *Bottom panels*, observational STA/EUVI images. The observation time is 2011 March 7 20:00 UT. Picture credit: Sokolov et al. (2013).

Models based on MHD, such as the ones incorporating AWs, have successfully described the solar wind from tens to hundreds of solar radii (Gombosi et al., 2018) and reference therein. The advantage of the thermodynamic approach is its ability to describe shock related phenomena. Unlike the first generation incorporated an ad-hoc function to heat and accelerate the solar wind. They succeeded in reproducing observed solar wind parameters at 1 AU but failed when reproducing the emergence of the slow and fast solar wind. For a comprehensive understanding of the first generation models check the following studies; Groth et al. (1999); Lionello, Linker, & Mikić (2001); Riley et al. (2006); Feng, Zhou, & Wu (2007); Nakamizo et al. (2009); Feng et al. (2010), and Downs et al. (2010).

I will come back to the AWSoM model in chapter 5, in a stellar wind modelling context.

Winds and Coronae of Cool Main Sequence Stars Late-F to Late-M

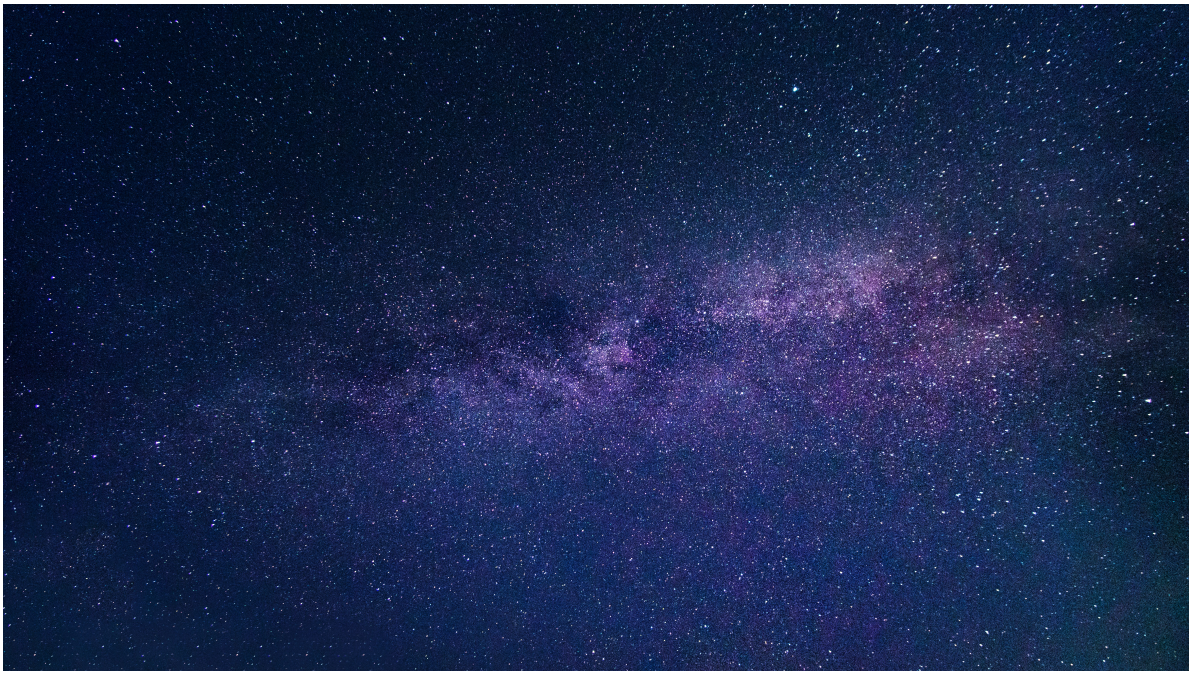

Figure 5.1: Picture credit: Felix Mittermeier.

The Milky Way, our home galaxy, is a vast cosmic entity teeming with a multitude of stars. Among these, cool stars, often red dwarfs, are particularly abundant. These stars, smaller and less hot than our Sun, emit light at the cooler end of the spectrum, giving them a distinctive red hue. Despite their lower temperature, they are incredibly long-lived, burning their fuel much more slowly than larger stars. This abundance of cool stars in the Milky Way provides a fascinating insight into stellar evolution and the potential for habitable planets around these stars. Their prevalence and longevity make them intriguing subjects for ongoing astronomical research.

5.1 The Sun: A Guide for Stellar Physics

"To the best of our knowledge, our Sun
is the only star proven to grow vegetables."
Philip Scherrer

Stellar evolution models suggest that the Sun evolved from a cooler, orange K-type star in its youth to the warmer, yellow G2-type star we see today. In about 4 billion years, the Sun is expected to turn into a red giant, eventually shed its outer layers to form a planetary nebula, and finally become a cool white dwarf. This transformation will significantly change the Sun's surface temperature, size, and brightness. For more information on stellar structure and evolution, see Prialnik (2009).

The "life cycle"" of a Sun-like star, as shown in Fig. 5.2, can be described as follows: In the beginning, the stellar winds are magnetic, so they can carry considerable angular momentum. As the star evolves, it spin down due to this loss of angular momentum. This change in surface rotation leads to a redistribution of internal angular momentum transport (Kraft, 1967; Skumanich, 1972). Consequently, the dynamo inside the star adapts to the changes and influences the properties of the resulting magnetic fields. With the new surface magnetism, the stellar wind and the element abundances also change (Reames, 2024). This completes a cycle that is repeated on the main sequence throughout the lifetime of the star. This also affects the star's environment and the radiation emission that a planet receives (Lammer et al., 2003; Cohen et al., 2015; Garraffo, Drake, & Cohen, 2016; Segura, 2018).

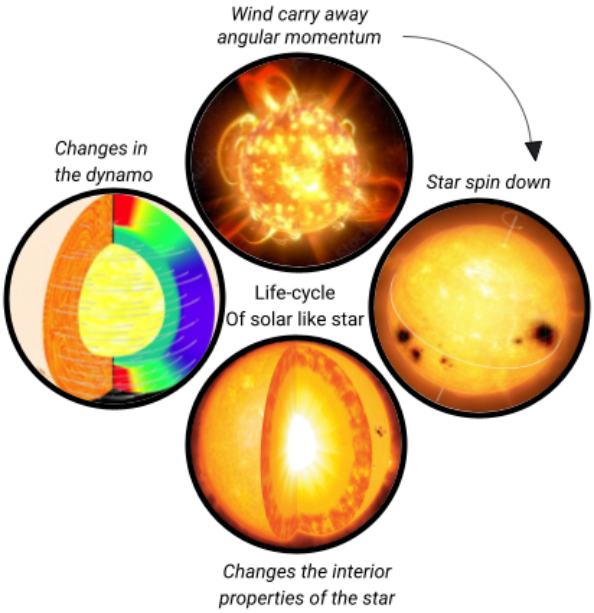

Figure 5.2: Illustration of the overall life cycle of an isolated cool main sequence star with the emphasis on the different evolutions such as: angular momentum removal due to magnetized winds, rotational evolution due to the spin down, changes in the interior of the star. Picture credit: J. Chebly.

What do we know about the magnetism and winds of other cool stars? Are we able to observe their winds? Do we expect similar wind properties between the solar wind and that of other cool stars, or does the Sun have unique properties? In the following sections, I will provide a comprehensive overview of our current understanding of stellar winds and the FIP effect in other cool stars. Note that I will use the term "stellar" instead of solar when I refer to stars other than the Sun.

5.2 Star Surface Mapping

"All we ever see of stars are their old photographs."
Alan Moore

The Sun has complex surface structures accessible to direct imaging with many ground-based instruments and space missions. With the exception of interferometric studies of nearby and particularly large stars (see Kervella 2016), the disks of other cool stars are not resolvable. They, therefore, cannot be studied with direct imaging. In this case, the only practical way to obtain information about the stellar surface structures is to apply a form of the inverse remote sensing method of *indirect imaging*, which can create a map of the stellar surface from spatially unresolved stellar observations.

In this section, I will briefly explain the rationale for reconstructing the stellar surface, moving from a 1D to a 2D representation. I will also discuss two different types of 2D maps: one derived from the Zeeman Broadening (ZB) technique and the other derived from the Zeeman Doppler Imaging (ZDI) technique and their respective limitations. Understanding the similarities and differences between these two techniques are critical to the work presented in this thesis. This is because the ZDI maps are used as inner boundary conditions in the stellar wind simulations (see Sec. 7). Therefore, knowing these properties helps to understand why it is more common to use ZDI rather than ZB technique.

Inhomogeneities on a star's surface alter the local line and continuum radiation that emerges. If these surface irregularities are large enough and have high contrast, their spectral signatures will appear as distortions in the disk-integrated line profiles. These distortions can be emission "bumps" for cool spots or additional absorption features for spots with a higher element concentration (Kochukhov, 2016). The light spectrum from a star's unresolved disk is a weighted average of all local spectral elements. These elements are Doppler-shifted based on their local projected rotational speed relative to the observer. As such, the star needs to be bright enough to yield high-quality spectra (high S/N) within a time frame that is relatively short compared to the star's rotational period. The resolution element's angular size at the star's equator is expressed in degrees (Eq. 5.1).

$$\delta l \approx 90^{\circ} \frac{\Delta\lambda}{\lambda} \frac{v_c}{v_e \sin i} \tag{5.1}$$

where $R{=}\Delta\lambda/\lambda$ is the instrumental resolution of the spectrograph, $v_e \sin i$ is the projected rotational velocity, and v_c is the speed of light.

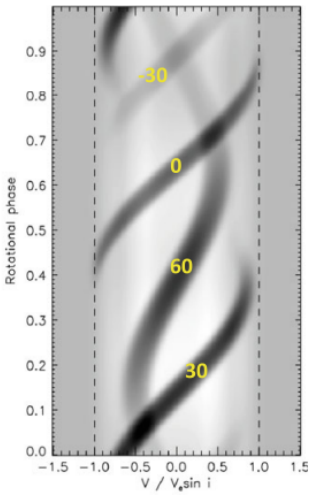

Figure 5.3: Image showing the dynamic difference spectrum as a function of the rotational phase. In this case, the stellar surface has four small spots at latitudes 30°, 0°, -30°, and -60°. This plot demonstrates how temporal variation of the spot signatures depends on their latitude position. Picture credit: Kochukhov (2016).

The velocity of the distortion relative to the line center is determined by the *longitude* of the surface feature (for simplicity, I will consider a spot on the star's surface) measured from the star's central meridian. As the star rotates, the spectral distortions first appear on the blue side of the spectral line profile and then gradually shift to the red side. As for the *latitude* position of the spot, it cannot be derived from a single observation. Instead, the latitude information is derived from the

time series behavior of the spot signatures (rotational phase)[1]. For more details, see Reiners (2012) and Kochukhov (2016). It is noteworthy that for slowly rotating stars, we need a long time series or a longer observation to collect enough information in the stellar spectra. For very fast-rotating stars (such as very active M dwarfs), the spots move rapidly from the observer, meaning we may not have enough integration time. This will require high temporal resolution observations to track the motion of the spots.

The spectroscopic observational gathered form of spectra along longitude and latitude go through regularization methods that add a simplicity criterion to limit possible solutions and ensure the uniqueness of the 2D solution. This was first introduced in the study by (Goncharskii et al., 1977). The two most popular regularization strategies are maximum entropy and Tikhonov regularization. Further details on both methods can be found in the cited references Lanza, Bonomo, & Rodonò (2007). One example of the reconstructed 2D map can be seen in Fig. 5.3. Now that we understand how to create a 2D map, how do we obtain the spectra?

When we talk about the spectra, we speak in terms of Stokes profile. The full state of polarisation of stellar radiation (Fig. 5.4) is characterized by the four Stokes parameters as defined by Stokes (1851): Stokes I (*total intensity*), V (*circular polarisation*), and QU (linear polarization). Stokes parameters are sums and differences of intensities, and they are *directly measurable*. The four Stokes parameters can be expressed in an intuitive way that also provides a clear observational strategy (e.g., Rees 1987; Rutten 2003). The set of equations is presented in Eq. 5.2.

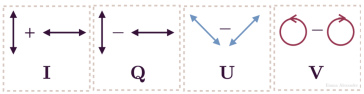

Figure 5.4: Representations of the Stokes parameters. Picture credit: Emma Alexander.

$$
\begin{aligned}
I &= \text{total Intensity} \\
Q &= I^{\text{linear}}_{0^\circ} - I^{\text{linear}}_{90^\circ} \\
U &= I^{\text{linear}}_{+45^\circ} - I^{\text{linear}}_{-45^\circ} \\
V &= I^{\text{circular}}_{\text{right}} - I^{\text{circular}}_{\text{left}}
\end{aligned}
\tag{5.2}
$$

The Stokes I spectra depend on the magnetic field modulus, while the Stokes QUV profiles are susceptible to the magnetic field orientation. The profiles are detected through the most successful method for direct detection of stellar magnetic fields known as the Zeeman effect (ZE, Zeeman 1897). This effect allows the detection of a magnetic field at the stellar surface through two phenomena: the *splitting* of magnetically sensitive lines and the presence of *polarization* in Zeeman components[2]. The spectral lines corresponding to the transitions between the split Zeeman levels divide into groups of π (linearly polarized[3])- and σ-components (circularly polarized[4]). More comprehensive discussions of ZE and equations for calculating Zeeman splitting in stellar atomic absorption lines can be found in Condon & Shortley (1963); Beckers (1969); Saar (1988); Landstreet (1992); Mestel & Landstreet (2005); Donati & Landstreet (2009) and Haken, Hermann and Wolf, Hans C. (2012).

Stokes QUV profiles being sensitive to magnetic field orientation means that polarization observations can provide extensive details about the geometry of the field. However, it also means that the analysis of intricate magnetic topology is subject to the cancellation of polarization signals in the disk-integrated spectra. For a comprehensive overview of the theory of polarization of spectral lines see Landi Degl'Innocenti & Landolfi (2004). Thus, all four Stokes parameters are, in principle, needed for a complete diagnostic of stellar magnetic field. Such observations are currently available for a small sample of strongly magnetic Ap stars (Wade et al., 2000; Silvester et al., 2012; Rusomarov et al., 2013) and for only one bright active RS CVn star (Rosén, Kochukhov, & Wade, 2014). In cool stars, ZB in Stokes I is subtle, and measurements of Stokes V, Q, and U are challenging to acquire and exhibit subtle Zeeman signals (Kochukhov & Piskunov, 2002). This has led to the practice of investigating either Stokes I (ZB) or Stokes V (ZDI) alone in cool stars. In table 5.1, you can find a summary of some of the characteristics of the usage of either Stockes I or V.

[1]This is because we have differential rotation, where the rotation varies at different altitudes on the surface of cool stars, similar to the Sun (faster near the equator). Therefore, with each spectrum we obtain, we calculate the velocity of the spot and can estimate from this the altitude at which it is located.

[2]The magnitude of this separation depends on the B-strength, magnetic sensitivity of a given spectral line is characterized by the Landé factor (g), and the central wavelength of this line (λ_0): $\Delta\lambda_B = g\frac{eB(G)\lambda_0(\mathring{\text{A}})^2}{4\pi m_e c} = 4.67\times10^{-13} gB\lambda_0^2$ where e is the elementary charge, c represents the speed of light, and m_e is the electron mass.

[3]Corresponds to the central line where the electric field is parallel to the magnetic field lines.

[4]Correspond to the outer lines where the electric field is perpendicular to the magnetic field.

Basri, Marcy, & Valenti (1992) introduced a method to detect a cool star's B by searching for enhanced equivalent widths of Zeeman-sensitive absorption lines. This method was used for example by Saar, Piskunov, & Tuominen (1992); Saar (1994) for Stokes I magnetic surface imaging. The advantage of this method is that equivalent widths are more easily measured than the subtle differences in line shape. Nevertheless, the method cannot lift degeneracies between B strength and other features like starspots or uncertainties in the model atmosphere. Moreover, typical B of non-degenerate stars[5] such as cool main sequence stars produce a Zeeman splitting much smaller than the intrinsic line width. This means that B of cool stars are not strong enough to cause a significant ZE, and that the observed spectral lines are still relatively broad compared to the splitting caused by B.

Table 5.1: Comparison of Zeeman Broadening and Zeeman Doppler Imaging techniques.

	Zeeman Broadening (Stokes I)	**Zeeman Doppler Imaging (Stokes V)**
Total field measured?	Yes: large and small scales	No: limited to large-scale fields
Topology studied? (i.e., vector B)	No: average over entire surface only	Yes: surface distribution of B_r, B_ϕ, B_θ
Ideal targets	Slow rotators (no rotational broadening)	Moderate/fast rotators

On the other hand, the ZDI technique gives us plenty of information regarding $\vec{B}$. Since $\vec{B}$ is a vector quantity, this necessitates the creation of three separate 2D maps. These maps depict the radial, meridional, and azimuthal components of $\vec{B}$. However, it only provides us with the net polarization[6]. Hence, it only recovers large-scale structures. In polarized light, the measurement of subtle signatures of net polarization requires an extremely high signal-to-noise ratio. Integrating over longer periods of time to accumulate sufficient photons is not practical, as the individual exposures must be kept sufficiently short to ensure adequate spatial resolution. There are a few possible solutions to this challenge. One approach is to use larger telescopes. Another strategy is to apply a technique known as Least Squares Deconvolution (LSD). For a comprehensive understanding and overview of the LSD method, see Donati et al. (1997); Wade et al. (2000); Kochukhov, Makaganiuk, & Piskunov (2010). In addition, the ZDI method is not sensitive to $\vec{B}$ within dark features such as starspots, the region with strongest B.

Although ZDI maps only show the net field, they are crucial in stellar wind simulations. They can be used as inner-boundary conditions to model the stellar wind. Consequently, predicting the properties of the wind in the vicinity of the star. Further details can be found in Sec. 5.5 and chapter 5. Observations for ZDI are carried out with spectropolarimeters, such as; ESPaDOnS, HARPSpol and NARVAL.

5.3 Stellar Coronal X-ray

"The immense distances to the stars and the galaxies mean
that we see everything in space in the past,
some as they were before Earth came to be.
Telescopes are time machines."
Carl Sagan

As discussed in Sec. 4.4, the corona emits X-rays, and such observations can only be made from space-based observatories. There are several X-ray telescopes available for these observations, including the Chandra X-ray Observatory, the *XMM-Newton Observatory*, SWIFT Observatory, among others. In this thesis, I will only briefly overview the XMM-Newton telescope. This is because the observations from XMM-Newton were used to determine whether moderately active M dwarfs follow a FIP or iFIP pattern, as will be discussed in chapter 8.

The *XMM-Newton* telescope, one of the most renowned space X-ray telescopes, derives its name from its unique mirror design, known as the highly nested X-ray Multi-Mirrors. It is the second of the four cornerstone projects of the European Space Agency's (ESA) long-term space program, Horizon 2000. The *XMM-Newton* telescope uses mirrors made of a material that does not readily absorb

[5] stars where thermal pressure, not degeneracy pressure, is the dominant force counteracting gravity.
[6] Residual of $\vec{B}$, since it suffers from cancellation

X-rays to overcome the difficulties in focusing the high-energy X-ray. The design ensures that the incident rays hit the mirror surface at a shallow angle, known as grazing incidence. This allows the X-rays to be efficiently reflected and directed to a focal point. The mirrors are barrel-shaped and angled along their length to focus the X-rays onto the detectors. See figure 5.5 for guidance.

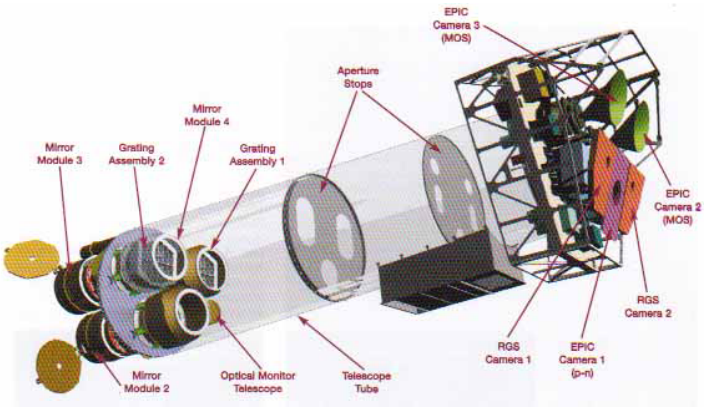

Figure 5.5: An exploited view of the telescope showing the different instruments. Picture credit: ESA

The telescope carries three co-aligned high throughput telescopes, each with a field of view of 30 arcmin and a spatial resolution of about 6 arcsec (Full Width at Half Maximum, FWHM). Each telescope has an imaging CCD detector at its focus. Behind two of the three telescopes, about half of the X-ray light is utilized by the Reflection Grating Spectrometers (RGS). The CCD cameras, collectively known as the European Photon Imaging Camera (EPIC). Two of these cameras are Metal Oxide Semi-conductor (MOS) referred to as the MOS cameras. They are installed behind the X-ray telescopes equipped with the RGS gratings. These gratings allow about 44% of the original incoming flux to reach the MOS cameras, taking structural obscuration into account.

The EPIC cameras are designed for highly sensitive imaging observations. They cover a field of view of 30 arcmin and an energy range of 0.15 to 15 keV, with an angular resolution of 6 arcsec. In contrast, the RGS is designed for high-resolution X-ray spectroscopy. It operates in an energy range of 0.33-2.5 keV and offers a spectral resolution of 100 to 500 arcsec (*XMM-Newton* technical description). *XMM-Newton* target distant X-ray sources over long periods of time (often > 10 h) and has a very high accuracy and stability. The spectra obtained are then analyzed following SAS handbook.

The X-ray spectrum is composed of both continuous (Bremsstrahlung emission) and characteristic emission. The continuous spectrum is generated by the deceleration of electrons in ion fields, which leads to a broad spectrum of X-ray energies. The characteristic spectrum, on the other hand, is generated by electronic transitions in the atoms, which lead to different emission lines at certain energies or temperatures that are unique for each element. Understanding the temperature distribution is crucial as different elements emit X-rays at different temperatures. This helps to identify the spectral lines that correspond to each element (Schmelz, Kimble, & Saba, 2012).

We saw in Sec. 4.4, that the corona of late-type stars contains plasma at temperatures up to several million Kelvin with low electron densities ranging from $n_e \sim 10^8$-10^{10} cm^{-3}. The low density implies that ions are predominantly in their ground states, and the plasma is expected to be in thermal equilibrium. The density only influences the strength of certain transitions and is only noticeable in *high-resolution* X-ray spectra. These properties simplify the modeling of the X-ray emission of coronal plasma, and the emission spectrum can be characterized by temperature, chemical composition, and density. Since the plasma is optically thin, we can consider all plasma at a single temperature, regardless of location. In this case, the volume emission measure (VEM) is defined by $n_e^2(T)V(T)$ (where n_e is the electron density and V is the volume). The latter plays a pivotal role in determining the height of the corona above the stellar surface and the fraction of the surface emitting X-rays, a concept known as the surface *filling factor* (Drake et al., 2000; Testa et al., 2004; Drake & Stelzer, 2023).

The volume emission measure provides valuable insight into the total amount of emitting material present in a specific region of space. On the other hand, the Differential Emission Measure (DEM), denoted by Eq. 5.3, offers more comprehensive information. It not only quantifies the amount of emitting material but also provides insights into how this material is distributed according to temperature. For the application of DEM, it is often recommended to use high-resolution spectra. A high-resolution spectrum provides more detailed information about the emission lines of different elements in the plasma,

which in turn allows for a more accurate determination of DEM. Conversely, a low-resolution spectrum lacks this level of detail, leading to greater uncertainties in the DEM analysis. For further information on DEM, VEM, and the filling factor, please refer to in Drake & Stelzer (2023).

$$DEM(T) = n_{\rm e}^2(T)\frac{dv(T)}{d\log(T)} \tag{5.3}$$

While *high*-resolution X-ray spectra offer detailed diagnostics for nearby stars, most stellar observations rely on low-resolution spectra due to instrument limitations (Weiler et al., 2020; Li & Lin, 2023). These observations are crucial for studying a broader range of stars and have led to significant discoveries, such as the correlation between X-ray luminosity and stellar effective temperature for various types of active stars, including main-sequence, giant, and binary stars Schmitt et al. (1990) and later refined by Johnstone & Güdel (2015). Once even very *low*-resolution X-ray spectra were possible, it became clear that more active stars appear to have an *extended range of coronal temperatures* (Johnstone & Güdel, 2015; Drake & Stelzer, 2023).

5.4 Cool Stars Magnetism and X-ray: What Have We Learned So Far?

"Are we human because we gaze at the stars, or do we gaze at them because we are human? Pointless really... Do the stars gaze back? Now that's a question."
Neil Gaiman

Stellar observations allow us to explore a larger parameter space of stellar properties such as activity, rotation, spectral type, and others;. In contrast, solar observations allow a much more detailed analysis of specific features. Together they provide a comprehensive understanding of stellar phenomena at different scales and contexts. The X-ray emission (or X-ray luminosity, $L_{\rm X}$) from stars is a key indicator of their age and activity. As stars age, their rotation slows down, leading to a decrease in X-ray activity (star in the unsaturated regime). This is described by the law defined in the work of Skumanich (1972), known as "Skumanich law". It is defined as follows, $\Omega_{\rm spin} \sim t^{-0.5}$, where $\Omega_{\rm spin}$ is the spin rate, and t the time. Consequently, $L_{\rm X}$ also diminishes, following a power law decay represented by $L_{\rm X} \sim t^{-1}$.

The decline in X-ray emission with age has been confirmed by satellite surveys of various clusters and studies of solar analogs across different ages. Einstein satellite observed a cluster Hyades of age 725 Myr and ROSAT enabled more extensive open cluster[7] observations and concerted campaigns resulted in surveys of approximately 30 different clusters with ages 10^7 to 10^9 yrs (Micela, 2002; Jeffries, 1999).

The initial research into the activity-rotation connection focused on stars in the lower main sequence, comparing activity indicators with spectroscopically derived rotation rates (*vsini* values). These studies, despite the *vsini* values limitations due to unknown inclination angles, confirmed a correlation with $L_{\rm X}$, as reported by Pallavicini et al. (1981). Further research expanded the sample of stars and observed a "saturation" level in the activity-rotation relationship for fast-rotating stars, using chromospheric resonance lines like the Ca II H&K doublet as activity proxies (Vilhu, 1984, 1987; Marsden, Carter, & Donati, 2009). Check Güdel (2004); Drake & Stelzer (2023) for a comprehensive review of the significance of X-ray studies in this field.

Early attempts to quantify coronal activity, such as those using data from the Einstein satellite (Walter, 1983), were inconclusive about saturation in the X-ray domain. The situation improved with ROSAT's all-sky survey and enhanced sensitivity, which provided a larger dataset of stellar X-ray detections. This led to the observation of a broad spectrum of X-ray activity levels across different spectral types, with an upper limit at the saturation value of approximately $L_{\rm X}/L_{\rm bol} = 10^{-3}$, as documented by Fleming et al. (1993). Notably, this saturation did not show a decline even at the boundary where stars become fully convective.

[7] Groups of stars that formed together and drifted apart over hundreds of millions of years. They are key to studying rotation-activity because they allow for the observation of many stars at once and provide a way to estimate the cluster's age through isochrone fitting. This helps understand the evolution of angular momentum and activity in stars.

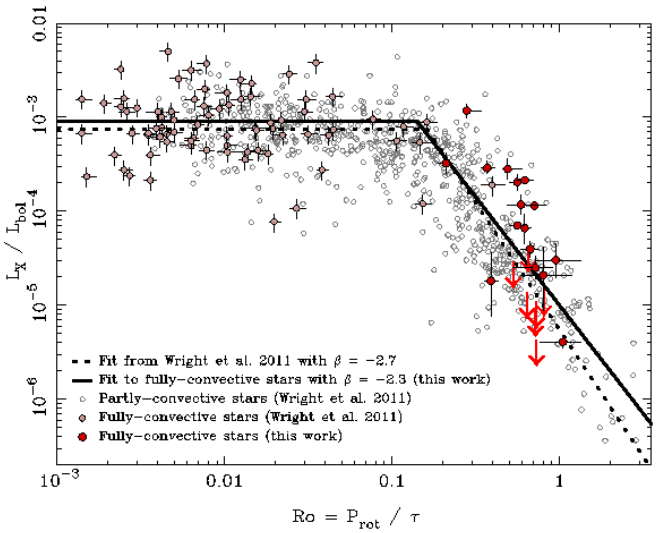

Figure 5.6: X-ray to bolometric luminosity ratio, plotted against the Rossby number. Large red points correspond to the fully convective stars observed in Wright et al. (2018), while the medium, light red represent the fully convective stars included in the sample of Wright et al. (2011). The remaining partly convective stars from that sample (grey empty circles). Upper limits are shown for the undetected fully convective stars as red arrows. The best-fitting for fully convective stars in Wright et al. (2011) and Wright et al. (2018) are shown in dotted and solid lines respectively. Picture credit: Wright et al. (2018).

The study of X-ray activity in stars reveals a complex interplay between stellar mass, rotation, and magnetic activity. The Rossby number "R_o", which is the ratio of rotation period (P_{rot}) to convective turnover time (σ_{conv}) serves as a bridge between stellar mass and magnetic activity. The Rossby number is considered the best proxy for dynamo efficiency, as it correlates with the theoretical dynamo number ($N_D = R_o^{-2}$) according to early models (Noyes et al., 1984). However, the inability to directly measure convective flows makes σ_{conv}, affect the detailed shape of the rotation-activity relation. Despite the drawbacks of R_o, it remains a valuable parameter that incorporates several intrinsic stellar properties, such as rotation period and magnetic field, independent of spectral type.

Pioneering work by Pizzolato et al. (2003) highlighted the dependence of X-ray saturation levels on mass and rotation (hence, on R_o), noting that for solar-type and lower-mass stars, the saturation level is influenced by L_X. They also observed that cooler stars transition from saturated to correlated regimes at longer rotation periods and that the decay law for slow rotators follows a power law with $\beta \approx -2$. Further studies, such as those by Wright et al. (2011, 2018), have expanded the sample size and spectral range, revealing a steeper power law (β= -2.7, β= -2.3 respectively). These studies also showed consistent rotation-activity behavior across different stellar types, including fully convective M dwarfs (see Fig. 5.6). Based on this, we expect a higher mass loss rates of stars in the saturated regime and a decrease as stars transition to the unsaturated regime, reflecting the underlying changes in magnetic activity and rotation.

Similar to the relationship between rotation-activity, the relationship between rotation and magnetic field also shows a break between slow and fast rotators, the saturated and the non-saturated of stars (Fig. 5.7). In the work of Reiners et al. (2022) the average magnetic field strength is defined in function of R_o. The magnetic fields of fast rotators ($R_o > 0.13$) are defined by $\langle B \rangle = 2050\,(\mathrm{G}) \times R_o^{-1.11}$, while the magnetic field of slow rotators ($R_o < 0.13$) is defined by $\langle B \rangle = 200\,(\mathrm{G}) \times Ro^{-1.25}$. In Kochukhov (2021) the average magnetic field strengths were determined by modeling the radiative transfer of intensity spectra. Both studies showed a similar relation between $\langle B \rangle$ and R_o as that of rotation-activity. However, in contrast to what we saw with the rotation activity, the rotation-magnetic field shows an indication of an increase in magnetic field strength as we go to a lower R_o. This means that there is no saturation. These studies concluded that it is likely that parameters other than stellar mass and rotational period influence dynamo efficiency in M dwarf stars.

The absence of a rotation dependence in the X-ray emission of fast-rotating stars has led to several hypotheses. One suggests a saturation of the dynamo mechanism responsible for magnetic field

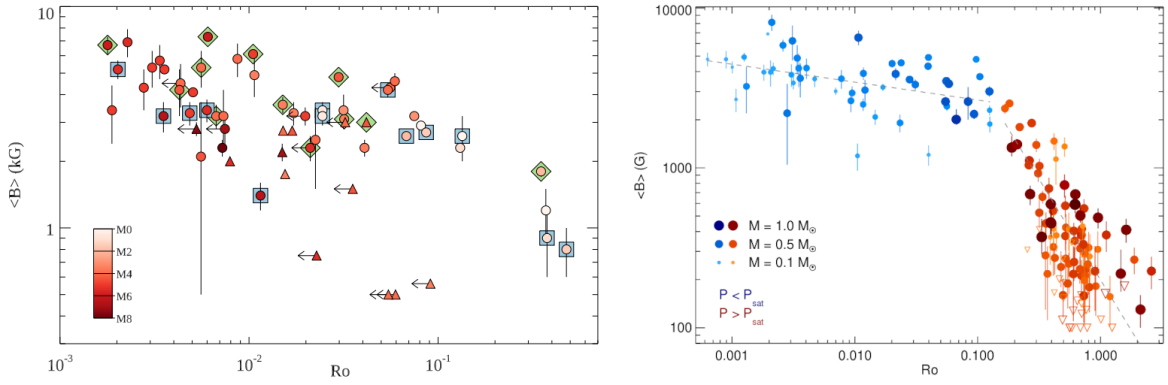

Figure 5.7: Magnetic field strength in function of Rossby number. *Left*, illustrate the relation between the total magnetic field strengths measured from Stokes I and the properties of global field topologies studied for a smaller number of M dwarfs with polarimetry. Picture credit: Kochukhov (2021). *Right*, magnetic field–rotation relation for solar-like and low-mass stars. Symbols for stars rotating slower than $R_o = 0.13$ are colored red, while those of faster rotators are colored blue. Larger and darker symbols indicate higher stellar mass than smaller and lighter symbols. The gray dashed lines show linear fits separately for the slowly rotating stars and the fast rotators. Downward open triangles show upper limits for $\langle B \rangle$. It seems that the magnetic field is still increasing for stars in the saturated regime. Picture credit: Reiners et al. (2022).

generation (Vilhu, 1984), while another proposes a limit to the active regions' surface area coverage or a decrease in coronal volume due to centrifugal forces (Jardine & Unruh, 1999). Interestingly, when magnetic field strength is considered in terms of magnetic flux, the saturation plateau vanishes, suggesting a single power-law relationship that encompasses all magnetic field and L_X values (Pevtsov et al., 2003). Vidotto et al. (2014) interpret this as a result of the diverse mass and interior structures of stars, which lead to different magnetic field saturation levels.

Furthermore, it has been observed that the rotation period demarcating the shift from saturated to unsaturated regimes in the X-ray activity-rotation relationship is longer than that seen in chromospheric measurements. This discrepancy supports the theory of "coronal stripping" induced by centrifugal forces (Núñez et al., 2017).

The empirical relationship between X-ray emission and stellar rotation shows a downturn in X-ray levels at the high-speed end of the spin distribution. The phenomenon of "supersaturation", where the fastest rotators exhibit lower X-ray emissions, is thought to be caused by mechanisms similar to those responsible for saturation (Fig. 5.8). However, the lack of supersaturation in chromospheric CaK emissions points to coronal stripping as a significant factor in the X-ray rotation-activity relationship. The regimes of unsaturated, saturated, and supersaturated X-ray activity vary with stellar mass and rotation period, as depicted in a referenced figure 5.8. These concepts are further detailed in studies such as Prosser et al. (1996); James et al. (2000); Jardine (2004); Jeffries et al. (2011), and Argiroffi et al. (2016), which discuss the potential causes of saturation and supersaturation in stellar emissions.

The solar-stellar connection suggests that active stars, such as the Sun, exhibit magnetic cycles that can be observed in various wavelengths from radio to X-rays (Hathaway, 2010). This cycle, driven by the solar dynamo's continuous conversion of poloidal to toroidal fields and vice versa, is a fundamental aspect of solar activity. The most used radiative diagnostics for the Sun's variable chromosphere are the prominent CaII emission lines. They can be observed with ground-based telescopes and have been continuously monitored since the early 1900s (Bertello et al., 2016).

The Mount Wilson Survey, initiated by Olin Wilson in 1966, has made a significant contribution to our understanding of stellar activity cycles. This project was designed to study stellar chromospheric activity and its variability. It carried out extensive observations of CaII lines and collected a wealth of data on stellar activity cycles. A few years later, in the study by Baliunas et al. (1995), they observed a pattern of variation in both the rotational period and the measure of chromospheric activity, the so-called S-index, in stars of spectral type G0-K5. Their investigations showed that young stars with fast rotation periods have a high level of chromospheric activity. This groundbreaking work has significantly

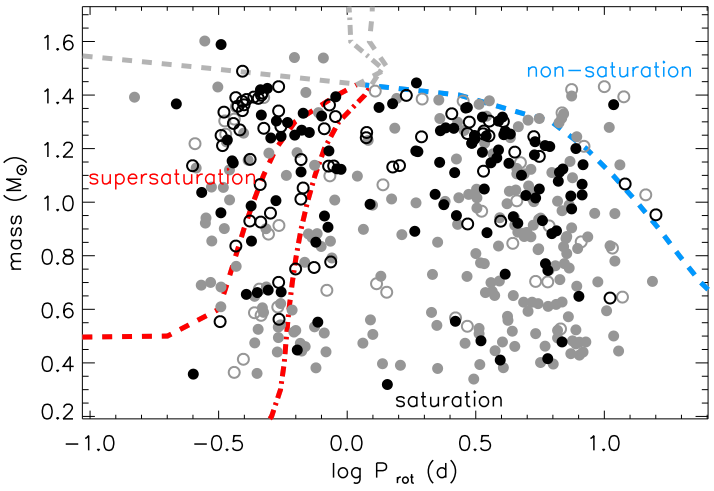

Figure 5.8: Mass vs. period of selected per-members detected (black) and undetected (gray) in X-rays. Filled and open symbols denote single and double stars, respectively. Red lines separate the locations corresponding to supersaturation and saturation, assuming centrifugal stripping (dash-dotted line) or polar updraft (dashed line). The blue dashed line marks the expected separation between non-saturation and saturation. Picture credit: Argiroffi et al. (2016).

improved our understanding of stellar activity cycles, especially those observed in the Ca H&K lines.

Moreover, researchers have investigated whether other late-type stars also exhibit similar cyclic variability, with Ca II emission changes detected in stars such as α Cen A and B, 61 Cyg A and B, ι Hor, and ϵ Eri (Wilson, 1978). However, the identification of X-ray cycles remains a challenge due to the significant amount of time required over long periods of time, limiting observations to only a few stars such as α Cen A and B, 61 Cyg A and B, ι Hor and ϵ Eri (Coffaro et al., 2020). These cycles, which are crucial for understanding stellar activity, affect the wind properties and element fractionation and subsequently influence the environment of the star (Lalitha & Schmitt, 2013; Wargelin et al., 2017).

5.5 Stellar Winds Measurements

"The universe is not required to be
in perfect harmony with human ambition."
Carl Sagan

As discussed in Sec. 4.5, the presence of a corona at MK temperatures in a star implies an outflow of plasma driven in part by the thermal pressure gradient. However, we have since learned that thermal pressure alone cannot fully explain the properties of the solar wind we observe near the Sun and Earth. Instead, we find a strong correlation between the wind and the properties and behavior of the stellar magnetic field, suggesting that the magnetic field is the main driving force of the wind. Furthermore, the existence of the corona itself is tied to the stellar magnetic field, as only this can provide the necessary energy density to heat such a large volume of plasma to the MK range.

We have seen in Sec. 4.5 that the solar winds are extremely thin, with density $\sim 1\,\mathrm{cm}^{-3}$ and $\dot{M}_\odot 2 \times 10^{-14}\,M_\odot \mathrm{yr}^{-1}$ at 1 AU. We should in principle not be able to observe the winds. The only reason we observe the solar wind is because we are embedded in it. For Sun-like stars and other cool low main sequence stars with hot corona, the wind is also as weak as the solar wind or even weaker (Fig. 5.9). The wind of these stars are among the hardest to detect as they are relatively weak compared to the stronger and more easily detectable winds of hot stars and cool giant and supergiant stars.

When low-mass stars become red giants in the post-main-sequence phase, the importance of thermal forcing decreases, leading to cooler stellar winds. The Hertzsprung-Russell diagram (HR), shown in Figure 5.9, provides a comprehensive overview of the observed stellar mass loss of main-sequence stars as well as hybrid and evolved stars. We can see clearly that the strongest winds are generated by hot

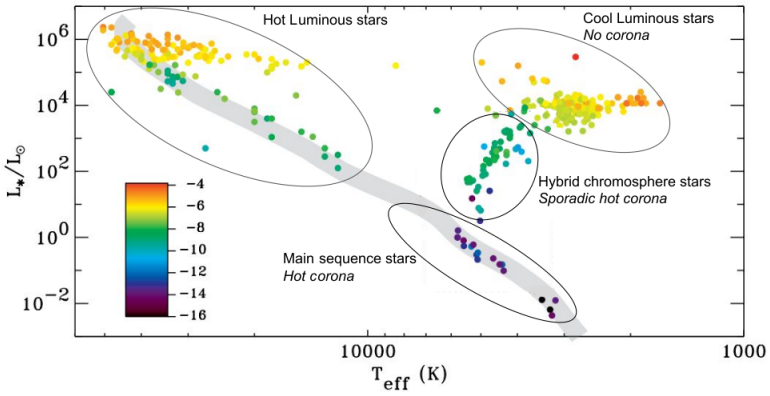

Figure 5.9: Hertzsprung–Russell diagram showing observed mass loss rates. The color scale at lower-left specifies $\log \dot{M}$, where $\dot{M}$ is measured in $M_\odot \mathrm{yr}^{-1}$. The diagram also shows the position of the zero-age main sequence. Hot, luminous stars, are located in the upper left. Conversely, cool, luminous stars with winds are in the upper right area. Evolved low-mass stars that show weak or sporadic signatures of a hot corona are denoted 'warm/hybrid'. It is clear from this diagram that the cool low-mass main sequence stars exhibit the weaker winds. Picture adapted from: Cranmer & Saar (2011).

and cool, luminous stars, while the winds from cool, low main sequence stars are the weakest.

As such, we cannot observe them directly. This is primarily because their winds are extremely thin and lack strong, detectable observational signatures, such as a P Cygni line profile (Israelian & de Groot, 1999; Robinson, 2007). This profile, typically observed in hot, massive stars with strong stellar winds, has an emission line at the rest wavelength and a blue-shifted absorption line. The emission comes from the outward-moving wind, while the blue-shifted absorption results from the absorption of radiation by the wind as it moves away from the star. The shape of the profile, which is characterized by an emission peak followed by a blue-shifted absorption trough, provides information about the velocity and density of the stellar wind.

Therefore, solar-like winds have only been detected using indirect techniques. These techniques do not measure the wind itself but its interaction or influence on its environment. I want to remind the reader that the only observable measurement of the wind is the mass-loss rate ($\dot{M}_\star$), hence whenever we talk about wind measurements, we mean $\dot{M}_\star$. In the following sections, I will list some indirect methods used to detect winds and highlight the significant results they have given us and their advantages and disadvantages. This will provide a comprehensive understanding of how we study and understand stellar winds.

Detection by Free-Free Radio Emission

The densest part of stellar wind, its innermost region, can emit at radio wavelengths. This provides a method for direct detection of the wind in radio (Güdel, 2002). If the densities are high enough, these innermost regions for radio wavelengths can become optically thick and form a radio photosphere (Ó Fionnagáin et al., 2019; Kavanagh et al., 2019). If this is detected, it can help us to measure ($\dot{M}_\star$) of the wind. In such a scenario, the underlying non-thermal radio emission of the star is obscured. However, if the wind has a low density, it would be transparent to radio waves, and the non-thermal radio emission from the stellar surface can pass through the wind without attenuation. These radio-transparent winds can nonetheless provide important upper limits to wind $\dot{M}_\star$ (Lim & White, 1996).

There have been several attempts to directly observe free-free thermal radiation at radio wavelengths, all of which have resulted in nondetections, putting important upper limits on the mass loss rates (Brown et al., 1990; Drake, Simon, & Brown, 1993; van den Oord & Doyle, 1997; Gaidos et al., 2000). The most sensitive limits on the winds of solar mass stars were derived for three young solar analogs by Gaidos et al. (2000), who found upper limits on the mass loss rates of $\sim 5\times 10^{-11}\, M_\odot \mathrm{yr}^{-1}$. Non-thermal radio emission, such as radio flares, has been detected in M dwarfs and solar-like stars (e.g., Lim & White 1996; Fichtinger et al. 2017). For example, Lim & White (1996) used this criterion to derive an upper limit of $10^{-12}\, M_\odot \mathrm{yr}^{-1}$ for the M dwarf YZ CMi. The main

current disadvantage of this method is that no wind of low-mass star has ever been detected; thus, all it has provided so far are upper limits on $\dot{M}_\star$.

Inference Using Exoplanets

The technique of transmission spectroscopy or spectroscopic transit observations is used to detect wind-planet interactions in hot Jupiters and warm Neptunes such as HD 209458 b, HD 189733 b and GJ 436 b, which orbit main sequence stars of spectral types F8, K2 and M3, respectively (e.g., Holmström et al. 2008; Bourrier & Lecavelier des Etangs 2013; Bourrier et al. 2016; Villarreal D'Angelo et al. 2014; Kislyakova et al. 2014). Due to their hydrogen-dominated atmospheres, these planets exhibit strong atmospheric escape, which is detectable in the Lyα line during planetary transits. By modeling the stellar Lyα line line profile transmitted through the planetary atmosphere, the conditions of the surrounding stellar wind can be derived.

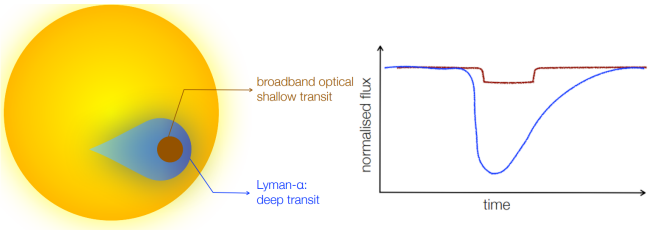

Figure 5.10: *Left*, illustration of a planet's outflow affected by the presence of stellar winds. *Right*, transmission spectra of an exoplanet affected by the presence of stellar wind will look like. Picture credit: Aline Vidotto.

The stellar winds influence the planetary outflow, in a similar way as the ISM shapes the astrosphere (5.10, *left*). This causes an interaction to occur on one side of the planet that will translate into an asymmetry in the lightcurve (Fig. 5.10 *right*). More details can be found in studies such as Villarreal D'Angelo, Jardine, & See (2018); McCann et al. (2019); Harbach et al. (2021); Cohen et al. (2022).

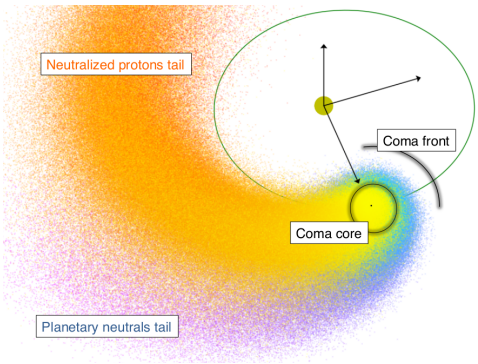

Figure 5.11: Illustration of the high-velocity neutrals created by stellar wind-neutral hydrogen escaping the planet atmosphere. Picture credit: Bourrier et al. (2016).

Additionally, the ionized wind exchanges charge with the escaping neutral hydrogen from the planetary atmosphere, leading to a high-velocity, blue-shifted component of the stellar Lyα line (e.g., Holmström et al. 2008). This allows for determining local densities and speeds of the stellar wind and consequently, the wind mass-loss rates (Kislyakova et al., 2014; Bourrier et al., 2016; Vidotto & Bourrier, 2017). There is only one case of $\dot{M}_\star$ inferred using exoplanet transit that was reported in Vidotto & Bourrier (2017). This technique has limitations, primarily that the Lyα line falls in UV, requiring expensive space instrumentation for observation. Currently, only the Hubble Space Telescope (HST) can observe in UV.

Inference Using Prominences

Slingshot prominences are extended structures that occur on fast-rotating stars and are detected as absorption in the Hα stellar line profile as the star rotates. They occur at/or beyond the co-rotation radius, which is several radii above the stellar surface (Collier Cameron & Robinson, 1989). These prominences are formed at the top of long magnetic loops that are filled with mass from the stellar wind as suggested by Jardine & van Ballegooijen (2005). By observing slingshot prominences, one can estimate the rate at which mass is loaded into the loop tops and thus derive $\dot{M}_\star$. They are visible

in Hα Doppler maps in absorption when they pass in front of the stellar disc. When they are out of transit, they can be detected in emission. In this case, however, the geometrical dilution of the stellar flux is such that this emission is very hard to detect unless these prominences are very close to the stellar surface (Odert et al., 2020).

The existence and dynamics of these slingshot prominences depend on their formation location relative to the Alfvén and sonic surfaces of a stellar wind (For more information on the AS, see Sec. 4.7). The prominences can only exist when the co-rotation radius lies below AS (Jardine & Collier Cameron, 2019). This is because the magnetic field lines are open above the AS.

Older solar-like stars cannot support these types of prominences as their co-rotation radius is above the AS (Villarreal D'Angelo, Jardine, & See, 2018). The relative location between a prominence and the sonic point also matters. If the prominence is formed above the sonic point, the star keeps loading the prominence with stellar wind material until it erupts, representing the 'limit-cycle regime' as proposed in Jardine & Collier Cameron (2019). If the prominence is formed below the sonic point, the mass-loading from the surface gets readjusted, leading to occasional eruptions in the 'hydrostatic regime'. The formation of slingshot prominences thus occurs more easily in faster rotators in the sub-Alfvénic regime, where the winds need to be relatively hotter for the sonic point to occur at lower heights.

Inference by Charge-Exchange

The interaction between an ionized stellar wind and a neutral ISM can lead to charge exchange, where the ISM neutral atom transfers charge to a solar wind ion during a collision. This process excites a highly-charged ion, particularly oxygen, to a high excitation state, followed by a single or a cascade of radiative decays, leading to emission in the X-ray range. This gives rise to an X-ray 'halo' (Wargelin & Drake, 2001). This method was applied to Proxima Centauri, an M dwarf star, but no signature of charge-exchange induced X-ray emission was detected, placing an upper limit for the $\dot{M}_\bigstar$ of Proxima Cen of about 14 times that of the present-day Sun (Wargelin & Drake, 2002). Another consequence of these charge exchange interactions is the build-up of a wall of hot, neutral hydrogen at the edge of a stellar system's astrosphere, requiring that the stellar system is embedded in a region of the ISM that contains a large enough quantity of neutral hydrogen (Wood et al., 2001).

It is not until recently that we were able to detect wind from this method. In the study b Kislyakova et al. (2024) they were able to estimate the corresponding $\dot{M}_\bigstar$ for three main sequence stars; 70 Oph ($66.5 \pm 11.1\,\dot{M}_\odot/R_\odot^2$), ϵ Eri ($15.6 \pm 4.4\,\dot{M}_\odot/R_\odot^2$), and 61 Cyg ($9.6 \pm 4.1\,\dot{M}_\odot/R_\odot^2$)[8]. This method has the advantage of not being dependent on the geometry of the line of sight and seems to be detectable with *XMM-Newton*. Further research is needed to determine how far we can observe the star, potentially more than 10 pc.

Detection Through Astrospheric Absorption

Stellar winds extend into ISM and form a structure known as the "astrosphere", similar to the "heliosphere" around the Sun (for more details on the interaction of the wind with ISM check Sec. 4.5). The astrosphere has several distinct regions: the termination shock, where the stellar wind speed goes from supersonic to subsonic; the astropause, which separates the stellar wind and the ISM stream; and the hydrogen wall, a region of increased hydrogen density between the astropause and the bow shock.

The Lyα photons emitted by the star have a long journey ahead of them before they reach us (see Fig. 5.12). They first pass through the stellar wind and the hydrogen wall around the astrosphere, then the ISM itself, and finally the hydrogen wall around the heliosphere and interplanetary space (solar wind). During this journey, the neutral hydrogen in these regions absorbs the Lyα spectral line at different speeds, changing the original line profile.

The Lyα line at 1216 Å is a resonance line that corresponds to a specific frequency of light that an atom can absorb or emit. Cool stars produce very little continuum emission at 1216 Å, but strong emission lines (Wood, 2004). Lyα lines are usually the strongest. However, these lines are always heavily

[8] $\dot{M}$ represents the rate of mass loss from a star and it's usually measured in solar masses per year ($M_\odot$/yr). $R_\odot^2$ is the square of the radius of the star. It is used to convert the total mass loss into a rate per unit area. $\dot{M}_\odot/R_\odot^2$ gives us a measure of the mass loss per unit area from the star. This is useful because it allows us to compare the mass loss rates of different stars, regardless of their size. This unit was introduced by Wood et al. (2002).

contaminated by interstellar absorption. Due to the strong absorption by interstellar neutral hydrogen, only a small fraction of the emitted Lyα flux is observed. In addition to astrospheric absorption, from our own heliosphere is sometimes observed in the slipstream of the ISM flux seen from the Sun, depending on the amount of obscuring absorption from the ISM itself. Measuring this additional absorption requires reconstructing the intrinsic stellar Lyα emission line and then modeling the ISM absorption. Once the additional absorption has been measured, it can be compared with the results of the hydrodynamic models of the wind-ISM interactions to estimate the wind mass fluxes. For more details on the Lyα astrospheric method, I refer the reader to the following studies: Linsky & Wood (1996); Wood et al. (2002); Wood (2004).

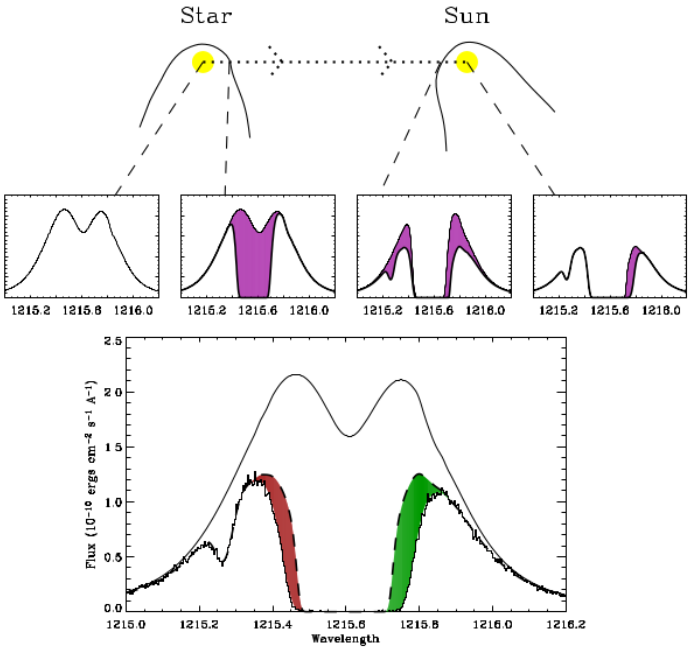

Figure 5.12: Schematic showing how a stellar Lyα profile changes from its initial appearance at the start and then through various regions that absorb parts of the profile before it reaches an observer at Earth. Picture credit: (Wood, Redfield, & Linsky, 2001). The lower panel shows the actual observed Lyα profile of α Cen B. The upper solid line is the assumed stellar emission profile and the dashed line is the ISM absorption alone. The excess absorption is due to heliospheric H I (green shading) and astrospheric H I (red shading). Picture credit: Wood et al. (2018).

By modeling these different absorption components, one can infer the neutral hydrogen column density in the wall surrounding an astrosphere. The extraction of quantitative mass loss measurements from the data requires the support of astrospheric models analogous to the heliospheric models (Holzer, 1989; Baranov, 1990; Suess, 1990; Zank, 1999). However, this is associated with several problems. One problem is finding enough heliospheric Lyα absorption to properly constrain the models, although the situation has gradually improved (see studies such as; Hébrard et al. 1999; Wood, Linsky, & Zank 2000; Kruk et al. 2002; Wood et al. 2005, 2007). This brings us to the second problem, which is trying to derive the ambient ISM parameters from the heliospheric Lyα data (Izmodenov, Wood, & Lallement, 2002). The results currently seem to be very model-dependent. 3D models are required to include the heliospheric field, and they also need to account for orientations of the ISM magnetic field other than parallel to the flow vector (Ratkiewicz et al., 1998). Such magnetic field is poorly known for the ISM, given that current observational constraints are inaccessible.

The Lyα method is by far the most successful one in providing stellar winds in cool stars. Therefore, I will revise these results in more detail in chapter 7, as they are an essential part of the analysis performed in this Thesis.

5.6 Results from Lyα Astrospheric Method

"Space is big. Really big. You just won't believe how vastly, hugely, mind-bogglingly big it is."
Douglas Adam

Mass loss rates estimated from astrospheric Lyα absorption have been used to assess how coronal winds relate to coronal activity, as quantified by X-ray surface flux ($F_{\rm X}$). Because $F_{\rm X}$ is a measure of stellar activity, it can be used as a rough proxy for age-stars with relatively large X-ray fluxes tend to be younger than stars with lower X-ray fluxes. Hence, from these results it is possible to infer what the solar wind was like when the Sun was younger and more active.

In their study, Wood et al. (2001) applied the Lyα absorption technique to infer $\dot{M}_\star$ for the binary system α Cen ($\dot{M}_\star/R_\star^2 = 2\ \dot{M}_\odot/R_\odot^2$) and an upper limit for Proxima Cen ($\dot{M}_\star/R_\star^2 = 0.2\ \dot{M}_\odot/R_\odot^2$). Measurements using this technique are now available for several low-mass stars. Figure 5.13 shows an overview of different mass loss rate detected for low mass stars G, K, and M dwarfs, alongside subgiants/giants. These results indicate that the majority of stars within the narrow sample have mass-loss rates comparable to those of the Sun. However, a selected group of active stars show significantly higher rates. In particular, stars classified as "slingshot prominences" - fast rotators - show the highest mass-loss rates, especially near the co-rotation radius.

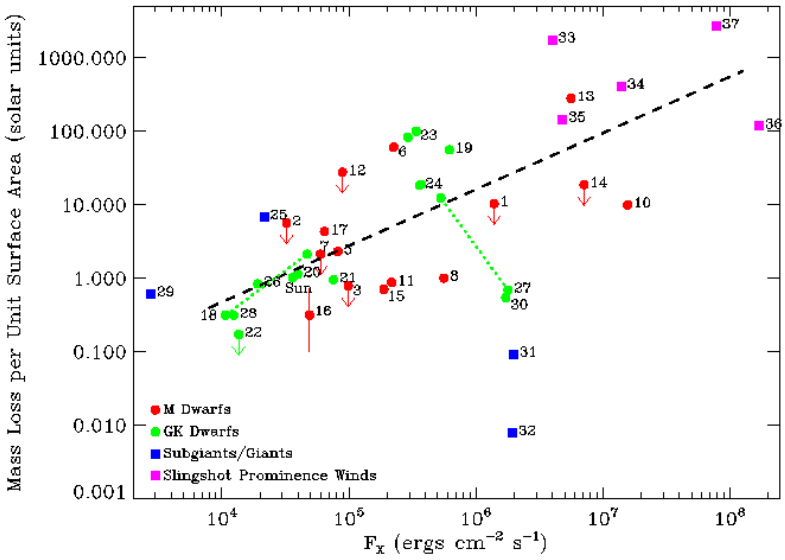

Figure 5.13: Mass-loss rate per unit surface area vs. X-ray surface flux for coronal winds. Dotted lines connect members of binary systems. Most constraints are from the astrospheric Lyα absorption diagnostic, but there are also results from slingshot prominence wind measurements from Jardine & Collier Cameron (2019). The M dwarf with the error bar is $\dot{M}$ constraint from Lyα absorption seen during an exoplanet transit for GJ 436 (Vidotto & Bourrier, 2017). A power law of $\dot{M} \propto F_X^{0.77\pm0.04}$ is fitted to the data points, excluding the subgiant/giant stars. Picture credit: Wood et al. (2021).

The results shows that $\dot{M}_\star/R_\star^2$ varies as a function of $F_{\rm X}$ as ($\dot{M}_\star/R_\star^2 \propto F_{\rm X}^{0.77\pm0.04}$). The general trend for most main-sequence stars is that, at a given stellar radius, the mass loss rate scales with age as $\dot{M}_\star/R_\star^2 \propto t^{-2.33}$ (Wood et al., 2005). Combining this with Skumanich's well-known result that stars spin down with age according to $\Omega \approx t^{-1/2}$ (implies that $\dot{M}_\star/R_\star^2 \propto \Omega^{4.66}$). However, this relation appears to break down for the most active stars in the sample, which exhibit much lower $\dot{M}_\star$ than predicted. For stars with $F_{\rm X} > 10^6$ erg s^{-1} cm^{-2}, Wood (2004) proposed the existence of a "wind dividing line," beyond which the power-law fit would cease to be valid. For solar-like stars, this X-ray flux of $F_{\rm X} > 10^6$ erg s^{-1} cm^{-2} roughly corresponds to an age of 600 Myr. The drop in the wind mass-loss rate by more than 2 orders of magnitude around this age remains an intriguing question.

It has been suggested that the magnetic topology of stars with $F_X > 10^6$ erg s^{-1} cm^{-2} undergoes an abrupt change that could affect their winds (Wood et al., 2005; Garraffo et al., 2018). However, magnetic field reconstructions of young stars do not show such abrupt changes but rather a smooth transition from a magnetic field dominated by a toroidal component at young ages (fast rotation) to a topology dominated by a poloidal field at older ages (Petit et al., 2008; Folsom et al., 2018; See et al., 2015; Vidotto et al., 2016).

The studies suggest that $\dot{M}_\star$ are influenced not only by the F_X, but also by their magnetic field topology. Therefore, it is worth investigating how these $\dot{M}_\star$ change as a function of magnetic field topology and also as a function of R_o. This is explored in more detail in chapter 5.

The Lyα astrospheric method has been the most successful method for evaluating mass-loss rates in stellar winds of cool stars. There are nearly 30 measurements, including upper limits for spectral types M to F on the main sequence and some evolved cool stars. Its use is limited by the state of the ISM and the distance to the observer. The ISM must be partially neutral for the method to work, and stars –in fully ionized ISM regions at distances greater than 10-15 pc make the method ineffective. At distances greater than 10 pc may have such a high ISM column density that astrospherical absorption is obscured in Lyα observations (Linsky & Wood, 2014; Wood et al., 2021).

In addition, the proper motion of the star and the geometry of the line of sight are of crucial importance. The motion of the star can change the interaction dynamics between the stellar wind and the ISM, which affects the observed absorption features. The geometry of the line of sight also plays an important role as it determines the path through which we observe the astrospheric and ISM absorption, which affects the detectability and properties of the Lyα signature. These factors must be taken into account to ensure accurate measurements and interpretations of the astrospheric data. Further details on Lyα absorption by the wind-ISM interaction considering these aspects are discussed in the corresponding section. A good review of this topic can be found in Wood (2004).

Due to the limitations of current observational methods, which include a scarcity of telescopes specialized for stellar wind measurements and challenges in predicting the characteristics of a star's vicinity, numerical models are essential for supplementing observational data. This is particularly relevant for M dwarfs, where wind properties are expected to be more intense, as we will see in Chap. 8.

5.7 Stellar Winds Modelling

"The universe seems neither benign nor hostile, merely indifferent."
Carl Sagan

The first analytical expression relating mass and angular momentum loss was provided by Weber & Davis (1967). They extended the purely hydrodynamic solar wind model of Parker (1958) to an MHD model by including the Lorentz force caused by the solar magnetic field (see Sec. 4.5 for more details on the Parker wind model). This model assumes a simple radial magnetic field at the surface of the star. It uses an idealized monopole field to model $\dot{J}_\star$ in the solar wind (Eq. 5.4). While this model provides a good starting point for calculating stellar $\dot{J}_\star$, this relation breaks down for more complex magnetic topologies. The model already gives an overestimation of angular momentum loss rate from a dipole configuration (Kawaler, 1988).

$$\dot{J}_\star = \frac{2}{3}(\Omega \dot{M}_\star) R_A^2 \tag{5.4}$$

where $\dot{J}_\star$ is the angular momentum loss rate, Ω the angular velocity, $\dot{M}_\star$ the mass loss rate, and where a constant radial field was assumed at the surface of the star.

Furthermore, while accurately measuring the magnetic field geometries of stars is a challenge, they are known to be far from a split monopole, with the simplest configuration being a dipole field (Donati & Landstreet 2009; Morin et al. 2010, and references therein). Young and fast-rotating stars in particular often exhibit more complex field configurations (e.g., Donati & Landstreet 2009).

With a better understanding of the solar winds, the stellar wind models were also improved and made more realistic. An important milestone in the modeling of stellar winds was achieved by (Cranmer

& van Ballegooijen, 2005). In their study, they presented a model that incorporated the effects of AWs in the simulations of stellar winds. The model uses AWs to provide additional heating and momentum to the winds, taking into account the detailed physics of wave dissipation, turbulence, and energy transfer mechanisms. As a result, it provides a more accurate representation of the high wind speeds and temperatures observed in stellar winds. However, this model requires detailed information about the wave spectra and their interaction with the plasma, which makes it more computationally intensive due to the additional physics of the wave dynamics. The model is 1D, meaning it also lacks the 3D nature necessary to fully capture the complexity of stellar winds.

The model by (Cranmer & van Ballegooijen, 2005) incorporates wave-driven dynamics but may not explicitly account for all the detailed physics of MHD equations, as can be seen in numerical codes such as BATS-R-US (Block-Adaptive Tree Solar-wind Roe Upwind Scheme). The development of such sophisticated numerical codes has greatly improved our ability to model stellar winds. BATS-R-US is a versatile MHD code capable of simulating solar wind interactions in various astrophysical and geophysical systems (Powell et al., 1999; Tóth et al., 2012).

Magneto-hydrodynamic models of stellar winds, including some applications of the BATS-R-US code, often assume a pre-existing hot corona and an implicitly accelerating wind by assuming a thermally driven (Parker) wind (e.g. Matt et al. 2012; Vidotto et al. 2014; Réville et al. 2015). However, other applications of the BATS-R-US code, such as the 3D MHD Alvén Wave Solar Model (AWSoM, introduced in Sec. 4.7), use a version of the BATS-R-US MHD code developed for the solar corona (Cohen et al., 2007). Hence, the model includes the dynamics of the AWs and takes into account the magnetic field of the star, unlike the thermally driven model mentioned above.

The Alfvén Wave Solar Model includes the effects of AWs, which are key for additional heating and momentum in the solar and stellar wind. This model uses BATS-R-US to solve MHD equations for mass, momentum, magnetic induction and conservation of energy. It is driven by boundary conditions for the radial surface magnetic field, where the initial condition for the 3D magnetic field being potential (Altschuler & Newkirk, 1969). The model allows input parameters to be changed at the inner boundary condition, allowing the simulations to be customized for each star. These parameters include the mass of the star, its radius and its rotation period. The model also employs Adaptive Mesh Refinement (AMR) to resolve fine-scale structures, enhancing simulation accuracy without significantly increasing computational cost. Its versatility allows it to be applied to a wide range of stars with different magnetic field configurations, making it highly effective for stellar wind studies Sokolov et al. (2013); Oran et al. (2017). Example of studies using the AWSoM model; Garraffo et al. (2013); Cohen et al. (2014); Garraffo, Drake, & Cohen (2015); Garraffo et al. (2018); Chebly, Alvarado-Gómez, & Poppenhaeger (2022); Chebly et al. (2023).

The Alfvén Wave Solar Model stands out due to its *realistic* features, including a semi-empirical relationship between the magnetic topology, wind speed, and base density. This base density is adjusted to mirror the observed density difference between slow and fast winds, which is key in determining the mass loss rate of each solution. Moreover, the 3D nature of the model provides a more accurate representation of wind models and AS, offering deeper insights. The ability to control the parameters of the numerical experiment and relate each solution to a specific set of parameters is a significant advantage of this approach.

Applying solar wind physics to other stars is a major step forward in studying stellar winds. However, there are uncertainties in our understanding of solar wind physics and how these models apply to other stars. For example, the Cranmer & Saar (2011) model, an enhancement of the Cranmer & van Ballegooijen (2005) model, heavily relies on the magnetic flux filling factor estimates[9], has an uncertain derivation from observations of low-mass main-sequence stars (Reiners, 2012; Reiners, Schüssler, & Passegger, 2014) and prediction from stellar parameters such as mass and rotation rate. Furthermore, the AWSoM model, which requires coronal density and temperature as input parameters, presents challenges in determining these distributions for cool stars, especially M dwarfs, which necessitate the use of solar corona values.

The AWSoM model, being the most sophisticated physics-based solar model to date, was employed in my research for several purposes. On one hand, it was used to create a grid of idealistic models for comparative study and wind parameter exploration in function of the star's magnetic geometry (see chapter 6). On the other hand, it was used to quantify for the first time the wind of late-F, G, K, and M dwarf main sequence stars (see chapter 7). The results are general enough to be applied

[9]This factor, often seen in the expression for the surface averaged field strength (fB).

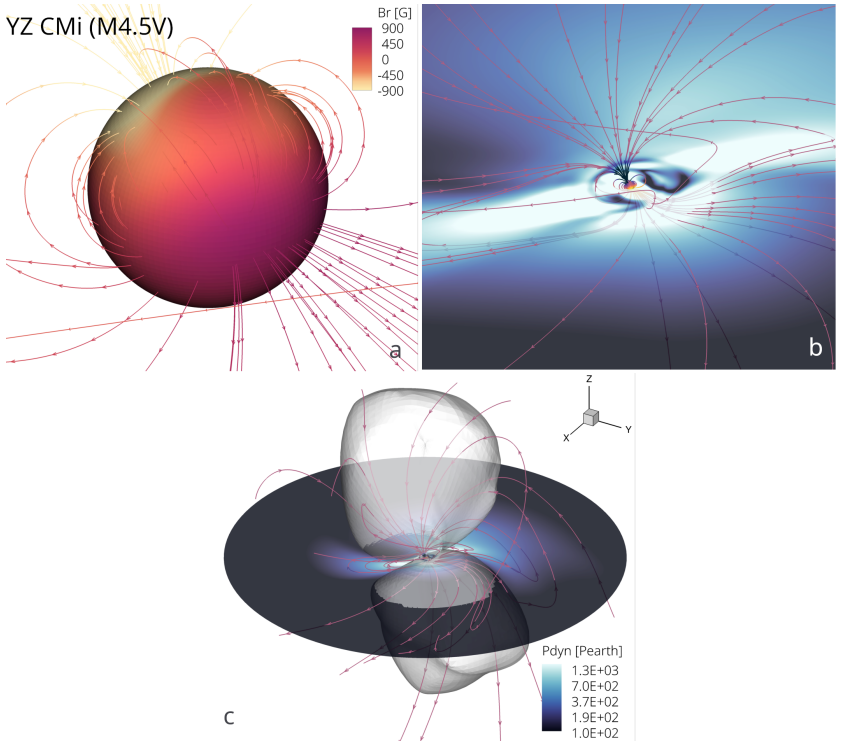

Figure 5.14: Simulated stellar wind environment using AWSoM model for the M dwarf star: YZ CMi (M4.5V). Panels a, b, and c show a zoom-out perspective of the simulation starting near the star. We see in *panel a* an example of the distribution of the surface field (in Gauss) of YZ CMi provided by the ZDI map and used for the AWSoM solution in the Solar/Stellar Corona spherical region. The orange-pink color bar represents the radial magnetic field strength on the stellar surface. Selected 3D magnetic field lines with arrows are shown and color-coded by the radial magnetic field strength. *Panel b*, zoom out view of the star surface and also color-coded is the dynamic wind pressure (Pdyn = ρU^2), normalized to the nominal Sun-Earth value ($\sim$1.5 nPa), visualized in the equatorial plane. We can clearly see the closed loops near the equator and the open field line at the pole. The gray translucent iso-surface corresponds to the AS of the stellar wind. All panels have the same 3D orientation, which can be seen in *panel c*. One last thing: If you look at both *panel b* and c, you will notice that the dynamic pressure is stronger near the star and the density decreases the further we move away from the star. Picture credit: J. Chebly done with *Tecplot 360*.

to other cool main sequence stars with hot coronas. More details on the boundary conditions, input parameters, and how we calculate $\dot{J}_\star$, $\dot{M}_\star$, and the wind speed in the simulation done in this thesis, can be found in chapter 8. In Fig. 5.14, I show an example of the AWSoM model for stellar wind simulation of an M dwarf while also giving an explanation of what we see in each panel. Note, all the 3D simulation visualizations you will see in this manuscript were done using TecPlot 360.

5.8 Element Abundances and the FIP Effect

"The Universe is under no obligation to make sense to you."
Neil deGrasse Tyson

The study of elemental abundances in stellar coronae has revealed intriguing patterns linked to FIP effect. Typically, stars with low activity levels, including the Sun, show the FIP effect where elements with low FIP are more abundant in the corona than those with high FIP (Feldman & Laming, 2000). This was detailed in an earlier section 4.6. However, very active stars often display no FIP effect or an inverse FIP effect, where low-FIP elements are less abundant in the corona (e.g., Audard et al.

2003). The launch of the ASCA and EUVE satellites in the early 1990s allowed for a clearer picture of these abundance anomalies (see, for example, early reviews by Drake, Laming, & Widing 1996; White 1996; Drake 2002). While some low activity stars like α Cen AB exhibited a solar-like FIP effect, active stars showed the opposite trend (Drake, Laming, & Widing, 1997). This inverse FIP effect "iFIP" was confirmed with high-resolution X-ray spectra from the Chandra and XMM-Newton satellites, particularly in the active binary HR 1099 (Brinkman et al., 2001; Drake, 2001).

The most promising mechanism proposed to date is based on the ponderomotive forces on ions resulting from AWs (Laming, 2015). This mechanism is the only one that was able to explain both FIP and iFIP effect. As we saw in Sec. 4.6, AWs are likely to be initiated from below in the photosphere, excited by convection and turbulence. As Alfvén waves ascend through the solar atmosphere, they traverse regions where the Alfvén speed increases due to the decrease in plasma density with altitude.

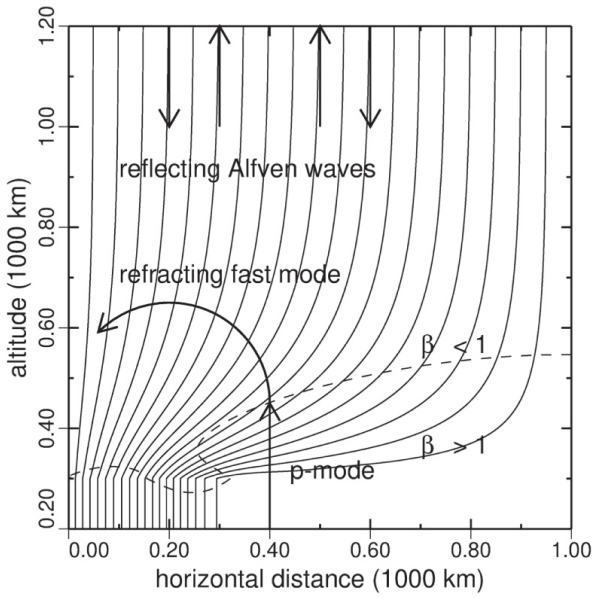

Figure 5.15: Schematic diagram of mode conversion changing upcoming acoustic waves to fast mode at $\beta_{\rm plasma} = \frac{6}{5}$, and total internal reflection of the merging fast modes. This is the key to strongly mass-dependent fractionation. Altitude is given by the y-axis. The x -axis give lateral expansion. In this plot the layer where $\beta_{\rm plasma} = 1$, is at an altitude of approximately 650 km in the Sun. Picture credit: Laming & Kuroda (2023).

Fig. 5.15, shows a diagram of the mode conversion changing of the AW as it ascends from the photosphere to the chromosphere, represented by altitude. When $\beta_{\rm plasma} < 1$, AWs propagate along magnetic field lines and are nearly undisturbed (Laming, 2009; Nariyuki, 2022). If the frequency of AW is much lower than the ion cyclotron frequency[10], it behaves as if propagating in a non-dispersive medium (Stix, 1992; Bellan, 2006). In this case, the ponderomotive force can lead to the reflection of AWs. Reflection occurs due to the steepened edge of the backward-traveling AW, creating a field-aligned proton beam propagating backward at the Alfvén speed. This reflection phenomenon is more pronounced in low-$\beta_{\rm plasma}$, where the magnetic pressure dominates over the plasma pressure. The waves are partially reflected downward when their energy does not suffice to keep up with the rising Alfvén speed. For more in depth explanation of the behavior of AWs in low- and high-$\beta_{\rm plasma}$, check these studies: Laming (2009, 2015); Laming & Kuroda (2023).

This reflection is more pronounced in stars with strong magnetic fields, as the heightened Alfvén speed permits the waves to journey farther before being reflected. Low-FIP elements, which ionize more readily, are thus more prone to interact with the magnetic field and AWs. When these elements ionize in the lower chromosphere, they become susceptible to the forces exerted by AWs. The reflection of AWs induces a preferential movement of these ions. The interaction between the waves and the ions can generate a downward force that propels the ions back toward the photosphere. Consequently, there is a depletion of low-FIP elements in the upper atmosphere, as they are forced downward before they have the opportunity to rise further. Therefore, we anticipate this pronounced reflection to occur in more active stars, such as M dwarfs. This implies that such stars are likely to exhibit elemental abundances distinct from those observed in the Sun.

As the observation of stars increased, researchers noticed that the FIP and inverse-FIP (iFIP) effects

[10]The cyclotron frequency (or, equivalently, gyrofrequency) is the number of cycles a particle completes around its circular circuit every second and is given by $f = \frac{qB}{2\pi m}$

varied with the star's spectral type. The term "F_{bias}" refers to the relative abundance of high FIP elements compared to the low FIP element iron (Fe), against a standard solar photospheric composition. This concept is demonstrated in Wood et al. (2018) through an analysis of Chandra/LETG+HRC-S spectra, depicted in Fig. 5.16. The F_{bias} is negative when low FIP elements are enhanced, as seen in the solar FIP effect, and positive in the case of the iFIP effect, where high FIP elements are enhanced.

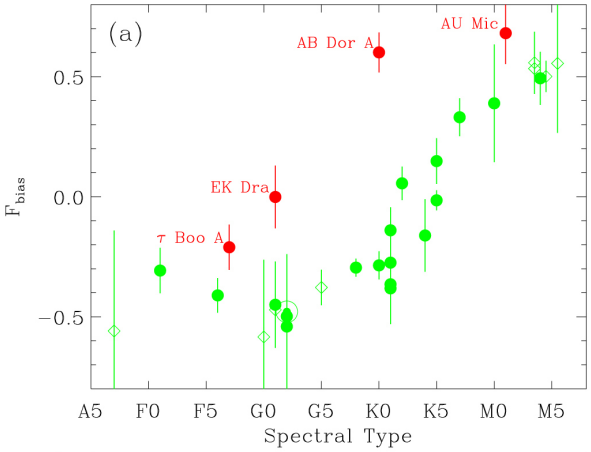

Figure 5.16: FIP bias, F_{bias}, vs. spectral type for Low Energy Transmission Grating (LETGS) stars in Wood et al. 2018, represented by filled circles. The diamond shaped values are from the literature. Red symbols indicate four stars inconsistent with the FBST relation as a result of high activity or exoplanet effects. Picture credit: Wood et al. (2018).

A clear pattern was observed showing that the F_{bias} increases with the later spectral types of stars and also increases with the level of stellar activity. This pattern mirrors the results of previous studies of stars. The question is whether less active M dwarfs also exhibit an iFIP effect or whether they follow the pattern observed in F, G and K stars. This is an ongoing area of research in which I have been involved and which I have explored further in Chapter 8.

The variation of the FIP effect with the spectral type of the stars suggests a connection with the properties of convection within the convection zones of the stars. Since the depth and properties of the convection zone change with the effective temperature of the star, the intensity and spectrum of the AW also changes (e.g. Lodders, Palme, & Gail 2009). The negative F_{bias} observed in more active stars corresponds to the properties of the saturated regime. Stars in this regime have strong magnetic fields due to their fast rotation, which influence the elemental abundances of their coronae. The fact that these stars are in the saturated regime supports the idea that their magnetic dynamo is operating at maximum efficiency.

Part II

The Vicinity of Cool Stars

5.9 Space Weather

"The universe is not required to be
in perfect harmony with human ambition."
Carl Sagan

Stellar magnetic fields play a crucial role in shaping the space weather of exoplanets. In cool dwarf stars, their magnetic activity drives stellar winds and coronal mass ejections (CMEs) and generates high-energy irradiation in the extreme ultraviolet (UV) and X-rays. The magnetic properties of cool stars depend on factors such as rotation, age and internal structure (Reiners & Basri, 2009; Vidotto et al., 2014). While magnetic activity decreases with time and associated high-energy phenomena such as coronal XUV emission and flares are reduced, stellar winds persist throughout the evolution of the system. These winds have a cumulative effect that dominates both the star and possible orbiting exoplanets, affecting the expected conditions for habitability.

These winds can affect the planets both directly and indirectly. By reducing angular momentum, the winds cause their host stars to spin down over time. This spin-down leads to a decrease in magnetic activity as low-mass stars age, which affects the emission of UV and X-rays. (Skumanich, 1972; Güdel, Guinan, & Skinner, 1997; Vidotto et al., 2014; Ribas et al., 2005). Planetary atmospheres are very sensitive to high-energy radiation from stars (Lammer et al., 2010). For example, EUV radiation can cause planetary atmospheres to expand, leading to significant hydrodynamic escape (Lammer et al., 2003, 2014; Tian et al., 2005, 2008; Lichtenegger et al., 2010). Winds also have a direct influence on planetary atmospheres. Planets are exposed to a continuous stream of supersonic electrons and protons from the wind, which compresses their magnetospheres and causes non-thermal escape and erosion of the upper atmospheres (Holmström et al., 2008; Khodachenko et al., 2012; Kislyakova et al., 2014; Alvarado-Gómez et al., 2016, 2018).

It is, therefore clear that understanding the interaction between the stellar winds of host stars and the planets orbiting them will play an important role in the search for life outside our solar system. However, this area of research is still in its infancy, as it is difficult to either detect and measure stellar winds directly or to model them based on the information we can obtain about their magnetic field behavior. Let us now explore this further.

When wind particles collide with a planet's magnetic field, they can generate plasma waves that propagate in the atmosphere and cause ionization (Brain et al., 2016). This ionization can lead to the formation of the beautiful spectacle of auroras and other visible phenomena. At the same time, these winds can erode a planet's atmosphere over time, which can lead to a planet becoming inhabitable. Below, I will list some wind-planet interactions that can take place (use Fig. 5.17 as a guide to some processes that have taken place).

Bow Shock

On a planet without a magnetic field, the stellar wind creates a bow shock around the planet and its atmosphere. If the density of the stellar wind is low enough, this bow shock does not form and the stellar wind is absorbed directly by the atmosphere. When a bow shock occurs, the material behind the shock has a speed of sound approximately equal to the speed of the stellar wind ($c_s \sim v_w$) due to the supersonic speed of the wind. The flow after the shock will envelop the planet's front hemisphere and form a turbulent mixing layer where the shocked wind meets the planet's ionosphere. In the stagnation region of the bow shock, the shocked wind remains stationary, but its speed increases towards the wings of the bow shock, reaching speeds close to v_w at the periphery of the leading hemisphere.

As for a planet with a magnetic field, the stellar winds interacting with an exoplanet's magnetic field can create bow shocks upon reaching supersonic speeds, akin to those observed around Solar system planets. Under certain conditions, these magnetospheric shocks can absorb excess stellar radiation ahead of a planet's orbit, leading to deeper transits, earlier transit ingresses, and possibly pre-transit absorption at wavelengths where the shock is optically thick (Brain, Kao, & O'Rourke, 2024).

Planetary Radio Emission

Cyclotron radiation is a crucial process in planetary magnetospheres, where charged particles like electrons orbit magnetic field lines at relativistic speeds, emitting radiation at specific frequencies known as cyclotron frequencies. In our solar system, giant planets like Jupiter exhibit intense radio emissions due to cyclotron radiation generated by their strong magnetic fields and interactions with moons like Io. Exoplanets, especially those close to their host stars, are also expected to produce cyclotron radiation due to their interaction with stellar winds. Detecting this radiation is challenging, but the Low-Frequency Array (LOFAR) offers a promising opportunity to study exoplanetary magnetic fields and space weather. Further details on the challenges and opportunities of detecting exoplanetary radio emissions can be found in the studies by Bastian, Dulk, & Leblanc (2000); Zarka, Queinnec, & Crary (2001); Grießmeier et al. (2005); Lazio & Farrell (2007); Jardine & Collier Cameron (2008); Vidotto et al. (2010); Nichols (2011)

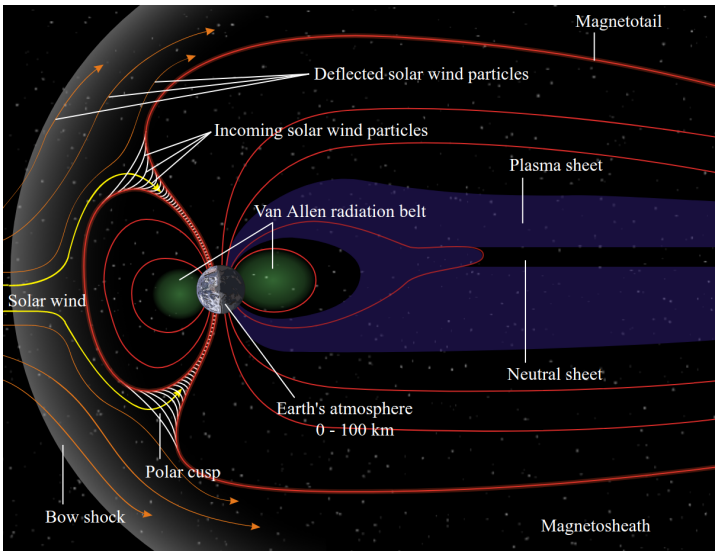

Figure 5.17: Diagram of Earth's magnetosphere. We also see different phenomena that can take place due to the win-planet magnetosphere interaction. Picture credit: NASA.

Atmospheric Erosion

The high-energy radiation emitted by stars, such as X-rays and UV radiation, is strongly absorbed in planetary atmospheres with low gas density. This absorption heats and expands the upper atmosphere, making it more susceptible to interactions with the stellar wind, which can lead to atmospheric erosion. In our solar system, empirical evidence suggests that the solar wind was a dominant mechanism for atmospheric loss on early Earth, Mars and Venus (Catling & Kasting, 2017). A study by Modi, Estrela, & Valio (2023) shows that for planets in the HZ orbiting early-type M dwarfs at distances greater than 0.1 AU, photoevaporation is the primary mechanism for atmospheric loss. However, for planets orbiting late-type M dwarfs at closer orbits (0.01-0.03 AU), both stellar wind and photoevaporation contribute significantly to atmosphere loss, with photoevaporation being more effective. The Trappist-1 system is an example of how both processes lead to a significant loss of atmosphere due to the close orbit of the planets.

Moreover, in a recent work by Poppenhaeger et al. (2024), they showed that a planet such as GJ 367 b with high iron content and a potentially thin gaseous atmosphere, is likely to have its atmosphere completely evaporated due to the high-energy environment and the low-activity level of its host star, an M dwarf. The study suggests that the planet's atmosphere would have evaporated in approximately 15 million years, given the intense high-energy irradiation from the host star. This finding indicates that it is statistically unlikely for the planet to currently retain any atmosphere, despite the low activity level of the host star.

Alteration in Galactic Cosmic Rays Flux

Stellar winds not only drive atmospheric erosion, but also influence the flow of cosmic rays reaching the surface of the planet. Winds affect the number of galactic cosmic rays reaching the inner regions of stellar systems, thus altering the flux of cosmic rays reaching a planet's atmosphere (Cohen, Drake, & Kóta, 2012; Herbst et al., 2022). This is particularly important for weakly magnetized planets where synchronous rotation is common. Despite the potentially extreme surface temperatures resulting from this rotation pattern, the habitability of such planets is still possible (Heath et al., 1999). However, the presence of small magnetic moments on these planets further complicates the assessment of their habitability.

5.10 Stellar Winds and Close-in Planets

"We don't want to conquer the cosmos,
we simply want to extend the boundaries
of Earth to the frontiers of the cosmos."
Stanislaw Lem

Researchers have been looking for exoplanets for over two decades (Mayor & Queloz, 1995; Marcy & Butler, 1996; Butler & Marcy, 1996), with a focus on finding habitable extra-solar Earth analogues (Kaltenegger & Traub, 2009; Fressin et al., 2012; Borucki et al., 2012). The habitable zone (HZ, Fig. 5.18) of a planet is a standard criterion for determining whether it is suitable for life. This region is defined by the orbital distances at which liquid water can exist on a planet's surface (Huang, 1960; Hart, 1978; Kasting, Whitmire, & Reynolds, 1993; Kopparapu et al., 2013), and it is determined by taking the radiation flux incident on the planet into account. A stable atmosphere, which is required to regulate surface temperatures, could be eroded away by sufficiently strong stellar winds, rendering a planet uninhabitable (Khodachenko et al., 2007; Zendejas, Segura, & Raga, 2010; Vidotto et al., 2011; Lammer et al., 2012; Garraffo, Drake, & Cohen, 2015, 2016; Alvarado-Gómez et al., 2018; Cohen et al., 2007).

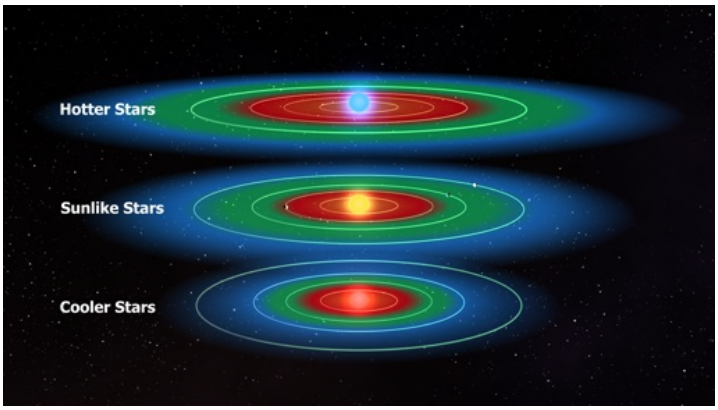

Figure 5.18: Diagram of the Habitable Zone of planets based on the temperature of the Star. The dimmer and cooler the star, the narrower the habitable zone and closer to the star. Picture credit: NASA.

Due to their relatively low mass, low luminosity and high abundance ($\approx 70\%$ of stars in the solar neighborhood), M dwarfs are often targeted for the search for habitable planets. New types of star-planet interactions can also occur for planets around M stars and late K stars, since the planets orbit closer to the star and in this case the interaction with AS has to be taken into account. Close in orbits, have distances significantly smaller than Mercury's orbit. For comparison, the innermost planet in the solar system is Mercury, with a semi-major axis of 0.4 AU (see Fig. 5.19 for guidance).

An important concept for close-in exoplanets is the nature of star-planet interactions relative to the Alfvén surface (AS) of the star. The AS defines where the stellar wind is dominated by magnetic forces (inside) and inertial forces (outside). Within the AS, the stellar wind is sub-Alfvénic, allowing Alfvén "wing" currents to connect the star and the planet (Strugarek et al., 2015). Outside this region, the connection is lost. The AS and star-planet interactions change with the stellar magnetism

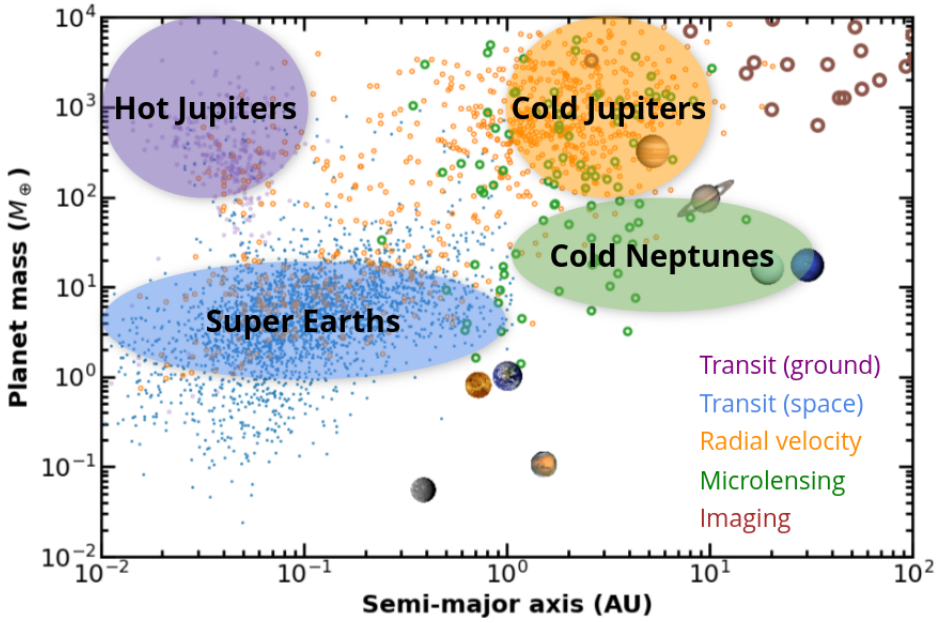

Figure 5.19: Plot showing different known planets compared to the planets in our solar system. The planets are shown with respect to the mass and the orbital distance from their host star. Data is based on NASA Exoplanet Archive. The different colors represent the different method used to detect the planets. The image also shows the group of planets divide into: Hot Jupiters, cold Jupiter, cold Neptunes, and super Earth. Picture credit: Wei Zhu (Assistant Professor in the Department of Astronomy at Tsinghua University in Beijing).

evolution, e.g. through activity cycles (Nicholson et al., 2016; Kavanagh et al., 2019). This can lead to intermittent star-planet interactions. Further details on the properties and formation of the AS can be found in section 4.7 and chapter 5.

Super-Alfvénic Regime

As in the case of the planets in our solar system and the sun. All planets are outside the AS of the sun. In super-sonic (or super-Alfvénic) interactions, i.e bow shocks, (Vidotto et al., 2010; Carolan et al., 2019). In addition, depending on the properties of the system (i.e. the physical conditions of the stellar winds and the planets), evaporated planetary material may trail the planet (Villarreal D'Angelo, Jardine, & See, 2018; Daley-Yates & Stevens, 2019) and form a comet-like tail structure. Alternatively, in some configurations, material can be funnelled towards the star and form an inspiralling accretion stream (Matsakos, Uribe, & Königl, 2015).

Sub-Alfvénic Regime

In this regime, the planet has a direct magnetic connection with its host star. This leads to various magnetic interactions that we are not familiar with in the solar system. I will list some of them.

Alfvén wings: A planet moving at sub-Alfvénic speed through the magnetized wind of its host star can trigger MHD AWs, which can travel along the magnetic field lines towards the star. As they travel, these waves can then dissipate their energy and the maximum power that is radiated can be estimated by integrating the Poynting flux of the stellar wind over the cross-section of two Alfvén 'wings' (Saur et al., 2013). In the limit of sub-Alfvénic speeds, with an Alfvén Mach number ($\mathrm{M_A} < 1$), the dissipated power is

$$P_{\rm wg} \simeq P(2\pi r^2 \mathrm{M_A})\alpha^{2MA}\sin\theta = \frac{\Delta u}{2B\sin^2\theta}\frac{2r^2\mathrm{M_A}\alpha_p^2}{4\pi\rho}$$

where, $P_{\rm wg}$ is the wind-generated pressure exerted by the stellar wind on the planet, P is the dynamic

pressure of the stellar wind, r is the radius of the planet, α is a dimensionless parameter related to the conductive properties of the planet. The angle between the stellar wind speed vector and the planetary $\vec{B}$ is denoted by θ, Δu is the change in stellar wind velocity due to the presence of the planet B is the magnetic field strength of the planet, ρ is the density of the stellar wind, and α_p is a parameter related to the conductive properties of the planet in the interaction.

Magnetic reconnection: The magnetic field lines of opposite polarity belonging to these two different bodies can undergo reconnection, releasing energetic particles that move along the stellar magnetic field lines towards the star (Ip, Kopp, & Hu, 2004). When these particles hit the stellar chromosphere at the magnetic footpoints, chromospheric hot spots can be excited. As the planet moves through its orbit, it interacts with various stellar field lines so that hot spots are "activated" by the orbit and thus modulated by the planet's orbital period (Saar & Cuntz, 2001). As the planet moves from one branch of the closed loops to another, the activated chromospheric hot spots appear to jump at different positions in the stellar chromosphere, creating a phase lag or jumping effect (e.g. McIvor, Jardine, & Holzwarth 2006; Strugarek et al. 2019).

Also, there is scenario presented by Lanza (2013), in which a magnetic loop connecting the star and the planet would suffer a rupture after being stretched by the planet. The idea is that one footpoint of the loop sits at the surface of the star, while the other footprint lies at the surface of the planet. As the planet moves through its orbit, the magnetic loop is stretched (stressed) and when it breaks, it can release energy, which travels towards the star, giving rise, for example to anomalous hot spots at the stellar surface (Shkolnik et al., 2005; Cauley et al., 2019). This is the scenario that Strugarek et al. (2022) named 'stretch and break'. Magnetic reconnection has been studied by several authors in the case of star-planet interactions (e.g. Jardine & Collier Cameron 2008; Lanza 2009; Vidotto et al. 2010. In their study Jardine & Collier Cameron (2008) and Vidotto et al. (2010) considered reconnection events as the cause of radio emission from exoplanets, while Lanza (2009) investigated how reconnection events could trigger chromospheric hot spots.

Moreover, magnetic reconnection significantly enhances the mass-to-charge ratio (A/Q)[11] in stellar environments, as described by Meyer (1985). This influx of particles can alter the magnetic field strength of the star and possibly influence the behavior of the star. In addition, these particles can cause increased stellar activity, such as flares or coronal mass ejections.

Interconnecting magnetic loop between star and planet: An interconnecting loop that extends from the stellar surface to the planetary orbit (Lanza, 2013). For similar planetary field strengths, the interconnecting loop scenario produces maximum powers that are about three to four orders of magnitude larger than the other scenarios. In this scenario, it is assumed that the stellar magnetic field remains closed up to the orbital distance of the planet.

Strong energy flux: The motion of close-in exoplanets may disturb the plasma sufficiently to induce strong energy fluxes that go back down to the star (e.g. Saur et al. 2013; Matsakos, Uribe, & Königl 2015), producing visible chromospheric starspots (Shkolnik et al., 2008) or bursts of radio emission (Pineda & Villadsen, 2023).

Sub-Super-Alfvénic

A planet moving inside and outside the AS experiences different stellar wind conditions, leading to unstable interactions. This is particularly important for planets orbiting M dwarfs, where the stellar wind is more intense and the planet may not have time to recover between exposures (more on wind conditions in Chapter 7). These changes can occur over orbital timescales. For example, when an exoplanet is inside the AS, it interacts with a stronger stellar magnetic field, leading to a more intense star-planet interaction (Cohen et al., 2014). If, on the other hand, the planet moves outside the AS, the weaker stellar magnetic field leads to less or even no interaction (Kislyakova et al., 2014). Such fluctuations can lead to enhanced stellar emission, which could be interpreted as triggered by magnetic reconnection events (Harbach et al., 2021).

[11] According to classical electrodynamics, particles with the same A/Q ratio follow identical paths in a vacuum under the influence of electric and magnetic fields.

Part III

A Series of Exploration in Cool Stars' Playground

Destination Exoplanet: Habitability Conditions Influenced by Stellar Winds Properties

Judy J. Chebly[1,2], *Julián D. Alvarado-Gómez*[1], *Katja Poppenhäger*[1,2]
[1]Stellar Physics and Exoplanets, Leibniz Institute for Astrophysics, Potsdam, Germany
[2]Institute of Physics and Astronomy, University of Potsdam, Potsdam, Germany
Astronomische Nachrichten, Volume 343, Issue 4, article id. e10093.
10.1002/asna.20210093

The cumulative effect of the magnetized stellar winds on exoplanets dominates over other forms of star-planet interactions. When combined with photoevaporation, these winds will lead to atmospheric erosion. This is directly connected with the concept of Habitable Zone (HZ) planets around late-type stars. Our knowledge of these magnetized winds is limited, making numerical models useful tools to explore them. In this preliminary study we focus on solar-like stars exploring how different stellar wind properties scale with one another. We used one of the most detailed physics-based models, the 3D Alfvén Wave Solar Model part of the Space Weather Modeling Framework, and applied it to the stellar winds domain. Our simulations showed that the magnetic field topology on the star surface plays a fundamental role in shaping the different stellar wind properties (wind speed, mass loss rate, angular momentum loss rate). We conclude that a characterization of the Alfvén surface is crucial when studying star-planet interaction as it can serve as an inner-boundary of the HZ.

6.1 Introduction

The majority of what we know about stellar winds comes from our knowledge of the Sun. We believe that the same mechanisms behind the coronal heating and stellar wind acceleration on the Sun, take place on solar-like stars and low-mass main sequence stars. All of these objects are X-ray sources with coronal temperatures of several million Kelvin. The high gas-pressure gradient in the hot plasma that surrounds these stars will expand as supersonic wind (Parker, 1958). However, there are large uncertainties in our knowledge of the evolution of stellar winds on the main sequence, due to a lack of direct measurements as well as an incomplete understanding of the solar wind. This reflects in our ability on using stellar winds for rotational evolution models, particularly as some stars experience a rapid spin-down whereas others of the same mass and age do not (Spada et al., 2011).

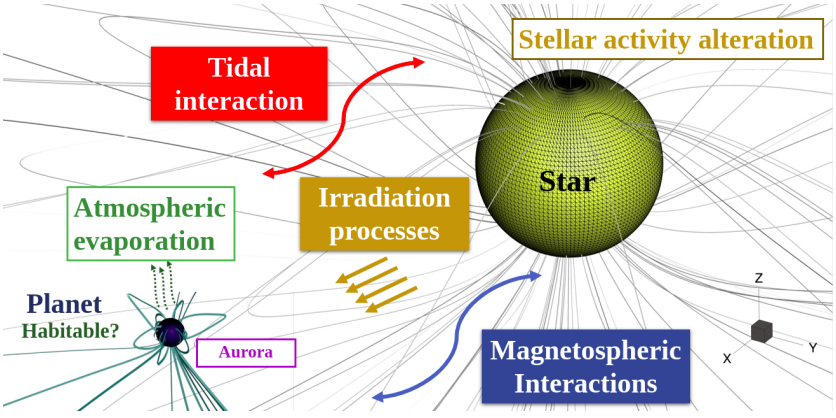

Figure 6.1: Schematic view of the different star-planet interactions and some of their expected influence.

Given the sensitivity of planetary atmospheres to stellar wind and radiation conditions, these uncertainties can be significant for our understanding of the evolution of planetary environments. Since the information is so limited, models provide a pathway to explore how these stellar winds look like, and how they behave. A detailed parametrization of these magnetized winds is crucial especially when it comes to close-in systems such as M dwarfs where the HZ is close to the star. Current observational constraints indicate that M dwarfs have winds comparable or even stronger than that of a G star (Wood et al., 2021). As the wind strength experienced by a planet decreases with the square of its orbital distance, even relatively weak winds will have an extremely strong effect on close-in exoplanets. In addition, as illustrated in Fig. 6.1, when a planet roams in the vicinity of its star, different interactions can occur such as tidal (Ibgui, Spiegel, & Burrows, 2011; Winn et al., 2010), magnetic (Lanza, 2013; Cohen et al., 2018), and processes mediated by radiation (Bourrier & Lecavelier des Etangs, 2013; Fossati et al., 2013).

The magnetic perturbations may lead to a modification of the stellar activity (Shkolnik et al., 2008), but may also be observationally swamped by intrinsic stellar variability (Poppenhaeger et al., 2011). They can potentially induce planetary aurorae and associated radio emission (Zarka, 2007; Grießmeier, Zarka, & Spreeuw, 2007). Moreover, the radiation emitted by the star provokes planet inflation, yielding the outer material more easily taken away by the stellar wind, leading to atmospheric evaporation on the planet (Gronoff et al., 2020). While magnetic activity decreases with time reducing the quiescent and transient phenomena such as flares and high-energy emission (e.g., Skumanich 1972), stellar winds persist throughout the entire stellar evolution (Wood, 2004). For this reason, their cumulative effect will be dominant for both, the star's angular momentum evolution (Garraffo, Drake, & Cohen, 2015), as well as for possible exoplanets orbiting in the system, affecting in this way the expected habitability conditions (Alvarado-Gómez et al., 2016; Meadows & Barnes, 2018). This is because sufficiently strong magnetized winds can erode a stable atmosphere and render a planet inhabitable (Khodachenko et al., 2007; Zendejas, Segura, & Raga, 2010; Vidotto et al., 2011).

Here we study how different properties of the magnetized stellar wind scale with one another and isolate the most important dependencies between the parameters involved. These results will be later used to constrain planet habitability from a stellar wind perspective. Section 6.2 contains a description of the numerical model and parameters employed in the stellar wind simulations. Preliminary results, including dependencies with stellar rotation period, magnetic field strength, and geometry, are presented in Sect. 6.3. A discussion of these results is presented in Sect. 6.4 and we conclude our work in Sect. 6.5.

6.2 Model description

In this work, we employ the Alfvén Wave Solar Model (AWSoM-R, van der Holst et al. 2014; Sokolov et al. 2021, which is part of the Space Weather Modeling Framework (SWMF, Tóth et al. 2012). This model has been tested, validated, and was proved to be one of the closest models in agreement with observations(Sachdeva et al., 2019). The model uses the BATS-R-US code to solve in 3D the MHD equations for the conservation of mass, momentum, magnetic induction, and energy in finite volume form (Powell et al., 1999). Simulations employing the SWMF can cover a domain extending from the solar chromosphere up to 1 au in heliosphere and beyond (Tóth et al., 2005). The distribution of the surface magnetic field of the star is the main driver of the solution, from which the heating of the corona and the stellar wind acceleration are calculated self-consistently.

Our main assumption is that the mechanism incorporated in the AWSoM-R model can be extended to stars of different spectral type than the Sun. This is justified due to the fact that the coronal emission from these stars shows several similarities with that of the Sun (Testa, Saar, & Drake, 2015). In order to use the model on solar-like stars and lower main sequence stars, we modify the parameters that control the properties of the winds (e.g. magnetic field strength, geometry, stellar rotation, stellar mass, etc). In this way, we create a generic synthetic grid of simplified models from which we can study and extract the dependencies of interest.

We employ the Solar Corona (SC) module of the SWMF whose 3D domain encompasses the region between the surface of the star ($\sim 1\ R_\star$) up to 85 $R_\star$. We use a spherical grid with a maximum base resolution of $\Delta R = 0.025\ R_\star$, $\Delta\Phi = 1.4°$, stretching radially following a logarithmic function of R. The choice of the grid resolution affects the speed of the convergence of the simulation to a steady-state

stellar wind solution. In all our models we consider a restricted case in which the magnetic field axis is perfectly aligned with the rotation axis of the star and all the initial solar parameters of AWSoM-R are kept intact except the ones related to the surface magnetic field distribution as discussed below.

In the following sections, we will talk about each stellar wind parameter separately showing how different parameters changes their behavior.

6.3 Results

6.3.1.Average terminal stellar wind speed

We calculated the average terminal wind speed by integrating over 3 different spherical shells in the vicinity of the outer boundary of the simulation (70 $R_\star$, 75 $R_\star$, 85 $R_\star$).

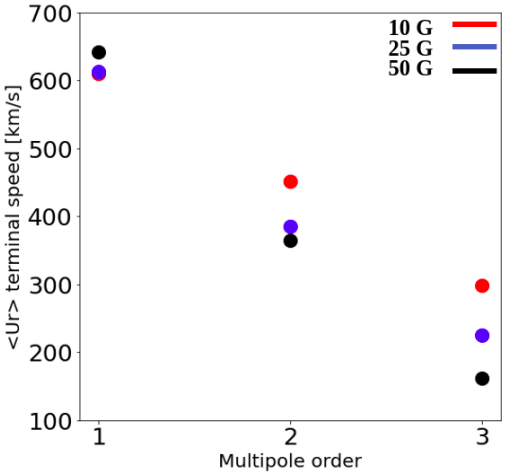

Figure 6.2: Average terminal stellar wind speed as a function of the surface magnetic field properties (strength and geometry) for a fixed stellar rotation (P_{rot} = 30 d). The stellar wind emerging from the simpler geometries is faster.

Our calculation of the average terminal radial wind speed $\langle U_r \rangle$ showed that the more complex the surface geometry, the slower the wind speed becomes (Fig. 6.2). For a dipolar field (multipole order of 1) the wind speed is $\sim$ 600 km/s almost two times faster than the one of the octopole (multipole order 3). This result is expected since simpler geometries have a smaller number of closed field lines, allowing the plasma to flow out easier (analogous to the solar wind during activity minimum). We can also see that the distribution of the wind speed changes when we go from a dipole to higher orders. The 10 G wind speed becomes faster than the 50 G, and this is due to the modification in the plasma density when we change the magnetic field geometry (Vidotto, 2021).

Moreover, Fig. 6.2 shows that the magnetic field strength plays a secondary role in modifying the wind speed compared to changes in its global geometry. For instance, the simulations with a dipole field of B_r = 10 G and B_r = 50 G, yield stellar wind speeds of 609 km/s and 642 km/s, respectively. Still, the increase in magnetic field strength will modify the distribution of both, the stellar wind speed and the coronal density. The combination of these two dictates the mass loss rate as discussed in the following section. We also notice that when the geometry becomes more complex the spread in the terminal wind speed between the different magnetic field strengths becomes wider. Because the more complex magnetic field structure will introduce more streamers, those will carry away higher densities especially when we go higher in the magnetic field strength. The increase in streamers will reduce the local wind speed.

6.3.2.Mass loss rate

Stellar mass loss through magnetized winds is an important parameter to consider when trying to understand the rotational evolution of a star, and it is possibly one of the most important drivers of

atmospheric evaporation of exoplanets.

The Alfvén surface (AS) sets the boundary between these winds and magnetically-coupled outflows that do not carry angular momentum away from the star (such as loops and prominences). It is a mix between wind speed, plasma density, and the local magnetic field strength. From a numerical approach, this surface is used for different stellar wind parameters calculations. Formally, the AS is given when the Alfvénic Mach number –calculated as the ratio of the stellar wind speed to the Alfvén speed– is equal to one ($M_a = 1$). When calculating the stellar mass loss rate we consider 3 spherical shells located beyond the AS (Fig. 6.3) to integrate the mass flux. This is because beyond the AS all the outflows are considered to be carrying mass that will be lost with the wind.

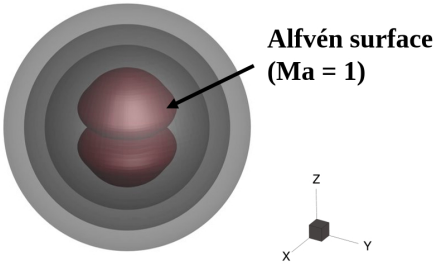

Figure 6.3: Illustration of the numerical calculation of the mass loss rate.

Based on the continuity equation in MHD, the mass should be conserved everywhere, so that a similar mass loss rate is obtained from the integration across each sphere:

$$(\frac{dM}{dt}) = \rho(\mathbf{u} \cdot dA) \tag{6.1}$$

Here, ρ represents the wind density, $\mathbf{u}$ is the wind speed vector and dA is the vector surface element.

We expect that more active stars should in principle have more mass loss. They have strong magnetic fields, so they should have more energy to provide to these winds. The mass loss rate also decreases for higher multipole orders, in line with the argument of (Garraffo, Drake, & Cohen, 2015) which confirms that simpler geometries power up more mass loss (Fig. 7.4, left).

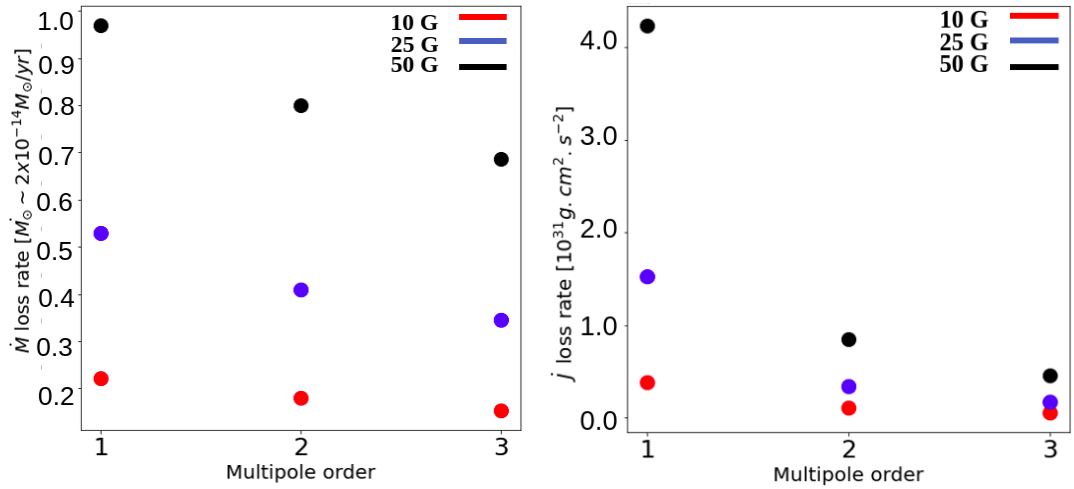

Figure 6.4: Mass loss rate (left) and angular momentum loss rate (right) as a function of the surface magnetic field properties (strength and geometry) for a fixed stellar rotation ($P_{rot} = 30$ d). The mass loss rate is highly affected by the magnetic field strength, while the angular momentum loss rate is higher for simpler geometries and stronger magnetic field strength.

6.3.3. Angular momentum loss rate

For the numerical calculation of the angular momentum loss rate, we integrated every single point on the AS. We took into account its actual shape rather than considering it as a sphere. The relation for calculating the angular momentum loss in spherical coordinates is provided by (see Fig.7.4).

$$(\frac{dJ}{dt}) = \Omega \rho R^2 \sin^2\theta (\mathbf{u} \cdot dA) \tag{6.2}$$

Here Ω is the angular frequency of the star and θ is the angle between the lever arm and the rotation axis. Ω changes with the different stellar rotation $\Omega = 2\pi/P_{rot}$, hence it is not the same in all realisations of the simulations.

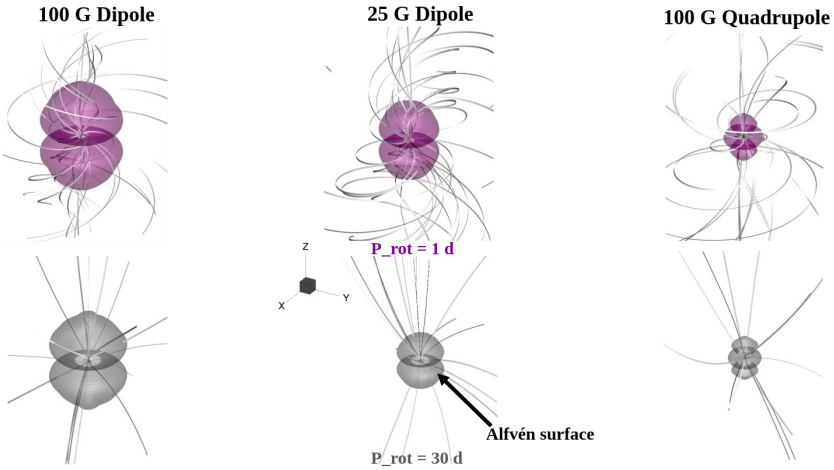

Figure 6.5: Illustration of the effect of magnetic field strength and geometry on the AS for different values of the stellar rotation period (*Top:* $P_{rot} = 1$ d; *Bottom:* $P_{rot} = 30$ d. The magnetic fields anchored to the star will exert a drag force over the stellar surface. A fast rotation will lead to winding up the magnetic field which will be tighter as we increase the rotation. The AS is highly affected by the change in the surface geometry. The field of view of the visualizations is 243.7 $R_\star$.

For cool main sequence stars, the magnetised wind is believed to carry away stellar angular momentum, causing decay in both their rotation rates and their high-energy radiation. These losses will influence the atmosphere of any planets in the system (Johnstone, 2021).

The dipole configuration is the one that has the most effective angular momentum loss. What Fig. 7.4 (right) is showing is basically the ballerina effect: the star is spinning fast when we have more complex geometries. As we go to higher multipole orders, the number of closed field lines will increase, reducing the AS size and therefore the angular momentum loss rate. We also see that a stronger magnetic field has a higher angular momentum loss rate. A 50 G magnetic field will lead to an angular momentum loss rate larger than the 25 G but the difference between these cases is up to a factor of ~ 1.5, while the difference from a 50 G dipole to a quadrupole is a factor of ~ 3 (Fig. 7.4, right). There is a large increase by almost an order of magnitude of the angular momentum loss just by changing the geometry from a quadrupole to a dipole for the same magnetic field strength. In Fig. 7.5 we can see that for the same magnetic field strength, simpler geometries have larger AS and the surface decreases whenever we have higher multipole orders.

We can say that the mass loss contributes to the angular momentum loss rate, but here the quantity that is playing a major role is the size of the AS. This result was expected since the angular momentum loss rate is dependent on the AS size (R^2 dependency in Eq. 6.2).

6.4 Discussion

The redistribution of the plasma density due to the change in the magnetic field geometry plays an important role in the behavior of the different stellar wind properties. The drastic change in the behavior of the wind property was clearly seen when we calculated the terminal wind speed. This means that when trying to understand what is the role played by the winds and by the environment they generate for the planets is much more complicated than simply knowing what is the magnetic field strength of the star. The effect of the geometry on the terminal stellar wind speed, mass loss, and angular momentum loss rate was highlighted in Sect. 6.3.

Stellar activity cycles change globally the geometry of the magnetic field. For example, the Sun during the solar cycle changes from having dipole properties to a more quadrupole configuration, with wind speeds of ∼800 km/s and ∼300 km/s, respectively. The maximum solar wind speed is higher than the one of the 10 G dipole (609 km/s) of $P_{rot} = 30$ d which means that the solar wind speed is lower in density. The plasma becomes denser as we go to higher multipole orders. Moreover, the velocity and plasma density dictates the dynamic pressure of the wind, which is a crucial parameter to explore when studying star-planet interaction. These parameters are connected to the AS and will change the surface size and modify the stellar wind properties.

The size of the AS surface determines both the total area of integration, as well as the size of the lever arm that applies a torque on a star to spin it down. Equations 7.3 and 6.2 show the interplay between the actual mass flux through the AS (dictated by the density, and magnetic field geometry) and its size. The magnetic particles carried away by this loss can erode the atmosphere of the planet and transform a habitable planet into a non-habitable one even if located in the habitable zone (Lammer et al., 2012; Vidotto et al., 2011).

It has been shown that the angular momentum loss controls the bimodal distribution of rotation periods that we observe in young open clusters (Skumanich, 1972; Brown, 2014) explained this distribution based on the idea that rotating stars fall into two different regimes; one in which the dynamo is strongly coupled to the wind and another one where it is weakly coupled to the wind. The initial distribution of rotation periods will yield to another one when the star becomes older. This is manifested as a bipolarity in how the rotation periods distribute (see Garraffo et al. 2018).

In Fig. 7.4 (right) we have an estimation of the angular momentum loss rate for stars with the same characteristics, but different rotations. We notice that fast-rotating stars have a large angular momentum loss rate, because they have big AS. These stars will spin down faster than the slow rotators.

Angular momentum loss rates are highly affected by the change of geometry rather than by the change of magnetic field strength. In the study of Finley & Matt (2018) they show that angular momentum loss rates vary by 30-40% over the solar cycle. This shows that despite the dramatic change in the surface magnetic field strength of the Sun during the cycle, the changes in the solar wind properties are not drastic. Additional works have been done showing the angular momentum changes in function of the star rotation period (e.g. Bouvier et al. 2014; Shoda et al. 2020).

6.5 Conclusion

The magnetic field geometry of the star surface plays a fundamental role in defining the AS shape and size leading to alteration in stellar wind properties. Hence, a detailed characterisation of the AS is needed because it sets the boundary between the stellar winds and magnetically-coupled outflows and especially the equatorial AS - where many of the known exoplanets are located (Winn & Fabrycky, 2015). The AS can be used as the inner boundary of the actual HZ. However, we may find that the inner boundary that was once predicted by the classical description based on surface temperature, is pushed further away from the star, because atmospheres may be easily eroded inside the HZ. If the planet is almost embedded in the magnetic field of the star we can imagine that we have reconnection events taking place. If the planet is magnetized, we can have interactions between the magnetic fields.

Simulating the stellar wind domain requires prior knowledge of the large scale surface star magnetic field geometry which can be retrieved to some extent by techniques such as Zeeman Doppler-Imaging (ZDI). It has been argued that ZDI reconstructions have limited spatial resolution because they are

insensitive to the small-scale surface field. However, far away from the star, these small-scale phenomena on the star surface won't be very relevant but they will matter when we want to simulate the corona (Garraffo et al., 2013; Alvarado-Gómez et al., 2016). The more constraints we have on stellar properties and the magnetic field of the star, like a detailed ZDI maps and also constraints by Zeeman broadening, the more accurate models we will be able to obtain. Different observation satellites e.g. XMM-Newton, Chandra and the future mission ATHENA will help us to improve and generate more realistic numerical simulations. For further investigation, we will explore different main-sequence spectral types with the ultimate goal of constraining planetary habitability from a stellar winds perspective.

Acknowledgments: This research is supported by the German Leibniz Community grant P67/2018.

Numerical quantification of the wind properties of cool main sequence stars

Judy J. Chebly[1,2], *Julián D. Alvarado-Gómez*[1], *Katja Poppenhäger*[1,2], *Cecilia Garraffo*[3]
[1]Leibniz Institute for Astrophysics, An der Sternwarte 16, D-14482, Potsdam, Germany
[2]Institute of Physics and Astronomy, University of Potsdam, Potsdam-Golm, D-14476, Germany
[3]Harvard-Smithsonian Center for Astrophysics, 60 Garden Street, Cambridge, MA 02138, USA
Monthly Notices of the Royal Astronomical Society, Volume 524, Issue 4, pp.5060-5079.
10.1093/mnras/stad2100

As a cool star evolves, it loses mass and angular momentum due to magnetized stellar winds which affect its rotational evolution. This change has consequences that range from the alteration of its activity to influences over the atmosphere of any orbiting planet. Despite their importance, observations constraining the properties of stellar winds in cool stars are extremely limited. Therefore, numerical simulations provide a valuable way to understand the structure and properties of these winds. In this work, we simulate the magnetized winds of 21 cool main-sequence stars (F-type to M dwarfs), using a state-of-the-art 3D MHD code driven by observed large-scale magnetic field distributions. We perform a qualitative and quantitative characterization of our solutions, analyzing the dependencies between the driving conditions (e.g., spectral type, rotation, magnetic field strength) and the resulting stellar wind parameters (e.g., Alfvén surface size, mass loss rate, angular momentum loss rate, stellar wind speeds). We compare our models with the current observational knowledge on stellar winds in cool stars and explore the behaviour of the mass loss rate as a function of the Rossby number. Furthermore, our 3D models encompass the entire classical Habitable Zones (HZ) of all the stars in our sample. This allows us to provide the stellar wind dynamic pressure at both edges of the HZ and analyze the variations of this parameter across spectral type and orbital inclination. The results here presented could serve to inform future studies of stellar wind-magnetosphere interactions and stellar wind erosion of planetary atmospheres via ion escape processes.

7.1 Introduction

For many decades, scientists have known that the Sun has a mass outflow, which is most visible in the behavior of comet tails (e.g., Biermann 1957). It has also been established that solar wind is a natural byproduct of the heating processes that produce the hot solar corona ($T \sim 10^6$ K). As a result, all cool main-sequence stars ($M_\star \leqslant 1.3$ M$_\odot$) with analogous hot coronae, evidenced from their measured X-ray properties (Schmidt et al. 1995; Pizzolato, Maggio, & Sciortino 2000; Wright et al. 2011), should have similar winds (Parker 1958). Magnetic fields are thought to play a key role as an energy source for the corona and the expanding solar atmosphere (e.g., Aschwanden 2005; Klimchuk 2015; Velli et al. 2015). Recent theories have shown that in addition to magnetic fields, wave dissipation (via turbulence) and magnetic reconnection could also play a role in energizing and shaping the spatial properties of the solar wind (see, Ofman 2010; Cranmer 2012; Hansteen & Velli 2012; Cranmer et al. 2015).

Winds, even if relatively weak, play an important role in stellar evolution for stars of different spectral types causing the star to lose angular momentum and slow its rotation over time (Weber & Davis 1967; Skumanich 1972; Matt et al. 2012; Gallet & Bouvier 2013, 2015; Johnstone & Güdel 2015; Johnstone et al. 2015; Ahuir, Brun, & Strugarek 2020). As a result, the magnetic activities that constitute the space weather (i.e., stellar winds, flares, coronal mass ejections) will decrease with age in low-mass stars (Skumanich 1972; Güdel, Guinan, & Skinner 1997; Ribas et al. 2005; Vidotto et al. 2014). These changes in the host star will also affect the evolution of planetary atmospheres and habitability (Hurford et al. 2008; Mancini et al. 2014; Airapetian et al. 2017).

Direct measurements of the solar wind by spacecraft such as the Advanced Composition Explorer (ACE, Stone et al. 1998; McComas et al. 1998), Ulysses (McComas et al., 2003), and Parker solar probe (Kasper et al., 2021) have improved our knowledge and understanding of its properties. On the other

hand, detecting a solar-like wind emitted by another star has proven extremely challenging. This is not surprising, given how difficult it is to observe the solar wind remotely. The latter carries a very low mass loss rate ($\dot{M}_\odot = 2 \times 10^{-14}$ M$_\odot$ yr^{-1}, see Feldman 1977; Wood 2004), which implies relatively low densities (near the heliopause: ~ 0.002 cm^{-3}, McComas et al. 1998). Similarly, its high temperature and elevated ionization state, make it difficult to detect with simple imaging or spectroscopic techniques. As a result, properties such as the associated mass loss rates, angular momentum loss rates, and terminal velocities, crucial to understand stellar winds in low-mass stars, remain poorly constrained.

Attempts to directly detect thermal radio emission from the plasma stream in cool stars have not yet led to any discovery (Lim & White 1996; Drake, Simon, & Brown 1993; van den Oord & Doyle 1997; Gaidos et al. 2000; Villadsen et al. 2014; Fichtinger et al. 2017). Current radio telescopes are not optimized for this method; they can only detect winds much stronger than those from the Sun. Moreover, the coronae of these active stars are also radio sources, making it difficult to determine the exact source of the emission. Nevertheless, this method has been able to establish upper limits for solar analogs of 1.3×10^{-10} $\dot{M}_\odot$ yr^{-1} (Gaidos et al. 2000; Fichtinger et al. 2017). Another proposed method for direct detection is to look for X-ray emission from nearby stars. As the star's winds propagate, they collide with the Local Interstellar Medium (ISM), forming "astrospheres" similar to the Sun's heliosphere (Wood, 2004). The charge exchange between the highly ionized stellar wind and the ISM produces X-ray photons with energies ranging from 453 to 701 eV. However, this method was unable to detect circumstellar charge exchange X-ray emission even from the nearest star, Proxima Centauri (Wargelin & Drake, 2002).

Similar to the charge exchange X-ray emission method, the Ly-α absorption technique assumes the presence of the charge exchange phenomenon. In this case, however, we are interested in the neutral hydrogen wall formed at the astrospherical outer boundary by the interaction between the stellar wind and the ISM. This exchange has been detected as excess HI Ly-α absorption in Hubble Space Telescope UV stellar spectra (Linsky & Wood, 2014). With nearly 30 measurements to date, spectroscopic analyses of the stellar HI lines have proven to be the best method to unambiguously detect and measure weak solar-like winds as well as some evolved cool stars (Wood et al., 2021). Using this method,Wood et al. (2005) found evidence for some increase in $\dot{M}$ with magnetic activity, corresponding to a power-law relation in the form $\dot{M} \propto F_{\rm X}^{1.34\pm0.18}$ with $F_{\rm X} < 10^6$ erg cm^{-2} s^{-1}. However, this relation does not seem to hold anymore for more active stars ($F_{\rm X} > 10^6$ erg cm^{-2} s^{-1}), mainly M dwarfs (Wood et al., 2005; Wood, Mueller, & Redfield, 2014). Recently, Wood et al. (2021) established a power law ($\dot{M} \propto F_{\rm X}^{0.77\pm0.04}$) between the $\dot{M}$ per unit surface area and the X-ray surface flux for coronal winds for a broader selection of stars, including G, K, and new $\dot{M}$ estimates for M dwarfs. They found that the relation breaks even for stars with $F_{\rm X} < 10^6$ erg cm^{-2} s^{-1} (e.g., GJ 436, which has $F_{\rm X} = 4.9 \times 10^4$ erg cm^{-2} s^{-1}, where the $\dot{M}$ was estimated by using the planet as a probe for the stellar wind Vidotto & Bourrier 2017) with the magnetic topology being a possible factor for the scatter.

While extremely useful, the search for astrospherical absorption is influenced by a number of critical factors. For instance, this method is strongly dependent on the relative velocity of the stellar rest frame and the ISM flow velocity ($V_{\rm ISM}$). As well as on the angle, θ, between the upwind direction of the ISM flow and the line-of-sight to the star (Wood et al., 2021). It also requires prior knowledge of the properties of the ISM such as the density and its ionization state (Wood et al. 2005; Redfield & Linsky 2008). Finally, its applicability is limited to relatively nearby stars ($\lesssim 15$ pc) due to the absorption of the ISM.

Due to the scarcity of observational data and associated limitations, numerical simulations can be used to improve our understanding of stellar winds. Models based on Alfvén waves are more commonly used to simulate the stellar wind from stars other than the Sun (Suzuki & Inutsuka, 2006). This is because these waves are considered to be key mechanism for heating and accelerating the solar wind (van der Holst et al. 2014; Van Doorsselaere et al. 2020).

In this study, we present a detailed numerical characterization of the stellar wind properties of cool main-sequence stars (early F to M dwarfs) covering a range of rotation rates and magnetic field strengths. We compute steady-state stellar wind solutions using a state-of-the-art 3D MHD model and provide consistent qualitative and quantitative comparisons. Our goal is to better understand the different stellar wind properties as a function of the driving parameters, allowing us to explore the expected stellar wind conditions in the circumstellar region around planet-hosting stars.

This paper is organized as follows: Section 7.2 describes the numerical model and properties of the selected stellar sample. In Sect. 7.3, we present our numerical results, discuss the derived trends in

the stellar wind properties, and compare our results with observations. This information is then used to quantify the stellar wind conditions and explore their implications in the context of the classical habitable zone (HZ) around cool main-sequence stars. Conclusions and summary are provided in Sect. 7.4.

7.2 Model description

We simulate stellar winds in cool main-sequence stars using the state-of-the-art Space Weather Modeling Framework (SWMF; Sokolov et al. 2013; van der Holst et al. 2014; Gombosi et al. 2018). The SWMF is a set of physics-based models (from the solar corona to the outer edge of the heliosphere) that can be run independently or in conjunction with each other (Tóth et al., 2012).

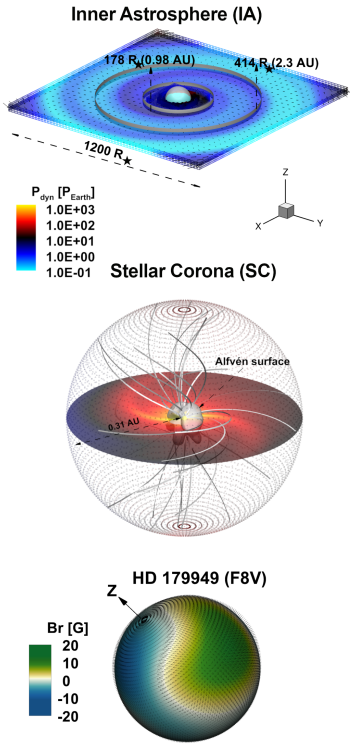

Figure 7.1: Simulated stellar wind environment for HD 179949 including multi-domain models. The bottom panel contains the surface field distribution (in Gauss) provided by the ZDI map and used to drive the AWSoM solution within the stellar corona (SC) domain (middle panel). The blue-green color bar represents the radial magnetic field strength on the stellar surface. Within SC, the gray iso-surface corresponds to the Alfvén surface of the stellar wind (see Sect. 7.3.1). Selected magnetic field lines are shown in white. The steady-state solution is propagated from the coupling region (62 - 67R$_\star$) to the entire Inner Astrosphere (IA) domain (1200 R$_\star$ in each cartesian direction; upper panel). The central gray sphere in the top panel denotes the boundary of IA with the SC domain at 67 $R_\star$. This domain contains the inner and outer edges of the habitable zone (gray circles). Color-coded (top and middle panel) is the wind dynamic pressure ($P_{\rm dyn} = \rho U^2$), normalized to the nominal Sun-Earth value ($\simeq$ 1.5 nPa), visualized on the equatorial plane of both domains. The z-axis indicates the assumed stellar rotation axis of the star.

This model uses the numerical schemes of the Block Adaptive Tree Solar Roe-Type Upwind Scheme (BATS-R-US; Powell et al. 1999) MHD solver. For a detailed description of the model, see Gombosi et al. (2021). The multi-domain solution starts with a calculation using the Solar/Stellar Corona (SC) module which incorporates the Alfvén Wave Solar Model (AWSoM; van der Holst et al. 2014). This module provides a description of the coronal structure and the stellar wind acceleration region. The

simulation is then coupled to a second module known as the Inner Heliosphere/Astrosphere[1] (IA). In this way, it is possible to propagate the stellar wind solution up to Earth's orbit and beyond. The model has been extensively validated and updated employing remote sensing as well as in-situ solar data (e.g., Oran et al. 2017; Sachdeva et al. 2019; van der Holst et al. 2019).

AWSoM is driven by photospheric magnetic field data, which is normally available for the Sun in the form of synoptic magnetograms (Riley et al., 2014). A potential field source surface method is used to calculate the initial magnetic field (more details in the following section). This information is used by AWSoM to account for heating and radiative cooling effects, as well as the Poynting flux entering the corona, and empirical turbulent dissipation length scales. With the interplay between the magnetic field distribution, the extrapolation of the potential field, and the thermodynamic properties, the model solves the non-ideal magnetohydrodynamic (MHD) equations for the mass conservation, magnetic field induction, energy (coronal heating), and momentum (acceleration of the stellar wind). These last two aspects are controlled by Alfvén waves propagating along and against the magnetic field lines (depending on the polarity of the field). In the momentum equation, the heat and acceleration contributions are coupled by an additional term for the total pressure and a source term in the energy equation. The numerical implementation is described in detail in van der Holst et al. (2014). Once these conditions are provided, the simulation evolves all equations locally until a global steady-state solution is reached.

7.2.1.Simulation parameters and setup

In our work, we apply the SWMF/AWSoM model to main-sequence F, G, K, and M-type stars by assuming that their stellar winds are driven by the same process as the solar wind. We analyze the properties of the stellar wind by a coupled simulation covering the region of the stellar corona (SC, spherical) and the resulting structure within the inner astrosphere (IA, cartesian). Figure 7.1 illustrates the coupling procedure in one of our models. This coupling was necessary only in the case of F, G, and K stars, in order to completely cover the habitable zones (HZ)[2], which are larger and farther away from the star. Parameters such as stellar radius ($R_\star$), mass ($M_\star$), and rotation period ($P_{\rm rot}$), are also taken into account in the simulations. We followed the approach in Kopparapu et al. (2014) in order to determine the optimistic HZs boundaries of each star in our sample.

Simulation domain

The star is positioned in the center of the SC spherical domain. The radial coordinate in SC ranges from 1.05 $R_\star$ to 67 $R_\star$, except for M dwarfs, where it extends to 250 $R_\star$. The choice of the outer edge value of the SC domain was chosen in a way to obtain both edges of the HZ in one domain. The habitable zones limits were calculated using Kopparapu et al. (2014) approach and the reported measured $L_\star$ and $T_{\rm eff}$ for each star in our sample (see Table 7.1). As will be discussed in Sect. 7.3, in the case of M dwarfs, the extension had to be performed in order to cover the entire Alfvén surface (AS)[3], while keeping the default parameters for AWSoM fixed (see Sect. 7.2.1). The domain uses a radially stretched grid with the cartesian z-axis aligned with the rotation axis. The cell sizes in the meridional (ϕ) and azimuthal (θ) directions are fixed at $\sim 2.8°$. The total number of cells in the SC domain is $\sim 8 \times 10^5$.

The steady-state solutions obtained within the SC module are then used as inner boundary conditions for the IA component. An overlap of 5 $R_\star$ (from 62 $R_\star$ to 67 $R_\star$) is used in the coupling procedure between the two domains for F, G, and K stars (more details on the necessity of the overlap when coupling between domains can be found in Tóth et al. 2005). The IA is a cube that extends from 62 $R_\star$ to 600 $R_\star$ in each cartesian component. Adaptive Mesh refinement (AMR) is performed within IA, with the smallest grid cell size of ~ 1.17 $R_\star$ increasing up to 9.37 $R_\star$ with a total of 3.9 million cells. As the simulation evolves, the stellar wind solution is advected from SC into the larger IA domain where the local conditions are calculated in the ideal MHD regime.

[1] This module is formally labeled IH within the SWMF, but since we are working with low-mass main sequence stars, we will refer to it as the Inner Astrosphere (IA) domain.

[2] The range of orbits around a star in which an Earth-like planet can sustain liquid water on its surface.

[3] This structure sets the boundary between the escaping wind and the magnetically coupled outflows that do not carry angular momentum away from the star.

Magnetic boundary conditions

In the initial condition of the simulation, observations are used to set the radial component of the magnetic field B_r [G] anchored at the base of the wind (at the inner boundary). As mentioned earlier, a finite potential field extrapolation procedure is carried out to obtain the initial configuration of the magnetic field throughout SC (Tóth, van der Holst, & Huang, 2011). This procedure requires setting an outer boundary (source surface, r_s), beyond which the magnetic field can be considered to be purely radial and force-free. The magnetic field can therefore be described as a gradient of a scalar potential and determined by solving Laplace's equation in the domain. For the simulations discussed here, we set r_s at 45% of the SC domain size for F, G, and K stars, and 70% for M dwarfs. While the choice of this parameter does not alter significantly the converged solutions, it can modify the required run time of each model to achieve convergence. Therefore, our selection was done to guarantee convergence to the steady-state in a comparable number of iterations between all spectral types.

The stellar magnetic field as reconstructed from Zeeman Doppler Imaging (ZDI)[4], is used as the inner boundary condition of SC (Fig. 7.2). Therefore, the resulting wind solutions are more realistic than models based on simplified/idealized field geometries (Chebly, Alvarado-Gómez, & Poppenhaeger, 2022). Although the reconstructed maps provide the distribution of vector magnetic fields, we use only the radial component of the observed surface field. The magnetogram is then converted into a series of spherical harmonic coefficients with a resolution similar to that of the original map. The order of the spherical harmonics should be chosen so that artifacts such as the "ringing" effect do not appear in the solution (Tóth, van der Holst, & Huang, 2011). In our models, we performed the spherical harmonics expansion up to $l_{\max} = 5$.

Input parameters

After we set the initial conditions, we define several parameters for the inner boundary. In order to reduce the degree of freedom of the parameter set, we only modify the parameters related to the properties of the stars, such as mass, rotation period, and radius. As for the other parameters, we implement the same values that are commonly used in the solar case (van der Holst et al. 2014; Sachdeva et al. 2019). The Poynting flux ($S/B_\star = 1.1 \times 10^6$ J m^{-2} s^{-1} T) is a parameter that determines the amount of wave energy provided at the base of a coronal magnetic field line. The other parameter is the proportionality constant that controls the dissipation of Alfvén wave energy into the coronal plasma and is also known as the correlation length of Alfvén waves ($L_\perp = 1.5 \times 10^5$ m $\sqrt{\mathrm{T}}$). We use the values given in Sokolov et al. (2013) to define the base temperature ($T_o = 2 \times 10^6 K$) and the base density ($n_o = 2 \times 10^{11} \mathrm{cm}^{-3}$).

We note that the choice of these parameters will affect the simulation results, as reported in several studies that followed different approaches (e.g., Boro Saikia et al. 2020; Jivani et al. 2023). Recently, Jivani et al. (2023) performed a global sensitivity analysis to quantify the contributions of model parameter uncertainty to the variance of solar wind speed and density at 1 au. They found that the most important parameters were the photospheric magnetic field strength, $S/B_\star$, and $L_\perp$. Furthermore, in Boro Saikia et al. (2020), an increase in the mass loss rate ($\dot{M}_\star$), and angular momentum loss rate ($\dot{J}_\star$) was reported when $S/B_\star$ is increased from the solar value to 2.0×10^6 J m^{-2} s^{-1} T), which is expected because $S/B_\star$ drives the energy of the Alfvén wave, resulting in higher $\dot{M}_\star$ and $\dot{J}_\star$.

In this work, however, we are interested in isolating the expected dependencies with the relevant stellar properties (e.g., mass, radius, rotation period, photospheric magnetic field) which can only be analyzed consistently if the AWSoM related parameters are kept fixed between spectral types. Moreover, as will be discussed in detail in Sect. 7.3.3, the results obtained using the standard AWSoM settings are either consistent with current stellar wind observational constraints for different types of stars or the apparent differences can be understood in terms of other physical factors or assumptions made in the observations. For these reasons, we have chosen not to alter these parameters in this study, which also reduces the degrees of freedom in our models.

[4] A tomographic imaging technique that allows the reconstruction of the large-scale magnetic field (strength and polarity at the star's surface from a series of polarized spectra (see e.g., Donati et al. 2006; Morin et al. 2008; Fares et al. 2009; Alvarado-Gómez et al. 2015; Hussain et al. 2016; Kochukhov & Piskunov 2002).

7.2.2.The sample of stars

Our investigation is focused on main sequence stars, with effective temperatures ranging from 6500 K down to 3030 K, and masses $M_\star < 1.34\ M_\odot$ (spectral types F to M). All of these stars are either fully or partially convective. We use a sample of 21 stars whose large-scale photospheric magnetic fields were reconstructed with ZDI (See et al. 2019 and references therein). Some of these stars were observed at different epochs. In this case, the ZDI map with the best phase coverage, signal-to-noise ratio, and most spectra used in the reconstruction was chosen. The sample includes radial magnetic field

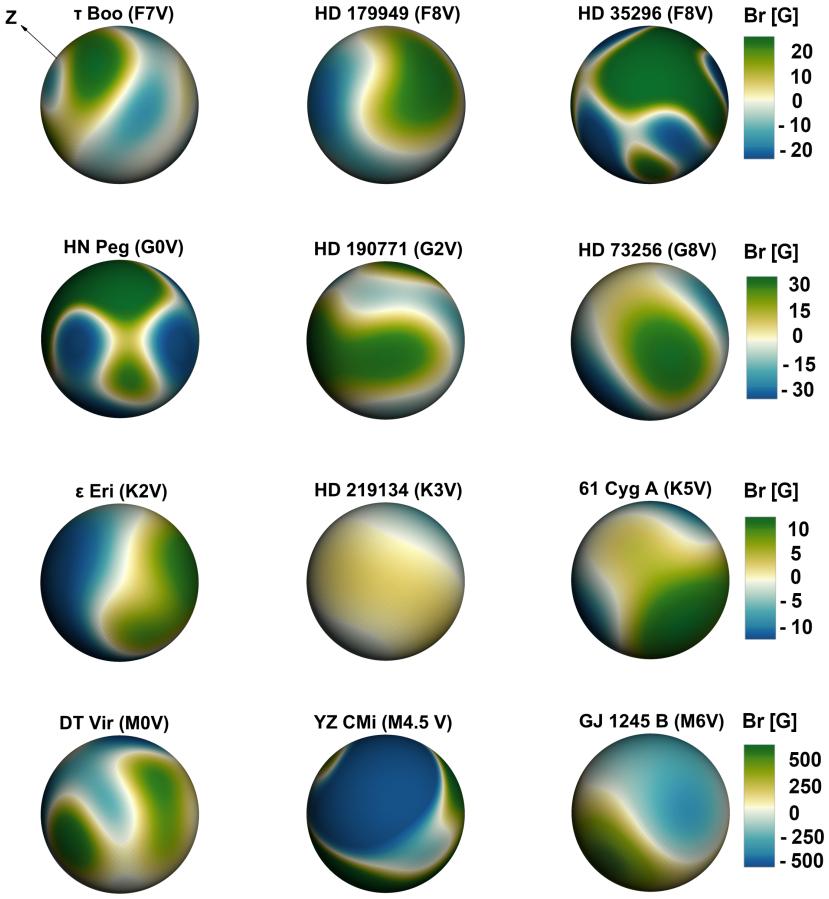

Figure 7.2: Examples of surface field distribution (in Gauss) of our sample stars retrieved from ZDI maps. The rows represent different spectral types going from late F-(top) to M dwarfs (bottom) as indicated. The color-code represents the normalized radial magnetic field for a given row. The z-axis indicates the assumed stellar rotation axis for all the stars in the panel. The slowest rotation in our sample of 21 stars is HD 219134 (K3V, $P_{\rm rot} = 42.2$ d), and the fastest is GJ 1245 B (M6V, $P_{\rm rot} = 0.71$ d). The radial magnetic field strength ranges from 5 G to 1.5 kG.

strengths in the ZDI reconstruction between 5 G and 1.5 kG corresponding to HD 130322 (K0V) and EV Lac (M3.5V), respectively. Spectral types range from F7 (τ Boo, $M_\star = 1.34\ M_\odot$, $R_\star = 1.46\ R_\odot$) to M6 (GJ 1245 B, $M_\star = 0.12\ M_\odot$, $R_\star = 0.14\ R_\odot$). The rotation periods vary between fractions of a day to tens of days, with GJ 1245 B (M6V) having the shortest rotation period ($P_{\rm rot} = 0.71$ d) and HD 219134 (K3V) the longest one ($P_{\rm rot} = 42.2$ d). Table 7.1 contains the complete list of the sample stars and a summary of the stellar properties incorporated in our models.

7.3 Results & Discussion

Table 7.1: Fundamental parameters of our sample. Columns 1–8 list the star number, name, spectral type (SpT), stellar mass ($M_\star$), stellar radius ($R_\star$), rotation period ($P_{\rm rot}$), effective temperature ($T_{\rm eff}$), and luminosity, respectively (See et al. 2019 and references therein).

ID number	Star	SpT	$M_\star$ [$M_\odot$]	$R_\star$ [$R_\odot$]	$P_{\rm rot}$ [d]	$T_{\rm eff}$ [K]	$L_\star$ [$L_\odot$]
1	τ Boo	F7V	1.34	1.46	3	6387	3.0
2	HD 179949	F8V	1.21	1.19	7.6	6168	1.80
3	HD 35296	F8V	1.06	1.1	3.48	6202	1.60
4	HN Peg	G0V	1.1	1.04	4.55	5974	1.20
5	HD 190771	G2V	1.06	1.01	8.8	5834 ± 50	0.99
6	TYC 1987-509-1	G7V	0.9	0.83	9.43	5550†	0.52 ± 0.03
7	HD 73256	G8V	1.05	0.89	14	5480†	0.72
8	HD 130322	K0V	0.79	0.83	26.1	5400 †	0.5
9	HD 6569	K1V	0.85	0.76	7.13	5170	0.36 ± 0.01
10	ϵ Eri	K2V	0.85	0.72	11	5125 ± 87	0.3 ± 0.06
11	HD 189733	K2V	0.82	0.76	12.5	4939	0.34
12	HD 219134	K3V	0.81	0.78	42.2	4835 †	0.27
13	TYC 6878-0195-1	K4V	0.65‡	0.64‡	5.72	4600†	0.8 ± 0.32
14	61 Cyg A	K5V	0.66	0.62	34.2	4655 †	0.15
15	HIP 12545	K6V	0.58‡	0.57‡	4.83	4300 †	0.4 ± 0.06
16	TYC 6349-0200-1	K7V	0.54‡	0.54‡	3.39	4100†	0.3 ± 0.02
17	DT Vir	M0V	0.59	0.53	2.85	3850†	0.055
18	GJ 205	M1.5V	0.63	0.55	33.6	3690†	0.061± 0.006
19	EV Lac	M3.5V	0.32	0.3	4.37	3267	0.013
20	YZ CMi	M4.5V	0.32	0.29	2.77	3129	0.012
21	GJ 1245 B	M6V	0.12	0.14	0.71	3030§	0.0016

‡ Reference from Vidotto et al. (2014)
† Reference from Pecaut & Mamajek (2013)
§ Reference from Vidotto et al. (2013)

7.3.1.The effect of star properties on the wind structure

The Alfvén surface (AS) is defined by the collection of points in the 3D space that fulfils the Alfvén radius criterion[5]. Numerically, it is determined by finding the surface for which the wind velocity reaches the local Alfvén velocity, $v_A = B/\sqrt{4\pi\rho}$, where B and ρ are the local magnetic field and plasma density, respectively. The Alfvén surface can be interpreted as the lever arm of the wind torque –the "position" at which the torque acts to change the angular rotation of the star[6]. The Alfvén Surface is used in numerical models to characterize ($\dot{M}_\star$) and ($\dot{J}_\star$) (e.g., Vidotto et al. 2015; Boro Saikia et al. 2020; Garraffo, Drake, & Cohen 2015; Alvarado-Gómez et al. 2016). We compute $\dot{J}_\star$ by performing a scalar flow rate integration over the AS and another one over a closed spherical surface (S) beyond the AS to determine $\dot{M}_\star$:

$$\dot{M}_\star = \int_S \rho(\mathbf{u}\cdot\mathbf{dA}) \tag{7.1}$$

$$\dot{J}_\star = \int_{AS} \Omega\rho \mathrm{R}^2 \sin^2\theta(\mathbf{u}\cdot\mathbf{dA}) \tag{7.2}$$

Here $\dot{J}_\star$ is the component of the change in angular momentum in the direction of the axis of rotation. The distance to the Alfvén surface is represented by R. The angle between the lever arm and the rotation axis is denoted by θ, which depends on the shape/orientation of the AS with respect to the rotation axis (and accounted for in the surface integral). The stellar angular velocity is represented by $\Omega = 2\pi/\mathrm{P}_{\rm rot}$. The surface element is denoted by $\mathbf{dA}$.

Figure 7.3 shows the AS of the stellar wind, with plasma streamers along with the equatorial section flooded with the wind velocity ($U_{\rm r}$) for three K stars in our sample (HIP 12545, HD 6569, 61 Cyg A). If we compare two stars with similar $P_{\rm rot}$ but different $B_{\rm R}^{\rm max}$, we can clearly see that the size of AS increases with increasing magnetic field strength. This is a direct consequence of the dependence of the Alfvén velocity on these quantities (Eq. 7.1) and the distance from the star at which the Alfvén

[5]The Alfvén radius ($R_{\rm A}$) is defined as the distance around a star at which the kinetic energy density of the stellar wind equals the energy density of the astrospheric magnetic field.

[6]In other words, the angular momentum per unit mass within the stellar wind can be computed as if there were solid body rotation, at an angular velocity $\Omega_\star = 2\pi/P_{\rm rot}$, out as far as the Alfvén surface.

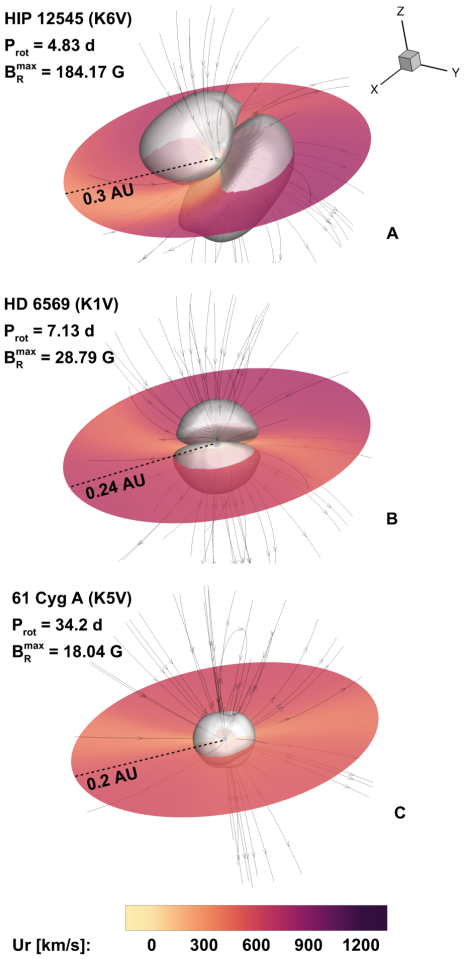

Figure 7.3: Simulation results in the SC domain for 3 K stars: HD 12545 (panel A), HD 6569 (panel B), 61 Cyg A (panel C) driven by ZDI magnetic field maps. All panels contain the projection onto the equatorial plane ($z = 0$) of the radial wind velocity (U_r).The translucent gray shade denotes the Alfvén surface calculated from the steady-state solution. The corresponding color scale U_r is preserved among the different panels. Selected 3D magnetic field lines are shown in black. The absolute size of the SC domain is indicated in each case.

velocity is exceeded by the wind. For instance, for very active stars with stronger magnetic fields, the expected coronal Alfvén velocity is greater than for less active stars, increasing the radial distance that the wind velocity must travel to reach the Alfvén velocity. The associated Alfvén surface has a characteristic two-lobe configuration (Fig. 7.3, gray translucent area), with average sizes of 27 $R_\star$, 18 $R_\star$ and 13 $\mathrm{R}_\star$ for HIP 12545, HD 6569, and 61 Cyg A, respectively (see Table 7.2).

When we compare two stars with similar magnetic field strengths but different P_rot (see Fig. 7.3, panels B and C), the change in AS size is not as dramatic. The rotation period has primarily a geometric effect on the resulting AS. The Alfvén surface assumes a different tilt angle in all three cases. This tilt is mainly connected to the open magnetic field flux distribution on the star's surface (Garraffo, Drake, & Cohen, 2015). We also notice in Fig. 7.3 that the stellar wind distribution is mainly bipolar with a relatively fast component reaching up to $\sim$891 km s^{-1} for HIP 12545 $\sim$, 702 km s^{-1} for HD 6569, and $\sim$593 km s^{-1} for 61 Cyg A. In section 7.3.3 we will discuss further the relation between the wind velocity with regard to P_rot and B_R.

Figure 7.4 shows the $\dot{M}_\star$, $\dot{J}_\star$, $\overline{AS}$ as estimated by the previously described method, against the sub-spectral type of our star sample (left column) and the average radial magnetic field strength ($B_\mathrm{R}^\mathrm{avg}$, right column). Similar relations have been obtained for the maximum radial magnetic field strength and are presented in Appendix 7.5.1. The average Alfvén surface size was calculated by performing a mean integral over the radius at each point of the 3D AS. The extracted quantities are represented by different colors and symbols for each spectral type (F, G, K, and M).

As expected, the AS increases as we move toward more magnetically active stars (Fig. 7.4, top-right panel). From our simulations, we were able to establish a relation between AS and $B_\mathrm{R}^\mathrm{avg}$ using the bootstrap technique (1000 realizations) to find the mean of the slope and the intercept along with their uncertainties. We use this approach to determine all relations from our simulations. The relation

is as follows:

$$\log \overline{AS_{\rm R}} = (0.42 \pm 0.06) \log B_{\rm R}^{\rm avg} + (0.71 \pm 0.07) \tag{7.3}$$

Our simulated steady-state $\dot{M}_\star$ show a scatter within the range [0.5 $\dot{M}_\odot/R_\odot^2$, 30 $\dot{M}_\odot/R_\odot^2$], which is comparable to that estimated from the observed Lyα absorption method of G, K, and M dwarfs in Wood et al. (2021). The variations in $\dot{M}_\star$ are related to differences in the strength and topology of the magnetic field driving the simulations (see Alvarado-Gómez et al. 2016; Vidotto et al. 2016; Evensberget et al. 2022), as well as to the Alfvén wave energy transfer to the corona and wind implemented in the model (Boro Saikia et al. 2020; Jivani et al. 2023). For this reason, we tried to isolate the effects introduced by the star (e.g., $M_\star$, $R_\star$, $P_{\rm rot}$, magnetic field strength) over the ones from the Alfvén wave heating (i.e., $n_{\rm o}$, $T_{\rm o}$, $S/B_\star$, $L_\perp$).

In terms of mass loss rate, stronger winds are expected to be generated by stronger magnetic fields (see Fig. 7.4) implying that the winds are either faster or denser. This interplay determines $\dot{M}_\star$ (Eq. 7.1), which increases with increasing magnetic field strength regardless of spectral type. We see a common increase for F, G, K, and M dwarfs (excluding EV Lac) in the saturated and unsaturated regime that can be defined from the simulations as follows:

$$\log \dot{M}_\star/R_\star^2 = (0.48 \pm 0.09) \log B_{\rm R}^{\rm avg} + (0.11 \pm 0.10) \tag{7.4}$$

On the other hand, we observe a slightly different behavior for M dwarfs, whose $\dot{M}_\star$ and $\dot{J}_\star$ values tend to be lower. As discussed by Garraffo et al. (2018), the magnetic field complexity could also affect $\dot{M}_\star$ for a given field strength. We consider this possibility in the following section. Note that, as has been shown in previous stellar wind studies of M dwarfs (e.g., Garraffo et al. 2017; Kavanagh et al. 2021; Alvarado-Gómez et al. 2022), modifications to the base AWSoM parameters (either in terms of the Poynting flux or the Alfvén wave correlation length) would lead to strong variations in $\dot{M}_\star$. This would permit placing the M dwarfs along the general trend of the other spectral types in particular, the $\dot{M}_\star$ value obtained for the star with the strongest $B_{\rm R}$ in our sample (EV Lac). While these modifications have physical motivations behind them (i.e. increased chromospheric activity, stronger surface magnetic fields), in most regards, they remain unconstrained observationally. Furthermore, the values we obtain in our fiducial AWSoM models are still within the range of observational estimates available for this spectral type (see Sect. 7.3.3), with the added benefit of minimizing the degrees of freedom and isolating the effects of the stellar parameters on the results.

Similarly, we see a large scatter of $\dot{J}_\star$ with respect to the spectral type (Fig. 7.4, bottom left column), ranging from 10^{26} g cm^2 s^{-2} to 10^{31} g cm^2 s^{-2}. This range is within the expected $\dot{J}_\star$ values estimated for cool stars with the lowest value corresponding to M dwarfs (See et al. 2019 and references therein). The maximum $\dot{J}_\star$ values reached in our simulations are comparable to $\dot{J}_\odot$ reached at solar minimum and maximum (7×10^{30} and 10×10^{30} g.cm^{2}s^{-2}, Finley & Matt 2018; Boro Saikia et al. 2020). We note that this is the only parameter for which we have retained units in absolute values (as is commonly done in solar/stellar wind studies; see Cohen et al. 2010; Garraffo, Drake, & Cohen 2015; Finley & Matt 2018). Using absolute units, we expect a decrease in $\dot{J}_\star$ as we move from F to M dwarfs, since $\dot{J}_\star$ is a function of R^2 (Eq. 7.2). The scatter around this trend is dominated by the relatively small $\dot{M}_\star$ values, the distribution of $\Omega_\star$ in our sample (variations up to a factor of 5), and the equatorial AS size where the maximum torque is applied ($\sin\theta$ in Eq. 7.2).

We also note that the sample is biased toward weaker magnetic field strengths. To better estimate how the magnetic field affects the properties of the stellar winds, we need a larger sample, not only in terms of stellar properties but also with stellar wind constraints such as $\dot{M}_\star$. The latter is so far the only stellar wind observable parameter for which comparisons can be made. For this reason, we will focus on the behavior of the $\dot{M}_\star$ as a function of different stellar properties in the following sections of the analysis.

7.3.2.Stellar mass-loss rate and complexity

Coronal X-ray luminosity is a good indicator of the level of magnetic activity of a star and the amount of material heated to 10^6 K temperatures. The dependence of magnetic activity on dynamo action (i.e., dynamo number $D = R_{\rm o}^{-2}$, Charbonneau 2020) has led a number of authors to use the Rossby number to characterize stellar activity, for a wide range of stellar types (Wright et al., 2011). The

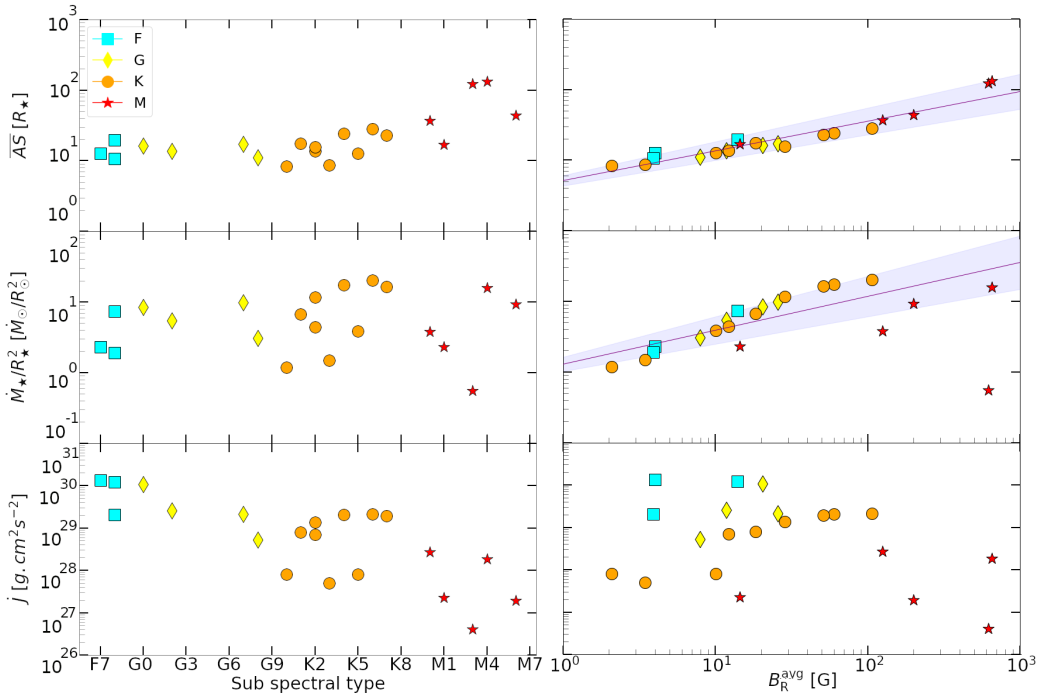

Figure 7.4: Simulated average Alfvén surface ($\overline{AS}$, top), mass loss rate per unit surface area ($\dot{M}_\star/R_\star^2$, middle), and angular momentum loss rate ($\dot{J}$, bottom) as a function of the spectral type (left) and the surface-average radial magnetic field (B_R^{avg}, right). The mass loss rate is expressed in units of the average solar values ($\dot{M}_\odot = 2 \times 10^{-14}\ M_\odot\ \mathrm{yr}^{-1} = 1.265 \times 10^{12}\ \mathrm{g\ s}^{-1}$), normalized to the surface area of each star ($A_\star = 4\pi R_\star^2$). Individual points denote the results of each simulation presented in Sect. 7.3, Table 7.2. The different symbols and colors represent the spectral types (F, cyan/squares; G, yellow/diamonds; K, orange/circles; M, red/star). The purple line and shaded area represent the fitted power-law with its uncertainties.

Rossby number is defined as $R_o = P_{rot}/\tau_c$, where P_{rot} is the stellar rotation period and τ_c is the convective turnover time (Noyes et al. 1984; Jordan & Montesinos 1991; Wright et al. 2011). We adopted the approach of Wright et al. (2018) to calculate τ_c. In this case, the latter is only a function of the stellar mass ($M_\star$):

$$\log \tau_c = 2.33 - 1.50(M_\star/M_\odot) + 0.31(M_\star/M_\odot)^2 \tag{7.5}$$

As it was mentioned in Sect. 7.1, the study of Wood et al. (2021) suggests that coronal activity increases with $\dot{M}_\star$. The overall increase in $\dot{M}_\star$ with X-ray flux F_X ($\dot{M}_\star \propto F_X^{0.77\pm0.04}$), is most likely due to their dependence on magnetic field strength (see Sect. 7.3.1). However, they report a scatter of about two orders of magnitude of $\dot{M}_\star$ around the trend line. This suggests that coronal activity and spectral type alone do not determine wind properties. The geometry of the magnetic field may also play a role.

The correlation between $\dot{M}_\star$ and magnetic complexity has already been suggested by Garraffo, Drake, & Cohen (2015), which could in principle contribute to the scatter in (Wood et al. 2021, Fig. 10). The large-scale distribution of the magnetic field on the stellar surface is mainly determined by the rotation period and the mass of the star, namely R_o (Morin et al. 2010; **?**; Garraffo et al. 2018). The Rossby number was used to determine the complexity function in Garraffo et al. (2018), which was able to reproduce the bimodal rotational morphology observed in young open clusters (OCs). The complexity function of Garraffo et al. (2018) is defined as

$$n = \frac{a}{R_o} + 1 + bR_o. \tag{7.6}$$

The constant 1 reflects a pure dipole. The coefficients a = 0.02 and b = 2 are determined from observations of OCs. The first term is derived from the ZDI map observation of stars with different

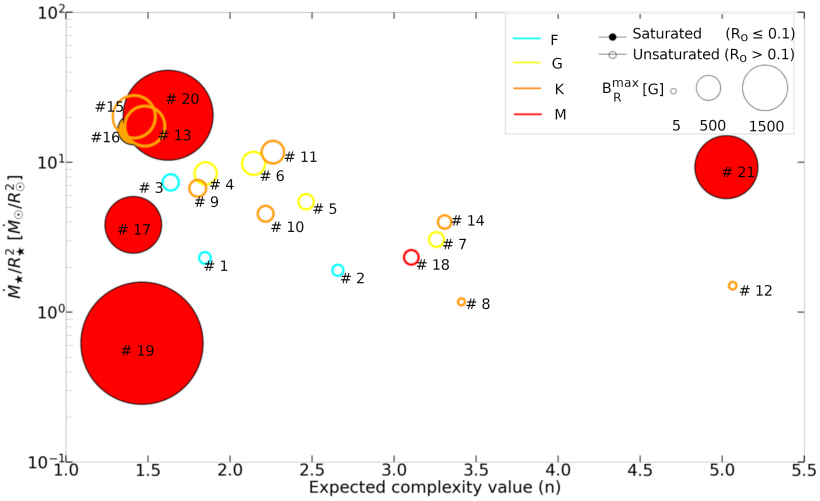

Figure 7.5: Simulated mass loss rate ($\dot{M}_\star/R_\star^2$) versus the expected complexity value (n, Garraffo et al. 2018) given the Rossby number (R_o) of each star. The mass loss rate is expressed in solar units, normalized by the unit surface area of each star. Individual points denote the results of each simulation presented in Sect. 3 (Table 7.2). The different colors (cyan, orange, yellow, red) represent the different spectral types respectively (F, G, K, and M). The filled circles and the empty ones represent stars in the saturated and unsaturated regimes, respectively. The symbol size denotes the maximum magnetic field strength (B_R^{max}) in each case. The numbers refer to the ID of the star in our sample. The complexity value n = 1 corresponds to the dipole, and n increases as we move to the right.

spectral types and rotation periods. The third term is motivated by Kepler's observations of old stars (van Saders et al., 2016; van Saders, Pinsonneault, & Barbieri, 2019).

We emphasize that the complexity number (n), estimated from Eq. 7.6, differs from the complexity derived from the ZDI maps themselves (e.g., Garraffo et al. 2022). The complexity number from R_o is expected to be higher. This is due to the fact that many of the small-scale details of the magnetic field are not captured by ZDI.

We expect to lose even more information about the complexity of the field given that the ZDI maps are not really available to the community (apart from the published images). Image-to-data transformation techniques (which we applied to extract the relevant magnetic field information from the published maps) can lead to some losses of information, both spatially and in magnetic field resolution. These vary depending on the grid and the projection used to present the ZDI reconstructions (i.e., Mercator, flattened-polar, Mollweide). Using the star's raw ZDI map would prevent these issues and would aid with the reproducibility of the simulation results.

Finally, note that the expected complexity is also independent of the spherical harmonic expansion order used to parse the ZDI information to the simulations. The obtained R_o and n values for each star in our sample are listed in Table 7.2.

Figure 7.5 shows the behaviour of coronal activity and $\dot{M}_\star$ with respect to the expected magnetic field complexity (n). The coronal activity is denoted by full and empty symbols corresponding to saturated and unsaturated stars, respectively. We consider stars with $R_o \leq 0.1$ in the saturated regime and stars with $R_o > 0.1$ in the unsaturated regime based on X-ray observations (Pizzolato et al. 2003; Wright et al. 2011; Stelzer et al. 2016; Wright & Drake 2016; Wright et al. 2018). The colors correspond to the different spectral types, whereas the numbers indicate the ID of each star in our sample. The symbol size represents the maximum radial magnetic field strength of each star extracted from the ZDI observations.

We anticipate seeing a trend in which the $\dot{M}_\star$ decreases as the magnetic field complexity increases (leading to an increment of closed loops on the stellar corona), for stars in saturated and unsaturated regimes. For instance, ϵ Eri (#10, B_R^{max} = 25 G, n = 2.21724) has an $\dot{M}_\star$ = 4.53 $\dot{M}_\odot/R_\odot^2$ lower than HD 6569 (#9, B_R^{max} = 29 G, n = 1.80346) with $\dot{M}_\star$ = 6.70 $\dot{M}_\odot/R_\odot^2$. This is also true for τ Boo and HD 179949 where τ Boo (#1, B_R^{max} = 14 G, n = 1.84728, $\dot{M}_\star$ = 2.30 $\dot{M}_\odot/R_\odot^2$) has a higher $\dot{M}_\star$

compared to HD 179949 (#2, $B_{\rm R}^{\rm max} = 12$ G, n = 2.65746, $\dot{M}_\bigstar = 1.90\ \dot{M}_\odot/R_\odot^2$).

We also noticed that as we go to more active stars, like in the case of M dwarfs, the field strength starts to dominate over the complexity in terms of contribution to the $\dot{M}_\bigstar$. For example, GJ 1245 B (#21, $B_{\rm R}^{\rm max} = 404$ G , n = 5.02602 , $\dot{M}_\bigstar = 9.27\ \dot{M}_\odot/R_\odot^2$) has an $\dot{M}_\bigstar$ higher than DT Vir even though the complexity of the former is almost 5 times higher (DT Vir, #17, $B_{\rm R}^{\rm max} = 327$ G, n = 1.41024, $\dot{M}_\bigstar = 3.81\ \dot{M}_\odot/R_\odot^2$). However, in order to better understand the contribution of the complexity in $\dot{M}_\bigstar$, we will need to run simulations for a wider range of stars with sufficiently high resolution of the driving magnetic field to capture directly the complexity of the field (and not estimate it from a scaling relation as it was performed here).

Moreover, our results show that whenever we have a case in which the star properties ($M_\bigstar$, $R_\bigstar$, and $P_{\rm rot}$), magnetic field strength and complexity are comparable, we end up with similar $\dot{M}_\bigstar$. This will be the case of TYC 6878-0195-1 (#13, $B_{\rm R}^{\rm max} = 162$ G, n = 1.48069, $\dot{M}_\bigstar = 17.42\ \dot{M}_\odot/R_\odot^2$) and HIP 12545 (# 15, $B_{\rm R}^{\rm max} = 184$ G, n = 1.41505, $\dot{M}_\bigstar = 20.11\ \dot{M}_\odot/R_\odot^2$).

Furthermore, two stars with similar coronal activity with respect to X-ray flux, i.e., EV Lac and YZ CMi ($F_{\rm X} \approx 10^7$ ergs cm^{-2}s^{-1}), but with slightly different magnetic field complexity, result in different wind properties: respectively $\dot{M}_\bigstar = 0.62\ \dot{M}_\odot/R_\odot^2$, and $\dot{M}_\bigstar = 20.57\ \dot{M}_\odot/R_\odot^2$. A similar situation occurs when two stars have a comparable field complexity but different coronal activity i.e., YZ CMi and GJ 205 (#18, $\dot{M}_\bigstar = 2.32\ \dot{M}_\odot/R_\odot^2$, $F_{\rm X} \approx 10^5$ ergs cm^{-2}s^{-1}).

The lowest $\dot{M}_\bigstar$ corresponds to the saturated M-dwarf EV Lac (#19), which has the strongest $B_{\rm R}$ (1517 G) and one of the simplest complexities in our sample (n = 1.46331). The low complexity of the field means that the wind is dominated by open field lines, leading to very high wind velocities in the standard AWSoM model, but with a very low density, which in turn leads to small $\dot{M}_\bigstar$ values. We remind the reader that the base density of the stellar wind is fixed at the stellar surface and is the same for all the stars in the sample (Sect. 7.2.1).

7.3.3.Stellar wind mass-loss rate and Rossby number

Table 7.2: A summary of the resulting stellar wind properties with their corresponding driving parameters. Columns 1–11, list the star number, name, mass-loss rate per unit surface area† ($\dot{M}_\bigstar/{\rm R}_\bigstar^2$), angular momentum loss rate ($\dot{J}_\bigstar$), average terminal velocity ($\overline{U_{\rm R}^{\rm 1au}}$), average terminal velocity ($\overline{U_{\rm R}^{\rm T}}$), average Alfvén surface radius ($\overline{AS}$), absolute maximum surface radial magnetic field ($|B_{\rm R}|^{\rm max}$), average surface radial magnetic field ($B_{\rm R}^{\rm avg}$), Rossby number‡ ($R_{\rm o}$), and the expected complexity number§ (n).

ID number	Name	$\dot{M}_\bigstar/R_\bigstar^2$	$\dot{J}_\bigstar$ [$g.cm^2.s^{-1}$]	$\overline{U_{\rm R}^{\rm 1au}}$ [km s^{-1}]	$\overline{U_{\rm R}^{\rm T}}$ [km s^{-1}]	$\overline{AS}$ [R$_\bigstar$]	$\lvert B_{\rm R}\rvert^{\rm max}$ [G]	$B_{\rm R}^{\rm avg}$ [G]	$R_{\rm o}$	n
1	τ Boo	2.30	1.35E+30	320	332	13	14	4.01	0.39855	1.84728
2	HD 179949	1.90	2.07E+29	345	356	11	12	3.91	0.81648	2.65746
3	HD 35296	7.33	1.20E+30	270	289	20	27	13.94	0.28396	1.63835
4	HN Peg	8.42	1.07E+30	545	549	16	50	20.48	0.40079	1.85148
5	HD 190771	5.45	2.58E+29	431	432	14	24	11.75	0.71806	2.46397
6	TYC 1987-509-1	9.82	2.11E+29	547	530	17	54	25.63	0.55388	2.14387
7	HD 73256	3.04	5.18E+28	457	458	11	22	7.91	1.12036	3.25857
8	HD 130322	1.17	8.01E+27	436	440	9	5	2.08	1.19721	3.41113
9	HD 6569	6.70	7.88E+28	704	702	18	29	18.41	0.37507	1.80346
10	ϵ Eri	4.53	6.89E+28	554	553	14	25	12.26	0.59172	2.21724
11	HD 189733	11.67	1.34E+29	535	534	16	51	28.43	0.61443	2.26141
12	HD 219134	1.50	4.97E+27	425	429	9	6	3.44	2.02732	5.06451
13	TYC 6878-0195-1	17.42	2.08E+29	734	692	24	162	60.14	0.18682	1.48069
14	61 Cyg A	3.98	7.98E+27	609	593	13	18	10.07	1.14548	3.30842
15	HIP 12545	20.11	2.13E+29	906	891	28	184	106.62	0.13145	1.41505
16	TYC 6349-0200-1	16.55	1.92E+29	657	642	23	93	51.36	0.08314	1.40684
17	DT Vir	3.81	2.67E+28	—	1102	37	327	125.08	0.07979	1.41024
18	GJ 205	2.32	2.28E+27	—	690	17	22	14.41	1.04304	3.10525
19	EV Lac	0.62	4.10E+26	—	3675	122	1517	620.21	0.05738	1.46331
20	YZ CMi	20.57	1.81E+28	—	1709	132	822	655.66	0.03637	1.62264
21	GJ 1245 B	9.27	1.90E+27	—	1164	44	404	200.43	0.00498	5.02602

† Normalized to solar units ($\dot{M}_\odot/R_\odot^2 = 1.0$).

‡ Predicted by the empirical model of Wright et al. (2011).

Using the results of our stellar winds models, we can study how the $\dot{M}_\star$ changes as a function of the Rossby number (R_o). The Rossby number is a useful quantity because it not only removes the dependence on spectral type, but also relates the rotation period to magnetic field strength, complexity, and even stellar coronal activity. The latter is also important because cool stars exhibit a well-defined behavior between L_X (or F_X) and R_o (saturated and unsaturated regimes). Thus, if we analyze $\dot{M}_\star$ using this parameter, we can see (to some extent) all dependencies simultaneously.

Figure 7.6 shows the stellar mass-loss rate per unit surface area ($\dot{M}_\star/R_\star^2$) as a function of the Rossby number (R_o). The circles show our 3D MHD numerical results, while the empty, filled, and the plus sign within a square corresponds to observational estimates of astrospheres (Wood et al., 2021), slingshot prominences (Jardine & Collier Cameron, 2019), and absorption during an exoplanetary transit (Vidotto & Bourrier, 2017), respectively. We use the same method as for the simulated stars (Eq. 7.5) to calculate the R_o of stars with constraints on their mass loss rate. Spectral types are indicated by different colors: cyan (F), yellow (G), orange (K), and red (M). The Sun is represented by a yellow star symbol. Dashed lines connect the common stars in our models and the observations. In this section, we will focus only on the resulting $\dot{M}_\star$ from the numerical results.

As was mentioned earlier, our 3D MHD simulated $\dot{M}_\star$ values are in the same range as the $\dot{M}_\star$ estimates from the Lyα astrospheric absorption method. Note that since we are only simulating steady-state stellar winds, our comparison is mostly focused on the steady mass loss $\dot{M}_\star$ (filled squares and squares with a plus sign). As such, it is not surprising that our $\dot{M}_\star$ values appear 1 - 2 orders of magnitude below the estimates associated with sporadic mass loss events such as slingshot prominences in very active stars in the saturated regime (filled squares, Jardine & Collier Cameron 2019).

Based on the relation between F_X and R_o (**?**), and the broad correlation observed between $\dot{M}_\star$ and F_X (Wood et al., 2021), we expect to see traces of a two-part trend (albeit with significant scatter) between $\dot{M}_\star$ and R_o: a flat or saturated part that is independent of stellar rotation ($R_o \lesssim 0.1$, rapidly rotating stars), and a power law showing that the stellar wind mass loss rate decreases with increasing R_o ($R_o > 0.1$, slowly rotating stars).

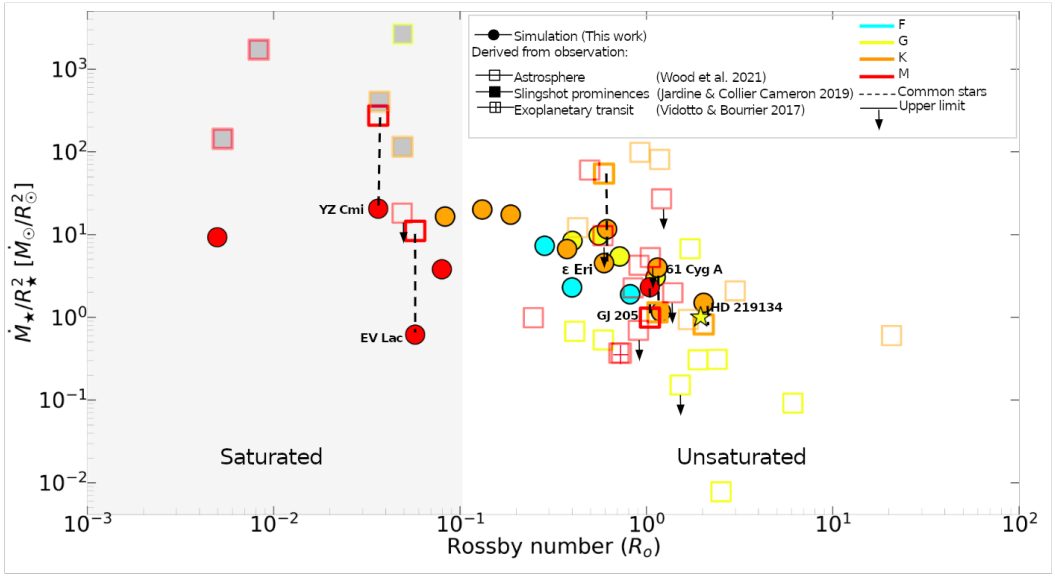

Figure 7.6: Numerical results of the stellar mass loss rate ($\dot{M}_\star/R_\star^2$, circles), astrosphere stellar mass loss rate (squares, Wood et al. 2021), slingshot prominences mass loss rate (diamonds, Jardine & Collier Cameron 2019), and absorption during an exoplanetary transit (plus within a square, Vidotto & Bourrier 2017) against the Rossby number (R_o). Colors illustrate the different spectral types: cyan (F), yellow (G), orange (K), and red (M). The Sun is represented by a star symbol. Dashed lines connect the common stars between our sample and the ones with estimated $\dot{M}_\star/R_\star^2$ values by the astrospheric Lyα absorption technique. Black arrows pointing downward correspond to the upper limits given by observations.

For stars in the unsaturated regime, we do see a trend in which $\dot{M}_\star$ increases with decreasing R_o. The relationship between $\dot{M}_\star$ and R_o retrieved from our simulations is

$$\log \dot{M}_\star / R_\star^2 = (-1.13 \pm 0.23) \log R_\mathrm{o} + (0.50 \pm 0.07). \tag{7.7}$$

The majority of the $\dot{M}_\star$ derived from observation appears to follow the established relationship $\dot{M}_\star$–R_o, with some scatter within the error range. We do, however, notice four outliers, including three K stars and one G star. The K stars with the high $\dot{M}_\star$ correspond to the binary 70 Oph A (K0V) and 70 Oph B (K5V). As for the 3$^{\mathrm{rd}}$ K star and the G star, they correspond to evolved stars: δ Eri (K0IV, $\dot{M}_\star = 0.6\ \dot{M}_\odot / R_\odot^2$, $Ro \sim$ 21) and DK UMA (G4III-I, $\dot{M}_\star = 0.0077\ \dot{M}_\odot / R_\odot^2$, $R_\mathrm{o} \sim 2.51$). We do not expect evolved stars to follow the same trend as unsaturated main sequence stars because their winds might be generated from a different mechanism (such as pulsations, see Vidotto 2021). As for 70 Oph A and B, we do not have much insight into their eruptive activity levels in order to rule out whether or not the $\dot{M}$ inferred from the astropsheric technique was influenced by slingshot prominences or CME activity.

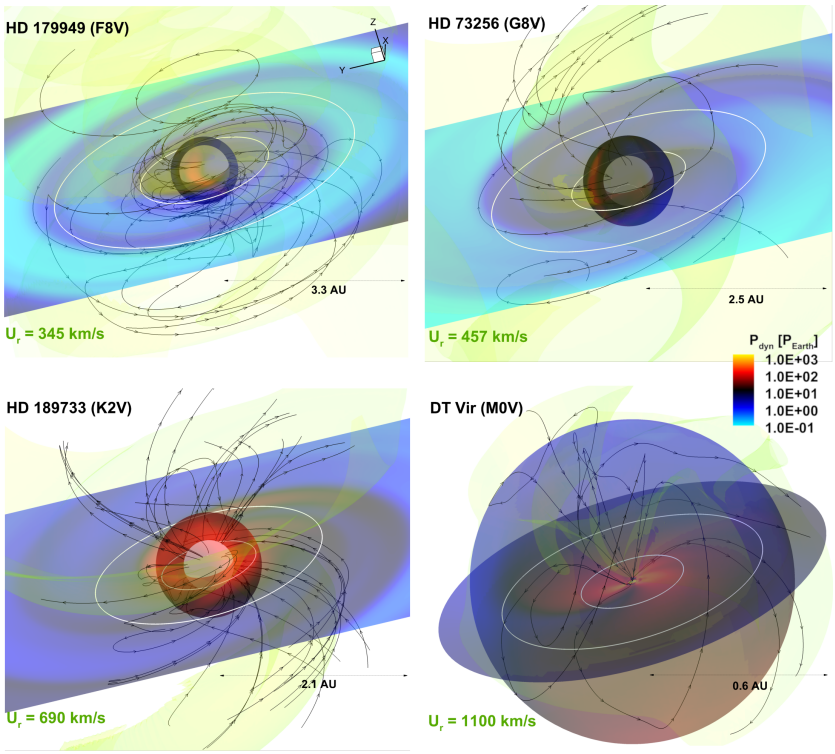

Figure 7.7: Simulated stellar wind environment for HD 179949, HD 73256, HD 189733, and DT Vir. Multi-domain models for HD 179949, HD 73256, HD 189733 are shown. The steady-state solution of the multi-domain cases is propagated from the coupling region (62 − 67 $R_\star$) to the entire IA domain (1200 R$_\star$ in each cartesian direction). The steady-state solution of DT Vir is shown in the spherical domain (SC). The green iso-surface represents the averaged wind velocity at 1 au for F, G, and K, as for M dwarfs it represents the highest averaged velocity. Color-coded is the wind dynamic pressure ($P_\mathrm{dyn} = \rho \mathrm{U}^2$) normalized to the nominal Sun-Earth value ($\sim$ 1.5 nPa), visualized on the equatorial plane of both domains and on a translucent sphere (at R = 0.5 au). Selected magnetic field lines are shown in black. The 2 white circles represent the optimistic habitable zone boundaries. The white translucent sphere represents the coupling region (67 $R_\star$) between the SC and IH domains in the case of F, G, and K stars.

As can be seen in Fig. 7.6, our numerical results in this region are essentially bracketed by the observations for which the R_o reaches larger values. The largest Rossby number from our star sample corresponds to HD 219134 (K3V, $R_\mathrm{o} = 2.02732$), which is comparable to the accepted solar value. Since our models use ZDI maps as inner boundary conditions to simulate stellar winds, this implies that ex-

tending our numerical models to even larger R_o would be very challenging as those ZDI reconstructions would require prohibitively long observing campaigns.

While we have limited data points, we see that for objects with $R_o \lesssim 0.15$, we do not obtain larger numerical values $\dot{M}_\star$ even when the magnetic field strengths increase dramatically. For example, in the case of YZ CMi ($B_R^{max} = 822$ G, $\dot{M}_\star/R_\star^2 = 20.57\ \dot{M}_\odot/R_\odot^2$) and GJ 1245 B ($B_R^{max} = 404$ G, $\dot{M}_\star = 9.27\ \dot{M}_\odot/R_\odot^2$). All stars on the left-hand side of Fig. 7.6 lie beneath the maximum $\dot{M}_\star$ value obtained for YZ CMi ($B_R^{max} = 822$ G, $\dot{M}_\star/R_\star^2 = 20.57\ \dot{M}_\odot/R_\odot^2$). This is true even when R_o varies by more than one dex, magnetic field strength by factors of 100, and the expected complexity number by ~ 4.

These results indicate that the contribution from the steady wind will only account for a small fraction of the $\dot{M}_\star$ budget in the case of very active stars. Furthermore, the obtained behaviour hints of a possible saturation of the steady-state stellar wind contribution to $\dot{M}_\star$, while the star could still lose significant mass through other mechanisms such as slingshot prominences or CME activity due to flares among others.

According to Villarreal D'Angelo, Jardine, & See (2018) and references therein, cool stars can support prominences if their magnetospheres are within the centrifugal regime (i.e. $R_K < R_A$, where $R_K = \sqrt[3]{GM_\star/\Omega_\star^2}$ is the co-rotation radius). They provide estimates for the prominence masses (m_p) and the ejection time-scales (t_p) for a sample of cool stars. According to their analysis, DT Vir would have $m_p = 1.5 \times 10^{15}$ g and $t_p = 0.1$ d, while the values for GJ 1245 B would be $m_p = 4.4 \times 10^{14}$ g, $t_p = 0.3$ d. Using these values, they also reported the expected mass loss rate from prominences for these two stars in absolute units. In order to compare with the steady state wind, we convert their results to units of $\dot{M}_\odot/R_\odot^2$. For DT Vir we have $\dot{M}_\star^p/R_\star^2 = 0.49\ \dot{M}_\odot/R_\odot^2$ and for GJ 1245 B the resulting value is $\dot{M}_\star^p/R_\star^2 = 0.68\ \dot{M}_\odot/R_\odot^2$.

For the CMEs contribution, we can obtain an order of magnitude estimate by following the approach in Odert et al. (2017). They estimate the mass-loss rate from the CME ($\dot{M}_\star^{CME}$) as a function of L_X and the power law index (α) of the flare frequency distribution. For the X-ray luminosity, we used the NEXXUS2 database, and for the flare frequency distribution exponent we took $\alpha = 2$ (Hawley et al., 2014). For DT Vir, with $\log L_X = 29.75$, we obtain $\dot{M}_\star^{CME}/R_\star^2 \sim 160\ \dot{M}_\odot/R_\odot^2$. For GJ 1245 B, with $\log L_X = 27.47$, the estimated CME-mass loss rate is $\dot{M}_\star^{CME}/R_\star^2 \sim 12.8 \dot{M}_\odot/R_\odot^2$.

We emphasize here that this approach assumes that the solar flare-CME association rate holds for very active stars (see the discussion in Drake et al. 2013). As such, it does not consider the expected influence due to CME magnetic confinement (e.g. Alvarado-Gómez et al. 2018, 2019) which currently provides the most suitable framework to understand the observed properties of stellar CME events and candidates (Moschou et al., 2019; Alvarado-Gómez et al., 2022; Leitzinger & Odert, 2022). Still, we can clearly see that the input from CMEs to the total $\dot{M}_\star$ could be higher than the steady wind and prominences for these two stars (with the latter contributing less in these cases). For instance, the estimated contribution of CMEs to the total $\dot{M}_\star$ of DT Vir is almost 40 times higher than the value obtained for the steady stellar wind. We will discuss the cases of EV Lac and YZ CMi in Section 7.3.3

Comparison between simulations and observations

In addition to analyzing the general trends, we can compare the models for common stars between our sample and the observations in Wood et al. (2021) and references therein. The stars in Wood et al. (2021) contain a total number of 37 stars with a mix of main-sequence and evolved stars. The sample includes 15 single K-G stars among them 4 evolved stars, and 4 binaries. Wood et al. (2021) reports individual $\dot{M}$ values for the G-K binary pairs (this means that it was possible to model their individual contribution to the astrosphere of the system or they were separated enough not to share a common astrosphere). This is important as, in principle, one could treat the binary pairs as individual stars. The rest of the star sample includes 22 M dwarfs with 18 single M dwarfs, 3 binaries, and 1 triple system. Unlike the G-K stars, $\dot{M}_\star$ values for the M dwarf binaries/triple system are listed as a single value (therefore, it means that it has to be taken as the aggregate of all the stars in the system). For the binary system GJ 338 AB we were unable to include it in the plot of Fig. 7.6 due to a lack of needed information to estimate its R_o.

Following on the results from Sect. 7.3.3, our simulated mass loss rates for stars in the unsaturated regime agree well with those estimated from astrospheric detections (see Fig. 7.6). Specifically, for

GJ 205 (M1.5V), 61 Cyg A (K5V), and HD 219134 (K3V) we obtain $\dot{M}_\star/R_\star^2$ of 2.32, 3.98, and 1.50, respectively. These values are all consistent with their respective observational estimates, taking into account the typical uncertainties of the astrospheric absorption method[7]. While further observations could help to confirm this, the agreement between our asynchronous models and the observations indicates that, within this R_o range, the temporal variability of $\dot{M}_\star$ is minimal. This is certainly the case for the Sun ($R_o \sim 2.0$) in which long-term monitoring has revealed only minor variability of the solar wind mass loss rate over the course of the magnetic cycle (Cohen 2011, Finley & Matt 2018; Finley et al. 2019).

On the other hand, $\dot{M}_\star$ from the 3D MHD simulations appear to fall short by an order of magnitude or more from the available estimates for ϵ Eri (K2V), EV Lac (M3.5V), and YZ CMi (M4.5V) with $\dot{M}_\star/R_\star^2$ of 4.53, 0.62 and 20.57, respectively. We will discuss different possibilities for these discrepancies on each star in Sect. 7.3.3. However, it is important to remember that the $\dot{M}_\star$ estimates from the Ly-α absorption technique contain systematic errors that are not easily quantified. One example is that they depend on the assumed properties and topology of the ISM (Linsky & Wood, 2014), which have not been fully agreed upon in the literature (e.g., Koutroumpa et al. 2009; Gry & Jenkins 2014; Redfield & Linsky 2015). While studies have provided a detailed characterization of the local ISM (see Redfield & Linsky 2008, 2015; Gry & Jenkins 2014), intrinsic uncertainties and additional observational limitations can greatly alter the estimated mass-loss rate values. These include column densities, kinematics, and metal depletion rates (Redfield & Linsky 2004, 2008), as well as local temperatures and turbulent velocities (Redfield & Linsky, 2004).

Furthermore, we would also like to emphasize the variation of the $\dot{M}_\star$ in the astrospheric estimates with the assumed stellar wind velocity, as we believe that this factor is one of the largest potential source of uncertainty and discrepancy with our models. As discussed by Wood et al. (2021), this parameter is used as input in 2.5D hydrodynamic models to quantify the stellar wind mass loss rate. The Ly-α absorption signature, leading to $\dot{M}_\star$, is determined to first order by the size of the astrosphere. The latter depends on the stellar wind dynamic pressure ($P_{dyn} \propto \dot{M}_\star U_{sw}$), which implies an inverse relation between $\dot{M}_\star$ and U_{sw} (Wood et al., 2002).

The astrospheric analysis of Wood et al. (2021) assumed a stellar wind velocity of 450 km s^{-1} at 1 au (matching models of the heliosphere) for all main-sequence stars. However, we find that stellar wind velocities can vary significantly between different types of stars and even among the same spectral type for different magnetic field strengths and rotation periods. To quantify this, we compute the average terminal velocity of the wind, ($\overline{U_R^T}$), by averaging U_R over a sphere extracted at 99% of the maximum extent of each simulation domain (594 $R_\star$ for F, G, and K stars and 248 $R_\star$ for M dwarfs; see Sect. 7.2). In the cases in which the spatial extension of our numerical domain allowed, we also computed the average wind velocity at 1 au. The resulting values, listed in Table 7.2, indicate variations in the wind velocity by factors of 5 or more when moving from F-type stars ($\overline{U_R^T} \sim 325$ km s^{-1}) to M-dwarf ($\overline{U_R^T} \sim 1500$ km s^{-1}). This is also illustrated in Fig. 7.7, which portrays the simulated stellar wind environment for HD 179949 (F8V), HD 73256 (G8V), HD 189733 (K2V), and DT Vir (M0V). We include a green iso-surface that corresponds to the wind velocity at 1 au for F, G, and K stars as for M dwarfs it represents the average terminal wind velocity in the domain. The visualizations also include the equatorial projection of the wind dynamic pressure ($P_{dyn} = \rho U^2$), normalized to the nominal Sun-Earth value, as well as on a sphere highlighting the wind 3D structure at 0.5 au.

What is clear from this analysis is that is not ideal to use the same wind velocity for all spectral types. Even within the same spectral type, we can observe a wide range of terminal velocities (e.g., the velocity in K stars ranges from 400 km s^{-1} to 700 km s^{-1}). As such, for models that require wind velocity as an input parameter, we recommend using the average radial wind velocity among a given spectral type.

For G-K stars, we obtain wind velocities at 1 au in the range of 400 to 700 km s^{-1} which is not too different from the wind velocity assumption of Wood et al. 2021. This is also consistent with the fact that for these spectral types, we have a better agreement between $\dot{M}$ estimated from our simulations and those from the astropsheric technique (Wood et al., 2021). For lower mass stars with relatively small R_o we obtain velocities higher than 450 km s^{-1} up to 3675 km s^{-1}.

Note that due to computational limitations, the extent of our M-dwarf simulations does not reach

[7] Astrospheric estimates on $\dot{M}_\star$ should have an accuracy of about a factor of 2 with substantial systematic uncertainties (Wood et al., 2005).

up to 1 au (varying from 0.6 au for DT Vir to 0.16 au for GJ 1245 B). Nevertheless, as indicated by the calculated terminal velocities, even at closer distances the wind velocity is already > 450 km s^{-1}, a situation that should still hold when propagated out to 1 au. Wind velocities on the order of $1000 - 1500$ km s^{-1} at distances of 1 au and beyond had been reported in high-resolution AWSoM simulations of the environment around the M5.5V star Proxima Centauri (Alvarado-Gómez et al., 2020). This helps to explain why our simulated mass-loss rates for EV Lac, YZ CMi, and ϵ Eri were lower than the observed ones (differences larger than a factor of 2). We discuss these cases in more detail in the following section.

Exploring the cases of EV Lac, YZ CMi, ϵ Eri

1. **YZ CMi & EV Lac**

   Frequent stellar flares have been observed at YZ CMi in several wavelength ranges (Lacy, Moffett, & Evans 1976; Mitra-Kraev et al. 2005; Kowalski et al. 2013; Bicz et al. 2022). The flaring energy distribution of this star ranges from $10^{30.6}$ to $10^{34.09}$ erg (Bicz et al., 2022) with a total flaring time that varies from 21 to 306 minutes. Likewise, there is also significant flare activity on EV Lac (Leto et al. 1997; Muheki et al. 2020). From spectroscopic and photometric studies of EV Lac, Muheki et al. (2020) reports to have found 27 flares ($\sim$5.0 flares per day) in H α with energies between 1.61×10^{31} erg -1.37×10^{32} erg and 49 flares ($\sim$2.6 flares per day) from the TESS lightcurve with energies of 6.32×10^{31} erg -1.11×10^{33} erg. With such high flare activity, it is possible that a large fraction of the $\dot{M}_\star$ estimated in Wood et al. (2021) for these stars could arise from transient phenomena (e.g., prominences, CMEs).

   Following the same approach described at the end of Section 7.3.3, we can obtain a rough estimate of $\dot{M}$ from CMEs for EV Lac and YZ CMi. For EV Lac we find $\dot{M}_\star^{\rm CME}/R_\star^2 = 55.5\ \dot{M}_\odot/R_\odot^2$ assuming $\log(\mathrm{L_X}) = 28.69$. In the case of YZ CMi, an $\log(L_\mathrm{X}) = 28.53$ yields $\dot{M}_\star^{\rm CME}/R_\star^2 = 47.6\ \dot{M}_\odot/R_\odot^2$. However, given the magnetic field strength observed in EV Lac and YZ CMi (a few kG, Shulyak et al. 2010; Reiners et al. 2022; Cristofari et al. 2023), we expect that the magnetic confinement of CMEs would play an important role in these objects (see Alvarado-Gómez et al. 2019, Muheki et al. 2020, Maehara et al. 2021). Therefore, it is not straightforward to estimate exactly how large the contribution of CMEs to $\dot{M}_\star$ is for these stars.

   In addition, as discussed by Villarreal D'Angelo, Jardine, & See (2018), EV Lac and YZ CMi are considered in the slingshot prominence regime. For EV Lac they estimate $m_\mathrm{p} = 2.0 \times 10^{16}$ g and $t_\mathrm{p} = 0.6$ d, while for YZ CMi values of $m_\mathrm{p} = 4.5 \times 10^{16}$ g and $t_\mathrm{p} = 0.6$ d are given. Using the associated mass loss rate values reported in Villarreal D'Angelo, Jardine, & See (2018), we obtain $\dot{M}_\star^\mathrm{p}/R_\star^2 = 3.16\ \dot{M}_\odot/R_\odot^2$ for EV Lac and $\dot{M}_\star^\mathrm{p}/R_\star^2 = 8.32\ \dot{M}_\odot/R_\odot^2$ for YZ CMi.

   This suggests another possible explanation for the discrepancies between our models and the astrospheric estimates is that some of the stellar wind detected for EV Lac and YZ CMi contains material from the slingshot prominences. Indeed, the location of the latter in the $\dot{M}_\star - R_\mathrm{o}$ diagram (Fig. 7.6) appears more consistent with the mass loss rate estimates from slingshot prominences by Jardine & Collier Cameron (2019).

   Moreover, Wood et al. (2021) noted that the YZ CMi astrospheric absorption comes primarily from neutrals near and inside the astropause, rather than from the hydrogen wall where neutral H density is highest. Therefore, using Lyα absorption to calculate $\dot{M}_\star$ from YZ CMi will result in substantial uncertainty.

   Finally, as mentioned in Sect. 7.3.3, there is a significant difference between the wind velocity assumed by Wood et al. (2021) and our results. Our average terminal wind velocity for YZ CMi (1709 km s^{-1}) and EV Lac (3675 km s^{-1}) is significantly higher than the wind velocity of 450 km s^{-1} assumed in Wood et al. (2021) at 1 au. While the wind velocity in EV Lac might be overestimated in our models (due to the usage of fiducial AWSoM parameters), we still expect relatively large wind velocities for this star ($\sim 1000 - 1500$ km s^{-1}) given its magnetic field strength and Rossby number (see e.g., Kavanagh et al. 2021; Alvarado-Gómez et al. 2022). As was discussed in Sect. 7.3.3, while our terminal wind velocity for M dwarfs is calculated closer to the star (0.33 au for YZ CMi and 0.16 au for EV Lac), we do not expect a large reduction in the average velocity between these distances and 1 au. As such, the fast wind velocity resulting in

our simulations of YZ CMi and EV Lac would imply lower $\dot{M}_\star$ values when analyzed following the astrospheric technique of Wood et al. (2021).

2. ϵ **Eri**

With a relatively slow rotation period (11 d), and weak large-scale magnetic field (<50 G), ϵ Eri cannot be considered within the slingshot prominence regime (like in the cases of YZ CMi and EV Lac). Because of this, we do not expect a significant presence of slingshot prominences in the $\dot{M}$ value of this star. On the other hand, the analysis of Loyd et al. (2022), estimated the contribution of flare-associated CMEs to the mass loss rate. They reported an upper limit of 1.09 $\dot{M}_\odot$ $/R_\odot^2$, which is insignificant when compared to the star's overall estimated $\dot{M}_\star$ value by Wood et al. (2021) and the astrospheric technique (56 $\dot{M}_\odot$ $/R_\odot^2$). Therefore, the contribution from CMEs is also most likely not responsible for the elevated astrospheric $\dot{M}_\star$ value on this star and its discrepancy with our steady-state models.

On the other hand, multiple observations of the large-scale magnetic field geometry of ϵ Eri reveal that it evolves over a time-scale of months ((, 2014); Jeffers et al., 2017). According to ((2014)), the maximum field strength can reach up to 42 G. As shown in Fig. 7.3, a global increase in the magnetic field strength causes an increase in $\dot{M}_\star$. The Zeeman Doppler Imaging map of ϵ Eri used to drive the 3D MHD model has a $B_{\rm R}^{\rm max} = 25$ G leading to $\dot{M}_\star/R_\star^2 = 4.53\ \dot{M}_\odot/R_\odot^2$. This value is comparable to the numerical result obtained by Alvarado-Gómez et al. (2016) for this star ($\dot{M}_\star/R_\star^2 \sim 5.3\dot{M}_\odot/R_\odot^2$). Increasing the surface magnetic field strength of ϵ Eri to the maximum value reported in observations will raise the mass loss rate to $\sim$ 10 $\dot{M}_\odot/R_\odot^2$. As such, the variability of the stellar magnetic field and its expected modulation of the stellar wind properties could account for some of the differences between the simulated and the observed mass loss rates. However, corroborating this would require contemporaneous ZDI and astrospheric measurements which, to our knowledge, have not been performed on any star so far. As ϵ Eri goes through a magnetic/activity cycle (Metcalfe et al. 2013; Jeffers et al. 2017), we can expect relatively large variations in $\dot{M}_\star$ values in our Alfvén-wave driven stellar wind models.

Finally and following the discussion for YZ CMi and EV Lac, the average wind velocity for ϵ Eri at 1 au (554 km s^{-1}) resulting from our models exceeds the one assumed in Wood et al. (2021). This will result in a smaller estimated $\dot{M}_\star$ value from the pressure-balance astrospheric technique. In this way, the deviation between our models and the astrospheric detection of ϵ Eri could be due to the combined contribution of all the preceding elements (i.e., CMEs, cycle-related variability of the magnetic field, higher stellar wind velocity), and therefore we do not consider this discrepancy critical to our analysis.

7.3.4.Stellar wind and Circumstellar region

This section focuses on using the stellar wind results obtained from the 3D MHD simulations to assess the conditions an exoplanet would experience. This includes the characterization of the Alfvén surface for the various stellar wind solutions, the properties of the stellar wind in the habitable zone of these stars (in terms of the dynamical pressure of the wind), and the resulting magnetosphere size for these stellar wind conditions (assuming that a planet with the same properties/magnetization as Earth is in the HZ of these stars). The obtained quantities are listed in Table 7.2 and 7.3.

Stellar wind properties and orbital distances

1. **Alfvén surface size**

Figure 7.8 summarizes our results showing the stellar wind environment around cool main sequence stars. We include the average size of the AS, resulting from our 21 3D MHD models, indicated in filled diamonds. To complement this information, empty diamonds correspond to the expected average AS size employing the scaling relation provided in Sect. 7.3.1, and using the ZDI information from 29 additional stars (See et al. 2019 and reference therein). The green region corresponds to the optimistic HZ, calculated using the approach provided by Kopparapu et al. (2014) and the expected behaviour of the luminosity, temperature as a function of stellar mass on the main sequence (Kasting, Whitmire, & Reynolds 1993; Kopparapu et al. 2014; Ramirez

Table 7.3: Numerical results of different parameters in our sample at the habitable zone. Columns 1–8, respectively, list the star name, average dynamic pressure at the middle of the HZ ($\overline{P}_{\rm dyn,HZ}$), average dynamic pressure at the inner boundary of the HZ ($\overline{P_{\rm dyn}^{\rm Inn,HZ}}$), average dynamic pressure at the outer boundary of the *HZ* ($\overline{P_{\rm dyn}^{\rm Out,HZ}}$), the average magnetopause standoff radius ($\overline{R}_{\rm M}$), the inner habitable zone ($HZ_{\rm inner}$), the outer habitable zone ($HZ_{\rm outer}$), the average equatorial Alfvén surface ($\overline{AS}_{\rm eq}$). The habitable zones listed in this table were inferred using the measured $L_\bigstar$ and $T_{\rm eff}$ of each star in our sample (Table 7.1).

Name	$\overline{P}_{\rm dyn,HZ}$ [$P_\oplus$]	$\overline{P_{\rm dyn}^{\rm Inn,HZ}}$ [$P_\oplus$]	$\overline{P_{\rm dyn}^{\rm Out,HZ}}$ [$P_\oplus$]	$\overline{R}_{\rm M,HZ}$ [$R_{\rm E}$]	$HZ_{\rm inner}$ [au]	$HZ_{\rm outer}$ [au]	$\overline{AS}_{\rm eq}$ [$R_\bigstar$]
τ Boo	1.02	2.76	0.40	7.85	1.253	2.901	9.99
HD 179949	0.92	2.51	0.48	7.99	0.983	2.294	10.24
HD 35296	2.93	7.77	1.48	6.58	0.925	2.157	12.78
HN Peg	6.74	18.58	3.47	5.73	0.812	1.904	13.65
HD 190771	3.96	11.01	2.02	6.26	0.744	1.748	12.35
TYC 1987-509-1	10.21	28.49	5.20	5.30	5.35	1.299	15.47
HD 73256	2.32	6.45	1.18	6.85	0.648	1.539	10.73
HD 130322	0.91	2.56	0.46	8.00	0.542	1.291	8.12
HD 6569	10.77	30.21	5.46	5.30	0.466	1.11	16.25
ϵ Eri	6.45	18.16	3.23	5.77	0.426	1.024	13.64
HD 189733	13.56	38.82	6.88	5.10	0.458	1.108	13.4
HD 219134	2.01	5.81	1.01	7.01	0.410	0.996	8.33
TYC 6878-0195-1	13.42	39.39	6.71	5.11	0.713	1.751	23.16
61 Cyg A	10.06	29.47	5.01	5.36	0.308	0.754	11.93
HIP 12545	20.28	60.51	9.98	4.77	0.509	1.267	24.45
TYC 6349-0200-1	13	40	6	5.14	0.443	1.116	21
DT Vir	31.48	88.97	16.20	4.43	0.191	0.486	29.24
GJ 205	9.73	29.65	4.73	5.39	0.201	0.517	15.91
EV Lac	12.15	33.18	6.27	—-	0.094	0.245	119.16
YZ CMi	193.85	566.34	97.08	—-	0.09	0.237	75.23
GJ 1245 B	140.89	447.39	68.15	—-	0.033	0.087	38.12

2018). Each square indicates the limits of the optimistic HZ for each star in our sample. These

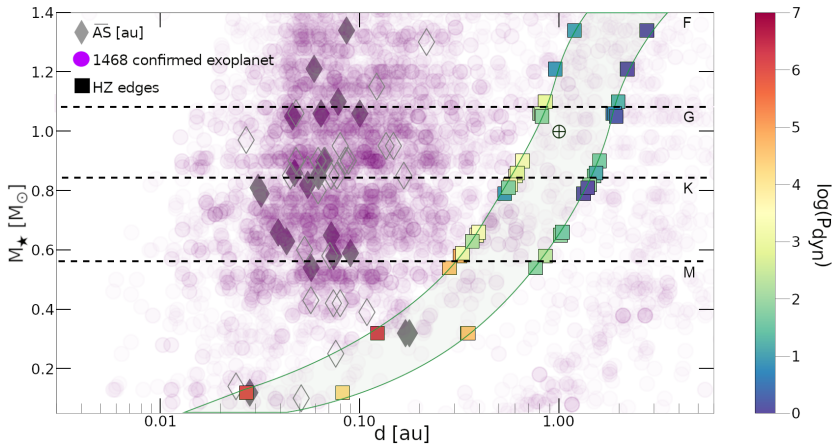

Figure 7.8: Numerical results of the average Alfvén surface size (diamonds), the inner and outer edge of the HZ (square, Kopparapu et al. 2014) derived using scaling laws that connect $M_\star$, $R_\star$, $L_\star$, and $T_{\rm eff}$, against $M_\star$. The filled diamonds correspond to the $\overline{AS}$ of the 21 stars in our sample. The empty diamonds are the $\overline{AS}$ of other stars derived from our $\overline{AS}$ - $B_{\rm R}$ relation: $\log \overline{AS_{\rm R}} = (0.42\pm0.06) \log B_{\rm R}^{\rm avg} + (0.71\pm0.07)$. The habitable zone boundaries are color-coded by the corresponding average dynamic pressure ($\overline{P_{\rm dyn}}$) in logarithmic scale. The green shaded area represents the optimistic habitable zone. Earth is represented by $\oplus$. The purple circles correspond to some confirmed exoplanets (taken from the NASA exoplanet archive). The dynamic pressure at the outer edge of the HZ of DT Vir and GJ 205 (derived from scaling laws) is missing in the plot since it goes beyond the simulation domain that was initially established using the measured $L_\star$ and $T_{\rm eff}$ (Table 7.1). The dashed lines separate the different spectral types.

have been color-coded by the stellar wind dynamic pressure, normalized to the average Sun-Earth value. The position of the Earth is indicated by the $\oplus$ symbol. In the background, a sample of the semi-major axis of some exoplanets is included.

There are a few noteworthy aspects of Fig. 7.8. First of all, the 3D MHD simulated $\overline{AS}$ values (filled diamonds) do not show a clear trend with stellar mass. Instead, we see more or less similar $\overline{AS}$ regardless of the spectral type of the star (Table 7.2). We see a similar behavior for stars whose $\overline{AS}$ were extracted from the scaling relationship presented in Eq. 7.3 (empty diamonds). There is a significant scatter in the obtained distribution of $\overline{AS}$ against $M_\star$, indicating that the intrinsic dependency with the surface magnetic field properties can in principle be replicated among multiple spectral types. However, we remind the reader that this result is also partly a consequence of our fixed choice for the base parameters of the corona and stellar wind solution (Sect. 7.2.1), which could in principle vary among different spectral types and activity stages (i.e. ages). As such, the generalization of the results presented here requires further investigation from both, observational constraints and numerical simulations.

We can also see that for late K and M dwarfs, $\overline{AS}$ reaches orbital distances comparable to their HZ limits. Examples of this from our sample are GJ 1245 B ($\overline{AS} = 0.028$ au, $HZ_{\rm inner} = 0.033$ au) and YZ CMi ($\overline{AS}$= 0.178 au, $HZ_{\rm inner}$= 0.09 au). This situation has been also identified in previous case studies of stellar winds and exoplanets (e.g, Vidotto et al. 2013; Cohen et al. 2014; Garraffo et al. 2017).

The location of the HZ relative to the stellar Alfvén surface must be considered when studying the interactions between a star and a planet. A planet orbiting periodically or continuously within the AS region could be directly magnetically connected to the stellar corona, which could have catastrophic effects on atmospheric conservation (Cohen et al., 2014; Garraffo et al., 2017; Strugarek, 2021). On the other hand, a planet with an orbit far outside this limit will be decoupled from the coronal magnetic field and interact with the stellar wind in a manner similar to the Earth (e.g. Cohen et al. 2020; Alvarado-Gómez et al. 2020). In the case of a planet orbiting in

and out of the AS, the planet will experience strongly varying wind conditions, whose magnetospheric/atmospheric influence will be greatly mediated by the typical time-scale of the transition (Harbach et al., 2021).

2. **Dynamic pressure**

We also see a general trend in Fig. 7.8 in which the dynamic pressure at the HZ boundaries increases as we move from earlier to later spectral types. For example, $\overline{P_{\rm dyn}^{\rm Inn,HZ}}$ for the lowest-mass star GJ 1245 B is 447.39 $P_\oplus$ nearly 200 times stronger than for the highest-mass star τ Boo with $\overline{P_{\rm dyn}^{\rm Inn,HZ}}$ = 2.76 $P_\oplus$. Our results also show a large variability in $\overline{P_{\rm dyn}}$ as we move from the inner to the outer edge of the HZ of G, K, and M dwarfs (Table 7.3). For these stars, the $\overline{P\rm dyn}$ at the inner HZ is almost 6 times stronger than that at the outer edge of the HZ (i.e., EV Lac $\overline{P_{\rm dyn}^{\rm Inn,HZ}}$ = 33.18 $P_\oplus$, $\overline{P_{\rm dyn}^{\rm Out,HZ}}$ = 6.27 $P_\oplus$). For F stars, the difference is smaller, around a factor of 2 like in the case of HD 179949, where $\overline{P_{\rm dyn}^{\rm Inn,HZ}}$ = 2.51 $P_\oplus$ and $\overline{P_{\rm dyn}^{\rm Out,HZ}}$ = 0.48 $P_\oplus$. The reason is that the HZs of these stars are farther from the star, where the wind density starts to become less variable.

Moreover, in some cases, we have $\overline{P}_{\rm dyn}$ at the inner and outer edge of the star HZ comparable to the typical range experienced by the Earth (0.75 and 7 nPa, Ramstad & Barabash 2021). For example, HD 73256 (G8V, 6.45 - 1.18 $P_\oplus \sim$ 9.675 - 1.77 nPa), HD 130322 (K0V, 2.56 - 0.46 $P_\oplus \sim$ 3.84 - 0.69 nPa), τBoo (F7V, 2.76 - 0.40 $P_\oplus \sim$ 4.14 - 0.6 nPa). For the case of M dwarfs, we have dynamic pressures higher than those experienced by Earth, as in the case of DT Vir (M0V, 88.97 - 16.20 $P_\oplus \sim$ 133.455 - 24.3 nPa). This is because the HZ is located near the star where the density is highest. This indicates that planets orbiting at very close distance to the star ($\sim$ 0.03 - 0.05 au) would experience extreme space weather conditions with $P_{\rm dyn}$ up to 10^3 and 10^4 $P_\oplus$. These values are comparable to the ones estimated in Alvarado-Gómez et al. (2020) for Proxima d and for Proxima b in Garraffo, Drake, & Cohen (2016). However, the reader is reminded here that any point from our simulations should be interpreted as an indication of the average conditions, but should not be treated as a specific absolute value (since it will change depending on the instantaneous local density and velocity of the wind (both a function of the evolving stellar magnetic field).

In addition, we notice a scatter in $\overline{P}_{\rm dyn}$ estimates at the HZ when comparing stars of the same spectral type. This is not surprising since the $P_{\rm dyn}$ depends on the wind velocity and density at a given place. This also translates into having a range of dynamic pressure that a planet will experience within the HZ. This will defer from one orbital distance to the other as we can see in Fig. 7.7 where we show the equatorial plane color-coded by the dynamic pressure.

We can use our 3D models to investigate also the influence due to the orbital inclination. To illustrate this, Fig. 7.9 shows a 2D projection of the normalized dynamic pressure $P_{\rm dyn}$ extracted from spherical surfaces matching the midpoint of the HZ of HD 179949 (F8V), TYC 198-509-1 (G7V), 61 Cyg A (K6V), and GJ 205 (M1.5V). We notice that in the case of F and G stars (i.e., HD 179949, and TYC-198-509-1) we have a large $P_{\rm dyn}$ variation with inclination around a factor 7. However, $P_{\rm dyn}$ values, are still relatively small in terms of absolute units (i.e., 0.01 - 10 $P_\oplus \sim$ 0.015 - 15 nPa). For K and M dwarfs, we see less variability in the $P_{\rm dyn}$ for the different inclinations, a more homogeneous $P_{\rm dyn}$, especially in the case of the K star. However, in these cases, the $P_{\rm dyn}$ can reach values $>$ 100 $P_\oplus$ ($>$ 150 nPa). Our results also show that even with an extreme orbit around the G-type star (TYC 198-509-1) with an inclination matching the current sheet, we would most likely not reach the very high $P_{\rm dyn}$ values as in the case of the K and M dwarfs as we move closer to the star. As such, the inclination of the orbit plays a secondary role compared to the distance. This is clearly seen in the color gradient that gets redder and redder as we move toward lower masses (so the HZ is closer).

On the other hand, the variability of $P_{\rm dyn}$, which we can see in Fig. 7.8 while represented in the same 'spatial scale', it does not coincide in terms of 'temporal scales'. In other words, the x-axis in Fig. 7.8 do not correspond to the same timescale units for each star, where the 360 degrees of longitude correspond to "1 orbital period". However, the orbital period is very different for a planet in the HZ of an F-type star (within a few au) compared to a planet orbiting an M-dwarf (within a fraction of an au). A planet orbiting an M-dwarf star experiences the variations in

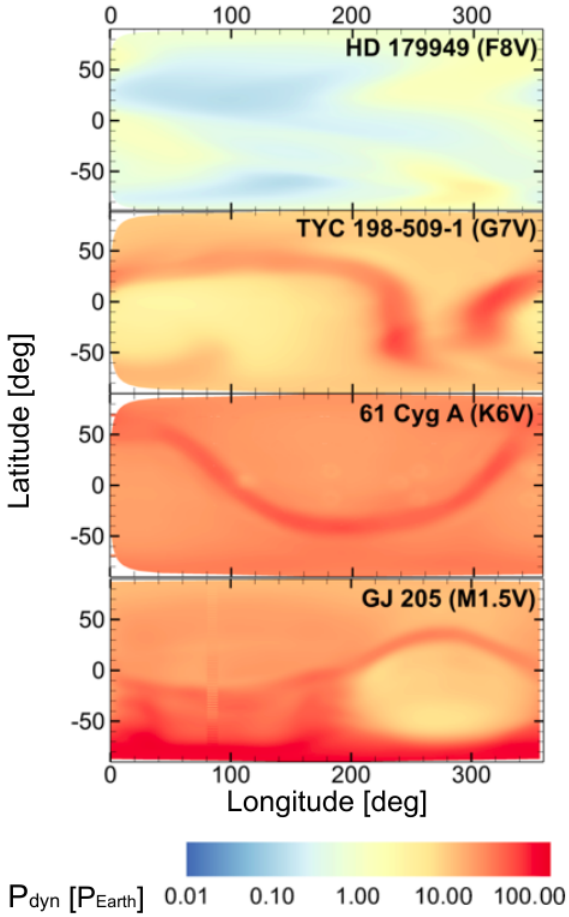

Figure 7.9: Two-dimensional Mercator projections of the normalized stellar wind dynamic pressure ($P_{\rm dyn}$) extracted from the 3D MHD models of four stars in our sample covering F to M spectral types (HD 179949, TYC 198-509-1, 61 Cyg A, and GJ 205). Each $P_{\rm dyn}$ distribution was extracted from a spherical surface located at the midpoint habitable zone of each star.

$P_{\rm dyn}$ on a much faster timescale ($\sim$ 1 day for each current sheet crossing), while these variations are much longer for more massive stars. This means that even if the $P_{\rm dyn}$ values were the same, the faster variability over the orbital period for low-mass stars would result in planets and their magnetospheres/atmospheres having less time to recover from passing through regions of high $P_{\rm dyn}$ than planets around more massive stars.

Finally, following the results compiled by Ramstad & Barabash (2021), if we consider the presence of a rocky exoplanet with an atmosphere similar to those of Venus and Mars at those mid-HZ locations, we would expect atmospheric ion losses between 2×10^{24} ions s^{-1} and 5×10^{24} ions s^{-1}. This of course assumes that all processes occur in the same way as in the solar system (which might not be necessarily true for some regions of the vast parameter space of this problem). The ion losses will depend heavily on the type of stars that the exoplanet orbits, both in terms of the high-energy spectra and the properties of the stellar wind (see e.g. Egan, Jarvinen, & Brain 2019; France et al. 2020). If the rocky exoplanet is found around the HZ of an M-dwarf, the planet might suffer from unstable stellar wind conditions as previously stated that might increase the ion losses in the exoplanetary atmosphere. We will consider the case of Earth with its magnetosphere in the following section.

Magnetopause Standoff Distances

Using the dynamic pressure, we can define a first-order approximation to determine the magnetosphere standoff distance ($R_{\rm M}$) of a hypothetical Earth-like planet orbiting at the HZ around each star in our sample. This is done by considering the balance between the stellar wind dynamic pressure and the planetary magnetic pressure (Eq. 7.8, Gombosi 2004; Shields, Ballard, & Johnson 2016):

$$R_{\rm M} = R_{\rm E}[\frac{{B_{\rm p}}^2}{8\pi P_{\rm dyn}}]^{\frac{1}{6}} \tag{7.8}$$

The Earth's equatorial dipole field and radius are represented by $B_{\rm p}$ and $R_{\rm E}$ respectively. Normally the total wind pressure should be considered (i.e., thermal, dynamic, and magnetic), but in all the cases here considered, we can neglect the contributions of the magnetic and thermal pressures. For this calculation, we assume an equatorial dipole magnetic field of 0.3 G, similar to that of the Earth (Pulkkinen, 2007). The magnetospheric standoff distance is expressed in Earth's radii (Eq. 7.8). The different $\overline{R}_{\rm M,HZ}$ values for the different stars in our sample are listed in table 7.3. Note that we only estimate the $R_{\rm M}$ in the cases where the HZ is in the super-Alfvénic regime (Cohen et al., 2014; Strugarek, 2018).

Our estimated $R_{\rm M,HZ}$ for F, G, and early K stars have values closer to the standard size of Earth's dayside magnetosphere ($\sim$ 10 $R_{\oplus}$, see Pulkkinen 2007; Lugaz et al. 2015. This is comparable to the value obtained by Alvarado-Gómez et al. (2020) for Proxima c ($\sim$ 6 - 8 $R_{\oplus}$ in both activity levels), assuming an Earth-like dipole field on the planet surface. For the late K and M dwarfs in our star sample, $R_{\rm M}$ starts to reach lower values $< 50\%$ from that of Earth. This suggests that a planet orbiting these stars must have a stronger dipole magnetic field than that of the Earth to withstand the wind conditions since $R_{\rm M} \propto B_{\rm p}^{1/3}$. However, in Ramstad & Barabash (2021) they show that contrary to what we have seen so far, the magnetosphere might actually not act as a shield for the stellar wind-driven escape of planetary atmospheres. In fact, they reported an ion loss for Earth that ranges from 6 $\times 10^{24}$ ions s^{-1} - 6 $\times 10^{26}$ ions s^{-1} which is higher than what Venus and Mars lose. Further modeling studies are needed in order to characterize the stellar wind influence on the atmospheric loss of rocky exoplanets (e.g., Egan, Jarvinen, & Brain 2019; France et al. 2020), whose input stellar wind parameters can be extracted from this investigation.

7.4 Summary & Conclusions

In this study we employed a state-of-the-art 3D MHD model (SWMF/AWSoM) to investigate the dependencies between different star properties ($R_\star$, $M_\star$, $B_{\rm R}$, and $P_{\rm rot}$) and a number of stellar wind parameters (AS, $\dot{M}_\star$, $\dot{J}_\star$, $P_{\rm dyn}$) of cool main sequence stars. We present numerical results of 21 stars going from F to M stars with magnetic field strengths between 5 and 1.5 kG and rotation periods between 0.71 d and 42.2 d. The large-scale magnetic field distribution of these stars, obtained by previous ZDI studies, were used to drive the solutions in the Stellar Corona domain, which are then self-consistently coupled for a combined solution in the Inner Astrosphere domain in the case of F, G, and K stars. Our results showed a correlation between the average AS size and $B_{\rm R}^{\rm avg}$, regardless of the spectral type of the star (Eq. 7.3). We also obtained a strong correlation between $\dot{M}_\star$ and $B_{\rm R}^{\rm avg}$ for the different spectral types (excluding EV Lac, Eq. 7.4). The correlation between $\dot{J}_\star$ and $B_{\rm R}$, on the other hand, was dominated by the absolute dependence on the stellar size, with significant scatter resulting mainly from the variability in $\dot{M}_\star$, the distribution of $\Omega_\star$ in our sample and the equatorial AS size where the maximum torque is applied.

Having established these star-wind relations, we looked in detail at $\dot{M}_\star$, since it is the only observable parameter of the stellar wind for which comparisons can be made. Using the complexity number as a function of the Rossby number $R_{\rm o}$–defined previously in the literature– we were able to investigate the dependence of magnetic complexity on $\dot{M}_\star$. Our results showed that for more active stars, as in the case of M dwarfs, the field strength starts to dominate over the complexity in the contribution on shaping $\dot{M}_\star$. Also, for cases in which the magnetic field strength and complexity were comparable, we obtained similar $\dot{M}_\star$. This indicates that in these cases the stellar properties ($R_\star$, $M_\star$, and $P_{\rm rot}$) play a secondary role in changing $\dot{M}_\star$. We then used our stellar wind results to investigate its behaviour with respect to the well-known stellar activity relationship ($F_{\rm X}$ vs $R_{\rm o}$ with the saturated and unsaturated regimes). For stars in the unsaturated regime, we see a trend where $\dot{M}_\star$ increases with decreasing $R_{\rm o}$ (Eq. 7.7). For stars in the saturated regime, we find that the contribution of the steady wind is only a small part of the $\dot{M}_\star$ budget. This suggests that there could be saturation in $\dot{M}_\star$ due to the steady stellar wind, while the star could lose even more mass through other mechanisms, such as transient events (i.e. prominences, coronal mass ejections).

In addition to analyzing the general trends, we compared the model results of stars in our sample and objects with astrospheric $\dot{M}_\star$ constraints. Our simulated $\dot{M}_\star$ for stars in the unsaturated regime agree well with those estimated from astrospheric detections (namely for GJ 205, 61 Cyg A, and HD 219134). On the other hand, $\dot{M}_\star$ from the 3D MHD simulations appear to differ by an order of magnitude or more from available estimates for ϵ Eri, EV Lac, and YZ CMi. We discussed how these results might be connected with the underlying assumption made by the observational analysis with respect to the stellar wind speed. Indeed, for all the stars in which our models differed largely from the literature estimates, we obtained much larger stellar wind speeds than the ones used in the astrospheric method. As such, we emphasized the importance of using the appropriate wind velocity when estimating $\dot{M}_\star$ from observations.

We further discussed various possibilities for the discrepancies in EV Lac, YZ Cmi, ϵ Eri. For the two flaring stars, EV Lac and YZ CMi, we suspect that the high $\dot{M}_\star$ estimates from the Ly-α absorption technique could be dominated by material from slingshot prominences and possibly CMEs (uncertain due to the expected magnetic confinement of CMEs in these stars). Note that this possibility was also considered by Wood et al. (2021) in the original astrospheric analysis. In the case of ϵ Eri, we do not expect a large contribution from prominences or CMEs to the observed $\dot{M}_\star$. However, as ϵ Eri undergoes a magnetic cycle, the stellar magnetic field and its expected modulation of stellar wind properties could explain some of the differences between the simulated and observed $\dot{M}_\star$.

Moreover, we used the stellar wind results from the 3D MHD simulations to assess the conditions that an exoplanet would experience, and provide the stellar wind conditions in the entire classical Habitable Zones of our target stars. Our results show a scatter in the obtained distribution of AS versus $M_\star$, suggesting that the intrinsic dependence with the surface magnetic field properties can be reproduced for several spectral types. With respect to the stellar wind dynamic pressure, our results show that the orbital inclination plays a secondary role compared to the orbital distance. We have also found that a planet orbiting K and M stars must have a stronger dipole magnetic field than that of Earth to withstand the wind conditions, if the planetary magnetic field is indeed acting as a shield (this paradigm, however, is starting to be challenged by solar system observations).

Finally, the properties of the stellar wind in the HZ of different spectral types obtained here can be used in future studies to, for instance, estimate the expected radio emission due to wind-magnetosphere interactions or the planetary atmospheric mass loss due to erosion of the stellar wind from ion escape processes.

Acknowledgements: The authors would like to thank the referee for valuable comments that improved the quality of the paper. The authors gratefully acknowledge the Gauss Centre for Supercomputing e.V. (`www.gauss-centre.eu`) for funding this project by providing computing time on the GCS Supercomputer SuperMUC-NG at Leibniz Supercomputing Centre (`www.lrz.de`) under application ID 21761 (PI: Alvarado-Gómez). JJC and KP acknowledge funding from the German *Leibniz Community* under project number P67/2018. CG was supported by NASA contract NAS8-03060 to the Chandra X-ray Center. This research has made use of NASA's Astrophysics Data System Bibliographic Services.

Data availability The data would be made available to the community on reasonable request due to the volume of the 3D simulations. Extractions of specific quantities discussed in the paper could be requested from the corresponding author.

7.5 Appendix

7.5.1. Trends with Maximum Radial Magnetic Field

We have also quantified $\overline{AS}_\mathrm{R}$ and $\dot{M}_\star$ / $R_\star^2$ as a function of the absolute maximum radial magnetic field strength ($|B_\mathrm{R}|^\mathrm{max}|$). It is important to also investigate $|B_\mathrm{R}|^\mathrm{max}$, since the average radial magnetic field strength may suffer from cancellations, especially if the star has a symmetric surface magnetic field distribution. Figure 7.10 shows the simulated average Alfvén surface area ($\overline{AS}$, top) and the mass-loss rate per unit surface area ($\dot{M}_\star/R_\star^2$, bottom) as a function of the maximum absolute radial magnetic field on the stellar surface ($|B_\mathrm{R}|^\mathrm{max}$). We see a trend where $\overline{AS}$ and $\dot{M}_\star/R_\star^2$ increase with increasing magnetic field strength. We fit this trend to a power law by applying the bootstrap method used to

derive this parameter as a function of the average radial magnetic field (similar to the procedure used in Sect. 7.3.1, Eqs. 7.3 and 7.4).

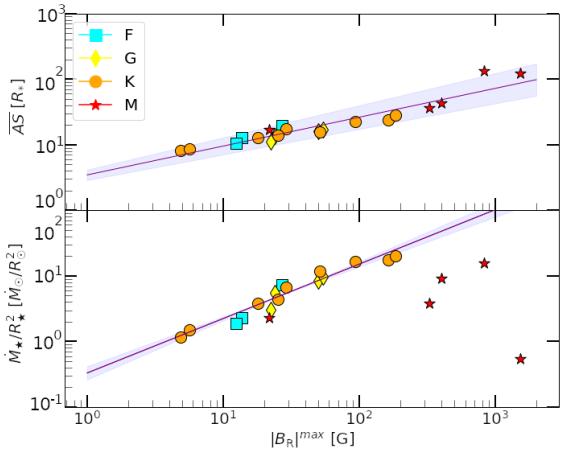

Figure 7.10: Simulated average Alfvén surface ($\overline{AS}$, top), and the mass loss rate per unit surface area ($\dot{M}_\star/R_\star^2$, bottom) as a function of the absolute surface-max radial magnetic field ($|B_\mathrm{R}|^\mathrm{max}$). The mass loss rate is expressed in units of the average solar values, normalized to the surface area of each star. Individual points denote the results of each simulation presented in Sect. 7.3, Table 7.2. The different symbols and colors represent the spectral types (F, cyan/squares; G, yellow/diamonds; K, orange/circles; M, red/star). The purple line with the shaded purple area represents the fitted power-law with its uncertainties.

$$\log \overline{AS_\mathrm{R}} = (0.44 \pm 0.05) \log |B_\mathrm{R}|^\mathrm{max} + (0.54 \pm 0.08) \tag{7.9}$$

$$\log \dot{M}_\star/R_\star^2 = (0.83 \pm 0.07) \log |B_\mathrm{R}|^\mathrm{max} - (0.48 \pm 0.10) \tag{7.10}$$

Coronal abundances of M dwarfs – a reversal in the First Ionization Potential pattern at low activity levels?

Judy J. Chebly[1,2], *Julián D. Alvarado-Gómez*[1], *Katja Poppenhäger*[1,2], *Brian Wood*[3]
[1]Leibniz Institute for Astrophysics, An der Sternwarte 16, D-14482, Potsdam, Germany
[2]Institute of Physics and Astronomy, University of Potsdam, Potsdam-Golm, D-14476, Germany
[3]Naval Research Laboratory, Space Science Division, Washington, DC 20375, USA
Submitted to Astronomy & Astrophysics journal.

Main sequence stars of spectral types F, G, and K exhibit a recognizable pattern known as the FIP effect, where elements with lower first ionization potentials are more abundant in the stellar corona than in the photosphere. In contrast, stars with high magnetic activity such as M dwarfs exhibit an inverse pattern, known as iFIP. We aim to determine whether or not the iFIP pattern persists in low-activity M dwarfs. We used *XMM-Newton* to observe the moderately active M dwarf HD 223889 that has an X-ray surface flux of $F_{\rm X,surf} = 5.1$, the lowest for an M dwarf studied so far for coronal abundance patterns. We used low-resolution CCD spectra of the star to constrain the iron to oxygen ratio in its corona. We observe for the first time an abundance pattern compatible with a null FIP or iFIP effect in a moderately active M dwarf. This challenges the current picture where all studied M dwarfs exhibit a iFIP effect, and hints at a possible transition to FIP-pattern at even lower M dwarf activity levels. The results suggest that the $T_{\rm eff}$-$F_{\rm bias}$ relationship should be reconsidered as there might be deviation from the trend in low active M dwarfs depending on their intrinsic properties. Targeting stars with low coronal activity is essential for refining our understanding of (i)FIP patterns and their causes.

8.1 Introduction

Scientists have observed a significant difference in the composition of the solar corona and wind compared to the photosphere. In the corona, the elemental abundance ratio increases by a factor of 3 with a typical variation between 2 and 5 (Pottasch, 1963; Meyer, 1985; Feldman, 1992). These elements are characterized by low **f**irst **i**onization **p**otential (FIP) and include Al, Mg, Si, Ca, and Fe ($< 10\,$eV). This phenomenon has been detected by various means, including remote sensing techniques such as spectroscopic measurements and in situ observations as documented by Feldman & Laming (2000) and von Steiger et al. (2000). In contrast, elements with high FIP values ($\geqslant$ 10 eV), such as C, N, O, Ne, and Ar, have coronal abundances very similar to their photospheric values. This discrepancy in abundance is known as the FIP effect.

The FIP effect extends beyond our Sun and has been observed in stars with solar-like properties, as shown by the studies of Drake, Laming, & Widing (1994) and Laming & Drake (1999). For stars with strong magnetic activity, especially for very active M dwarfs ($\log\ L_{\rm X} \geq 29$), instead of a FIP effect, there is an inverse FIP effect (iFIP). There is a depletion of elements with low FIP compared to elements with high FIP(**?**Güdel et al. 2001; Audard et al. 2003; Huenemoerder et al. 2003; Ball et al. 2005; Sanz-Forcada, Affer, & Micela 2009). The model proposed by Laming (2004) provides the most comprehensive explanation for the observed FIP and iFIP effect in stars to date. This model focuses on the ponderomotive force generated by Alfvén waves, which leads to the separation of ions and neutrons within the chromosphere of the Sun and other stars.

The FIP effect is explained through resonant Alfvén waves traveling along coronal loops, as shown in the studies by (Laming 2015, 2021). The transmission of waves between the chromosphere and the corona with energy fluxes for coronal heating in the range of 10^6 to 10^7 erg cm^{-2} s^{-1} affects the abundance of elements in the upper chromosphere based on their ionization states. Elements with

low-FIP, which are predominantly ionized in the chromosphere, experience a significant increase in abundance as they ascend into the corona. The high FIP elements on the other hand, which are mainly neutral in the chromosphere, do not appear to be affected by these wave-induced processes.

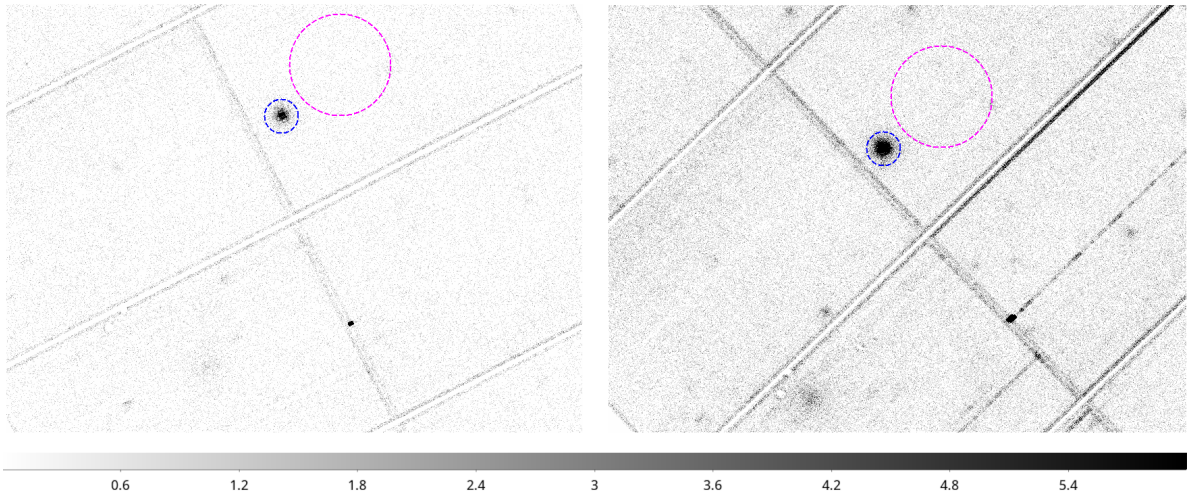

Figure 8.1: X-ray image from PN-detector of HD 223889 taken with the *XMM-Newton* telescope in the 0.2–2 keV energy band. The left and right panel shows respectively, *observation 1* and *2* (see Table 8.2). HD 223889 is marked by a blue dashed circle with a radius of 20 arcsec, while the background is represented by a magenta dashed-circle with a radius of 60 arcsec.

In contrast, the iFIP effect is thought to be driven by the ability of upward-propagating p-modes or magneto-acoustic waves (waves driven by magnetic pressure) to undergo reflection or refraction back into the chromosphere. In the latter, the pressure of the magnetic field exceeds the thermal effects of charged particle motion, plasma $\beta < 1$ (Baker et al. 2019, 2020; Laming 2021). In addition, iFIP is more likely to occur under conditions of restricted magnetic field expansion through the chromosphere (?Laming 2021). This is observed, for example, in stars with high filling factors[1].

The filling factor of cool main sequence stars estimated from Zeeman broadening correlates with Rossby number [2] in a similar way to the activity-rotation relation (Cranmer & Saar, 2011; Reiners, 2012). This means that more active stars have larger estimated filling factors. This is consistent with observations of M dwarfs (e.g. Donati & Landstreet 2009; Reiners & Basri 2009). If this interpretation is correct, then stars with low magnetic activity and therefore low filling factors should display a FIP effect, while stars with high filling factors display an iFIP effect.

It has also been observed that the transition from the FIP to the iFIP regime correlates with the stellar mass, especially when excluding extremely active stars characterized by a L_X of 10^{29} erg s^{-1}, as shown in Wood & Linsky (2010); Wood, Laming, & Karovska (2012). The pattern also decreases as we progress to the later spectral types, eventually reaching a null effect around K5, with an iFIP effect for M stars.

However, so far mainly M dwarfs with high magnetic activity levels have been investigated for their coronal abundances. This is due to the issue that a large number of X-ray photons is required to determine coronal abundances from high-resolution spectra. M dwarfs, which have small surfaces, therefore need to be intrinsically X-ray bright and therefore highly active, or located very nearby in order to supply high enough X-ray fluxes.

It is therefore currently unclear whether M dwarfs with a low activity level (log $L_X < 29$) can have low enough filling factors to display a FIP pattern, instead of an iFIP pattern, in their coronal abundances. The lowest activity M dwarfs studied for coronal abundances so far are the two stars in the moderately active wide binary system GJ 338 AB, which consists of two M0 dwarfs located at a distance of about 5 pc from the Sun. The stellar system was the subject of a Chandra-LETGS observation performed by Wood, Laming, & Karovska (2012). The study showed the presence of a

[1] Proportion of the stellar surface covered by active regions.
[2] Defined as R_o = rotation period/ convective turnover time

mild iFIP pattern in this binary star; however, the uncertainties in the measurements were large and almost encompassed the abundances in the solar photosphere.

In this study, we investigate whether or not the iFIP pattern persists in low-to-moderately activity M dwarfs by examining a critical coronal temperature range. Our study uses *XMM-Newton* observations to investigate the coronal abundances of the nearby M dwarf HD 223889, which is one of the lowest active M dwarf suitable for studying the iFIP effect. The paper is structured as follows: Section 8.2 gives an overview of the observations and the methods used for data analysis. Section 8.3 outlines the results of this study. Section 8.4 provides a detailed discussion and comparative analysis based on the findings from previous observations. The concluding remarks can be found in section 8.5.

8.2 Observations and data analysis

The star HD 223889 (HIP 117828) is a moderately active M dwarf (M2V) at a distance of 10.1 pc from the Sun. This star was observed twice with *XMM-Newton* in 2020 and again in 2022. HD 223889 is a good target for this study because although it has low to moderate coronal activity, it has an estimated mean coronal temperature higher than 2 MK (determined from 2020 observation). At a coronal temperature of more than 2 MK, iron emission with *XMM-Newton* can actually be observed.

Table 8.1: HD 223889 intrinsic properties taken from Stassun et al. (2019), except for the effective temperature ($T_{\rm eff}$) taken from Gaia DR3.

Parameter	Value
Mass ($M_\odot$)	0.52 ± 0.02
Radius ($R_\odot$)	0.52 ± 0.02
$T_{\rm eff}$ (K)	3254^{+157}_{-12}
log g	4.7 ± 0.26

The details of the observations are listed in table 8.2. To distinguish between the two observations, we will refer to the 2020 observation as the "*observation 1*" and the 2022 observation as the "*observation 2*". *Observation 2* extended over 100 ks , whereas observation 1 extended only over 28 ks. Both observations used the EPIC and RGS instruments of the *XMM-Newton* observatory to obtain both CCD and RGS spectra. It is noteworthy that the EPIC observations (MOS1, MOS2, and PN) used the same filter configuration as observation 1, which ensures the consistency of the observations.

The extracted X-ray images from the three CCD detectors are shown in Fig 8.1. A circular extraction region with a radius of 20 arcsec was centered on the expected proper motion corrected position of HD 223889 during the epoch of each *XMM–Newton* observation (blue dashed-circle). In addition, a source-free background region with a radius of 60 arcsec was carefully defined (magenta dashed-circle). Lightcurves and CCD spectra were extracted for the MOS and PN detectors, along with RGS1 and 2, according to the procedure from the *XMM-Newton* SAS 12.12.1 user handbook. We used the same data processing methods for both observations.

Table 8.2: *XMM-Newton* data of HD 223889

	ObsDate	ObsID	Exposure time (ks)
Obs 1	April 2020	0840844101	28
Obs 2	May 2022	0900940101	100

8.3 Results

8.3.1.Temporal variability of HD 223889's corona

We have extracted the lightcurve from the source and background regions of the two MOS cameras and the PN detector for both observations with 500 s time binning in the energy range: 0.2-2 keV. Fig. 8.2

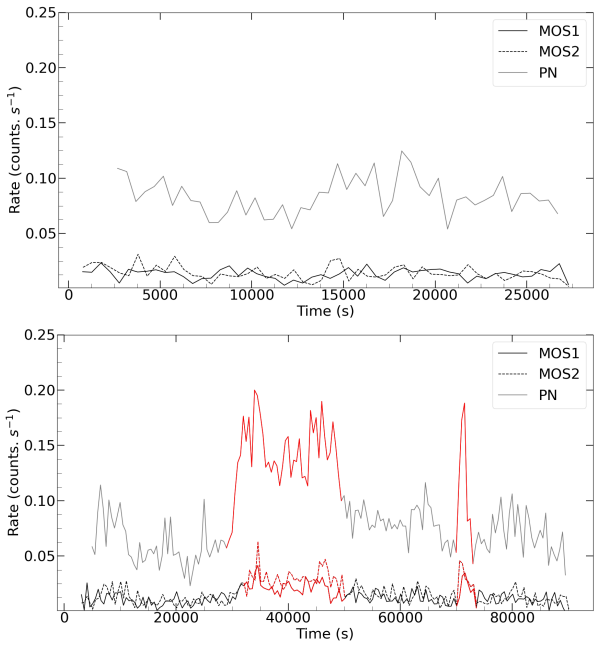

Figure 8.2: The XMM–Newton X-ray light curves of HD 223889, with 500 s time binning in the energy range: 0.2-2 keV. On the left side, we show the signal from the two MOS detectors and the PN signal for *observation 1*, while on the right side, we show the signals from *observation 2*. In both panels, we show the light curves subtracted from the background, normalized to the ratio of the aperture area sizes of source and background $(60/20)^2$. The solid gray line represents the light curve of the PN detector, while the solid and dashed black lines correspond to MOS1 and MOS2, respectively. The red lines in the right panel represent the flare regions (0.125 counts flux threshold).

shows the background subtracted lightcurves of MOS1, MOS2, and PN normalized to the ratio of the aperture area sizes of the source and background for both observations. The solid gray line represents the light curve of the PN detector, while the solid and dashed black lines correspond to MOS1 and MOS2, respectively. The red lines in the right panel represent the flare regions (0.125 counts flux threshold).

In *observation 2* (Fig. 8.2, right panel) the corona of HD 223889 shows a clear variability (shown in red). The resulting lightcurve shows two significant flares, one between 30 ks and 50 ks and the other between 69 ks and 73 ks. Therefore, we divided the lightcurve into two phases: the "quiet" phase and the "flare" phase. This distinction was important because reconnection events associated with flares usually introduce new material into the star's corona, potentially altering its physical and chemical characteristics (Hiei, 1987). Conversely, there was no evidence of flare activity during *observation 1* (Fig. 8.2, right panel). Therefore, we consider the spectra obtained during *observation 1* as representative of a quiescent phase.

8.3.2.HD 223889 coronal properties from X-ray spectra

We extracted CCD spectra of HD 223889 from two MOS cameras, PN detector, and RGS spectra for both observations. For observation 2, we distinguished between two spectra for MOS1, MOS2, PN, RGS1, RGS2, one of which represents the quiescent phase and the other the original spectra with flaring. Using XSPEC version 12.12.1, we conducted a spectral fit with the coronal plasma model vAPEC (Smith et al., 2001) with the solar photospheric abundances from Grevesse & Sauval (1998).

It is common to use the composition of the solar photosphere as a reference for M dwarfs, considering how difficult it is to determine the abundances of these stars (Wood & Linsky, 2010; Wood, Laming, & Karovska, 2012; Wood et al., 2018). This challenge arises from their low effective temperature, which leads to the formation of predominantly molecular lines in their spectra.

A notable aspect of the vAPEC model is the ability to account for variable abundances of different elements in the plasma. When using the vAPEC for spectrum fitting, several free parameters are

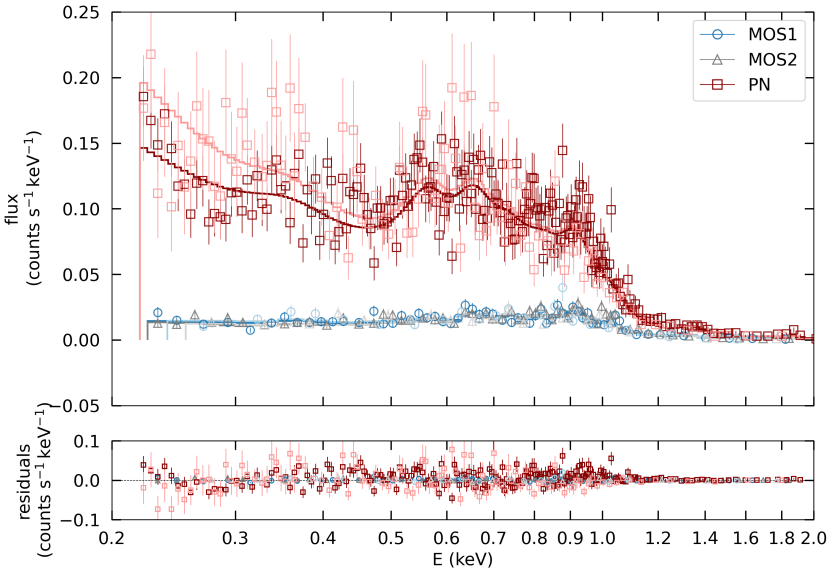

Figure 8.3: Spectra of the EPIC detector as a function of energy (keV), with MOS1 presented by a blue circle, MOS2 by a gray triangle, and PN by red squares. The residuals of the fits are shown in the bottom row. The spectrum has a soft nature, with an average coronal temperature of about 4.4 MK. Vivid colors correspond to *observation 2* quiescent phase, while weak colors represent *observation 1.*

.

available to optimize the fit of the model to the observed data. These parameters include the temperature (kT), which represents the thermal plasma temperature, usually measured in keV. The parameters also include the coronal abundances, which indicate the abundance values for different elements that can be varied independently. Ultimately, our goal is to calculate the O/Fe ratio, a key parameter for assessing FIP bias ($F_{\rm bias}$). The latter provides information on whether there is an iFIP effect.

In Fig. 8.3 we show the best-fit model of the spectra from *observation 1* with the quiescent spectra from *observation 2*. On the top panel, we display MOS1, MOS2, and PN spectra and on the bottom panel, we show the RGS1 and 2. We only show the quiescent spectra of *observation 2* given that we obtained similar results between the quiescent phase and the original spectra (including the flare). The spectral shape clearly shows that HD 223889 is a very soft X-ray source. While HD 223889 demonstrates characteristics of soft X-ray emission, it remains relatively more energetic compared to the Sun. Table 8.3 shows the parameters of the best-fit model for fitting 1 and 2, respectively. The table also shows the emission measure characterized by the parameter "norm" of the vAPEC model along with the X-ray flux in the energy band 0.2–2 keV.

We calculate the average coronal temperature of HD 223889 for the case of fitting Obs. 1 and Obs. 2 to be respectively 4.4 MK and ∼4.5 MK. The estimated X-ray luminosity in the energy band 0.2–2 keV for fitting Obs. 1 is $L_{\rm X} = 4.32 \times 10^{27}$ erg s^{-1}, and $L_{\rm X} = 4.54 \times 10^{27}$ erg s^{-1} for fitting Obs. 2. Its low activity is characterized by an X-ray surface flux of $F_{\rm X,surf} = 5.1$, which is lower than any other M dwarf that has been studied for iFIP patterns.

8.3.3.FIP or iFIP effect?

Our main goal is to quantify the $F_{\rm bias}$ in the corona of HD 223889. To determine the $F_{\rm bias}$, we applied the approach described in Wood, Laming, & Karovska (2012). Ideally, this would require a complete analysis of the line fluxes as described in Wood & Linsky (2010). However, due to the limited number of lines available, such analysis is currently not possible. Instead, we opt for an estimation of the $F_{\rm bias}$ by using only the strongest lines in the spectrum, in particular the lines of Fe and O. Fe is the representative of the elements with low FIP, while O represents the elements with high FIP. This approach allows us to represent the $F_{\rm bias}$ as a single number, with the aim of quantifying $F_{\rm bias}$ in a stellar corona. This method accounts for the abundance measurements of O and Fe for both the coronal abundances derived from X-ray spectra and the photospheric abundances obtained from optical spectra (Eq. 8.1).

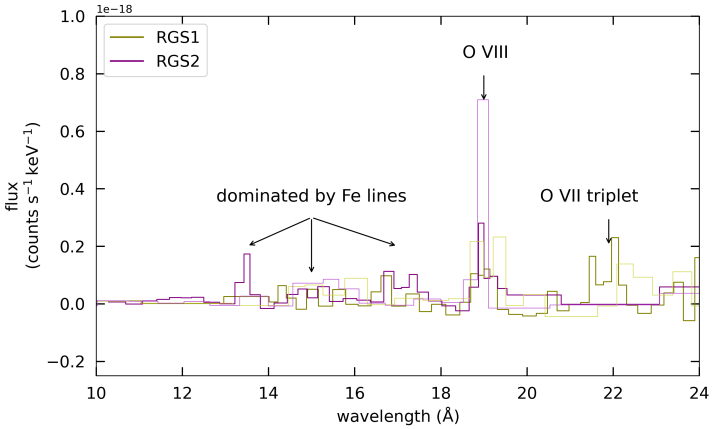

Figure 8.4: Given the relatively low S/N in the high-resolution RGS instruments, we show for guidance the position of the most important O and Fe lines. Spectra of the RGS instruments flux (counts s^{-1}keV) plotted against wavelength (Å). RGS1 is represented by a green line and RGS2 by a purple line. Vivid colors correspond to *observation 2*, while weak colors represent *observation 1*. The different discernible spectral lines such as Fe lines, O VIII, and O VII triplet are indicated by arrows with annotation.

We remind the reader that solar photospheric abundances are used in this study. The abundances shown in Table 8.3 represent the element abundance of O and Fe in the corona corrected to the one from the solar photosphere.

$$\mathrm{F_{bias}} = \frac{\log[\mathrm{O/Fe}]_{\mathrm{corona}}}{\log[\mathrm{O/Fe}]_{\mathrm{photosphere}}} \tag{8.1}$$

For solar-like FIP effect, the F_{bias} has a negative value, while it has a positive value in the case of the iFIP effect. However, HD 223889 shows a FIP pattern in both fittings of $\mathrm{Obs_1}$+ $\mathrm{Obs_2^Q}$ and $\mathrm{Obs_1}$+ $\mathrm{Obs_2^F}$ with a $F_{\mathrm{bias}} \sim$ -0.02. The error associated with F_{bias} was calculated using Gaussian error propagation. We obtained an error around ± 0.04 which is not large when we put it in the context of M dwarf stars and other main-sequence stars (typically ∼0.160, Seli et al. 2022 and references therein).

8.3.4.Estimation of uncertainty

While the uncertainties from the spectra fitting are nominally quite small, we expect the true uncertainties to be larger, since our low-resolution spectra used here contain less information than the high-resolution X-ray spectra used in previous studies of the FIP effect. To quantify the uncertainty associated with our F_{bias} value from low-resolution spectra, we consider the scatter of Fe/O ratios derived from low-resolution XMM spectra and the values derived from high-resolution analyses, as seen in Poppenhaeger 2022 (Figure 4). Using a bootstrap technique with 1000 iterations over this scatter, we determined an overall uncertainty of 0.153. While the numerical uncertainty arising from our low-resolution spectra is a modest 0.04, it is important to note that the systematic uncertainty arising from the low-resolution spectra should be larger about 0.153. This uncertainty places our star in the region of F_{bias} around 0, which is the first M dwarf star to show a flat to almost no iFIP effect.

8.4 Discussion

8.4.1.T_{eff}-F_{bias} diagram

In this section, we look at the properties of HD 223889 compared to other cool main sequence stars to understand the factors that influence the F_{bias}. Figure 8.5 shows a T_{eff}-F_{bias} diagram that includes data from different main sequence stars. Each data point is color-coded according to its X-ray luminosity ($\log L_{\mathrm{X}}$) that serves as an indicator of stellar activity. The selection of stars for this analysis comes from the star list in Wood et al. (2018), along with their intrinsic properties. This selection includes

Table 8.3: Best-fitting parameters of the three-temperature coronal model to the MOS, PN, and RGS data for the *observations 1* and *2* of HD 223889. The first column lists the different resulting parameters, while the second column shows the values obtained when fitting the quiescent spectra of *observation 2* ($\mathrm{Obs}_2^{\mathrm{Q}}$) with *observation 1* ($\mathrm{Obs}_1$), whereas the third column lists the obtained values from the fitting of the original spectrum from the *observation 2* ($\mathrm{Obs}_2^{\mathrm{F}}$) with Obs_1. The values used later in our analysis are represented in bold.

Parameter	Obs_1+ $\mathrm{Obs}_2^{\mathrm{Q}}$	Obs_1+ $\mathrm{Obs}_2^{\mathrm{F}}$
kT_1 (keV)	$0.16^{+0.02}_{-0.03}$	$0.16313^{+0.03}_{-0.02}$
kT_2 (keV)	$0.30^{+0.01}_{-0.01}$	$0.29685^{+0.08}_{-0.07}$
kT_3 (keV)	$0.94^{+0.18}_{-0.16}$	$0.93^{+0.16}_{-0.14}$
norm$_3$ ($\times 10^{-5}$)	1.20	2.12
norm$_1$ ($\times 10^{-5}$)	3.11	2.95
norm$_2$ ($\times 10^{-5}$)	5.15	5.39
O	$0.61^{+0.029}_{-0.029}$	$0.60^{+0.03}_{-0.02}$
Ne	1.0	1.0
Si	1.0	1.0
Fe	$0.64^{+0.05}_{-0.05}$	$0.62^{+0.05}_{-0.05}$
flux (erg cm^{-2}s^{-1}), 0.2-2 keV	$\mathbf{3.52 \times 10^{-13}}$	3.70×10^{-13}
L_{X} (erg s^{-1}), 0.2-2 keV	$\mathbf{4.32{\times}10^{27}}$	$4.54{\times}10^{27}$
F_{bias}	$\mathbf{-0.02\ ^{+0.153}_{-0.153}}$	$-0.02\ ^{+0.153}_{-0.153}$

a mixture of single and binary main sequence stars representing a wide range of activity levels. The X-ray luminosities range from $\log L_{\mathrm{X}} = 26.99$ to $\log L_{\mathrm{X}} = 30.06$, measured directly from the LETGS spectra within the canonical *ROSAT* PSPC bandpass for soft X-ray of 0.1-2.4 keV (e.g., 5–120 Å).

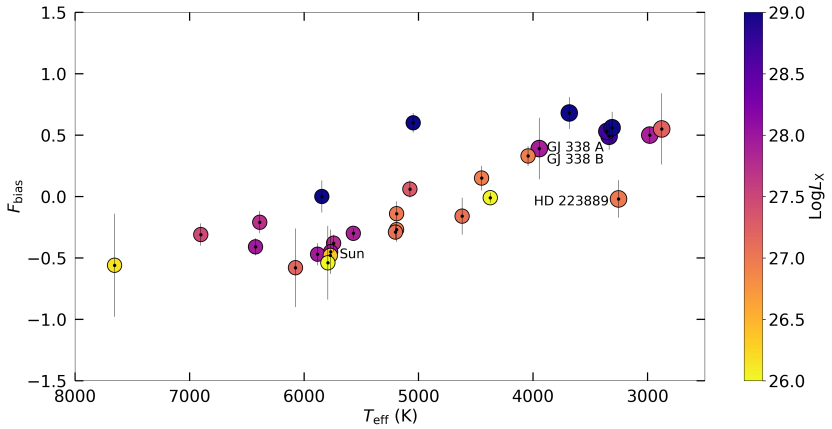

Figure 8.5: T_{eff}-F_{bias} diagram for F, G, K, and M main-sequence stars taken from Wood et al. (2018). The color-coded data points indicating log L_{X} (X-ray luminosity) which is also taken as an activity indicator.

According to the T_{eff}-F_{bias} relationship described in Wood & Linsky (2010) and Wood et al. (2018), an iFIP effect would be expected for HD 223889 that is consistent with the pattern observed in M dwarfs, regardless of their activity level. This relationship is particularly evident in the almost linear progression of stellar composition across spectral types F to M in the X-ray spectra of moderately active stars (L_{X} less than 10^{29} erg s^{-1}). From our low-resolution spectra we have determined $F_{\mathrm{bias}} \sim 0$ with large uncertainties (e.g., no FIP or iFIP bias) for HD 223889 (Section 8.3.4). This places HD 223889 below the M0V wide binary star GJ 338 AB, which is reportedly associated with the smallest documented

iFIP effect to date ($F_{\rm bias} = 0.39$, Wood, Laming, & Karovska 2012).

HD 223389 and the binary star GJ 338 have similar properties in terms of radius, X-ray surface fluxes, and activity level, with GJ 338 AB being slightly more active than HD 223889 (details on the properties of GJ 338 AB can be found in Wood et al. 2018). Based on these similarities, we expect a similar filling factor, and consequently a comparable $F_{\rm bias}$ for the binary and HD 223889. Since this is not the case, we have gone one step further and investigated what is the expected unsigned average magnetic field strength of the binary system GJ 338 and HD 223889.

By analyzing the ratio between X-ray luminosity and bolometric luminosity ($L_{\rm X}/L_{\rm bol}$) plotted against the average magnetic field represented by $\langle B \rangle$ in the study of Reiners et al. (2022), we have determined an average surface magnetic field strength of about 500 G for the binary star GJ 338 and about 300 G for HD 223389. These magnetic field strengths correspond to $L_{\rm X}/L_{\rm bol} = 4.13 \times 10^{-5}$ for HD 223389 and $L_{\rm X}/L_{\rm bol} = 2.95 \times 10^{-5}$ for GJ 338 AB. It is important to point out that the uncertainties associated with $\langle B \rangle$ cannot be estimated due to the significant scatter observed in the aforementioned plot of Reiners et al. (2022). The difference in $\langle B \rangle$ expected for the binary GJ 338 and HD 223889 suggests that the discrepancy in $F_{\rm bias}$ could be due to either a higher filling factor or a lower filling factor associated with regions of intense magnetic fields for the binary star GJ 338. In the first scenario, the higher $F_{\rm bias}$ in the GJ 338 binary system could be due to the limited volume available for magnetic field expansion (Baker et al. 2019; Laming 2021). Consequently, Alfvén waves leaving the chromosphere cannot diverge, which increases the probability of reflection and refraction back into the chromosphere. Alternatively, if the high $F_{\rm bias}$ is associated with concentrated regions of high activity, this increases the probability of Alfvén waves being reflected into the chromosphere, since in these regions plasma $\beta < 1$. This assumption can be supported by the X-ray observations of Wood, Laming, & Karovska (2012), in which they detected several short flares in GJ 338 A, the kind of flares that are common in M dwarfs (e.g.,Osten et al. 2005; Kowalski et al. 2009). However, to better understand what influences the FIP effect, we need further knowledge about the different intrinsic properties of the two binary star systems GJ 338 and HD 223889, such as the magnetic field distribution on the surface of the stars.

Furthermore, one could argue that the discrepancy in the $F_{\rm bias}$ between the binary stars GJ 338 and HD 223889 is due to the fact that GJ 338 B hosts a nearby exoplanet at about 1 AU. The study in Wood et al. (2018) suggests that the nearby massive exoplanets (e.g., those with Jupiter-like mass), could possibly influence the coronal abundances of their host stars. This hypothesis is based on high-resolution X-ray spectra, which show expected higher than values for the host star τ Boo A. In this case, the value of $F_{\rm bias}$ slightly exceeds expectations, and the ratio of coronal to photospheric iron abundance is significantly lower. A similar scenario was observed for another host star, HD 189733 A, which was also orbited by a close-in planet of Jupiter mass. However, this explanation does not apply to GJ 388 B as it is orbited by a super-Earth planet with a mass of about $10.27^{+1.47}_{-1.38}$ $M_{\oplus}$ (González-Álvarez et al. 2020), and located at a distance ∼0.142 AU (González-Álvarez et al., 2020; DiTomasso et al., 2023). Furthermore, the measurements of *XMM-Newton* obtained in Wood, Laming, & Karovska (2012) for GJ 388 B show no anomalies.

The observation of HD 223889 raises the question of whether there may be a plateau in the $F_{\rm bias}$ values for M dwarfs. Further investigation is essential to determine whether the $F_{\rm bias}$ of M dwarfs converges to zero or can reach lower values. In the latter case, this could indicate that an M dwarf is going through a transition phase. In addition, these results suggest that the relationship between $T_{\rm eff}$ and $F_{\rm bias}$ established in Wood, Laming, & Karovska (2012) needs to be re-evaluated, as there may be cases where M dwarfs deviates from the expected correlation between $T_{\rm eff}$ and $F_{\rm bias}$. Changes in stellar properties, such as changes in radius, surface gravity, or convective motions resulting from the propagation of Alfvén waves through the chromosphere, can influence the FIP and iFIP effect for M dwarfs, as suggested in Wood, Laming, & Karovska (2012).

8.4.2.More than one bimodality in $T_{\rm eff}$-$F_{\rm bias}$ diagram?

In the study conducted by Seli et al. (2022), the aim was to extend the $T_{\rm eff}$-$F_{\rm bias}$ diagram originally developed by Wood, Laming, & Karovska (2012) and later refined by Laming (2015) to involve evolved stars. The original diagram focused only on main sequence stars namely Sun-like stars and M dwarfs. To achieve this, they systematically compiled data on all active stars for which coronal abundance values were available in the literature, which facilitated the calculation of $F_{\rm bias}$. Their results showed that the

$T_{\rm eff}$-$F_{\rm bias}$ relation now has almost parallel branches that are about 0.5 apart in $F_{\rm bias}$. In particular, in their work low-mass M dwarf stars (Teff $< 4000\,$K) show a clear position in the continuation of the original relation. The bimodal distribution of $F_{\rm bias}$ values was hinted in (Wood et al. (2018), Fig. 7a).

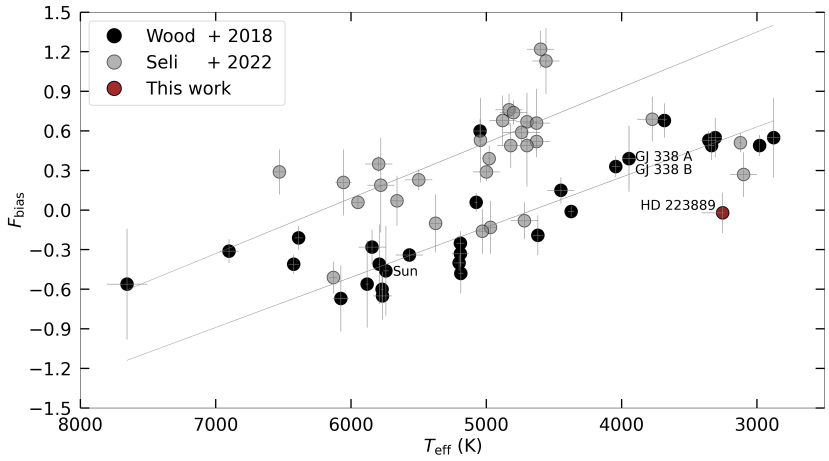

Figure 8.6: $T_{\rm eff}$-$F_{\rm bias}$ diagram. The black dots represent the stars from Wood et al. (2018) and the gray dots correspond to the additional stars from the sample of Seli et al. (2022). The red dot represents one of the $F_{\rm bias}$ of HD 223889 as the values are very close to each other. Each data point is plotted with the corresponding error bars for the effective temperature ($T_{\rm eff}$) and the FIP bias value ($F_{\rm bias}$). The 2 gray lines represent the fit of the lower and upper branches from Seli et al. (2022), Eq. 2 and 4 respectively.

In Fig. 8.6 we show the $T_{\rm eff}$-$F_{\rm bias}$ diagram with the additional $F_{\rm bias}$ of HD 223889 (red dot). The black dots represent the stars from Wood et al. (2018) and the gray dots correspond to the additional stars from the sample of Seli et al. (2022). Each data point is plotted with its corresponding error bars for the effective temperature ($T_{\rm eff}$) and the FIP bias value ($F_{\rm bias}$). The 2 gray lines represent one of the two fitted lines for each one of the trends seen in Seli et al. (2022) that corresponds to Eq. 2 and 4.

The diagram in Fig.8.6 suggests a possible divergence in the $T_{\rm eff}$-$F_{\rm bias}$ relation among M dwarfs. To fully understand the factors contributing to this deviation it is essential to perform further observations on M dwarfs with low activity.

8.5 Conclusions

In this study, we have performed a detailed analysis of the coronal abundance patterns of HD 223889 using *XMM-Newton* data. This star is the lowest activity M dwarf star studied so far with respect to the FIP effect. Our observation of HD 223889 showed for the first time a flattened to null iFIP, in an M dwarf. These results challenge the assumption that all M dwarfs should exhibit a iFIP effect. They also prompt us to re-evaluate the $T_{\rm eff}$-$F_{\rm bias}$ relationship. Our results motivate the study of a small sample of low coronal temperature range M dwarfs. This information will allow us to update our current understanding of (i)FIP patterns and their causes. It will also tell us whether this pattern is broken by M dwarfs at even lower coronal temperatures. Finally, a comprehensive study of elemental abundances in the corona provides valuable insight into the composition of energetic particles and serves as a representative sample of coronal material. This research is of particular importance for planetary habitability, as these particles can affect surface chemistry and thus influence the prospects for a planet's long-term habitability over geological timescales.

Acknowledgments: J.J.C. and K.P. acknowledge support from the German Leibniz-Gemeinschaft under project number P67/2018.

Far beyond the Sun-IV. A numerical exploration in the realm of Horologium

Judy J. Chebly[1,2], *Julián D. Alvarado-Gómez*[1], *Eliana-Amazo-Goméz*[1], *Katja Poppenhäger*[1,2], *et al.*
[1]Leibniz Institute for Astrophysics, An der Sternwarte 16, D-14482, Potsdam, Germany
[2]Institute of Physics and Astronomy, University of Potsdam, Potsdam-Golm, D-14476, Germany
In preparation. To be submitted to Astronomy & Astrophysics journal.

This is the fourth paper in the campaign "*Far beyond the Sun*'. This campaign is an observational and numerical study aimed at characterizing the magnetic cycle of ι Hor using high-resolution spectropolarimetry and determining how this evolving field affects the corona and wind environment around the star. In Paper I (Alvarado-Gómez et al., 2018) we presented precise measurements of the star's magnetic activity and radial velocity and their variability on different timescales. In Paper II (Amazo-Gómez et al., 2023), by analyzing TESS data taken simultaneously with the HST data, we were able to derive correlations between different observational data and study the star from its photosphere to its corona. In Paper III (Alvarado. Gomez et al. 2024 in prep.), we presented 18 large-scale ZDI magnetic field maps of ι Hor spanning almost three years, sufficient to cover two complete coronal cycles and reveal the magnetic cycle. The aim of this last part of the investigation (this work) is to study the evolving magnetic field in this star that affects its circumstellar environment through magnetic winds. The analyzed observations provided by the Zeeman Doppler imaging maps provide detailed information about the large-scale field evolution and the cyclic activity phenomena, essential parameters for any physical mechanism proposed for the magnetic field generation (e.g. dynamo theories). Moreover, the obtained maps of the surface magnetic field serve as input for a state-of-the-art self-consistent solar model to simulate the coronal structure and magnetized winds. The analyzed observations are also used to predict the conditions to which the exoplanet is exposed during its orbit and during the magnetic cycle of its parent star. The fact that the location and properties of the exoplanets are very well known makes the study of the circumstellar region of the star even more precise.

9.1 A Brief Introduction on ι Hor

ι Horologii (ι Hor, HD 17051, HR 810), estimated to be about $\sim$ 625 Myr (Lebreton, Fernandes, & Lejeune, 2001), roughly consistent with the age of $\sim$ 500 Myr calculated from the X-ray emission by Sanz-Forcada et al. (2011), $\sim$ 625 Myr from asteroseismology (Vauclair et al., 2008), and 740 Myr from gyrochronology (Barnes, 2007). ι Hor has features reminiscent of the young Sun. It falls under the spectral classification F8V-G0V, has a temperature of $\sim$ 6,080 K and a radius of $\sim$ 1.16 $R_\odot$ (Vauclair et al., 2008; Bruntt et al., 2010), see Tab.9.1) located at a distance of 17.24±0.16 pc (van Leeuwen, 2007). This stellar system harbors a Jupiter-like exoplanet at a distance of 1 AU, a discovery carefully confirmed by Kürster et al. (2000); Zechmeister et al. (2013); Naef et al. (2001) and Butler et al. (2001). It hosts a planet with M sin i = 2.26 MJ orbiting at a separation of 0.92 AU (Kürster et al., 2000).

Table 9.1: Fundamental properties of ι Hor

Parameter	Value	Reference
Spectral Type	F8V-G0V	Bruntt et al. 2010
Teff (K)	6080 ± 80	Bruntt et al. 2010
log(g)	4.399 ± 0.022	Bruntt et al. 2010
$R_\star$ ($R_\odot$)	1.16 ± 0.04	Bruntt et al. 2010
$M_\star$ ($M_\odot$)	1.23 ± 0.12	Bruntt et al. 2010
hvRi (km s^{-1})	16.943 ± 0.002	Alvarado-Gómez et al. 2018
Prot (days)	$7.70^{+0.18}_{-0.67}$	Alvarado-Gómez et al. 2018
Age (Myr)	∼625	Vauclair et al. 2008

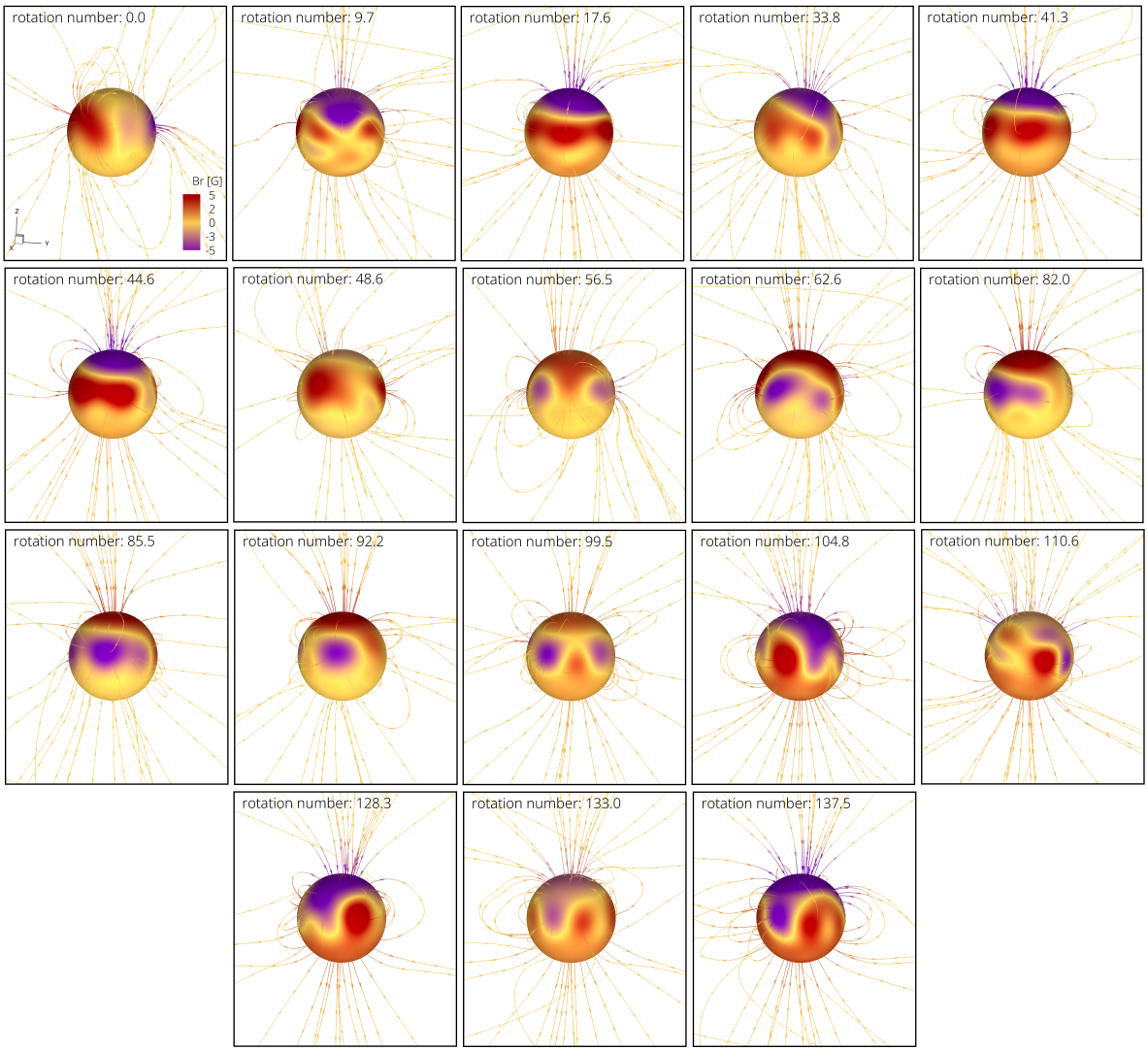

Figure 9.1: Examples of surface field distribution (in Gauss) of 18 epochs of ι Hor retrieved from ZDI maps. Each epoch is represented by its corresponding rotation number (top row left to right). The star surface as well as the magnetic field streams are color-coded by the normalized radial magnetic field. The 3D orientation axis in the first panel indicates the assumed stellar rotation axis for all the epochs. The radial magnetic field strength ranges from 3.3 G to 11.6 G.

What's Next?

On this journey, we have seen that dealing with magnetic fields involves many intricacies but also reveals fascinating phenomena. I have given an overview of the current state of stellar wind research, emphasizing that both observations and simulations are needed to better understand the mechanisms that drive stellar winds and their influence on planets in orbit. This should be a complementary effort, with both disciplines working together to optimize and overcome the limitations of each approach.

We also saw the evolution of our understanding of stellar wind generation and acceleration, the mechanisms behind the FIP effect, and much more. Despite the progress, there is still much to do and discover. Each new finding opens the door to further research, especially when the results are unexpected. Each study mentioned in this manuscript has contributed to our knowledge in this field, with some revolutionizing our understanding of stellar winds and the FIP effect. My work, in particular, has opened new horizons and led to new insights.

The results described in Chapter 6 propose a new approach to defining the habitable zone (HZ) and emphasize the importance of the Alfvén surface (AS). We suggest that the AS could serve as the inner boundary of the HZ. This redefinition could push the inner boundary further away from the star than previously predicted based on surface temperature alone, as atmospheres within this new HZ boundary could be easily eroded.

In Chapter 7 we did a study that can be applied to several cool main sequence stars. In doing so, we make an important contribution to the field of space weather and provide a fundamental framework for future investigations, particularly with respect to the observation of stellar winds and their effects on planetary atmospheres. The different wind velocities obtained in this chapter emphasize the need to carefully select velocity properties when using hydrodynamic models to quantify $\dot{M}_\star$ from the astrosphere. Our comparative study has revealed differences in mass loss between some stars, prompting us to investigate these discrepancies further and understand what they might mean for future research. This project also opens the door to exploring whether there is saturation of the stellar wind for fast-rotating stars in the saturated regime. This could also include the study of stars in the so-called supersaturated regime and potentially provide valuable insights. In addition, we saw even though we had a spread in spectral type stars with ZDI maps, we are still missing fast and slow rotators to cover different masses and rotations.

The results from Chapter 8 suggest that even the study of a single star can provide meaningful information about the persistence of the inverse FIP (iFIP) pattern. If the iFIP pattern is disrupted or weakened at moderately low coronal temperatures, it is useful to study a small sample of such stars to collect more data points in the lower temperature range.

Overall, this work raises many questions and greatly enhances our understanding of both the stars themselves and their effects on the planets orbiting them. It opens up new avenues for exploration at different scales and advances our knowledge of star-planet interactions.

10.1 Probing the Corona and Winds

In order to optimize simulations of stellar coronae and winds, we need to improve our inner and outer boundary conditions. A detailed coronal temperature and density distribution defining the inner boundary is crucial. This data can be obtained from X-ray observations with instruments such as *XMM-Newton* and *Chandra*. In addition, we need more observational and simulated data on the stellar wind to define the outer boundary conditions. With a detailed characterization of the corona and the winds, we can constrain the inner edge condition of the HZ given by the AS and the outer edge condition given by the wind.

However, accurate measurements and estimates depend on indirect methods to detect the wind and on the quality of the ZDI maps. Zeeman Doppler imaging maps are necessary to constrain the magnetic field but the problem is that ZDI are highly inhomogeneous and sometimes not comparable (even for the same star). That certainly will create issues on any models derived from them. Currently, among all cool stars, there are only three M dwarf systems with $\dot{M}$ constraints (see Fig. 10.1).

Better Constraint on the Inner Boundary Conditions

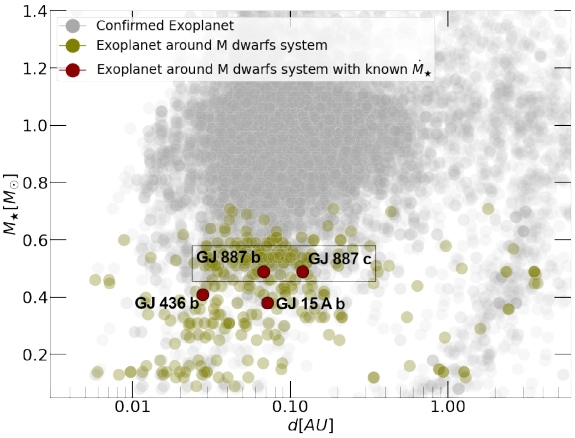

Figure 10.1: Confirmed exoplanets with respect to the stellar mass and orbital distance. The plot was created using data from NASA's exoplanet archive of confirmed exoplanets. Exoplanets orbiting an M dwarf are shown in green. In red, we show the exoplanet orbiting an M dwarf with a constraint on the wind mass loss. The two exoplanets of our requested target are highlighted with a black box. Picture credit: J.chebly.

Coronal Temperature and Density

So far we have relied on the coronal density and temperature of the Sun in the wind simulations. This is because the Sun is the only cool star for which we have a detailed characterization of its coronal properties. Determining the coronal temperature and density distributions for a number of cool main-sequence stars is a challenge, especially for M dwarfs. These stars are fainter and cooler than the Sun, leading to the formation of molecular lines in their spectra. This makes it difficult to accurately extract the line profiles and apply differential emission measurement techniques.

However, if we take advantage of the concept of *freeze-in* picture of the ionized elements in the wind, we can trace back the temperature and density distributions (see Sec. 4.5). The temperature of the corona determines the ionization states of elements such as oxygen. Higher temperatures lead to higher ionization states, which are associated with certain spectral lines. The intensity and shape of these lines can be altered by the presence of a magnetic field through the Zeeman effect. Temperature fluctuations influence the width and intensity of the spectral lines. Hot regions cause broader lines due to increased thermal motion, while cooler regions result in narrower lines.

By accurately measuring these ionization states and their spectral lines, we can infer the coronal temperature and density distributions. This approach would allow us to tailor simulations to the unique properties of different stars and gain deeper insights into their coronal structures and stellar wind properties. This is particularly beneficial for M dwarfs, where it is more difficult to obtain high-resolution spectral data. This will help with more accurate $F_{\rm bias}$ estimations along other benefits.

Better ZDI maps

For M dwarfs the upcoming near-infrared spectropolarimetric data from SPIRou[1] (SpectroPolarimètre InfraRouge) on the CFHT (Canada-France-Hawaii Telescope) and the improved CRIRES[2] (CRyogenic high-resolution InfraRed Echelle Spectrograph) at the VLT (Very Large Telescope) will facilitate the detection and monitoring of global magnetic fields in slowly rotating, inactive M dwarfs. Theoretically, larger telescopes are the solution, but we have to keep in mind that M dwarfs can have extremely long rotation periods (for example Proxima Cen with 83 days). A ZDI campaign for such a slowly rotating star is not only a challenge for the observations (as there are not many Doppler components to work with), but also because we will not be able to (realistically) follow a star with ZDI for that long.

A broad spectrum of molecular and atomic diagnostic lines in the near infrared is suitable for effective measurements of Zeeman broadening. The broadening is proportional to the square of the magnetic field strength. This allows the measurement of weaker total fields in inactive stars and provides

[1] High-resolution spectropolarimeter designed for near-infrared (NIR) observations. It is installed at the Canada-France-Hawaii Telescope (CFHT), located on Mauna Kea, Hawaii. SPIRou's main objectives include the discovery of exoplanets around M dwarfs through radial velocity measurements and the study of stellar magnetism. The NIR capability is particularly advantageous for observing M dwarfs, which emit most of their light in this part of the spectrum.

[2] An instrument on the Very Large Telescope (VLT) located at the Paranal Observatory in Chile. It has been upgraded to CRIRES+ to improve its capabilities. CRIRES+ is a high-resolution infrared spectrograph that operates in the near-infrared. Improvements include an extended wavelength range and higher sensitivity, enabling more detailed and precise observations of celestial objects.

more reliable field strength distributions for active M dwarfs. However, at these wavelengths there is also all the confusion due to the molecular bands and the extreme difficulty of properly modeling these molecular signatures in the presence of a magnetic field. There are other problems, such as laboratory knowledge of the line lists for these molecules and important properties such as their Landé factors (which is related to the previous point of quantum description of these systems). Therefore, the advantages of going more into the "red" are usually not compensated by the drawbacks.

One can think of Zeeman broadening (ZB) technqiue is a valuable tool for studying stellar magnetic fields as it allows for magnetic field strength measurements without requiring polarization, thus applicable to a wider range of stars, including those with long rotation periods. However, it lacks information on field geometry, which requires techniques like ZDI. When considering observational strategies, larger telescopes offer higher sensitivity and resolution essential for detailed exoplanet atmospheric characterization and detecting weaker signals, whereas smaller, dedicated telescopes can provide more frequent and consistent observations of stellar magnetic fields. A balanced approach, utilizing large telescopes for high-impact targets and small, dedicated ones for extensive magnetic field surveys, would maximize scientific return, offering detailed characterization and comprehensive datasets. More information on the advantages and drawbacks of both ZB and ZDI techniques can be found in Sec. 5.2.

High signal-to-noise ratio (S/N) spectra of low-mass stars, especially those obtained with CRIRES powered by the 8-m VLT, will allow the study of polarization in individual spectral lines. This capability will overcome many of the assumptions and simplifications associated with Least Squares Deconvolution (LSD) modeling and allow the reconstruction of more robust and physically realistic ZDI maps (Donati et al., 1997; Wade et al., 2000; Kochukhov, Makaganiuk, & Piskunov, 2010). This in turn will solve the problem of unrealistically large local field strengths resulting from the global field filling factor approach used in tomographic mapping of low-mass stars.

Better Constraint on the Outer Boundary Conditions

Recent studies have shown promising results in using the charge exchange method to infer mass loss in cool main sequence stars. This method has already been successfully applied to at three stars and few upper limits, indicating its potential reliability Kislyakova et al. (2024). The charge exchange method appears to have several advantages over the Lyα absorption method. One major advantage is that it is not heavily dependent on line-of-sight as in the case of Lyα astrospheric technique. Also, this method can cover a wider range of stars given that it is not limited to 10 pc (Wargelin & Drake, 2001, 2002). However, the charge exchange method is not as successful as the Lyα method and is not used as frequently because this depends on the size of the astrosphere around the star. The main difference between these techniques lies in the wavelengths they observe, which could affect their effectiveness and the type of data they produce.

There is also another possible wind detection method using transmission spectroscopy (see Sec. 5.5, for more information on the method), this technique requires UV observation. The method of transmission spectroscopy, which is based on UV observations, is currently limited to space telescopes such as the HST. However, recent discoveries of escaping atmospheres by ground-based instruments, such as Hα and the HeI triplet at 10,830 Å (Yan & Henning, 2018; Nortmann et al., 2018; Spake et al., 2018; Allart et al., 2019), offer new opportunities to study these phenomena and their interaction with stellar winds (Oklopčić & Hirata, 2018; Villarreal D'Angelo et al., 2021). Hα (6563 Å), which corresponds to electron transitions in hydrogen atoms, and the HeI triplet (5876, 6678, and 7065 Å), which represents transitions in neutral helium atoms, are often observed with ground-based telescopes equipped with appropriate spectrographs. These observations provide valuable insights into stellar activity, chromospheres, and atmospheric properties. Table 10.1 lists possible ground-based telescopes that are suitable for observing these emission lines.

What Science Cases Benefit from better Boundary Conditions?

Relation Between Wind Speed and FIP effect: In the study by Wood & Linsky (2006), they investigated the correlation between the observed abundance variations and the wind strength in three binary star systems: 36 Oph, ϵ Eri and 70 Oph. They found that the 36 Oph binary with the weakest wind has a modest FIP effect in the coronae of both stars, indicating a possible connection between weak winds and a strong $F_{\rm bias}$. The wind strength and the absence or weakness of the FIP effect

Table 10.1: Ground-based telescopes capable of observing H-alpha and He I triplet emission lines. Column 1 to 4 list respectively; the different telescopes, location, status, and the instruments associated with each telescope suitable for Hα and HeI observation. For the status, CA indicates currently available and UC indicates upcoming.

Telescope	**Location**	**Status**	**Instruments Suitable for H-alpha/He I Observations**
William Herschel Telescope (WHT)	La Palma, Canary Islands, Spain	CA	ISIS (Intermediate-dispersion Spectrograph and Imaging System)
Subaru Telescope	Maunakea, Hawaii, USA	CA	HSC (Hyper Suprime-Cam), FOCAS (Faint Object Camera and Spectrograph)
Very Large Telescope (VLT)	Paranal Observatory, Chile	CA	FORS2 (FOcal Reducer and low dispersion Spectrograph 2), UVES (Ultraviolet and Visual Echelle Spectrograph)
Gran Telescopio Canarias (GTC)	La Palma, Canary Islands, Spain	CA	OSIRIS (Optical System for Imaging and low-Intermediate-Resolution Integrated Spectroscopy)
Keck Observatory	Maunakea, Hawaii, USA	CA	LRIS (Low Resolution Imaging Spectrometer), HIRES (High-Resolution Echelle Spectrometer)
Giant Magellan Telescope (GMT)	Atacama Desert, Chile	UC	To be determined (various planned high-resolution spectrographs)
Extremely Large Telescope (ELT)	Atacama Desert, Chile	UC	ANDES (Atacama Near-infrared Differential Survey), HARMONI (High Angular Resolution Monolithic Optical and Near-infrared Integral field spectrograph), METIS (Mid-infrared ELT Imager and Spectrograph)

in ϵ Eri further support this connection. However, the presence of both high and no/inverse $F_{\rm bias}$ stars in 70 Oph complicates interpretation. Although the small sample size does not allow definitive conclusions, similarities with observations on the Sun suggest a plausible correlation between FIP and wind (von Steiger et al., 2000). It is important to emphasize that our X-ray spectra primarily represent brighter, high-density plasma confined in coronal loops, and not the outflowing wind material. Thus, any potential connection between FIP and wind would therefore be indirect. To explore this connection further, we need detailed data on coronal temperature and density for different spectral types of stars. This will allow us to better characterize both the $F_{\rm bias}$ and the wind and improve our understanding of a possible correlation between them.

Wind saturation of stars in saturated regime: Investigate whether there is indeed saturation of the stellar wind of stars in the saturated regime as seen in chapter 5.

Contribution of different factors in $\dot{M}_\star$ total budget: Further numerical simulations are needed to better understand the role of flares, coronal mass ejections (CMEs) and prominences in influencing $\dot{M}_\star$ for stars in the saturated regime. We saw in Chapter 7 have shown that the current methods for estimating $\dot{M}_\star$ from CME contributions are only a rough approximation. The method also neglect the expected influence due to CME magnetic confinement. Taking such considerations into account is crucial for developing a more accurate framework for interpreting the observed properties of stellar CME events and candidates.

Will Better Constraints Affect Current Results?

Higher-quality ZDI maps provide finer details of magnetic field structures on the stellar surface, potentially revealing previously unseen complexities, such as small-scale magnetic features. Moreover, a more detailed coronal density and temperature distribution is likely to affect wind parameters, especially for mid- to late-M dwarfs, as these stars are fully convective. More accurate coronal density and temperature measurements can lead to refined calculations of $\dot{M}_\star$, potentially indicating higher or lower rates than previously thought. Since the $\dot{M}_\star$ depends on coronal density, higher density results

in a higher $\dot{M}_{\star}$.

Better quality ZDI maps will provide a more accurate distribution of the magnetic field on the star's surface, greatly affecting AS size and shape, which in turn influences the estimated angular momentum loss. Consequently, the expected AS sizes for different spectral type cool main-sequence stars might be smaller or larger than currently estimated. Since the AS acts as an inner boundary condition for HZ, this boundary might be either narrower or further out than anticipated, changing the expected wind conditions, especially for close-in planets in HZ. This could make habitability conditions on potentially habitable planets even harsher. Lastly, better constraints will help us extend observations to a wider range of spectral type stars. This will allow us to explore how wind properties vary between different stellar populations.

10.2 Wind-Planet Interaction

More Insight on The Environment of Close-in Exoplanets

There are new advances in our understanding of wind conditions around exoplanets. Until recently, there were no in situ measurements of solar wind plasma at close distances to the Sun. Now, however, NASA's Parker Solar Probe (PSP) launched back in 2018, is now providing insights into the solar wind at distances of up to 31.79 $R_{\odot}$ (about 0.147 AU) from the Sun (The Sky Live 2024). The PSP mission is expected to continue its exploration along the heliospheric equator, gradually approaching the Sun after a series of Venus flybys. Eventually, it will reach a highly elliptical orbit with a perihelion of 0.046 AU, a configuration reminiscent of the orbits of hot Jupiter.

These efforts are complemented by the European Space Agency's Solar Orbiter, that was launched in February 2020. While Solar Orbiter will study the solar wind at small distances down to 0.29 AU, it will focus primarily on high heliospheric latitudes, particularly the polar regions. Together, these two spacecraft will provide unprecedented in-situ measurements of the solar wind at remarkably close distances to the heliosphere. By shedding light on the physical mechanisms responsible for the acceleration of the solar wind, they promise to deepen our understanding of the environment surrounding close-in exoplanets.

Simulate Different Wind-Planet Scenarios

The field of exoplanets is rapidly becoming one of the most dynamic areas of astrophysical research. As more and more exoplanets are discovered around other stars, innovative techniques have been developed to characterize these distant worlds. Understanding the evolution and potential habitability of these planets depends on two crucial factors: the behavior of the host star's winds and their interactions with the planets. By reconstructing the magnetic fields of planet-hosting stars using spectropolarimetric observations, we can create detailed magnetic field maps. These maps serve as the basis for simulations of stellar winds and provide information about the speed, pressure, and density of the wind as it moves away from the host star. In addition, these simulations help us to understand the effects of stellar winds on the space weather of the planets they orbit.

As discussed in section 5.10, nearby planets can experience different types of magnetic interactions depending on whether they are inside or outside AS. With advanced simulations, we can now model and quantify these scenarios. We can simulate a two-body system to estimate how wind conditions change with respect to the location of the planet with respect to AS alter the wind conditions. Also, we can study how the inclination of the star affects the wind-planet interactions. In addition, we can study the influence of the star's magnetic field distribution on the interaction with the exoplanet and simulate the star's magnetic cycle to understand its effects on the planet.

10.3 Benefits from Instruments/Missions

The use of current instruments such as HARPS, ESPaDOnS, and SPIRou, as well as current and future missions such as JWST and PLATO and advanced ground-based telescopes such as VLT and

ELT will significantly improve our ability to study stellar winds and magnetic fields. Higher quality ZDI maps and comprehensive observational data will enable more accurate simulations and a deeper understanding of how stellar environments affect exoplanets, which will ultimately help in the search for habitable worlds. In table 10.2, I list the different characteristics of each instrument/mission and explain how they are useful in the field of winds and exoplanets with some references.

Table 10.2: In this table I list the characteristics of the instruments and missions. Columns 1-4 list the name of the instrument/mission and whether it is a ground-based or space-based instrument. In column 2 I list the corresponding wavelength for each instrument/mission, while in column 3 I list the corresponding benefit and the last column is for references

Instrument/Mission	**Wavelength Range**	**Usage/Benefits**
	Ground-based Instruments	
HARPS	Optical	Detects exoplanets via radial velocity method; provides data on stellar activity correlated with magnetic field variations[1]. HARPS also has a polarimetric mode, so it is able to generate ZDI maps. It is also the only optical HR spectropolarimeter in the southern hemisphere. This is important because PLATO will initially focus on the southern field, which will be largely inaccessible to ESPADONS or SPIROU.
ESPaDOnS	Optical	High-resolution spectropolarimetry for mapping stellar magnetic fields; produces ZDI maps for understanding magnetic environments affecting exoplanets[2].
SPIRou	Near-Infrared (NIR)	Targets cooler stars (e.g., M dwarfs) brighter in the NIR; provides high-resolution spectropolarimetric data for mapping magnetic fields and studying stellar winds[3].
Very Large Telescope (VLT)	Optical to Infrared	Equipped with instruments like CRIRES for high-resolution spectroscopy; studies stellar atmospheres and magnetic fields through spectropolarimetric measurements[4].
Extremely Large Telescope (ELT)	Optical to Near-Infrared	Future telescope with unprecedented resolution and sensitivity; provides detailed spectropolarimetric data for precise mapping of stellar magnetic fields and understanding stellar winds[5].
	Space-based Instruments/Missions	
Hubble Space Telescope (HST)	Ultraviolet to Near-Infrared	High-resolution imaging and spectroscopy; useful for studying stellar atmospheres, magnetic activity, and inferring stellar wind properties[6].
James Webb Space Telescope (JWST)	Near-Infrared to Mid-Infrared	Revolutionizes understanding of exoplanet atmospheres and stellar environments; observes effects of stellar winds on exoplanetary atmospheres and detects indirect signatures of stellar magnetic fields[7].
PLATO	Optical	Detects exoplanets and characterizes host stars through asteroseismology; improves understanding of stellar interiors and magnetic fields[8].

[1] Mayor et al. (2003); Pepe et al. (2004)
[2] Donati et al. (2003)
[3] Donati et al. (2020)
[4] Kaeufl et al. (2004)
[5] Gilmozzi et al. (2007)
[6] Greenhouse et al. (1993)
[7] Gardner et al. (2006)
[8] Rauer et al. (2014)

10.4 Winds Simulations, A Piece of Bigger Puzzles

In these concluding remarks, I would like to emphasize the fact that simulations of the stellar winds can be used both as a stand-alone method and as part of a larger framework. I will mention a few studies that implemented stellar wind simulations in their models.

For instance, simulations of the stellar wind can serve as an inner boundary for astrospherical simulations. In the study of (Herbst et al., 2022), they aim to provide a comprehensive understanding of astrospheric environments and their impact on the surrounding space. Wind simulations are essential for modeling the interaction between the stellar wind and the interstellar medium, as well as for studying the effects of the azimuthal magnetic field component and the motion of the local interstellar medium with respect to the star. These simulations also play a crucial role in understanding the astrospheric environments of different types of stars, including cool stars and high-mass stars, and their impact on the surrounding space.

Another example in which stellar wind simulations are used as inner boundary conditions can be found in by (Scherer et al., 2015). In their study, the stellar wind is implemented to understand the cooling and heating processes within the astrosphere and to determine the transport of galactic cosmic rays and their possible impact on the observational data. In addition, the parameters of the stellar wind, such as mass loss rate, terminal velocity, and temperature, are important inputs for the hydrodynamic model. They are derived from observations or determined by sophisticated estimates to accurately represent the astrospheric conditions.

However, there are some challenges in the complexity of integrating different models, as each simulation may have its own assumptions, numerical methods, and input parameters. Ensuring the compatibility and consistency of data and results from different simulations can be a major challenge. In addition, discrepancies in resolution, domain size or time steps between simulations may introduce errors or inconsistencies when coupling the results. Furthermore, the computational cost of running multiple simulations and integrating their results can be considerable, requiring significant computational resources and time. Finally, the interpretation and validation of the coupled results can be more complex as it involves understanding the interactions and dependencies between the different simulated phenomena.

Lastly, the wind simulations can be used in particle transport models. For instance, in the study by (Fraschetti et al., 2022), they perform a detailed analysis of the propagation of charged particles energized in the proximity of AU Mic, i.e., by flares or CME-shocks, through a magnetized stellar wind calculated via the Space Weather Modeling Framework codes, in particular the Alfvén Wave Solar Model, out to the second confirmed planet.

With this, I come to the end of the manuscript.

Publications

11.0.1.First Author

Far beyond the Sun-IV. A numerical exploration in the realm of Horologium
Authors: **Chebly, J. J.**; Alvarado-Gómez, J. D.; Amazo-Gómez E.; Poppenhäger, K. et al.
In preparation

Coronal abundances of M dwarfs – a reversal in the First Ionization Potential pattern at low activity levels?
Authors: **Chebly, J. J.**; Poppenhäger, K.; Alvarado-Gómez, J. D.; Brian Wood
Submitted to Astronomy and Astrophysics journal.

Numerical quantification of the wind properties of cool main sequence stars.
Authors: **Chebly, J. J.**; Alvarado-Gómez, J. D.; Poppenhäger, K., C. Garraffo.
DOI: 10.1093/mnras/stad2100.
URL: https://ui.adsabs.harvard.edu/abs/2023MNRAS.524.5060C/abstract.

Destination exoplanet: Habitability conditions influenced by stellar winds properties.
Authors: **Chebly, J. J.**; Alvarado-Gómez, J. D.; Poppenhäger, K.
DOI: 10.1002/asna.20210093.
URL: https://onlinelibrary.wiley.com/doi/10.1002/asna.20210093.

11.0.2.Contribution

Planetary perturbers: flaring star-planet interactions in Kepler and TESS
Authors: Ekaterina Ilin, Katja Poppenhäger, **Judy Chebly**, Nikoleta Ilíc, and Julián D. Alvarado-Goméz
DOI: 10.1093/mnras/stad3398
URL: https://ui.adsabs.harvard.edu/abs/2024MNRAS.527.3395I/abstract

Using my expertise in stellar winds and circumstellar environments, we have found a way to assess the likelihood of magnetic SPI in the systems considered in the study.

Simulating the Space Weather in the AU Mic System: Stellar Winds and Extreme Coronal Mass Ejections.
Authors: Alvarado-Gómez, J. D.; Cohen, O.; Drake, J. J.; Fraschetti, F.; Poppenhäger, K; Garraffo, C.; **Chebly, J.**; Ilin, E.; Harbach, L; Kochukhov, O.
DOI: 10.3847/1538-4357/ac54b8.
URL: https://ui.adsabs.harvard.edu/abs/2022arXiv220207949A/abstract.

In this study, I was involved in the editing of the manuscript.

BIBLIOGRAPHY

Ahuir J., Brun A. S., Strugarek A., 2020, A&A, 635, A170. doi:10.1051/0004-6361/201936974

Airapetian V. S., Glocer A., Khazanov G. V., Loyd R. O. P., France K., Sojka J., Danchi W. C., et al., 2017, ApJL, 836, L3. doi:10.3847/2041-8213/836/1/L3

Alazraki G., Couturier P., 1971, A&A, 13, 380

Alfvén H., 1942, Natur, 150, 405. doi:10.1038/150405d0

Alfven H., 1957, Tell, 9, 92. doi:10.3402/tellusa.v9i1.9064

Alfven H., 1977, RvGSP, 15, 271. doi:10.1029/RG015i003p00271

Allart R., Bourrier V., Lovis C., Ehrenreich D., Aceituno J., Guijarro A., Pepe F., et al., 2019, A&A, 623, A58. doi:10.1051/0004-6361/201834917

Allen J. W., Dupree A. K., 1969, ApJ, 155, 27. doi:10.1086/149844

Altschuler M. D., Newkirk G., 1969, SoPh, 9, 131. doi:10.1007/BF00145734

Alvarado-Gómez J. D., Hussain G. A. J., Grunhut J., Fares R., Donati J.-F., Alecian E., Kochukhov O., et al., 2015, A&A, 582, A38. doi:10.1051/0004-6361/201525771

Alvarado-Gómez J. D., Hussain G. A. J., Cohen O., Drake J. J., Garraffo C., Grunhut J., Gombosi T. I., 2016, A&A, 594, A95. doi:10.1051/0004-6361/201628988

Alvarado-Gómez J. D., Hussain G. A. J., Drake J. J., Donati J.-F., Sanz-Forcada J., Stelzer B., Cohen O., et al., 2018, MNRAS, 473, 4326. doi:10.1093/mnras/stx2642

Alvarado-Gómez J. D., Drake J. J., Moschou S. P., Garraffo C., Cohen O., NASA LWS Focus Science Team: Solar-Stellar Connection, Yadav R. K., et al., 2019, ApJL, 884, L13. doi:10.3847/2041-8213/ab44d0

Alvarado-Gómez J. D., Drake J. J., Garraffo C., Cohen O., Poppenhaeger K., Yadav R. K., Moschou S. P., 2020, ApJL, 902, L9. doi:10.3847/2041-8213/abb885

Alvarado-Gómez J. D., Cohen O., Drake J. J., Fraschetti F., Poppenhaeger K., Garraffo C., Chebly J., et al., 2022, ApJ, 928, 147. doi:10.3847/1538-4357/ac54b8

Amazo-Gómez E. M., Alvarado-Gómez J. D., Poppenhäger K., Hussain G. A. J., Wood B. E., Drake J. J., do Nascimento J.-D., et al., 2023, MNRAS, 524, 5725. doi:10.1093/mnras/stad2086

Antiochos S. K., Mikić Z., Titov V. S., Lionello R., Linker J. A., 2011, ApJ, 731, 112. doi:10.1088/0004-637X/731/2/112

Antiochos S. K., Linker J. A., Lionello R., Mikić Z., Titov V., Zurbuchen T. H., 2012, SSRv, 172, 169. doi:10.1007/s11214-011-9795-7

Argiroffi C., Caramazza M., Micela G., Sciortino S., Moraux E., Bouvier J., Flaccomio E., 2016, A&A, 589, A113. doi:10.1051/0004-6361/201526539

Aruldhas, G., 2002, Quantum Mechanics, Prentice Hall India Pvt., Limited, https://books.google.de/books?id=dRsvmTFpB3wC

Aschwanden M. J., 2005, psci.book

Atobe K., Ida S., Ito T., 2004, Icar, 168, 223. doi:10.1016/j.icarus.2003.11.017

Audard M., Behar E., Güdel M., Raassen A. J. J., Porquet D., Mewe R., Foley C. R., et al., 2001, A&A, 365, L329. doi:10.1051/0004-6361:20000246

Audard M., Güdel A., Sres A., Mewe R., Raassen A. J. J., Behar E., Foley C. R., et al., 2003, csss, 12, 293

Audard M., 2002, cosp

Ayres T. R., Brown A., Harper G. M., 2003, ApJ, 598, 610. doi:10.1086/378699

Badalyan O. G., Livshits M. A., 1992, SvA, 36, 70

Baker D., van Driel-Gesztelyi L., Brooks D. H., Valori G., James A. W., Laming J. M., Long D. M., et al., 2019, ApJ, 875, 35. doi:10.3847/1538-4357/ab07c1

Baker D., van Driel-Gesztelyi L., Brooks D. H., Démoulin P., Valori G., Long D. M., Laming J. M., et al., 2020, ApJ, 894, 35. doi:10.3847/1538-4357/ab7dcb

Bale S. D., Badman S. T., Bonnell J. W., Bowen T. A., Burgess D., Case A. W., Cattell C. A., et al., 2019, Natur, 576, 237. doi:10.1038/s41586-019-1818-7

Baliunas S. L., Donahue R. A., Soon W., Gilliland R., Soderblom D. R., 1995, AAS

Ball B., Drake J. J., Lin L., Kashyap V., Laming J. M., García-Alvarez D., 2005, ApJ, 634, 1336. doi:10.1086/496909

Bame S. J., Hundhausen A. J., Asbridge J. R., Strong I. B., 1968, PhRvL, 20, 393. doi:10.1103/PhysRevLett.20.393

Bame S. J., Asbridge J. R., Hundhausen A. J., Montgomery M. D., 1970, JGR, 75, 6360. doi:10.1029/JA075i031p06360

Bame S. J., Asbridge J. R., Feldman W. C., Fenimore E. E., Gosling J. T., 1979, SoPh, 62, 179. doi:10.1007/BF00150143

Baranov V. B., Malama Y. G., 1993, JGR, 98, 15157. doi:10.1029/93JA01171

Baranov V. B., Malama Y. G., 1995, JGR, 100, 14755. doi:10.1029/95JA00655

Baranov V. B., 1990, SSRv, 52, 89. doi:10.1007/BF00704240

Barnes A., 1966, PhFl, 9, 1483. doi:10.1063/1.1761882

Barnes A., 1968, ApJ, 154, 751. doi:10.1086/149794

Barnes S. A., 2007, ApJ, 669, 1167. doi:10.1086/519295

Basri G., Marcy G. W., 1994, ApJ, 431, 844. doi:10.1086/174535

Basri G., Marcy G. W., Valenti J. A., 1992, ApJ, 390, 622. doi:10.1086/171312

Bastian T. S., Dulk G. A., Leblanc Y., 2000, ApJ, 545, 1058. doi:10.1086/317864

Basu S., Antia H. M., 2003, ApJ, 585, 553. doi:10.1086/346020

Beckers J. M., 1969, SoPh, 10, 262. doi:10.1007/BF00145513

Beckers J. M., 1976, pspe.proc, 1, 89

Bedell M., Bean J. L., Meléndez J., Spina L., Ramírez I., Asplund M., Alves-Brito A., et al., 2018, ApJ, 865, 68. doi:10.3847/1538-4357/aad908

Belcher J. W., Davis L., Smith E. J., 1969, JGR, 74, 2302. doi:10.1029/JA074i009p02302

Belcher J. W., 1971, ApJ, 168, 509. doi:10.1086/151105

Bellan P. M., 2006, fpp..book

Benz A. O., 2017, LRSP, 14, 2. doi:10.1007/s41116-016-0004-3

Bertello L., Pevtsov A., Tlatov A., Singh J., 2016, SoPh, 291, 2967. doi:10.1007/s11207-016-0927-9

Bethe H. A., 1939, PhRv, 55, 103. doi:10.1103/PhysRev.55.103

Bice C., Toomre J., 2020, ASSP, 57, 285. doi:10.1007/978-3-030-55336-4_40

Bicz K., Falewicz R., Pietras M., Siarkowski M., Preś P., 2022, ApJ, 935, 102. doi:10.3847/1538-4357/ac7ab3

Biermann L., 1951, ZA, 29, 274

Biermann L., 1957, Obs, 77, 109

Billings D. E., 1966, gtsc.book

Boldyrev S., Cattaneo F., Rosner R., 2005, PhRvL, 95, 255001. doi:10.1103/PhysRevLett.95.255001

Bonetti A., Bridge H. S., Lazarus A. J., Rossi B., Scherb F., 1963, JGR, 68, 4017. doi:10.1029/JZ068i013p04017

Boro Saikia S., Jin M., Johnstone C. P., Lüftinger T., Güdel M., Airapetian V. S., Kislyakova K. G., et al., 2020, A&A, 635, A178. doi:10.1051/0004-6361/201937107

Borucki W. J., Koch D. G., Batalha N., Bryson S. T., Rowe J., Fressin F., Torres G., et al., 2012, ApJ, 745, 120. doi:10.1088/0004-637X/745/2/120

Bourrier V., Lecavelier des Etangs A., 2013, A&A, 557, A124. doi:10.1051/0004-6361/201321551

Bourrier V., Lecavelier des Etangs A., Ehrenreich D., Tanaka Y. A., Vidotto A. A., 2016, A&A, 591, A121. doi:10.1051/0004-6361/201628362

Bouvier J., Matt S. P., Mohanty S., Scholz A., Stassun K. G., Zanni C., 2014, prpl.conf, 433. doi:10.2458/azu_uapress_9780816531240-ch019

Brain D. A., Bagenal F., Ma Y.-J., Nilsson H., Stenberg Wieser G., 2016, JGRE, 121, 2364. doi:10.1002/2016JE005162

Brain D. A., Kao M. M., O'Rourke J. G., 2024, arXiv, arXiv:2404.15429. doi:10.48550/arXiv.2404.15429

Brandenburg A., Subramanian K., 2005, PhR, 417, 1. doi:10.1016/j.physrep.2005.06.005

Brinkman A. C., Behar E., Güdel M., Audard M., den Boggende A. J. F., Branduardi-Raymont G., Cottam J., et al., 2001, A&A, 365, L324. doi:10.1051/0004-6361:20000047

Brown A., Veale A., Judge P., Bookbinder J. A., Hubeny I., 1990, ApJ, 361, 220. doi:10.1086/169186

Browning M. K., 2008, ApJ, 676, 1262. doi:10.1086/527432

Brown T. M., 2014, ApJ, 789, 101. doi:10.1088/0004-637X/789/2/101

Bruno R., Carbone V., 2013, LRSP, 10, 2. doi:10.12942/lrsp-2013-2

Bruntt H., Bedding T. R., Quirion P.-O., Lo Curto G., Carrier F., Smalley B., Dall T. H., et al., 2010, MNRAS, 405, 1907. doi:10.1111/j.1365-2966.2010.16575.x

Burlaga L. F., Ness N. F., McDonald F. B., 1995, JGR, 100, 14763. doi:10.1029/95JA01557

Burlaga L. F., 2001, AGUFMSM22

Butler R. P., Marcy G. W., 1996, ApJL, 464, L153. doi:10.1086/310102

Butler R. P., Tinney C. G., Marcy G. W., Jones H. R. A., Penny A. J., Apps K., 2001, ApJ, 555, 410. doi:10.1086/321467

Böhm-Vitense E., 1989, isa1.book, 256

Caillault J.-P., Helfand D. J., 1985, ApJ, 289, 279. doi:10.1086/162888

Cargill P., de Moortel I., 2011, Natur, 475, 463. doi:10.1038/475463a

Carolan S., Vidotto A. A., Loesch C., Coogan P., 2019, MNRAS, 489, 5784. doi:10.1093/mnras/stz2422

Catling D. C., Kasting J. F., 2017, aeil.book

Cauley P. W., Shkolnik E. L., Llama J., Lanza A. F., 2019, NatAs, 3, 1128. doi:10.1038/s41550-019-0840-x

Chapman S., Zirin H., 1957, SCoA, 2, 1

Charbonneau P., Christensen-Dalsgaard J., Henning R., Larsen R. M., Schou J., Thompson M. J., Tomczyk S., 1999, ApJ, 527, 445. doi:10.1086/308050

Charbonneau P., 2020, LRSP, 17, 4. doi:10.1007/s41116-020-00025-6

Chebly J. J., Alvarado-Gómez J. D., Poppenhäger K., Garraffo C., 2023, MNRAS, 524, 5060. doi:10.1093/mnras/stad2100

Chebly J. J., Alvarado-Gómez J. D., Poppenhaeger K., 2022, AN, 343, e10093. doi:10.1002/asna.20210093

Clayton D. D., 1983, psen.book

Coffaro M., Stelzer B., Orlando S., Hall J., Metcalfe T. S., Wolter U., Mittag M., et al., 2020, A&A, 636, A49. doi:10.1051/0004-6361/201936479

Cohen O., Sokolov I. V., Roussev I. I., Arge C. N., Manchester W. B., Gombosi T. I., Frazin R. A., et al., 2007, ApJL, 654, L163. doi:10.1086/511154

Cohen O., Drake J. J., Kashyap V. L., Gombosi T. I., 2009, ApJ, 699, 1501. doi:10.1088/0004-637X/699/2/1501

Cohen O., Drake J. J., Kashyap V. L., Sokolov I. V., Gombosi T. I., 2010, ApJL, 723, L64. doi:10.1088/2041-8205/723/1/L64

Cohen O., Drake J. J., Glocer A., Garraffo C., Poppenhaeger K., Bell J. M., Ridley A. J., et al., 2014, ApJ, 790, 57. doi:10.1088/0004-637X/790/1/57

Cohen O., Ma Y., Drake J. J., Glocer A., Garraffo C., Bell J. M., Gombosi T. I., 2015, ApJ, 806, 41. doi:10.1088/0004-637X/806/1/41

Cohen O., Moschou S.-P., Glocer A., Sokolov I. V., Mazeh T., Drake J. J., Garraffo C., et al., 2018, AJ, 156, 202. doi:10.3847/1538-3881/aae1f2

Cohen O., Garraffo C., Moschou S.-P., Drake J. J., Alvarado-Gómez J. D., Glocer A., Fraschetti F., 2020, ApJ, 897, 101. doi:10.3847/1538-4357/ab9637

Cohen O., Alvarado-Gómez J. D., Drake J. J., Harbach L. M., Garraffo C., Fraschetti F., 2022, ApJ, 934, 189. doi:10.3847/1538-4357/ac78e4

Cohen O., Drake J. J., Kóta J., 2012, ApJ, 760, 85. doi:10.1088/0004-637X/760/1/85

Cohen O., 2011, MNRAS, 417, 2592. doi:10.1111/j.1365-2966.2011.19428.x

Coleman P. J., 1968, ApJ, 153, 371. doi:10.1086/149674

Collier Cameron A., Robinson R. D., 1989, MNRAS, 236, 57. doi:10.1093/mnras/236.1.57

Collier Cameron A., Robinson R. D., 1989, MNRAS, 238, 657. doi:10.1093/mnras/238.2.657

Condon E. U., Shortley G. H., 1963, tas..book

Cranmer S. R., van Ballegooijen A. A., 2005, ApJS, 156, 265. doi:10.1086/426507

Cranmer S. R., Saar S. H., 2011, ApJ, 741, 54. doi:10.1088/0004-637X/741/1/54

Cranmer S. R., van Ballegooijen A. A., 2012, ApJ, 754, 92. doi:10.1088/0004-637X/754/2/92

Cranmer S. R., Asgari-Targhi M., Miralles M. P., Raymond J. C., Strachan L., Tian H., Woolsey L. N., 2015, RSPTA, 373, 20140148. doi:10.1098/rsta.2014.0148

Cranmer S. R., Chhiber R., Gilly C. R., Cairns I. H., Colaninno R. C., McComas D. J., Raouafi N. E., et al., 2023, SoPh, 298, 126. doi:10.1007/s11207-023-02218-2

Cranmer S. R., van Ballegooijen A. A., Edgar R. J., 2007, ApJS, 171, 520. doi:10.1086/518001

Cranmer S. R., 2009, LRSP, 6, 3. doi:10.12942/lrsp-2009-3

Cranmer S. R., 2012, SSRv, 172, 145. doi:10.1007/s11214-010-9674-7

Cravens T. E., Gombosi T. I., 2004, AdSpR, 33, 1968. doi:10.1016/j.asr.2003.07.053

Cristofari P. I., Donati J.-F., Folsom C. P., Masseron T., Fouqué P., Moutou C., Artigau E., et al., 2023, MNRAS, 522, 1342. doi:10.1093/mnras/stad865

Cullity, B.D. and Graham, C.D., 2009, Wiley, https://books.google.de/books?id=ixAe4qIGEmwC

Daley-Yates S., Stevens I. R., 2019, MNRAS, 483, 2600. doi:10.1093/mnras/sty3310

Dewar R. L., 1970, PhFl, 13, 2710. doi:10.1063/1.1692854

DiTomasso V., Nava C., López-Morales M., Bieryla A., Cloutier R., Malavolta L., Mortier A., et al., 2023, AJ, 165, 38. doi:10.3847/1538-3881/ac9ccd

Donati J.-F., Semel M., Carter B. D., Rees D. E., Collier Cameron A., 1997, MNRAS, 291, 658. doi:10.1093/mnras/291.4.658

Donati, J.-F., et al. 2003, "ESPaDOnS: The new generation stellar spectropolarimeter: Performance and science objectives", Astronomical Society of the Pacific Conference Series, 307, 41-54

Donati J.-F., Howarth I. D., Jardine M. M., Petit P., Catala C., Landstreet J. D., Bouret J.-C., et al., 2006, MNRAS, 370, 629. doi:10.1111/j.1365-2966.2006.10558.x

Donati J.-F., Landstreet J. D., 2009, ARA&A, 47, 333. doi:10.1146/annurev-astro-082708-101833

Donati, J.-F., et al. 2020, "SPIRou: The Near-Infrared Spectropolarimeter/High-Precision Velocimeter for the Canada-France-Hawaii Telescope", Monthly Notices of the Royal Astronomical Society, 498, 5684-5703

Downs C., Roussev I. I., van der Holst B., Lugaz N., Sokolov I. V., Gombosi T. I., 2010, ApJ, 712, 1219. doi:10.1088/0004-637X/712/2/1219

Drake J. J., Peres G., Orlando S., Laming J. M., Maggio A., 2000, ApJ, 545, 1074. doi:10.1086/317820

Drake J. J., Cohen O., Yashiro S., Gopalswamy N., 2013, ApJ, 764, 170. doi:10.1088/0004-637X/764/2/170

Drake J. J., Stelzer B., 2023, hxga.book, 132. doi:10.1007/978-981-16-4544-0_78-1

Drake S. A., Simon T., Brown A., 1993, ApJ, 406, 247. doi:10.1086/172436

Drake J. J., Laming J. M., Widing K. G., 1994, AAS

Drake J. J., Laming J. M., Widing K. G., 1996, aeu..conf, 97

Drake J. J., Laming J. M., Widing K. G., 1997, ApJ, 478, 403. doi:10.1086/303755

Drake J., 2001, STIN, 01

Drake J. J., 2002, ASPC, 277, 75

Druckmüller M., Rušin V., Minarovjech M., 2006, CoSka, 36, 131

Durney B. R., De Young D. S., Roxburgh I. W., 1993, SoPh, 145, 207. doi:10.1007/BF00690652

Díaz Baso C. J., de la Cruz Rodríguez J., Leenaarts J., 2021, A&A, 647, A188. doi:10.1051/0004-6361/202040111

Edlén B., Swings P., 1942, ApJ, 95, 532. doi:10.1086/144421

Egan H., Jarvinen R., Brain D., 2019, MNRAS, 486, 1283. doi:10.1093/mnras/stz788

Elsasser W. M., 1950, PhRv, 79, 183. doi:10.1103/PhysRev.79.183

Evensberget D., Carter B. D., Marsden S. C., Brookshaw L., Folsom C. P., Salmeron R., 2022, MNRAS, 510, 5226. doi:10.1093/mnras/stab3557

Fares R., Donati J.-F., Moutou C., Bohlender D., Catala C., Deleuil M., Shkolnik E., et al., 2009, MNRAS, 398, 1383. doi:10.1111/j.1365-2966.2009.15303.x

Feldman U., Widing K. G., 1993, ApJ, 414, 381. doi:10.1086/173084

Feldman U., Laming J. M., 2000, PhyS, 61, 222. doi:10.1238/Physica.Regular.061a00222

Feldman W. C., 1977, JGR, 82, 667. doi:10.1029/JA082i004p00667

Feldman U., 1992, PhyS, 46, 202. doi:10.1088/0031-8949/46/3/002

Feng X., Yang L., Xiang C., Wu S. T., Zhou Y., Zhong D., 2010, ApJ, 723, 300. doi:10.1088/0004-637X/723/1/300

Feng X., Zhou Y., Wu S. T., 2007, ApJ, 655, 1110. doi:10.1086/510121

Fichtinger B., Güdel M., Mutel R. L., Hallinan G., Gaidos E., Skinner S. L., Lynch C., et al., 2017, A&A, 599, A127. doi:10.1051/0004-6361/201629886

Finley A. J., Matt S. P., 2018, ApJ, 854, 78. doi:10.3847/1538-4357/aaaab5

Finley A. J., Hewitt A. L., Matt S. P., Owens M., Pinto R. F., Réville V., 2019, ApJL, 885, L30. doi:10.3847/2041-8213/ab4ff4

Fleming T. A., Giampapa M. S., Schmitt J. H. M. M., Bookbinder J. A., 1993, ApJ, 410, 387. doi:10.1086/172755

Fletcher L., Dennis B. R., Hudson H. S., Krucker S., Phillips K., Veronig A., Battaglia M., et al., 2011, SSRv, 159, 19. doi:10.1007/s11214-010-9701-8

Folsom C. P., Bouvier J., Petit P., Lèbre A., Amard L., Palacios A., Morin J., et al., 2018, MNRAS, 474, 4956. doi:10.1093/mnras/stx3021

Fossati L., Ayres T. R., Haswell C. A., Bohlender D., Kochukhov O., Flöer L., 2013, ApJL, 766, L20. doi:10.1088/2041-8205/766/2/L20

France K., Duvvuri G., Egan H., Koskinen T., Wilson D. J., Youngblood A., Froning C. S., et al., 2020, AJ, 160, 237. doi:10.3847/1538-3881/abb465

Fraschetti F., Alvarado-Gómez J. D., Drake J. J., Cohen O., Garraffo C., 2022, ApJ, 937, 126. doi:10.3847/1538-4357/ac86d7

Fressin F., Torres G., Rowe J. F., Charbonneau D., Rogers L. A., Ballard S., Batalha N. M., et al., 2012, Natur, 482, 195. doi:10.1038/nature10780

Frisch, P. C. (1995). Characteristics of nearby interstellar matter. Space Science Reviews, 72(1), 499-592.

Eric Gaidos and Manuel Güdel and Geoffrey A. Blake, 2000, Geophysical Research Letters, 27. url=https://api.semanticscholar.org/CorpusID:15264566

Gallet F., Bouvier J., 2013, A&A, 556, A36. doi:10.1051/0004-6361/201321302

Gallet F., Bouvier J., 2015, A&A, 577, A98. doi:10.1051/0004-6361/201525660

Gardner, J. P., et al. 2006, "The James Webb Space Telescope", Space Science Reviews, 123, 485-606

Garraffo C., Cohen O., Drake J. J., Downs C., 2013, ApJ, 764, 32. doi:10.1088/0004-637X/764/1/32

Garraffo C., Drake J. J., Cohen O., Alvarado-Gómez J. D., Moschou S. P., 2017, ApJL, 843, L33. doi:10.3847/2041-8213/aa79ed

Garraffo C., Drake J. J., Dotter A., Choi J., Burke D. J., Moschou S. P., Alvarado-Gómez J. D., et al., 2018, ApJ, 862, 90. doi:10.3847/1538-4357/aace5d

Garraffo C., Alvarado-Gómez J. D., Cohen O., Drake J. J., 2022, ApJL, 941, L8. doi:10.3847/2041-8213/aca487

Garraffo C., Drake J. J., Cohen O., 2015, ApJL, 807, L6. doi:10.1088/2041-8205/807/1/L6

Garraffo C., Drake J. J., Cohen O., 2016, ApJL, 833, L4. doi:10.3847/2041-8205/833/1/L4

Gary G. A., 2001, SoPh, 203, 71. doi:10.1023/A:1012722021820

Gayley K. G., Zank G. P., Pauls H. L., Frisch P. C., Welty D. E., 1997, ApJ, 487, 259. doi:10.1086/304600

Gilmozzi, R., et al. 2007, "The European Extremely Large Telescope (E-ELT)", The Messenger, 127, 11-19

Giovanelli R. G., 1974, SoPh, 37, 301. doi:10.1007/BF00152489

Gombosi T. I., van der Holst B., Manchester W. B., Sokolov I. V., 2018, LRSP, 15, 4. doi:10.1007/s41116-018-0014-4

Gombosi T. I., Chen Y., Glocer A., Huang Z., Jia X., Liemohn M. W., Manchester W. B., et al., 2021, JSWSC, 11, 42. doi:10.1051/swsc/2021020

Gombosi T. I., 2004, pse..book, 357

Goncharskii A. V., Stepanov V. V., Kokhlova V. L., Yagola A. G., 1977, SvAL, 3, 147

González-Álvarez E., Zapatero Osorio M. R., Caballero J. A., Sanz-Forcada J., Béjar V. J. S., González-Cuesta L., Dreizler S., et al., 2020, A&A, 637, A93. doi:10.1051/0004-6361/201937050

Goossens M., 1994, SSRv, 68, 51. doi:10.1007/BF00749116

Gray D. F., Nagel T., 1989, ApJ, 341, 421. doi:10.1086/167505

Greenhouse, M. A. 1993, "Hubble Space Telescope", Physics Today, 46, 62-63

Grevesse N., Sauval A. J., 1998, SSRv, 85, 161. doi:10.1023/A:1005161325181

Griessmeier J.-M., Stadelmann A., Lammer H., Grenfell L., Patzer B., von Paris P., Motschmann U., 2006, epsc.conf, 323

Grießmeier J.-M., Stadelmann A., Penz T., Lammer H., Selsis F., Ribas I., Guinan E. F., et al., 2004, A&A, 425, 753. doi:10.1051/0004-6361:20035684

Grießmeier J.-M., Stadelmann A., Motschmann U., Belisheva N. K., Lammer H., Biernat H. K., 2005, AsBio, 5, 587. doi:10.1089/ast.2005.5.587

Grießmeier J.-M., Zarka P., Spreeuw H., 2007, A&A, 475, 359. doi:10.1051/0004-6361:20077397

Gringauz K. I., Bezrukikh V. V., Ozerov V. D., Rybchinskii R. E., 1962, P&SS, 9, 103. doi:10.1016/0032-0633(62)90180-0

Gringauz K. I., 1963, P&SS, 11, 281. doi:10.1016/0032-0633(63)90030-8

Gronoff G., Arras P., Baraka S., Bell J. M., Cessateur G., Cohen O., Curry S. M., et al., 2020, JGRA, 125, e27639. doi:10.1029/2019JA02763910.1002/essoar.10502458.1

Groth C. P. T., de Zeeuw D. L., Gombosi T. I., Powell K. G., 1999, SSRv, 87, 193. doi:10.1023/A:1005136115563

Grotrian W., 1939, NW, 27, 214. doi:10.1007/BF01488890

Gry C., Jenkins E. B., 2014, A&A, 567, A58. doi:10.1051/0004-6361/201323342

Gurnett D. A., Kurth W. S., 2019, NatAs, 3, 1024. doi:10.1038/s41550-019-0918-5

Güdel M., Audard M., Briggs K., Haberl F., Magee H., Maggio A., Mewe R., et al., 2001, A&A, 365, L336. doi:10.1051/0004-6361:20000220

Güdel M., Guinan E. F., Skinner S. L., 1997, ApJ, 483, 947. doi:10.1086/304264

Güdel M., 2002, ARA&A, 40, 217. doi:10.1146/annurev.astro.40.060401.093806

Güdel M., 2004, A&ARv, 12, 71. doi:10.1007/s00159-004-0023-2

Haken, Hermann and Wolf, Hans C., 2012, Springer Publishing Company, Incorporated, 4th edition, isbn = 3642975690

Hansteen V. H., Velli M., 2012, SSRv, 172, 89. doi:10.1007/s11214-012-9887-z

Harbach L. M., Moschou S. P., Garraffo C., Drake J. J., Alvarado-Gómez J. D., Cohen O., Fraschetti F., 2021, ApJ, 913, 130. doi:10.3847/1538-4357/abf63a

Hart M. H., 1978, Icar, 33, 23. doi:10.1016/0019-1035(78)90021-0

Hathaway D. H., 2010, LRSP, 7, 1. doi:10.12942/lrsp-2010-1

Hawley S. L., Davenport J. R. A., Kowalski A. F., Wisniewski J. P., Hebb L., Deitrick R., Hilton E. J., 2014, ApJ, 797, 121. doi:10.1088/0004-637X/797/2/121

He L.-B., Xu L., Yu P., 2016, arXiv, arXiv:1603.08205. doi:10.48550/arXiv.1603.08205

Heath M. J., Doyle L. R., Joshi M. M., Haberle R. M., 1999, OLEB, 29, 405. doi:10.1023/A:1006596718708

Heinemann M., Olbert S., 1980, JGR, 85, 1311. doi:10.1029/JA085iA03p01311

Henry T. J., McCarthy D. W., 1993, AJ, 106, 773. doi:10.1086/116685

Herbst K., Baalmann L. R., Bykov A., Engelbrecht N. E., Ferreira S. E. S., Izmodenov V. V., Korolkov S. D., et al., 2022, SSRv, 218, 29. doi:10.1007/s11214-022-00894-3

Hiei E., 1987, SoPh, 113, 249. doi:10.1007/BF00147705

Hollweg J. V., 1986, JGR, 91, 4111. doi:10.1029/JA091iA04p04111

Holmström M., Ekenbäck A., Selsis F., Penz T., Lammer H., Wurz P., 2008, Natur, 451, 970. doi:10.1038/nature06600

Holzer T. E., Axford W. I., 1970, JGR, 75, 6354. doi:10.1029/JA075i031p06354

Holzer, T. E. (1989). Interaction of the Solar Wind with the Interstellar Medium. Annual Review of Astronomy and Astrophysics, 27(1), 199-234.

Holzwarth V., Jardine M., 2007, A&A, 463, 11. doi:10.1051/0004-6361:20066486

Huang S.-S., 1960, PASP, 72, 489. doi:10.1086/127586

Huenemoerder D. P., Canizares C. R., Drake J. J., Sanz-Forcada J., 2003, ApJ, 595, 1131. doi:10.1086/377490

Huenemoerder D. P., Canizares C. R., Schulz N. S., 2001, ApJ, 559, 1135. doi:10.1086/322419

Hughes D. W., 2007, sota.conf, 275

Hundhausen A. J., Asbridge J. R., Bame S. J., Gilbert H. E., Strong I. B., 1967, JGR, 72, 87. doi:10.1029/JZ072i001p00087

Hundhausen A. J., Gilbert H. E., Bame S. J., 1968, ApJL, 152, L3. doi:10.1086/180165

Hundhausen, A. J., The Solar Wind. In: Kivelson, M.G. and Russell, C.T., Eds., Introduction to Space Physics, Sect. 4.4, Cambridge University Press, New York, 91-128.

Hundhausen A. J., 1968, SSRv, 8, 690. doi:10.1007/BF00175116

Hundhausen A. J., 1972, cesw.book, 101. doi:10.1007/978-3-642-65414-5

Hurford T., Bruce B., Helfenstein P., Greenberg R., Hoppa G., Hamilton D., 2008, DPS

Hussain G. A. J., Alvarado-Gómez J. D., Grunhut J., Donati J.-F., Alecian E., Oksala M., Morin J., et al., 2016, A&A, 585, A77. doi:10.1051/0004-6361/201526595

Hébrard G., Mallouris C., Ferlet R., Koester D., Lemoine M., Vidal-Madjar A., York D., 1999, A&A, 350, 643. doi:10.48550/arXiv.astro-ph/9909061

Ibgui L., Spiegel D. S., Burrows A., 2011, ApJ, 727, 75. doi:10.1088/0004-637X/727/2/75

Ionson J. A., 1978, ApJ, 226, 650. doi:10.1086/156648

Ip W.-H., Kopp A., Hu J.-H., 2004, ApJL, 602, L53. doi:10.1086/382274

Israelian G., de Groot M., 1999, SSRv, 90, 493. doi:10.1023/A:1005223314464

Izmodenov V., Wood B. E., Lallement R., 2002, JGRA, 107, 1308. doi:10.1029/2002JA009394

Jacques S. A., 1977, ApJ, 215, 942. doi:10.1086/155430

Jacques S. A., 1978, ApJ, 226, 632. doi:10.1086/156647

James D. J., Jardine M. M., Jeffries R. D., Randich S., Collier Cameron A., Ferreira M., 2000, MNRAS, 318, 1217. doi:10.1046/j.1365-8711.2000.03838.x

Jardine M., Unruh Y. C., 1999, A&A, 346, 883

Jardine M., van Ballegooijen A. A., 2005, MNRAS, 361, 1173. doi:10.1111/j.1365-2966.2005.09256.x

Jardine M., Collier Cameron A., 2008, A&A, 490, 843. doi:10.1051/0004-6361:20078658

Jardine M., Vidotto A. A., van Ballegooijen A., Donati J.-F., Morin J., Fares R., Gombosi T. I., 2013, MNRAS, 431, 528. doi:10.1093/mnras/stt181

Jardine M., Collier Cameron A., 2019, MNRAS, 482, 2853. doi:10.1093/mnras/sty2872

Jardine M., 2004, A&A, 414, L5. Doi:10.1051/0004-6361:20031723

Jeffers, S.V., Petit, P., Marsden, S.C., Morin, J., Donati, J.-F., and Folsom, C.P.: 2014, *Astronomy and Astrophysics* **569**, A79. doi:10.1051/0004-6361/201423725.

Jeffers S. V., Boro Saikia S., Barnes J. R., Petit P., Marsden S. C., Jardine M. M., Vidotto A. A., et al., 2017, MNRAS, 471, L96. doi:10.1093/mnrasl/slx097

Jeffries R. D., Jackson R. J., Briggs K. R., Evans P. A., Pye J. P., 2011, MNRAS, 411, 2099. doi:10.1111/j.1365-2966.2010.17848.x

Jeffries R. D., 1999, MNRAS, 309, 189. doi:10.1046/j.1365-8711.1999.02822.x

Jess D. B., Morton R. J., Verth G., Fedun V., Grant S. D. T., Giagkiozis I., 2015, SSRv, 190, 103. doi:10.1007/s11214-015-0141-3

Jivani A., Sachdeva N., Huang Z., Chen Y., van der Holst B., Manchester W., Iong D., et al., 2023, SpWea, 21, e2022SW003262. doi:10.1029/2022SW003262

Johnstone C. P., Güdel M., Brott I., Lüftinger T., 2015, A&A, 577, A28. doi:10.1051/0004-6361/201425301

Johnstone C. P., Güdel M., 2015, A&A, 578, A129. doi:10.1051/0004-6361/201425283

Johnstone C. P., 2021, arXiv, arXiv:2105.11243. doi:10.48550/arXiv.2105.11243

Jordan C., Montesinos B., 1991, MNRAS, 252, 21P. doi:10.1093/mnras/252.1.21P

Jordan C., 1969, MNRAS, 142, 501. doi:10.1093/mnras/142.4.501

Jordan C., 1970, MNRAS, 148, 17. doi:10.1093/mnras/148.1.17

Kaeufl, H.-U., et al. 2004, "CRIRES: a high-resolution infrared spectrograph for ESO's VLT", Proceedings of SPIE, 5492, 1218-1227

Kaltenegger L., Traub W. A., 2009, ApJ, 698, 519. doi:10.1088/0004-637X/698/1/519

Kasper J. C., Klein K. G., Lichko E., Huang J., Chen C. H. K., Badman S. T., Bonnell J., et al., 2021, PhRvL, 127, 255101. doi:10.1103/PhysRevLett.127.255101

Kasting J. F., Whitmire D. P., Reynolds R. T., 1993, Icar, 101, 108. doi:10.1006/icar.1993.1010

Kavanagh R. D., Vidotto A. A., Ó. Fionnagáin D., Bourrier V., Fares R., Jardine M., Helling C., et al., 2019, MNRAS, 485, 4529. doi:10.1093/mnras/stz655

Kavanagh R. D., Vidotto A. A., Klein B., Jardine M. M., Donati J.-F., Ó Fionnagáin D., 2021, MNRAS, 504, 1511. doi:10.1093/mnras/stab929

Kawaler S. D., 1988, ApJ, 333, 236. doi:10.1086/166740

Kervella P., 2016, LNP, 127. doi:10.1007/978-3-319-24151-7_6

Khodachenko M. L., Ribas I., Lammer H., Grießmeier J.-M., Leitner M., Selsis F., Eiroa C., et al., 2007, AsBio, 7, 167. doi:10.1089/ast.2006.0127

Khodachenko M. L., Alexeev I., Belenkaya E., Lammer H., Grießmeier J.-M., Leitzinger M., Odert P., et al., 2012, ApJ, 744, 70. doi:10.1088/0004-637X/744/1/70

Kislyakova K. G., Holmström M., Lammer H., Odert P., Khodachenko M. L., 2014, Sci, 346, 981. doi:10.1126/science.1257829

Kislyakova K. G., Fossati L., Johnstone C. P., Holmström M., Zaitsev V. V., Lammer H., 2015, ApJL, 799, L15. doi:10.1088/2041-8205/799/2/L15

Kislyakova K. G., Güdel M., Koutroumpa D., Carter J. A., Lisse C. M., Boro Saikia S., 2024, NatAs.tmp. doi:10.1038/s41550-024-02222-x

Kislyakova K. G., Güdel M., Koutroumpa D., Carter J. A., Lisse C. M., Boro Saikia S., 2024, NatAs.tmp. doi:10.1038/s41550-024-02222-x

Kivelson M. G., Russell C. T., 1995, isp..book, 586. doi:10.1017/9781139878296

Klimchuk J. A., 2015, RSPTA, 373, 20140256. doi:10.1098/rsta.2014.0256

Ko Y.-K., Roberts D. A., Lepri S. T., 2018, ApJ, 864, 139. doi:10.3847/1538-4357/aad69e

Kochukhov O., Piskunov N., 2002, A&A, 388, 868. doi:10.1051/0004-6361:20020300

Kochukhov O., Makaganiuk V., Piskunov N., 2010, A&A, 524, A5. doi:10.1051/0004-6361/201015429

Stellar Magnetic Fields. In J. Sánchez Almeida & M. J. Martínez González (Eds.), Cosmic Magnetic Fields (pp. 47–86). chapter, Cambridge: Cambridge University Press.

Kochukhov O., 2016, LNP, 177. doi:10.1007/978-3-319-24151-7_9

Kochukhov O., 2021, A&ARv, 29, 1. doi:10.1007/s00159-020-00130-3

Kopparapu R. K., Ramirez R., Kasting J. F., Eymet V., Robinson T. D., Mahadevan S., Terrien R. C., et al., 2013, ApJ, 765, 131. doi:10.1088/0004-637X/765/2/131

Kopparapu R. K., Ramirez R. M., SchottelKotte J., Kasting J. F., Domagal-Goldman S., Eymet V., 2014, ApJL, 787, L29. doi:10.1088/2041-8205/787/2/L29

Koutroumpa D., Lallement R., Raymond J. C., Kharchenko V., 2009, ApJ, 696, 1517. doi:10.1088/0004-637X/696/2/1517

Kowalski A. F., Hawley S. L., Hilton E. J., Becker A. C., West A. A., Bochanski J. J., Sesar B., 2009, AJ, 138, 633. doi:10.1088/0004-6256/138/2/633

Kowalski A. F., Hawley S. L., Wisniewski J. P., Osten R. A., Hilton E. J., Holtzman J. A., Schmidt S. J., et al., 2013, ApJS, 207, 15. doi:10.1088/0067-0049/207/1/15

Kraft R. P., 1967, ApJ, 150, 551. doi:10.1086/149359

Kreidberg L., 2018, haex.book, 100. doi:10.1007/978-3-319-55333-7_100

Kruk J. W., Howk J. C., André M., Moos H. W., Oegerle W. R., Oliveira C., Sembach K. R., et al., 2002, ApJS, 140, 19. doi:10.1086/339131

Kürster M., Endl M., Els S., Hatzes A. P., Cochran W. D., Döbereiner S., Dennerl K., 2000, A&A, 353, L33

Lacy C. H., Moffett T. J., Evans D. S., 1976, ApJS, 30, 85. doi:10.1086/190358

Lalitha S., Schmitt J. H. M. M., 2013, A&A, 559, A119. doi:10.1051/0004-6361/201321723

Laming J. M., Drake J. J., 1999, ApJ, 516, 324. doi:10.1086/307112

Laming J. M., Kuroda N., 2023, ApJ, 951, 86. doi:10.3847/1538-4357/acd69a

Laming J. M., 2004, ApJ, 614, 1063. doi:10.1086/423780

Laming, J. M., Hwang, U. 2009, The Astrophysical Journal, 707(1), L60. DOI: 10.1088/0004-637X/707/1/L60

Laming J. M., 2015, ApJ, 805, 102. doi:10.1088/0004-637X/805/2/102

Laming J. M., 2017, ApJ, 844, 153. doi:10.3847/1538-4357/aa7cf1

Laming J. M., 2021, ApJ, 909, 17. doi:10.3847/1538-4357/abd9c3

Lammer H., Lichtenegger H. I. M., Kolb C., Ribas I., Guinan E. F., Abart R., Bauer S. J., 2003, Icar, 165, 9. doi:10.1016/S0019-1035(03)00170-2

Lammer H., Lichtenegger H. I. M., Biernat H. K., Erkaev N. V., Arshukova I. L., Kolb C., Gunell H., et al., 2006, P&SS, 54, 1445. doi:10.1016/j.pss.2006.04.022

Lammer H., Selsis F., Chassefière E., Breuer D., Grießmeier J.-M., Kulikov Y. N., Erkaev N. V., et al., 2010, AsBio, 10, 45. doi:10.1089/ast.2009.0368

Lammer H., Güdel M., Kulikov Y., Ribas I., Zaqarashvili T. V., Khodachenko M. L., Kislyakova K. G., et al., 2012, EP&S, 64, 179. doi:10.5047/eps.2011.04.002

Lammer H., Stökl A., Erkaev N. V., Dorfi E. A., Odert P., Güdel M., Kulikov Y. N., et al., 2014, MNRAS, 439, 3225. doi:10.1093/mnras/stu085

Landi Degl'Innocenti E., Landolfi M., 2004, ASSL. doi:10.1007/978-1-4020-2415-3

Landin N. R., Mendes L. T. S., Vaz L. P. R., Alencar S. H. P., 2023, MNRAS, 519, 5304. doi:10.1093/mnras/stac3823

Landstreet J. D., 1992, A&ARv, 4, 35. doi:10.1007/BF00873569

Landstreet J. D., 2009, EAS, 39, 1. doi:10.1051/eas/0939001

Lange J., Scherb F., 1970, JGR, 75, 6350. doi:10.1029/JA075i031p06350

Lang K. R., 2013, esas.book. doi:10.1007/978-3-642-35963-7

Lanza A. F., Bonomo A. S., Rodonò M., 2007, A&A, 464, 741. doi:10.1051/0004-6361:20066575

Lanza A. F., 2009, A&A, 505, 339. doi:10.1051/0004-6361/200912367

Lanza A. F., 2013, A&A, 557, A31. doi:10.1051/0004-6361/201321790

Lazio T. J., Farrell W. M., Dietrick J., Greenlees E., Hogan E., Jones C., Hennig L. A., 2004, ApJ, 612, 511. doi:10.1086/422449

Lazio T. J. W., Farrell W. M., 2007, ApJ, 668, 1182. doi:10.1086/519730

Lazio T. J. W., Shankland P. D., Farrell W. M., Blank D. L., 2010, AJ, 140, 1929. doi:10.1088/0004-6256/140/6/1929

Lebreton Y., Fernandes J., Lejeune T., 2001, A&A, 374, 540. doi:10.1051/0004-6361:20010757

Leitzinger M., Odert P., 2022, SerAJ, 205, 1. doi:10.2298/SAJ2205001L

Leroy B., 1980, A&A, 91, 136

Leto G., Pagano I., Buemi C. S., Rodono M., 1997, yCat, 332

Li X., Lin B., 2023, MNRAS, 521, 6354. doi:10.1093/mnras/stad831

Lichtenegger H. I. M., Lammer H., Grießmeier J.-M., Kulikov Y. N., von Paris P., Hausleitner W., Krauss S., et al., 2010, Icar, 210, 1. doi:10.1016/j.icarus.2010.06.042

Lim J., White S. M., 1996, ApJL, 462, L91. doi:10.1086/310038

Linsky J. L., Haisch B. M., 1979, ApJL, 229, L27. doi:10.1086/182924

Linsky J. L., Wood B. E., 1996, ApJ, 463, 254. doi:10.1086/177238

Linsky J. L., Wood B. E., 2014, ASTRP, 1, 43. doi:10.5194/ap-1-43-2014

Lionello R., Linker J. A., Mikić Z., 2001, ApJ, 546, 542. doi:10.1086/318254

Lodders K., Palme H., Gail H.-P., 2009, LanB...4B, 4B, 712. doi:10.1007/978-3-540-88055-4_34

Loukitcheva M., Solanki S. K., White S. M., 2009, A&A, 497, 273. doi:10.1051/0004-6361/200811133

Loyd R. O. P., Mason J. P., Jin M., Shkolnik E. L., France K., Youngblood A., Villadsen J., et al., 2022, ApJ, 936, 170. doi:10.3847/1538-4357/ac80c1

Lugaz N., Farrugia C. J., Huang C.-L., Spence H. E., 2015, GeoRL, 42, 4694. doi:10.1002/2015GL064530

Maehara H., Notsu Y., Namekata K., Honda S., Kowalski A. F., Katoh N., Ohshima T., et al., 2021, PASJ, 73, 44. doi:10.1093/pasj/psaa098

Magaudda E., Stelzer B., Covey K. R., Raetz S., Matt S. P., Scholz A., 2020, A&A, 638, A20. doi:10.1051/0004-6361/201937408

Mahajan S. S., Upton L. A., Antia H. M., Basu S., DeRosa M. L., Hess Webber S. A., Todd Hoeksema J., et al., 2024, SoPh, 299, 38. doi:10.1007/s11207-024-02282-2

Mancini L., Southworth J., Ciceri S., Dominik M., Henning T., Jørgensen U. G., Lanza A. F., et al., 2014, A&A, 562, A126. doi:10.1051/0004-6361/201323265

Mann G., Aurass H., Klassen A., Estel C., Thompson B. J., 1999, ESASP, 446, 477

Marcy G. W., Butler R. P., 1996, ApJL, 464, L147. doi:10.1086/310096

Marcy G. W., Butler R. P., Williams E., Bildsten L., Graham J. R., Ghez A. M., Jernigan J. G., 1997, ApJ, 481, 926. doi:10.1086/304088

Marsch E., von Steiger R., Bochsler P., 1995, A&A, 301, 261

Marsden S. C., Carter B. D., Donati J.-F., 2009, MNRAS, 399, 888. doi:10.1111/j.1365-2966.2009.15319.x

Matsakos T., Uribe A., Königl A., 2015, A&A, 578, A6. doi:10.1051/0004-6361/201425593

Matsumoto T., Suzuki T. K., 2012, ApJ, 749, 8. doi:10.1088/0004-637X/749/1/8

Matt S., Pudritz R. E., 2008, ApJ, 678, 1109. doi:10.1086/533428

Matt S. P., MacGregor K. B., Pinsonneault M. H., Greene T. P., 2012, ApJL, 754, L26. doi:10.1088/2041-8205/754/2/L26

Matt S. P., Brun A. S., Baraffe I., Bouvier J., Chabrier G., 2015, ApJL, 799, L23. doi:10.1088/2041-8205/799/2/L23

Mayor M., Queloz D., 1995, Natur, 378, 355. doi:10.1038/378355a0

Mayor, M., et al. 2003, "Setting New Standards with HARPS", The Messenger, 114, 20-24

McCann J., Murray-Clay R. A., Kratter K., Krumholz M. R., 2019, ApJ, 873, 89. doi:10.3847/1538-4357/ab05b8

McComas D. J., Bame S. J., Barraclough B. L., Feldman W. C., Funsten H. O., Gosling J. T., Riley P., et al., 1998, GeoRL, 25, 1. doi:10.1029/97GL03444

McComas D. J., Barraclough B. L., Funsten H. O., Gosling J. T., Santiago-Muñoz E., Skoug R. M., Goldstein B. E., et al., 2000, JGR, 105, 10419. doi:10.1029/1999JA000383

McComas D. J., Elliott H. A., Schwadron N. A., Gosling J. T., Skoug R. M., Goldstein B. E., 2003, GeoRL, 30, 1517. doi:10.1029/2003GL017136

McComas D. J., Velli M., Lewis W. S., Acton L. W., Balat-Pichelin M., Bothmer V., Dirling R. B., et al., 2007, RvGeo, 45, RG1004. doi:10.1029/2006RG000195

McIntosh S. W., de Pontieu B., Carlsson M., Hansteen V., Boerner P., Goossens M., 2011, Natur, 475, 477. doi:10.1038/nature10235

McIvor T., Jardine M., Holzwarth V., 2006, MNRAS, 367, L1. doi:10.1111/j.1745-3933.2005.00098.x

McKenzie D. L., Feldman U., 1992, ApJ, 389, 764. doi:10.1086/171249

Meadows V. S., Barnes R. K., 2018, haex.book, 57. doi:10.1007/978-3-319-55333-7_57

Mestel L., Landstreet J. D., 2005, LNP, 183. doi:10.1007/3540313966_8

Metcalfe T. S., Buccino A. P., Brown B. P., Mathur S., Soderblom D. R., Henry T. J., Mauas P. J. D., et al., 2013, ApJL, 763, L26. doi:10.1088/2041-8205/763/2/L26

Meyer J.-P., 1985, ApJS, 57, 173. doi:10.1086/191001

Micela G., 2002, ASPC, 269, 107

Mihalas D., 1973, ApJ, 184, 851. doi:10.1086/152375

Miller J. A., Cargill P. J., Emslie A. G., Holman G. D., Dennis B. R., LaRosa T. N., Winglee R. M., et al., 1997, JGR, 102, 14631. doi:10.1029/97JA00976

Misra A. P., Brodin G., 2022, RvMPP, 6, 5. doi:10.1007/s41614-022-00063-7

Mitra-Kraev U., Harra L. K., Güdel M., Audard M., Branduardi-Raymont G., Kay H. R. M., Mewe R., et al., 2005, A&A, 431, 679. doi:10.1051/0004-6361:20041201

Modi A., Estrela R., Valio A., 2023, MNRAS, 525, 5168. doi:10.1093/mnras/stad2557

Morgan H., Taroyan Y., 2017, SciA, 3, e1602056. doi:10.1126/sciadv.1602056

Morin J., Donati J.-F., Petit P., Delfosse X., Forveille T., Albert L., Aurière M., et al., 2008, MNRAS, 390, 567. doi:10.1111/j.1365-2966.2008.13809.x

Morin J., Donati J.-F., Petit P., Delfosse X., Forveille T., Jardine M. M., 2010, MNRAS, 407, 2269. doi:10.1111/j.1365-2966.2010.17101.x

Moschou S.-P., Drake J. J., Cohen O., Alvarado-Gómez J. D., Garraffo C., Fraschetti F., 2019, ApJ, 877, 105. doi:10.3847/1538-4357/ab1b37

Muheki P., Guenther E. W., Mutabazi T., Jurua E., 2020, MNRAS, 499, 5047. doi:10.1093/mnras/staa3152

Mégessier C., 1975, A&A, 39, 263

Naef D., Mayor M., Pepe F., Queloz D., Santos N. C., Udry S., Burnet M., 2001, A&A, 375, 205. doi:10.1051/0004-6361:20010841

Nakamizo A., Tanaka T., Kubo Y., Kamei S., Shimazu H., Shinagawa H., 2009, JGRA, 114, A07109. doi:10.1029/2008JA013844

Nariyuki Y., 2022, RvMPP, 6, 22. doi:10.1007/s41614-022-00085-1

Neugebauer M., Snyder C. W., 1962, Sci, 138, 1095. doi:10.1126/science.138.3545.1095.a

Neugebauer M., Snyder C. W., 1966, JGR, 71, 4469. doi:10.1029/JZ071i019p04469

Neugebauer M., Snyder C. W., 1967, JGR, 72, 1823. doi:10.1029/JZ072i007p01823

Neupert W. M., 1968, ApJL, 153, L59. doi:10.1086/180220

Newkirk G., 1980, asfr.symp, 293

Ni L., Kliem B., Lin J., Wu N., 2015, ApJ, 799, 79. doi:10.1088/0004-637X/799/1/79

Ni L., Lukin V. S., Murphy N. A., Lin J., 2018, ApJ, 852, 95. doi:10.3847/1538-4357/aa9edb

Nicholson B. A., Vidotto A. A., Mengel M., Brookshaw L., Carter B., Petit P., Marsden S. C., et al., 2016, MNRAS, 459, 1907. doi:10.1093/mnras/stw731

Nichols J. D., 2011, JGRA, 116, A10232. doi:10.1029/2011JA016922

Nindos A., Patsourakos S., Jafarzadeh S., Shimojo M., 2022, FrASS, 9, 981205. doi:10.3389/fspas.2022.981205

Nordon R., Behar E., 2008, A&A, 482, 639. doi:10.1051/0004-6361:20078848

Nortmann L., Pallé E., Salz M., Sanz-Forcada J., Nagel E., Alonso-Floriano F. J., Czesla S., et al., 2018, Sci, 362, 1388. doi:10.1126/science.aat5348

Noyes R. W., Hartmann L. W., Baliunas S. L., Duncan D. K., Vaughan A. H., 1984, ApJ, 279, 763. doi:10.1086/161945

Noyes R. W., Hartmann L. W., Baliunas S. L., Duncan D. K., Vaughan A. H., 1984, ApJ, 279, 763. doi:10.1086/161945

Núñez A., Agüeros M. A., Covey K. R., López-Morales M., 2017, ApJ, 834, 176. doi:10.3847/1538-4357/834/2/176

O. L. de Lange, R. E. Raab; Ladder operators for orbital angular momentum. Am. J. Phys. 1 April 1986; 54 (4): 372–375. https://doi.org/10.1119/1.14625

Odert P., Leitzinger M., Hanslmeier A., Lammer H., 2017, MNRAS, 472, 876. doi:10.1093/mnras/stx1969

Odert P., Leitzinger M., Guenther E. W., Heinzel P., 2020, MNRAS, 494, 3766. doi:10.1093/mnras/staa1021

Ofman L., 2010, LRSP, 7, 4. doi:10.12942/lrsp-2010-4

Ogilvie K. W., Vogt C., 1980, GeoRL, 7, 577. doi:10.1029/GL007i008p00577

Ogilvie K. W., Chornay D. J., Fritzenreiter R. J., Hunsaker F., Keller J., Lobell J., Miller G., et al., 1995, SSRv, 71, 55. doi:10.1007/BF00751326

Oklopčić A., Hirata C. M., 2018, ApJL, 855, L11. doi:10.3847/2041-8213/aaada9

Opher M., Drake J. F., Zieger B., Gombosi T. I., 2015, ApJL, 800, L28. doi:10.1088/2041-8205/800/2/L28

Oran R., van der Holst B., Landi E., Jin M., Sokolov I. V., Gombosi T. I., 2013, ApJ, 778, 176. doi:10.1088/0004-637X/778/2/176

Oran R., Landi E., van der Holst B., Sokolov I. V., Gombosi T. I., 2017, ApJ, 845, 98. doi:10.3847/1538-4357/aa7fec

Osten R. A., Hawley S. L., Allred J. C., Johns-Krull C. M., Roark C., 2005, ApJ, 621, 398. doi:10.1086/427275

Owocki S. P., Holzer T. E., Hundhausen A. J., 1983, ApJ, 275, 354. doi:10.1086/161538

Owocki S. P., 1982, PhDT

Pallavicini R., Golub L., Rosner R., Vaiana G. S., Ayres T., Linsky J. L., 1981, ApJ, 248, 279. doi:10.1086/159152

Parker E. N., 1958, ApJ, 128, 677. doi:10.1086/146580

Parker E. N., 1963, ICRC, 1, 175

Parker, E. N. (1965). Interplanetary Dynamical Processes. Interscience Publishers.

Parker E. N., 1988, ApJ, 330, 474. doi:10.1086/166485

Pecaut M. J., Mamajek E. E., 2013, ApJS, 208, 9. doi:10.1088/0067-0049/208/1/9

Pepe, F., Mayor, M., et al. 2004, "The HARPS search for southern extra-solar planets. I. HD 330075 b: A new "hot Jupiter"", Astronomy & Astrophysics, 423, 385-389

Petit P., Dintrans B., Aurière M., Catala C., Donati J.-F., Fares R., Gastine T., et al., 2008, sf2a.conf, 523

Petrucci, Ralph H, 1985, Internet Archive Books, General chemistry : principles and modern applications, New York : Macmillan ; London : Collier Macmillan

Pevtsov A. A., Fisher G. H., Acton L. W., Longcope D. W., Johns-Krull C. M., Kankelborg C. C., Metcalf T. R., 2003, ApJ, 598, 1387. doi:10.1086/378944

Phillips K. J. H., Chifor C., Dennis B. R., 2006, ApJ, 647, 1480. doi:10.1086/505518

Phillips K. J. H., 1995, gusu.book, 400

Pineda J. S., Villadsen J., 2023, NatAs, 7, 569. doi:10.1038/s41550-023-01914-0

Pizzolato N., Maggio A., Micela G., Sciortino S., Ventura P., 2003, A&A, 397, 147. doi:10.1051/0004-6361:20021560

Pizzolato N., Maggio A., Micela G., Sciortino S., Ventura P., 2003, A&A, 397, 147. doi:10.1051/0004-6361:20021560

Pizzolato N., Maggio A., Sciortino S., 2000, A&A, 361, 614

Poppenhaeger K., Lenz L. F., Reiners A., Schmitt J. H. M. M., Shkolnik E., 2011, A&A, 528, A58. doi:10.1051/0004-6361/201016008

Poppenhaeger K., Ketzer L., Ilic N., Magaudda E., Robrade J., Stelzer B., Schmitt J. H. M. M., et al., 2024, arXiv, arXiv:2401.17302. doi:10.48550/arXiv.2401.17302

Poppenhaeger K., 2022, MNRAS, 512, 1751. doi:10.1093/mnras/stac507

Poppenhaeger K., Ketzer L., Ilic N., Magaudda E., Robrade J., Stelzer B., Schmitt J. H. M. M., et al., 2024, arXiv, arXiv:2401.17302. doi:10.48550/arXiv.2401.17302

Pottasch S. R., 1963, ApJ, 137, 945. doi:10.1086/147569

Powell K. G., Roe P. L., Linde T. J., Gombosi T. I., De Zeeuw D. L., 1999, JCoPh, 154, 284. doi:10.1006/jcph.1999.6299

Preusse S., Kopp A., Büchner J., Motschmann U., 2005, A&A, 434, 1191. doi:10.1051/0004-6361:20041680

Prialnik D., 2009, itss.book

Prosser C. F., Randich S., Stauffer J. R., Schmitt J. H. M. M., Simon T., 1996, AJ, 112, 1570. doi:10.1086/118124

Pulkkinen T., 2007, LRSP, 4, 1. doi:10.12942/lrsp-2007-1

Qiu Z., Chen L., Zonca F., 2023, RvMPP, 7, 28. doi:10.1007/s41614-023-00130-7

Ramirez R. M., 2018, Geosc, 8, 280. doi:10.3390/geosciences8080280

Ramstad R., Barabash S., 2021, SSRv, 217, 36. doi:10.1007/s11214-021-00791-1

Ratkiewicz R., Barnes A., Molvik G. A., Spreiter J. R., Stahara S. S., Vinokur M., Venkateswaran S., 1998, A&A, 335, 363

Rauer, H., et al. 2014, "The PLATO 2.0 mission", Experimental Astronomy, 38, 249-330

Reale F., 2014, LRSP, 11, 4. doi:10.12942/lrsp-2014-4

Reames D. V., 2018, SoPh, 293, 47. doi:10.1007/s11207-018-1267-8

Reames D. V., 2021, LNP. doi:10.1007/978-3-030-66402-2

Reames D. V., 2024, FrASS, 11, 1368043. doi:10.3389/fspas.2024.1368043

Redfield S., Linsky J. L., 2004, ApJ, 602, 776. doi:10.1086/381083

Redfield S., Linsky J. L., 2004, ApJ, 613, 1004. doi:10.1086/423311

Redfield S., Linsky J. L., 2008, ApJ, 673, 283. doi:10.1086/524002

Redfield S., Linsky J. L., 2015, ApJ, 812, 125. doi:10.1088/0004-637X/812/2/125

Reep J. W., Russell A. J. B., Tarr L. A., Leake J. E., 2018, ApJ, 853, 101. doi:10.3847/1538-4357/aaa2fe

Rees D. E., 1987, nrt..book, 213

Reiners A., Basri G., 2009, A&A, 496, 787. doi:10.1051/0004-6361:200811450

Reiners A., Shulyak D., Käpylä P. J., Ribas I., Nagel E., Zechmeister M., Caballero J. A., et al., 2022, A&A, 662, A41. doi:10.1051/0004-6361/202243251

Reiners A., Schüssler M., Passegger V. M., 2014, ApJ, 794, 144. doi:10.1088/0004-637X/794/2/144

Reiners A., 2012, LRSP, 9, 1. doi:10.12942/lrsp-2012-1

Ribas I., Guinan E. F., Güdel M., Audard M., 2005, ApJ, 622, 680. doi:10.1086/427977

Richey-Yowell T., Shkolnik E. L., Schneider A. C., Osby E., Barman T., Meadows V. S., 2019, ApJ, 872, 17. doi:10.3847/1538-4357/aafa74

Rieutord M., Rincon F., 2010, LRSP, 7, 2. doi:10.12942/lrsp-2010-2

Riley P., Linker J. A., Mikić Z., Lionello R., Ledvina S. A., Luhmann J. G., 2006, ApJ, 653, 1510. doi:10.1086/508565

Riley P., Ben-Nun M., Linker J. A., Mikic Z., Svalgaard L., Harvey J., Bertello L., et al., 2014, SoPh, 289, 769. doi:10.1007/s11207-013-0353-1

, Robinson, Keith, The P Cygni Profile and Friends, Springer New York, pages 119–125, isbn= 978-0-387-68288-4, doi=10.1007/978-0-387-68288-4_10, url= https://doi.org/10.1007/978-0-387-68288-4_10

Rosén L., Kochukhov O., Wade G. A., 2014, IAUS, 302, 369. doi:10.1017/S1743921314002518

Roussev I. I., Gombosi T. I., Sokolov I. V., Velli M., Manchester W., DeZeeuw D. L., Liewer P., et al., 2003, ApJL, 595, L57. doi:10.1086/378878

Rusomarov N., Kochukhov O., Piskunov N., Jeffers S. V., Johns-Krull C. M., Keller C. U., Makaganiuk V., et al., 2013, A&A, 558, A8. doi:10.1051/0004-6361/201220950

Rutten R. J., 2003, rtsa.book

Ryden, B., 2020. Chapter 11: Solar Wind and the Heliosphere. In Physics of the Solar System (pp. 99–181). Springer.

Réville V., Brun A. S., Matt S. P., Strugarek A., Pinto R. F., 2015, ApJ, 798, 116. doi:10.1088/0004-637X/798/2/116

Réville V., Rouillard A. P., Velli M., Verdini A., Buchlin É., Lavarra M., Poirier N., 2021, FrASS, 8, 2. doi:10.3389/fspas.2021.619463

Saar S. H., Cuntz M., 2001, MNRAS, 325, 55. doi:10.1046/j.1365-8711.2001.04296.x

Saar S. H., Piskunov N. E., Tuominen I., 1992, ASPC, 26, 255

Saar S. H., 1988, ApJ, 324, 441. doi:10.1086/165907

Saar S. H., 1994, IAUS, 154, 493

Sachdeva N., van der Holst B., Manchester W. B., Tóth G., Chen Y., Lloveras D. G., Vásquez A. M., et al., 2019, ApJ, 887, 83. doi:10.3847/1538-4357/ab4f5e

Sanz-Forcada J., Micela G., Ribas I., Pollock A. M. T., Eiroa C., Velasco A., Solano E., et al., 2011, A&A, 532, A6. doi:10.1051/0004-6361/201116594

Sanz-Forcada J., Maggio A., Micela G., 2003, A&A, 408, 1087. doi:10.1051/0004-6361:20031025

Sanz-Forcada J., Affer L., Micela G., 2009, A&A, 505, 299. doi:10.1051/0004-6361/200912069

Saur J., Grambusch T., Duling S., Neubauer F. M., Simon S., 2013, A&A, 552, A119. doi:10.1051/0004-6361/201118179

Scherer K., van der Schyff A., Bomans D. J., Ferreira S. E. S., Fichtner H., Kleimann J., Strauss R. D., et al., 2015, A&A, 576, A97. doi:10.1051/0004-6361/201425091

Schiff L. I., Snyder H., 1939, PhRv, 55, 59. doi:10.1103/PhysRev.55.59

Schmelz J. T., Kimble J. A., Saba J. L. R., 2012, ApJ, 757, 17. doi:10.1088/0004-637X/757/1/17

Schmidt K. H., Bögner M., Buschhorn G., Kotthaus R., Oberhuber R., Rzepka M., 1995, NIMPA, 367, 215. doi:10.1016/0168-9002(95)00544-7

Schmitt J. H. M. M., Collura A., Sciortino S., Vaiana G. S., Harnden F. R., Rosner R., 1990, ApJ, 365, 704. doi:10.1086/169525

Schmitt J. H. M. M., 2001, IAUS, 203, 475

Schwadron N. A., Fisk L. A., Zurbuchen T. H., 1999, ApJ, 521, 859. doi:10.1086/307575

Schwenn R., 1990, pihl.book, 99. doi:10.1007/978-3-642-75361-9_3

Seaton D. B., Berghmans D., Nicula B., Halain J.-P., De Groof A., Thibert T., Bloomfield D. S., et al., 2013, SoPh, 286, 43. doi:10.1007/s11207-012-0114-6

See V., Jardine M., Vidotto A. A., Petit P., Marsden S. C., Jeffers S. V., do Nascimento J. D., 2014, A&A, 570, A99. doi:10.1051/0004-6361/201424323

See V., Jardine M., Vidotto A. A., Donati J.-F., Folsom C. P., Boro Saikia S., Bouvier J., et al., 2015, MNRAS, 453, 4301. doi:10.1093/mnras/stv1925

See V., Matt S. P., Folsom C. P., Boro Saikia S., Donati J.-F., Fares R., Finley A. J., et al., 2019, ApJ, 876, 118. doi:10.3847/1538-4357/ab1096

See V., Matt S. P., Folsom C. P., Boro Saikia S., Donati J.-F., Fares R., Finley A. J., et al., 2019, ApJ, 876, 118. doi:10.3847/1538-4357/ab1096

Segura A., 2018, haex.book, 73. doi:10.1007/978-3-319-55333-7_73

Seli B., Oláh K., Kriskovics L., Kővári Z., Vida K., Balázs L. G., Laming J. M., et al., 2022, A&A, 659, A3. doi:10.1051/0004-6361/202141493

Semel M., 1980, A&A, 91, 369

Shen F., Shen C., Xu M., Liu Y., Feng X., Wang Y., 2022, RvMPP, 6, 8. doi:10.1007/s41614-022-00069-1

Shields A. L., Ballard S., Johnson J. A., 2016, PhR, 663, 1. doi:10.1016/j.physrep.2016.10.003

Shivamoggi B., Rollins D., Pohl L., 2021, Entrp, 23, 1497. doi:10.3390/e23111497

Shkolnik E., Walker G. A. H., Bohlender D. A., Gu P.-G., Kürster M., 2005, ApJ, 622, 1075. doi:10.1086/428037

Shkolnik E., Bohlender D. A., Walker G. A. H., Collier Cameron A., 2008, ApJ, 676, 628. doi:10.1086/527351

Shoda M., Suzuki T. K., Matt S. P., Cranmer S. R., Vidotto A. A., Strugarek A., See V., et al., 2020, ApJ, 896, 123. doi:10.3847/1538-4357/ab94bf

Shulyak D., Reiners A., Wende S., Kochukhov O., Piskunov N., Seifahrt A., 2010, A&A, 523, A37. doi:10.1051/0004-6361/201015229

Silvester J., Wade G. A., Kochukhov O., Bagnulo S., Folsom C. P., Hanes D., 2012, MNRAS, 426, 1003. doi:10.1111/j.1365-2966.2012.21587.x

Skumanich A., 1972, ApJ, 171, 565. doi:10.1086/151310

Smith R. K., Brickhouse N. S., Liedahl D. A., Raymond J. C., 2001, ApJL, 556, L91. doi:10.1086/322992

Snyder C. W., Neugebauer M., 1964, spre.conf, 89

Sokolov I. V., van der Holst B., Oran R., Downs C., Roussev I. I., Jin M., Manchester W. B., et al., 2013, ApJ, 764, 23. doi:10.1088/0004-637X/764/1/23

Sokolov I. V., Holst B. van . der ., Manchester W. B., Su Ozturk D. C., Szente J., Taktakishvili A., Tóth G., et al., 2021, ApJ, 908, 172. doi:10.3847/1538-4357/abc000

Solanki S. K., Inhester B., Schüssler M., 2006, RPPh, 69, 563. doi:10.1088/0034-4885/69/3/R02

Spada F., Lanzafame A. C., Lanza A. F., Messina S., Collier Cameron A., 2011, MNRAS, 416, 447. doi:10.1111/j.1365-2966.2011.19052.x

Spake J. J., Sing D. K., Evans T. M., Oklopčić A., Bourrier V., Kreidberg L., Rackham B. V., et al., 2018, Natur, 557, 68. doi:10.1038/s41586-018-0067-5

Spiegel E. A., Zahn J.-P., 1992, A&A, 265, 106

Stassun K. G., Oelkers R. J., Paegert M., Torres G., Pepper J., De Lee N., Collins K., et al., 2019, AJ, 158, 138. doi:10.3847/1538-3881/ab3467

Stelzer B., Damasso M., Scholz A., Matt S. P., 2016, MNRAS, 463, 1844. doi:10.1093/mnras/stw1936

Stix T. H., 1992, wapl.book

, The Sun: An Introduction, Astronomy and astrophysics library, Springer, 2002. ISBN: 9783540537960. URL: https://books.google.de/books?id=4-Y1AQAAIAAJ.

Stokes G. G., 1851, TCaPS, 9, 399

Stone E. C., Frandsen A. M., Mewaldt R. A., Christian E. R., Margolies D., Ormes J. F., Snow F., 1998, SSRv, 86, 1. doi:10.1023/A:1005082526237

Stone E. C., Cohen C. M. S., Cook W. R., Cummings A. C., Gauld B., Kecman B., Leske R. A., et al., 1998, SSRv, 86, 357. doi:10.1023/A:1005027929871

Strugarek A., Brun A. S., Matt S. P., Réville V., 2015, ApJ, 815, 111. doi:10.1088/0004-637X/815/2/111

Strugarek A., Brun A. S., Donati J.-F., Moutou C., Réville V., 2019, ApJ, 881, 136. doi:10.3847/1538-4357/ab2ed5

Strugarek A., Fares R., Bourrier V., Brun A. S., Réville V., Amari T., Helling C., et al., 2022, MNRAS, 512, 4556. doi:10.1093/mnras/stac778

Strugarek A., 2018, haex.book, 25. doi:10.1007/978-3-319-55333-7_25

Strugarek A., 2021, arXiv, arXiv:2104.05968. doi:10.48550/arXiv.2104.05968

Suess S. T., Richter A. K., Winge C. R., Nerney S. F., 1977, ApJ, 217, 296. doi:10.1086/155579

Suess S. T., 1990, RvGeo, 28, 97. doi:10.1029/RG028i001p00097

Suzuki T. K., Inutsuka S.-. ichiro ., 2006, ApJL, 646, L89. doi:10.1086/506614

Suzuki T. K., Imada S., Kataoka R., Kato Y., Matsumoto T., Miyahara H., Tsuneta S., 2013, PASJ, 65, 98. doi:10.1093/pasj/65.5.98

Testa P., Drake J. J., Peres G., DeLuca E. E., 2004, ApJL, 609, L79. doi:10.1086/422747

Testa P., Saar S. H., Drake J. J., 2015, RSPTA, 373, 20140259. doi:10.1098/rsta.2014.0259

Thompson M. J., Christensen-Dalsgaard J., Miesch M. S., Toomre J., 2003, ARA&A, 41, 599. doi:10.1146/annurev.astro.41.011802.094848

Tian F., Toon O. B., Pavlov A. A., De Sterck H., 2005, ApJ, 621, 1049. doi:10.1086/427204

Tian F., Kasting J. F., Liu H.-L., Roble R. G., 2008, JGRE, 113, E05008. doi:10.1029/2007JE002946

Totten T. L., Freeman J. W., Arya S., 1995, JGR, 100, 13. doi:10.1029/94JA02420

Tsurutani B. T., Lakhina G. S., 1997, RvGeo, 35, 491. doi:10.1029/97RG02200

Tucker W. H., Gould R. J., 1966, ApJ, 144, 244. doi:10.1086/148601

Turnbull M. C., 2015, arXiv, arXiv:1510.01731. doi:10.48550/arXiv.1510.01731

Tóth G., Sokolov I. V., Gombosi T. I., Chesney D. R., Clauer C. R., de Zeeuw D. L., Hansen K. C., et al., 2005, JGRA, 110, A12226. doi:10.1029/2005JA011126

Tóth G., van der Holst B., Sokolov I. V., De Zeeuw D. L., Gombosi T. I., Fang F., Manchester W. B., et al., 2012, JCoPh, 231, 870. doi:10.1016/j.jcp.2011.02.006

Tóth G., van der Holst B., Huang Z., 2011, ApJ, 732, 102. doi:10.1088/0004-637X/732/2/102

Usmanov A. V., Besser B. P., Fritzer J. M., Goldstein M. L., 2000, AdSpR, 25, 1897. doi:10.1016/S0273-1177(99)00613-4

Usmanov A. V., Matthaeus W. H., Goldstein M. L., Chhiber R., 2018, ApJ, 865, 25. doi:10.3847/1538-4357/aad687

Van Doorsselaere T., Srivastava A. K., Antolin P., Magyar N., Vasheghani Farahani S., Tian H., Kolotkov D., et al., 2020, SSRv, 216, 140. doi:10.1007/s11214-020-00770-y

Vauclair S., Laymand M., Bouchy F., Vauclair G., Hui Bon Hoa A., Charpinet S., Bazot M., 2008, A&A, 482, L5. doi:10.1051/0004-6361:20079342

Velli M., Pucci F., Rappazzo F., Tenerani A., 2015, RSPTA, 373, 20140262. doi:10.1098/rsta.2014.0262

Verscharen D., 2012, PhDT. doi:10.5281/zenodo.50886

Vidotto A. A., Opher M., Jatenco-Pereira V., Gombosi T. I., 2009, ApJ, 703, 1734. doi:10.1088/0004-637X/703/2/1734

Vidotto A. A., Opher M., Jatenco-Pereira V., Gombosi T. I., 2010, epsc.conf, 233

Vidotto A. A., Jardine M., Opher M., Donati J. F., Gombosi T. I., 2011, MNRAS, 412, 351. doi:10.1111/j.1365-2966.2010.17908.x

Vidotto A. A., Jardine M., Morin J., Donati J.-F., Lang P., Russell A. J. B., 2013, A&A, 557, A67. doi:10.1051/0004-6361/201321504

Vidotto A. A., Jardine M., Morin J., Donati J. F., Opher M., Gombosi T. I., 2014, MNRAS, 438, 1162. doi:10.1093/mnras/stt2265

Vidotto A. A., Gregory S. G., Jardine M., Donati J. F., Petit P., Morin J., Folsom C. P., et al., 2014, MNRAS, 441, 2361. doi:10.1093/mnras/stu728

Vidotto A. A., Fares R., Jardine M., Moutou C., Donati J.-F., 2015, MNRAS, 449, 4117. doi:10.1093/mnras/stv618

Vidotto A. A., Donati J.-F., Jardine M., See V., Petit P., Boisse I., Boro Saikia S., et al., 2016, MNRAS, 455, L52. doi:10.1093/mnrasl/slv147

Vidotto A. A., Bourrier V., 2017, MNRAS, 470, 4026. doi:10.1093/mnras/stx1543

Vidotto A. A., Bourrier V., Fares R., Bellotti S., Donati J. F., Petit P., Hussain G. A. J., et al., 2023, A&A, 678, A152. doi:10.1051/0004-6361/202347237

Vidotto A. A., 2021, LRSP, 18, 3. doi:10.1007/s41116-021-00029-w

Vilhu O., 1984, A&A, 133, 117

Vilhu O., 1987, LNP, 110. doi:10.1007/3-540-18653-0_118

Villadsen J., Hallinan G., Bourke S., Güdel M., Rupen M., 2014, ApJ, 788, 112. doi:10.1088/0004-637X/788/2/112

Villarreal D'Angelo C. S., Schneiter M., Costa A., Velázquez P., Raga A., Esquivel A., 2014, RMxAC, 44, 170

Villarreal D'Angelo C., Jardine M., See V., 2018, MNRAS, 475, L25. doi:10.1093/mnrasl/slx206

Villarreal D'Angelo C., Vidotto A. A., Esquivel A., Hazra G., Youngblood A., 2021, MNRAS, 501, 4383. doi:10.1093/mnras/staa3867

Vishnu M., Nagaraju K., Mathur H., 2023, JApA, 44, 56. doi:10.1007/s12036-023-09944-w

Vogt S. S., Penrod G. D., 1983, PASP, 95, 565. doi:10.1086/131208

Vogt S. S., Penrod G. D., Hatzes A. P., 1987, ApJ, 321, 496. doi:10.1086/165647

Wade G. A., Donati J.-F., Landstreet J. D., Shorlin S. L. S., 2000, MNRAS, 313, 851. doi:10.1046/j.1365-8711.2000.03271.x

Walter F. M., 1983, IAUS, 102, 193

Wargelin B. J., Drake J. J., 2001, ApJL, 546, L57. doi:10.1086/318066

Wargelin B. J., Drake J. J., 2002, ApJ, 578, 503. doi:10.1086/342270

Wargelin B. J., Saar S. H., Pojmański G., Drake J. J., Kashyap V. L., 2017, MNRAS, 464, 3281. doi:10.1093/mnras/stw2570

Webb D. F., Howard T. A., 2012, LRSP, 9, 3. doi:10.12942/lrsp-2012-3

Weber E. J., Davis L., 1967, ApJ, 148, 217. doi:10.1086/149138

Weber M. A., Browning M. K., 2016, ApJ, 827, 95. doi:10.3847/0004-637X/827/2/95

Weiler M., Carrasco J. M., Fabricius C., Jordi C., 2020, A&A, 637, A85. doi:10.1051/0004-6361/201936908

Whang Y. C., Chang C. C., 1965, JGR, 70, 4175. doi:10.1029/JZ070i017p04175

White N. E., 1996, ASPC, 109, 193

Williams D. M., Kasting J. F., 1997, Icar, 129, 254. doi:10.1006/icar.1997.5759

Wilson O. C., 1978, ApJ, 226, 379. doi:10.1086/156618

Winn J. N., Fabrycky D., Albrecht S., Johnson J. A., 2010, ApJL, 718, L145. doi:10.1088/2041-8205/718/2/L145

Winn J. N., Fabrycky D. C., 2015, ARA&A, 53, 409. doi:10.1146/annurev-astro-082214-122246

Wood B. E., Linsky J. L., 1998, ApJ, 492, 788. doi:10.1086/305077

Wood B. E., Linsky J. L., Müller H.-R., Zank G. P., 2001, ApJL, 547, L49. doi:10.1086/318888

Wood B., Mueller H., Zank G., Izmodenov V., Linsky J., 2002, cosp

Wood B. E., Linsky J. L., Müller H.-R., Zank G. P., 2005, ESASP, 592, 387

Wood B. E., Linsky J. L., 2006, ApJ, 643, 444. doi:10.1086/501521

Wood B. E., Izmodenov V. V., Linsky J. L., Malama Y. G., 2007, ApJ, 657, 609. doi:10.1086/510844

Wood B. E., Linsky J. L., 2010, ApJ, 717, 1279. doi:10.1088/0004-637X/717/2/1279

Wood B. E., Laming J. M., Warren H. P., Poppenhaeger K., 2018, ApJ, 862, 66. doi:10.3847/1538-4357/aaccf6

Wood B. E., Müller H.-R., Redfield S., Konow F., Vannier H., Linsky J. L., Youngblood A., et al., 2021, ApJ, 915, 37. doi:10.3847/1538-4357/abfda5

Wood B. E., Alexander W. R., Linsky J. L., 1996, ApJ, 470, 1157. doi:10.1086/177939

Wood B. E., Linsky J. L., Zank G. P., 2000, ApJ, 537, 304. doi:10.1086/309026

Wood B. E., Redfield S., Linsky J. L., 2001, arXiv, astro-ph/0107033. doi:10.48550/arXiv.astro-ph/0107033

Wood B. E., Laming J. M., Karovska M., 2012, ApJ, 753, 76. doi:10.1088/0004-637X/753/1/76

Wood B., Mueller H. R., Redfield S., 2014, AAS

Wood B. E., 2004, AIPC, 719, 387. doi:10.1063/1.1809545

Wright N. J., Drake J. J., Mamajek E. E., Henry G. W., 2011, ApJ, 743, 48. doi:10.1088/0004-637X/743/1/48

Wright N. J., Drake J. J., 2016, Natur, 535, 526. doi:10.1038/nature18638

Wright N. J., Newton E. R., Williams P. K. G., Drake J. J., Yadav R. K., 2018, MNRAS, 479, 2351. doi:10.1093/mnras/sty1670

Yan F., Henning T., 2018, NatAs, 2, 714. doi:10.1038/s41550-018-0503-3

Yang Z., Bethge C., Tian H., Tomczyk S., Morton R., Del Zanna G., McIntosh S. W., et al., 2020, Sci, 369, 694. doi:10.1126/science.abb4462

Zaire B., Guerrero G., Kosovichev A. G., Smolarkiewicz P. K., Landin N. R., 2017, IAUS, 328, 30. doi:10.1017/S1743921317003970

Zank G. P., Pauls H. L., Williams L. L., Hall D. T., 1996, JGR, 101, 21639. doi:10.1029/96JA02127

Zank G. P., 1999, SSRv, 89, 413. doi:10.1023/A:1005155601277

Zarka P., Queinnec J., Crary F. J., 2001, P&SS, 49, 1137. doi:10.1016/S0032-0633(01)00021-6

Zarka P., 2007, P&SS, 55, 598. doi:10.1016/j.pss.2006.05.045

Zechmeister M., Kürster M., Endl M., Lo Curto G., Hartman H., Nilsson H., Henning T., et al., 2013, A&A, 552, A78. doi:10.1051/0004-6361/201116551

Zeeman P., 1896, VMKAN, 5, 181

Zeeman P., 1897, ApJ, 5, 332. doi:10.1086/140355

Zendejas J., Segura A., Raga A. C., 2010, Icar, 210, 539. doi:10.1016/j.icarus.2010.07.013

de Jager C., Nieuwenhuijzen H., 1987, A&A, 177, 217

van den Oord G. H. J., Doyle J. G., 1997, A&A, 319, 578

van Leeuwen F., 2007, A&A, 474, 653. doi:10.1051/0004-6361:20078357

van der Holst B., Sokolov I. V., Meng X., Jin M., Manchester W. B., Tóth G., Gombosi T. I., 2014, ApJ, 782, 81. doi:10.1088/0004-637X/782/2/81

van Saders J. L., Ceillier T., Metcalfe T. S., Silva Aguirre V., Pinsonneault M. H., García R. A., Mathur S., et al., 2016, Natur, 529, 181. doi:10.1038/nature16168

van der Holst B., Manchester W. B., Klein K. G., Kasper J. C., 2019, ApJL, 872, L18. doi:10.3847/2041-8213/ab04a5

van Saders J. L., Pinsonneault M. H., Barbieri M., 2019, ApJ, 872, 128. doi:10.3847/1538-4357/aafafe

von Steiger R., Schwadron N. A., Fisk L. A., Geiss J., Gloeckler G., Hefti S., Wilken B., et al., 2000, JGR, 105, 27217. doi:10.1029/1999JA000358

von Steiger R., Schwadron N. A., Fisk L. A., Geiss J., Gloeckler G., Hefti S., Wilken B., et al., 2000, JGR, 105, 27217. doi:10.1029/1999JA000358

von Steiger R., Zurbuchen T. H., McComas D. J., 2010, GeoRL, 37, L22101. doi:10.1029/2010GL045389

Ó Fionnagáin D., Vidotto A. A., Petit P., Folsom C. P., Jeffers S. V., Marsden S. C., Morin J., et al., 2019, MNRAS, 483, 873. doi:10.1093/mnras/sty3132

Acknowledgment

Whenever I read a thesis, I always start with the acknowledgment section. It provides insight into the person behind the work. Also, no one prepares you for writing the acknowledgment section; it took more time than summarizing the entire Thesis! I guess it is longer than the abstract. So, brace yourself for a long read—grab a coffee or a beer, whatever you prefer.

Reflecting on my PhD journey, I can confidently say it has been one of the best experiences of my life. This journey was not just about learning new things, giving talks, attending conferences, and traveling the world—it was also about meeting incredible people. The journey started ever since school. From school and high school to university and now during my PhD, I've encountered amazing friends. I hope that in a few years, when I revisit this section and read these names, I can still say we're friends or at least we are still in contact.

I want to express my appreciation for the bands, concerts, and other experiences that provided much-needed breaks and inspiration throughout this journey.

For my supervisors, *Katja* and *Julían*, thank you for being the best supervisors I could ask for. *Katja*, thank you for making one of my dreams come true. Your supervision and the welcoming environment you created made work truly enjoyable. Your personality and guidance are a constant inspiration.

Julían, you have been an outstanding supervisor and mentor, always caring and offering valuable tips. I still remember our first meeting over zoom back in 2020 during the pandemic. You emphasized the importance of enjoying the PhD journey and staying passionate about our research. You assured me that I would get to experience at least one in-person conferences, and here I am, almost four years later, having attended plenty conferences. You have always supported my decisions, listened to my concerns, and prioritized what is best for my career and aspirations. Thank you for correcting the Thesis in short time. Thank you for introducing the Scotch hour, and making me share the organization of it. The scotch hour became one of my favorite chilling times and made me meet amazing people. Lastly, your support has been invaluable and I know I have gained a person I can rely on.

Eliana, mi hermana de otro señor y madre. Your kindness and support have left an incredible mark on me. I truly appreciate your warm and welcoming personality and your readiness to lend a hand. Your assistance extended beyond education; you were instrumental in finding the perfect wedding dress for me. Without you, I wouldn't have found a gown that gave the "wow" factor I was looking for! And let's not forget the unforgettable bachelor party you organized for me. Most importantly, thank you for always reminding me that even the little things in life are worth celebrating.

Martina, you're one of the most dear people in my life. Reflecting on our journey together, I find it hard to know where to begin. From sharing our office space to embarking on hilarious adventures at Oktoberfest and St. Patrick's Day, and exploring unforgettable destinations like Prague, Nuremberg, Bamberg, and Erlangen, our experiences have been truly remarkable. Our shared aversion to whiskey made our whiskey tasting sessions during Scotch hour even funnier. I'm especially grateful for the Italian curse words you taught me; they'll undoubtedly come in handy when I visit Italy. Your enthusiasm for the little things made my time at the office enjoyable. Whether it was decorating for Halloween (our big spider says hi!), getting into the Christmas spirit, or simply sharing the office references. I know our adventures together are far from over, and I can't wait to create more memories with you. Overall, thank you for simply being you. And let's not forget to save Bandit!

Nikoleta, du bist eine meiner liebsten Personen geworden. Thank you for caring about me and showing it through your actions and follow-ups. I appreciate the traditions we've created, from our breakfasts to our spontaneous secondhand bookshop visits. Your daily visits to my office around 11:00 AM have become a cherished routine. Thank you for introducing me to new places such as: secondhand stores, secondhand bookstores, cheese shops, among others . I know we will explore more places together in the future and we will keep on creating new routines. I also want to thank you for helping me practice German and for translating the abstract.

Vada, thank you for being such a wonderful friend. The adventures we've shared have been nothing short of magical—from trips to bookstores, Prague, and coffee shops. I'll never forget our journey to Spreewald, the Devil's Bridge, and getting lost in the woods. And who could forget our memorable visit to Oranienburg, where we stumbled upon Café Louise amidst people wearing oxygen masks—it was quite the adventure. The book club meetings and our other escapades have added so much joy to my life. You bring a rainbow and sunshine wherever you go. I look forward to many more adventures

Elefteria, I am glad we met not too late in my PhD journey, or else it would have been a shame to

miss out on the great camaraderie and hangouts. I really appreciate these sudden board game nights or cinema outings. I really like your passion for the cinema, which we share, but you have it in larger dosage. Thank you for making me feel like I have known you for years. I am sure we will have more memories together and also with *Jibin* and the different food tasting cuisines.

Amy, of all the places we could have crossed paths, I never expected it to be in Korea. I'm incredibly grateful that you returned to AIP, and that we're embarking on this journey together, nearly finishing it side by side. Being part of this shared experience brings me immense joy, and I hope our journey together extends far beyond our time at AIP.

Anna, little did we know that our conference in South Korea would mark the beginning of our friendship. I will always remember our outings with me. From escape the room to the simple joy of taking random walks in the park or enjoying a beer together. Our double dates with you and Jonathan have been particularly memorable. Thank you for your constant support and caring personality.

For my D&D group: *Alex*, our dungeon master whose lack of drawing skills is more than compensated for by his incredible storytelling imagination. *Robert* (Hrotgar), you will forever be the bravest yet weakest barbarian I've ever known. *Ioannis* (Django), the womanizer bard who constantly charms our way out of trouble, and *Jad* (Asmodeus), the paladin who always ends up fixing our screw-ups. Thank you all for taking me on an adventure in the realm of imagination. I'm grateful for the outings we've had, from axe throwing to exploring the video game museum, tasting XXL Schnitzels, and attempting to empty that 10-liter beer barrel with Martina. Hanging out with you guys was a blast, and it still is.

Laura, you were the first person to welcome me and show me around. I'll never forget all the help you provided, from understanding German documents to being my side when I had to overtake an operation. You introduced me to the best kebab and falafel in Babelsberg. Thank you for the walks and for making me feel so welcome. And a special thank you for the special editions Christmas beers you brought me from Munich.

Engin, I have always admired your enthusiasm for astrophysics. Though we didn't interact much during your time at AIP, I'm confident we'll have more opportunities to connect in the future.

Katrin, you were the first person to volunteer to pick me up from the train station before even knowing me. Thank you for your kindness and for being there for me throughout my stay at AIP. Also, thank you for the occasional coffee from the fancy machine.

Ekaterina, I've always admired your passion for science and your unwavering focus.

Joanna, thank you for your support and enthusiasm, even for the little things. It was a pleasure sharing the office with you, even briefly.

Desmond, thank you for showing interest even in my stupid stories and Beer.

Grace, though our time together was brief and we didn't hang out much, I'll always cherish the day we went to the zoo. Despite the uncooperative weather, it was a memorable experience. Hopefully, we'll meet again, whether in Europe or the USA.

Yuki, it was a pleasure meeting you and having adventures together. Cheers to more in the future.

Laure, our friendship means a lot to me. You never failed to show how much you believe in me.

Lara, I still remember the days we spent applying for PhDs instead of working, and our walks around AUB talking about our dreams. Now, here we are—I'm finishing my PhD, and you're on your own journey toward it. After all these years, the universe didn't fail us. Sharing this experience with you has been invaluable. The support, laughter, and mutual understanding made the challenges bearable and the successes sweeter. You'll always be one of my dearest friends, and your determination continues to inspire me. Thank you for being part of this journey.

Leen, my dearest student/friend, thank you for always showing appreciation and for giving me the opportunity to be your tutor for couple of years. It was an honor.

Angela, I still remember when I told you I was shifting from nanoscience to astrophysics, and you said I was crazy! Here we are, seven years later, with me on my way to earning a doctorate in astrophysics. Thank you for your constant support throughout this journey.

Elie, thank you for your support over the years from our bachelor years till now.

Rosy, my dear friend, thank you for your constant support and your dark sense of humor.

Diana, I cherish our friendship beyond words. Thank you for your unwavering support.

Vanessa, thank you for always believing in me and supporting me.

Nayla, I've known you for over a decade, and whether we're in the same country or miles apart, you've never stopped showing me your support and admiration. You've even managed to get people

in the corporate industry to follow my work! Thank you for making me part of your family and for sharing memories with me, whether in Lebanon or in Europe.

Marie-Claire, my dear friend and personal medical advisor, I always enjoy our science discussions. I learn something new in the medical field, and you learn something in astrophysics. It never gets boring. Over the decade we've known each other, our passion for science has only grown stronger. Whether in person or over video call, you've consistently shown me your support and interest in my work and aspirations. Thank you for believing in me!

Paty, I've known you for more than two decades, which is incredible! What's even more incredible is how you've shown your care and support throughout all these years. I'm very grateful for that.

Nour, we had such a rare and special adventure. When we were younger, we always imagined how awesome it would be if we ended up going to the same university. A few years later, we did! Then, we both wanted to pursue research and get a PhD. You've already achieved yours, and I'm on my way to getting mine. Thank you for sharing some of my dreams; it made the journey even more interesting.

Tarek, thank you for laying the foundation for my understanding of basic concepts. I remember promising you that if I achieved my goals, I would never forget your help during my early school years. Thank you for everything.

For *mum* and *dad*, I want to say, "I MADE IT!!" I know my academic path hasn't always been smooth, but thank you for your unwavering support. Thank you for making my career path possible. You witnessed both my failures and successes, and I'm grateful I could share this journey with you. Thank you for your hard work. It all started when you helped me pursue my master's in astrophysics in France. I am forever grateful to have you as my parents, and I hope this milestone feels as great for you as it does for me. I love you so much.

For my *brother* and *sister*, thank you for your support and for showing how proud you are of me.

Special thanks to my *grandmother* and *aunts* for always believing in me.

To my *other family*, thank you for your support in my academic career and for always showing me how much you care and how much you believe in me.

Jad, my love, I don't know where to begin. Thank you for standing by my side and believing in me all these years. Your support has meant the world to me. From helping me with poster templates to editing and providing insights to improve my work, your assistance has been invaluable. I'm so grateful to have shared the milestones in my life with you and to have grown together. The fact that we transitioned from dating to engaged, and finally to married during my PhD years, makes this journey even more meaningful. I can't express enough gratitude for the amazing memories and priceless moments we've shared. Thank you for being the supportive and understanding partner you are, and for tolerating my isolation throughout the Thesis writing. I love you immensely.

Lastly, I would like to mention people I met throughout my masters/PhD years and hope to have more memories with them in the future; *Abinaya*, *Arouj*, *Cinta*, *Ekaterina dineva*, *Elena*, *Léna*, *Ola*, *Özgün*, *Silva*, *Steven*. I hope I haven't forgotten anyone.

EIDESSTATTLICHE ERKLÄRUNG

Hiermit bestätige ich, dass die vorliegende Arbeit selbständig verfasst und keine anderen als die angegebenen Quellen und Hilfsmittel benutzt sowie Zitate und gedankliche Übernahmen kenntlich gemacht wurden. Die Arbeit wurde ausschließlich an der Universität Potsdam und keiner anderen Hochschule eingereicht.

Ort, Datum Unterschrift